A Study of Pseudopotential Lattice Boltzmann Method with Applications to Thermal Bubble Nucleation

Kamil Pasieczynski

Submitted for the degree of Doctor of Philosophy

Heriot-Watt University
School of Engineering and Physical Sciences
Institute of Mechanical, Process and Energy Engineering
May 2020

Abstract

The nature of the work dealt with in this thesis is mathematical modelling of multiphase flows. The main objective of this doctoral work was to study multiphase lattice Boltzmann models (LBM) and to develop an advanced pseudopotential model. Specifically, advanced thermal lattice Boltzmann models were applied to study bubble nucleation in nucleate pool boiling at subatmospheric pressures. The numerical investigations carried out as part of this work follow the format well-established in the literature and allow further studies in more complex geometries.

The work carried out contributes to current discussions in the literature and fulfils the recommendations of a number of authors. Fluid-fluid interactions in the Yuan-Schaefer, multipseudopotential interaction and piecewise linear equation of state methods were investigated. Multipseudopotential interaction was established as a practicable method of multiphase simulations by combination with the multiple relaxation time collision operator, surface tension modification methods and with modified temperature double distribution function and hybrid (4^{th} order Runge-Kutta) thermal LBM models.

Thermal LBM simulations were found to agree well with experimental findings on the influence of subatmospheric pressure on bubble nucleation. It was found that as pressure is lowered in LBM simulations the size of bubbles nucleated increases, according to $bubble\ diameter \sim pressure^{-1}$, with results falling in between experimental data for brass and stainless steel tubes.

Dedication

I would like to dedicate this thesis to my partner, Camille, for her love and support during the time which has proved trying to me and to my parents, Monika and Waldemar, for instilling the value of education and knowledge in me from my earliest days.

Acknowledgement

First and foremost, I would like to thank my supervisor, Dr Baixin Chen, for his help and advice during the duration of my PhD study. I would also like to thank Dr Marius Dewar, Dr Sorush Khajepor, Dr Tariq Chaudhary, Stephen Burnside, Mehmood Mubbashar, Umer Saleem and Amin Zarareh for the enjoyable and interesting discussions during our group meetings.

HERIOT WATT UNIVERSITY

Research Thesis Submission

Name:	Kamil Pasieczynski		
School:	Engineering and Physical Sciences		
Version: *(i.e. First, Resubmission, Final)*	Final	Degree Sought:	Doctor of Philosophy in Mechanical Engineering

Declaration

In accordance with the appropriate regulations I hereby submit my thesis and I declare that:

1. The thesis embodies the results of my own work and has been composed by myself
2. Where appropriate, I have made acknowledgement of the work of others
3. The thesis is the correct version for submission and is the same version as any electronic versions submitted*.
4. My thesis for the award referred to, deposited in the Heriot-Watt University Library, should be made available for loan or photocopying and be available via the Institutional Repository, subject to such conditions as the Librarian may require
5. I understand that as a student of the University I am required to abide by the Regulations of the University and to conform to its discipline.
6. I confirm that the thesis has been verified against plagiarism via an approved plagiarism detection application e.g. Turnitin.

* *Please note that it is the responsibility of the candidate to ensure that the correct version of the thesis is submitted.*

Signature of Candidate:	K. Pasieczynski	Date:	03.05.2020

Submission

Submitted By *(name in capitals)*:	Kamil Pasieczynski
Signature of Individual Submitting:	K. Pasieczynski
Date Submitted:	03.05.2020

For Completion in the Student Service Centre (SSC)

Limited Access	Requested	Yes		No		Approved	Yes		No	
E-thesis Submitted ***(mandatory for final theses)***										
Received in the SSC by *(name in capitals)*:						Date:				

Contents

List of Tables

List of Figures

Nomenclature

ρ = density

u = velocity

L = characteristic length

μ = dynamic viscosity

ν = kinematic viscosity

c_s = speed of sound

λ = mean free path length, thermal conductivity, multipseudopotential interaction equation of state parameter

η = shear viscosity, thermal model constant

η_B = bulk viscosity

T = temperature

R = universal gas constant

α = von Karman relation constant, thermal diffusivity, acentric factor

t = time

p, P = pressure

P_c = threshold pressure

$\boldsymbol{F}$ = forces including body forces and intermolecular forces

σ = surface tension, differential cross section, surface tension adjustment term

$\boldsymbol{P}$ = stress tensor

$\boldsymbol{n}$ = unit normal to the interface

H = mean curvature

r = radius

d = diameter

g = acceleration due to gravity, relative speed

θ = angle

e = internal energy

E = total energy

c_V = heat capacity at constant volume

c_P = heat capacity at constant pressure

$\boldsymbol{\Pi}$ = viscous stress tensor

$\boldsymbol{\Pi}:\nabla\boldsymbol{u}$ = viscous heat dissipation

$\boldsymbol{q}$ = heat flux

w_i = lattice weight

$\boldsymbol{c}_i$ = lattice particle direction

$\boldsymbol{e}_i$ = lattice microscopic particle velocity

f = distribution function, also called probability density

f_{eq} = equilibrium distribution

$\boldsymbol{x}$ = position coordinate

ξ = microscopic particle velocity

ϵ = expansion/ smallness parameter

φ = solution of a generic partial differential equation

b = boundary condition constant

k = permeability, temperature equation constant

τ = relaxation time

$C_i(f_1, \ldots, f_b)$ = multibody collision operator

A_{ij} = scattering matrix

ω = relaxation rate

v = velocity

$\mathcal{H}$ = H-function

$\Omega(f)$ = collision operator

Π^{eq}= equilibrium moment

Δx = spatial change, lattice spacing

$\Delta t, \delta_t$ = temporal change, timestep

$\boldsymbol{H}^{(n)}(\boldsymbol{x})$ = Hermite polynomial of n-th order

$\omega(\boldsymbol{x})$ = weight/generating function

d = dimension

$\boldsymbol{a}^{(n)}$ = expansion coefficient

$P^{(N)}$ = polynomial of order n

ζ = parametrisation of a trajectory in space

Ω = solid angle

m = moment

m^{eq} = equilibrium moment

$\boldsymbol{M}$ = transformation matrix

$\boldsymbol{S}$ = relaxation matrix, source term in the thermal models

Λ = magic parameter

G = strength of interaction

ψ = pseudopotential

K = Runge-Kutta function

h = Runge-Kutta increment

g = temperature distribution function

$\boldsymbol{\Lambda}$ = temperature relaxation matrix

ϕ = term introducing the temperature equation into the modified temperature double distribution function LBM model

P_{ab} = momentum flux tensor

W = interface thickness

a, b= cubic equation of state constant

θ_V = pressure slope in the vapour branch

θ_M = pressure slope in the unstable branch

θ_L = pressure slope in the liquid branch

ρ_1 = vapour phase spinodal point

ρ_2 = liquid phase spinodal point

ε = multipseudopotential interaction equation of state parameter, mechanical stability condition constant

C = multipseudopotential interaction equation of state parameter

$\boldsymbol{I}$ = identity matrix

$\boldsymbol{C}$ = Li-Luo surface tension modification term

$\boldsymbol{Q_m}$ = Huang-Wu surface tension and thermodynamic consistency adjustment term

κ = surface tension modification parameter

m = molecular mass

k = Boltzmann's constant

a = molecular diameter

ω_α = lattice weights

χ = thermal diffusivity, parameter modifying G weightings in thermal MPI models

Non-dimensional numbers

Re = Reynolds number

Ma = Mach number

Kn = Knudsen number

We = Weber number

M = mobility

Ca = capillary number

Bo = Bond number

Pr = Prandtl number

Indices

i = phase, direction, particle, matrix coordinate

x, y = directions

α, β, γ = vector, matrix and tensor components

w = wetting phase

g = gas phase

B = boundary

j = direction, multipseudopotential index

p = linear momentum

$1, 2, 3, 4$ = molecule number or Runge-Kutta increment number

v = viscosity, vapour

l = liquid

ϵ = kinetic energy square

e = bulk viscosity

q = energy-flux

k = matrix coordinate

b = barycentric (applies to velocity in multicomponent models)

α = particle

r = reduced (e.g. temperature, pressure)

w = wall

Chapter 1 - Introduction

This doctoral work is motivated by the need for further research in the field of the lattice Boltzmann method (LBM) [1], in order to put this simulation method on an equal footing with the more mature computational fluid dynamics (CFD) technology and to reap the benefits this promising mesoscopic method offers. LBM is a relatively novel method for simulating fluid dynamics. It shows considerable potential in cases where traditional CFD is difficult or not practicable to use and it has the potential to be useful to the engineering community for the simulation of physical and chemical processes [2].

The objective of this study was to advance our understanding of the pseudopotential group of multiphase lattice Boltzmann models and to apply a thermal pseudopotential model to study nucleate pool boiling at subatmospheric pressures. The multitude of different pseudopotential models and schemes suggests that their understanding needs to be furthered. Thermal multiphase simulations were carried out in order to investigate the effects of lowering pressure on bubble nucleation during nucleate pool boiling. The effects of subatmospheric pressure on bubble nucleation have been identified to be of industrial importance as part of a doctoral study at Heriot-Watt University [3]. Salem recommended development of CFD models capable of simulation of nucleate boiling at subatmospheric pressures.

The approaches undertaken in this work in order to generate findings follow the accepted methods in the literature. Surface tension values were calculated using the typical test of Laplace's law. Thermodynamic consistency simulations were carried out to examine conformity to the Maxwell equal area construction [4] using flat interfaces to separate liquid and vapour. Using curved interfaces would result in the thermodynamic consistency being affected by the Laplace's law, instead of being exclusively determined by the mechanical stability condition [5, 6]. Spurious velocity was investigated by simulating a liquid droplet in a gravity free domain with periodic boundaries in all four directions. Stability effects in dynamic cases were examined using a droplet splashing on a thin liquid layer. Thermal models were validated by examining conformity to the D^2-law [7] for droplet evaporation following the approach by Li et al. [8]. Dimensionless numbers including the Reynolds number, Weber number and Bond number were used in order to examine the physical meaning of the results.

The main contributions contained in this work include: furthered understanding of pseudopotential models including understanding of simulated interparticle interactions; development of a hybrid pseudopotential model which consists of the Yuan-Schaefer method up to the upper spinodal point and of the piecewise linear method beyond the upper spinodal point; reformulation of fluid-solid interactions in the modified pseudopotential method; development of a method of combining multipseduopotential interaction with the multiple relaxation time collision operator and adjustment of thermodynamic consistency; development of a thermal MPI model; application of LBM to study nucleate pool boiling at subatmospheric pressures.

Chapter 2 - Literature Review

2.1. Multiphase Flow

One of the first questions that needs to be answered in fluid dynamics problems is about the nature of the fluid and about the nature of the flow. It is important to determine whether the fluid is compressible or incompressible in the case under investigation. It is also instructive to determine whether the flow is viscous or inviscid. Dimensionless numbers are valuable tools in answering this question. Fluid dynamics can be characterised using dimensionless numbers due to the law of similarity. Dimensionless numbers are ratios of forces. Hence, they provide an insight into physical phenomena directing the observable parameters. The main two dimensionless numbers used to characterise fluid flow are the Reynolds number (Re) and the Mach number (Ma) [9]:

$$Re^i = \frac{\rho_i u_i L}{\mu_i};\ Ma = \frac{u}{c_s} \qquad (1)$$

Reynolds number helps to answer the question whether the flow is viscous or inviscid and Mach number assists in determining whether the fluid is compressible or incompressible. At very high values of the Reynolds number, viscous forces can be considered to be negligible. Flow can be considered to be incompressible at low values of the Mach number.

A third useful dimensionless number, which provides an insight into the collisional dynamics of particles which comprise fluids, is the Knudsen number (Kn) [10]:

$$Kn = \frac{mean\ free\ path\ length}{characteristic\ length} \qquad (2)$$

Mean free path length is obtained from the following equation [11]:

$$Mean\ free\ path\ length\ (\lambda) = \frac{\mu\sqrt{\pi}}{\rho\sqrt{2RT}} \qquad (3)$$

The practical value of the Knudsen number consists of the ability to determine whether the continuum flow assumption is valid or whether statistical methods are needed to investigate the fluid flow which is being examined [10]. The second application of Knudsen number is in investigating boundary conditions [10]. The von Karman relation illustrates the relationship between the Knudsen number and the other two important non-dimensionless numbers [12]:

$$Kn = \alpha \frac{Ma}{Re} \tag{4}$$

Continuum fluid flow is commonly studied using the Navier-Stokes equations. Their practical usefulness consists of the ability to compute the flow velocity field. However, solving these equations presents challenges which are so considerable as to shape the field of fluid dynamics research. The continuity and the Navier-Stokes equations take the following forms, respectively [12]:

$$\frac{\partial \rho}{\partial t} + \nabla \cdot (\rho \boldsymbol{u}) = 0 \tag{5}$$

$$\frac{\partial (\rho u_\alpha)}{\partial t} + \frac{\partial \left(\rho u_\alpha u_\beta\right)}{\partial x_\beta} = -\frac{\partial p}{\partial x_\alpha} + \frac{\partial}{\partial x_\beta}\left[\eta\left(\frac{\partial u_\alpha}{\partial x_\beta} + \frac{\partial u_\beta}{\partial x_\alpha}\right) + \left(\eta_B - \frac{2\eta}{3}\right)\frac{\partial u_\gamma}{\partial x_\gamma}\delta_{\alpha\beta}\right] + \boldsymbol{F}_\alpha \tag{6}$$

Traditionally, equations governing continuum multiphase flow were obtained by extending single-phase equations and were semi-empirical in nature [13]. This approach is deficient in terms of including physical phenomena underpinning the evolution of macroscale variables in complex flow cases.

Conservation of mass and momentum requires that the velocity of both components in a multiphase flow situation be the same at the fluid interface as can be seen in Figure 1.

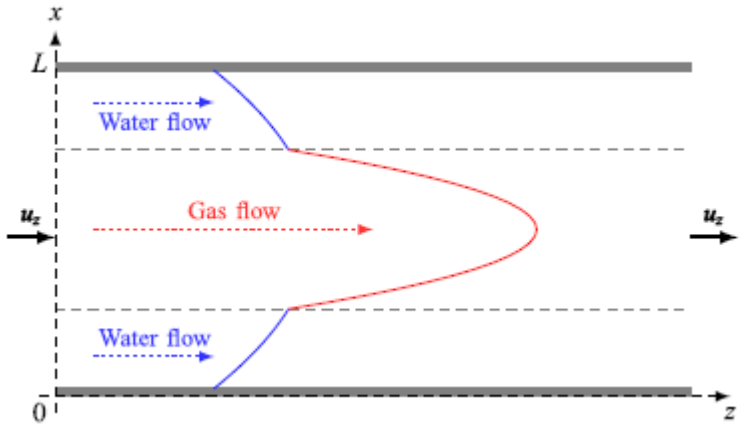

Figure 1- The velocity profile for two-phase Poiseuille flow [14, 15].

This requirement results in the following two equations at the interface [13]:

$$\boldsymbol{u}_1 = \boldsymbol{u}_2 \tag{7}$$

$$\boldsymbol{n} \times \boldsymbol{P}_1 - \boldsymbol{n} \times \boldsymbol{P}_2 + 2\sigma H \boldsymbol{n} = 0 \tag{8}$$

Relative adherence of the two fluids and lack of mass transfer are expressed in equations 7 and 8 [13]. Commonly, no-slip is assumed at the fluid-solid interface. A no-slip condition means that fluid does not move relative to the solid at the fluid-solid interface. As can be seen in Figure 2, no-slip flow occurs at low values of the Knudsen number, i.e. when Knudsen number is less than approximately 10^{-3}.

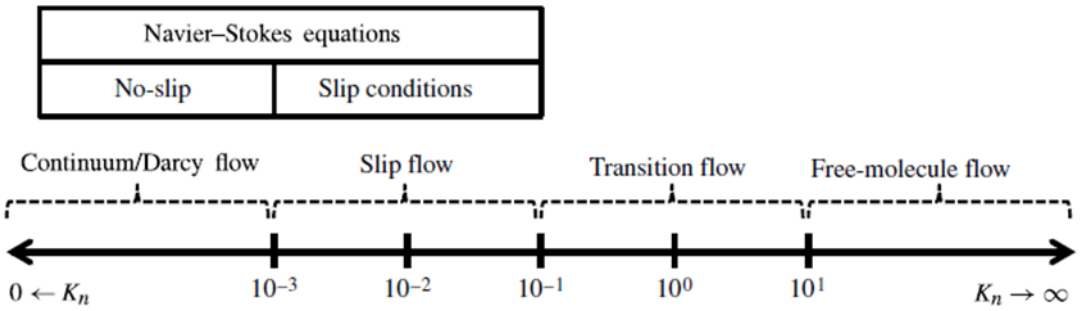

Figure 2- Flow regimes based on the Knudsen number [16].

Further difficulties arise when multiphase flow occurs in complex geometries, e.g. in porous media. The resultant difficulties have implications for both experimental measurements and mathematical modelling. At the microscale, the forces driving flow include: applied pressure difference, electric fields, capillary forces and gradients in interfacial tension [17]. Additional dimensionless numbers used to characterise multiphase flow in porous media include the mobility (M), capillary number (Ca) and bond number (Bo) [14]:

$$M = \frac{\mu_w}{\mu_g};\ Ca^i = \frac{\mu_i u_i}{\sigma};\ Bo = \frac{(\rho_w - \rho_g) g L^2}{\sigma} \qquad (9)$$

Weber number is also an important dimensionless number where droplet or bubble deformation is of interest [18]:

$$We = \frac{\rho u^2 d}{\sigma} \qquad (10)$$

It relates the inertial forces to the surface tension generated forces [10, 18]. Weber number is commonly used in the study of droplet and bubble break-up. For example, Unnikrishnan et al. [19] studied droplet splashing on chemically modified metallic surfaces at high Weber numbers (greater than 200). Montessori et al. [20] used the Entropic LBM model to simulate droplet collisions at high Weber numbers. Different Weber number expressions also exist for use in various correlations, which are used in,

for example, entrainment studies [21]. At very high values of the Weber number surface tension considerations can be neglected [10]. We = 1 means that inertial and surface tension forces are equally important. Weber number can also be used to predict the degree of surface turbulence, with Weber number less than 2.0 indicting lack of surface turbulence [22]. At very high values of Weber number, the concept of surface turbulence becomes obsolete as the flow becomes jetting, spraying or atomising in nature [22]. According to Campbell, Weber number has not been used to its full potential in some fields of research including casting research [22].

As an example of a multiphase case encountered in porous media, immiscible displacement in porous media can be classified into three categories: stable displacement, viscous fingering and capillary fingering (illustrated in Figure 3) [23]. Inertial and buoyancy (gravity) forces were neglected in Lenormand's et al. [23] models, inclusion of which could be examined by, for example, the addition of Bond number (as shown in the inset) [24]. Evidently, considerable complexity is encountered in this type of problems.

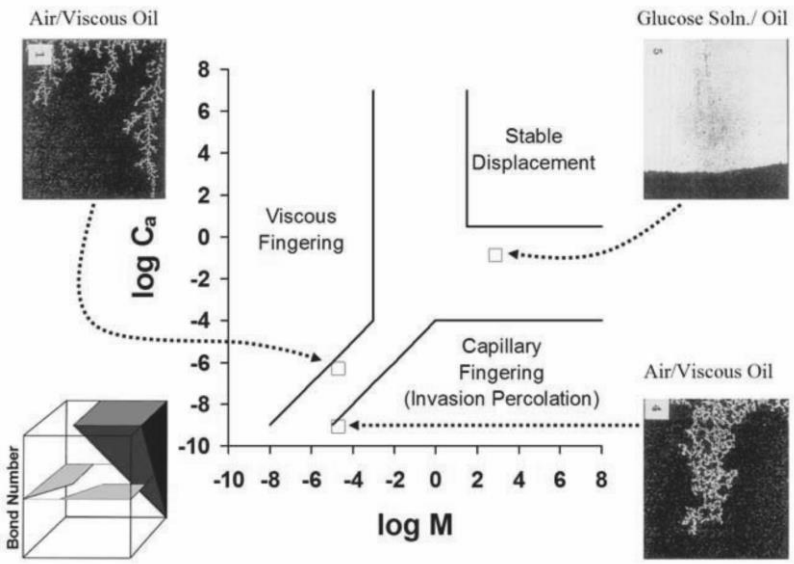

Figure 3- Types of immiscible displacement in porous media [23-25].

In order to penetrate the porous medium, the invading liquid needs to overcome capillary forces which manifest themselves in the form of threshold pressure (P_c), given by the Young-Laplace equation [23]:

$$P_c = \frac{2\sigma \cos\theta}{r} \tag{11}$$

Unstable displacement can lead to trapping of the non-wetting phase.

At low values of the Reynolds number, inertial forces can usually be ignored, leading to simplification. For inertial forces to be negligible, Reynolds number should be smaller than one. Reynolds number could be smaller than one due to low velocity and small diameter of pores/flow channels [13]. Low velocities mean that compressibility effects can be ignored [17].

2.1.1. Thermal Effects

The equations for studying thermal effects accompanying the Navier-Stokes equations can track either the internal energy or total energy.

$$Internal\ energy\ (e) = c_V T \tag{12}$$

$$Total\ energy\ (E) = e + 0.5|\boldsymbol{u}|^2 \tag{13}$$

These energy equations take the following respective forms [26]:

$$\frac{\partial(\rho e)}{\partial t} + \nabla \cdot (\rho e \boldsymbol{u}) = \nabla \cdot (\lambda \nabla T) - p\nabla \cdot \boldsymbol{u} + \boldsymbol{\Pi} : \nabla \boldsymbol{u} \tag{14}$$

$$\frac{\partial(\rho E)}{\partial t} + \nabla \cdot (\rho E \boldsymbol{u}) = \nabla \cdot (\lambda \nabla T) - \nabla \cdot (p\boldsymbol{u}) + \nabla \cdot (\boldsymbol{\Pi} \cdot \boldsymbol{u}) \tag{15}$$

Where $\boldsymbol{\Pi}$ is the viscous stress tensor and $\boldsymbol{\Pi} : \nabla \boldsymbol{u}$ is the viscous heat dissipation. Assuming that the compression work and viscous heat dissipation can be neglected, leads to the following equation after substituting in temperature for the internal energy [26]:

$$\frac{\partial(\rho c_V T)}{\partial t} + \nabla \cdot (\rho c_V T \boldsymbol{u}) = \nabla \cdot (\lambda \nabla T) \tag{16}$$

In the case of constant heat capacity, the above temperature equation simplifies further to [26]:

$$\frac{\partial T}{\partial t} = -\boldsymbol{u} \cdot \nabla T + \frac{1}{\rho c_V} \nabla \cdot (\lambda \nabla T) \tag{17}$$

Thermal conductivity (λ) is expressed in Fourier's law [27]:

$$\boldsymbol{q} = -\boldsymbol{\lambda} \nabla \mathrm{T} \tag{18}$$

Thermal conductivity is an important value in heat transfer and it is a thermophysical property [27]. Thermal conductivity is the most important property in the field of heat transfer [28]. It is closely related to a number of other heat transfer parameters. One of these related parameters is the thermal diffusivity (α), and it is given by [29]:

$$Thermal\ diffusivity\ (\alpha) = \frac{\lambda}{\rho c_P} \quad (19)$$

The use of heat capacity at constant pressure (c_P) or heat capacity at constant volume (c_V) depends on system conditions. Heat capacity at constant pressure is higher than heat capacity at constant volume for gases, due to the need to perform work during gas expansion. Heat capacity ratio is the value of heat capacity at constant pressure divided by heat capacity at constant volume and it is an important thermodynamic property. It is a constant for an ideal gas, but its value varies with temperature and pressure for non-ideal gases [30]. In multiphase studies of bubbles, the heat capacity ratio is usually assumed to be a constant [30]. However, small changes in the heat capacity ratio were found to have considerable effects on gas velocity, bubble diameter and distribution of velocity of characteristic bubbles [30].

Prandtl number (Pr) is a useful dimensionless number which is used in thermal analysis. It is specific to the fluid and fluid state and it compares the extent of momentum diffusivity to thermal diffusivity [31]:

$$Pr = \frac{kinematic\ viscosity}{\alpha} = \frac{c_P \mu}{\lambda} \quad (20)$$

If the amount of heat transfer is significant, thermal effects will have a substantial effect on the state of a system and will characterise it. After a certain value of heat flux, boiling will occur leading to phase change. In this process, bubbles are nucleated and grow until departure from the heating element. At high values of wall superheat, a vapour film forms which separates the liquid from the heating element. The transition region between the two modes of boiling is unstable [26, 32]. Boiling behaviour is often characterised in the form of boiling curves as illustrated in Figure 4.

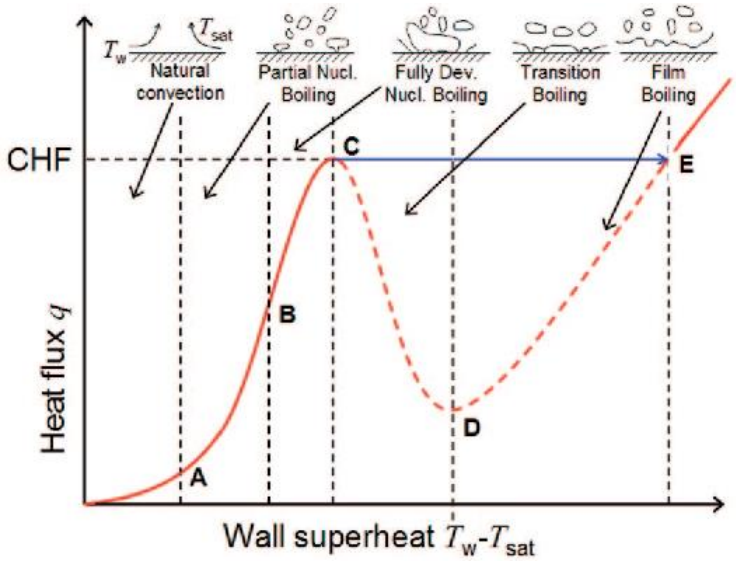

Figure 4- A pool boiling curve illustrating boiling phenomena (CHF stands for critical heat flux) [33].

Formation of a liquid film can hamper the boiling process due to reduced contact of liquid with the heating surface. Clearly, heat flux rapidly decreases after the critical heat flux value is exceeded and significant additional wall superheat is required to reach an equally high value of heat flux. Therefore, change from fully developed nucleate boiling to transition boiling is generally unwanted due to loss of efficiency. The boiling process is quite complex with different factors capable of enhancing or reducing heat transfer. Studies have found that dissolved gas in the liquid phase can boost the heat transfer coefficient [34]. Higher heat transfer coefficient allows to reach the same heat flux with lower wall superheats. The ability to use lower wall superheat is advantageous in terms of efficiency and the ability to use cheaper materials in construction of heat transfer equipment. It can also slow down corrosion and prevent degradation of heat sensitive substances, e.g. certain foods. Heat transfer in boiling processes can also be enhanced by artificial modification of surface properties and conditions [35]. For example, bubble nucleation is promoted by hydrophobic surfaces [35]. Artificial nucleation sites could be machined on heating surfaces. The role of surface roughness in droplet spreading on a surface is illustrated in Figure 5 [36]:

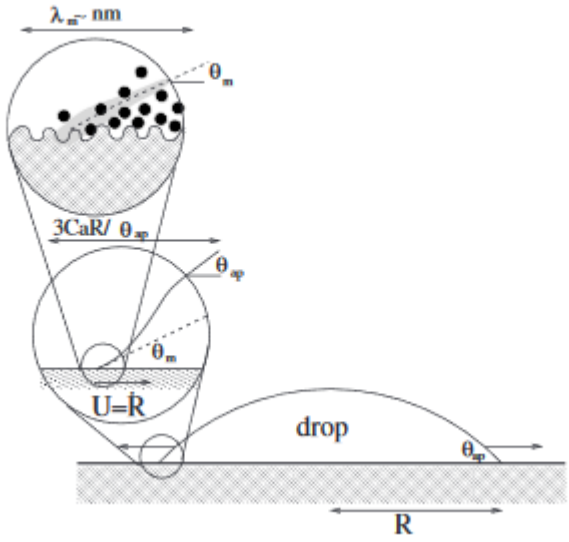

Figure 5- Visualisation of phenomena present in the edge of a spreading droplet at scales from nanometres to macroscale. Figure obtained from Reference [36].

2.2.Multi-Scale Modelling of Multiphase Flows

Methods for simulating fluid dynamics can be conveniently classified according to the scale (microscale, mesoscale and macroscale) on which they analyse the underlying physics. Physical complexities of fluid behaviour mean that physical phenomena exist which are difficult to capture accurately, even if the simulation method is well-matched to the scale of interest. This partly arises from the fact that multiphase flows include physical phenomena which span multiple scales. In other words, microscale physical behaviour can have a considerable impact on the macroscale observables.

2.2.1. Microscale

The smallest scale for computer simulations of fluid flows is the microscale. Models at this scale work with individual particles and aim to solve the Newton's equations of motion to obtain full information on the state of the system [9]. These models are not amenable to simulating domain sizes of practical interest in reasonable timescales. They are limited to microns and microseconds [37]. Their lack of practical use is a consequence of two factors. Firstly, computational expense due to the extremely large number of particles per mole of a substance given by the Avogadro's constant. And secondly, inability to deterministically predict the state of the system for times greater than the inverse of the Lyapunov exponent [9]. Molecular dynamics (MD) [38] and direct simulation Monte Carlo method (DSMC) [39] fall into this category [37]. Microscale methods are more successful at providing a qualitative understanding of phenomena rather than providing quantitative data [35].

2.2.2. Mesoscale

Mesoscale is smaller than the continuum scale but larger than the molecular scale. Mesoscopic models employ statistical mechanics to predict physical phenomena by working with statistical groups of molecules. The main advantages which these models aim to exploit are significantly reduced computational costs compared to microscale models and more accurate physical description of fluids than that offered by continuum models. These models are designed to recover macroscopic properties such as density, pressure and velocity. LBM is an example of a mesoscale fluid flow simulator. It is well-suited to multiphase and/or multicomponent flows which include interfacial dynamics connected to fluid interparticle interactions [40, 41]. A method of efficiently simulating macroscopic porous media using LBM was reported [42].

2.2.3. Macroscale

The majority of commercial codes fall into this category. Traditional computational fluid dynamics (CFD) is an example of a macroscopic method. CFD models are based on obeying the conservation laws for mass, momentum and energy and on solving Navier-Stokes and Poisson's equations [17].

Multiphase methods include the volume of fluid (VOF) [43], the level set method (LSM) [44], the phase-field (PF) method and the constrained interpolated propagation (CIP) method [45]. Hirt and Nichols' VOF method [46] has been extensively applied and it has been extended to thermal cases including nucleate pool boiling at a low density ratio [35].

The discretisation methods include finite volume, finite difference and finite element methods [47].

2.2.4. Thermodynamic Aspects of Multiphase Flows

Simulation of multiphase flows requires thermodynamic modelling. A wide-variety of equations of state exists in the literature for describing thermodynamic behaviour. They can be divided into different families of equations of state, including [48]:

- Cubic equations of state (Van der Waals, Carnahan-Starling [49], Peng-Robinson [50], Soave-Redlich-Kwong [51])
- Corresponding state methods (Lee-Kesler [52])
- Extended corresponding state methods (SPUNG [53])
- Statistical associating fluid theory (SAFT [54])
- Multiparameter equations of state (GERG-2008 [55])

The basics of the equations of state listed above derive from the ideal gas law, statistical mechanics or experimental data combined with an optimisation procedure [56]. Their complexity varies significantly and, naturally, some equations of state are better suited to computer simulations than others. Cubic equations of state are widely employed in computer simulations. Their main benefit is computational efficiency whilst the main drawback experienced by cubic equations of state is lack of accuracy [48].

The main properties required of equations of state for use in computer simulations are [48]:

- Accuracy/ consistency
- Computational speed/ robustness
- Predictive capability

Spinodal points are currently viewed as a good starting position for developing equations of state [56]. They denote the point at which homogeneous liquid becomes intrinsically unstable and spontaneously separates into two distinct stable phases [56]. In a phase diagram, spinodal points are located inside the two-phase region denoted by the coexistence curve [57]. Whilst the spinodal and coexistence curves are distinct, they do meet at the critical point. Both higher and lower spinodal points can be conveniently visualised in Figure 6, as the local maximum and local minimum, or alternatively as the beginning and end of the unstable region.

The usefulness of spinodal points comes from the fact that multiple thermodynamic values and identities are known to be equal to zero at these points including [56]:

- the bulk modulus,
- the inverse isobaric heat capacity,
- the second derivative of Gibbs free energy.

In order for an equation of state to be fit for use in computer simulations, the unstable region located within the spinodal points must not have local minima or maxima, i.e. it must resemble the shape of the unstable region curve in Figure 6 [56]. This particular property of the unstable branch is termed to be the thermodynamically consistent behaviour and the equation of state is said to have a single Maxwell loop if the condition is fulfilled [56]. A significant challenge facing thermodynamic researchers today is the fact that the most accurate group of equations of state, i.e. the multiparameter equations of state group, has a second artificial Maxwell loop [56].

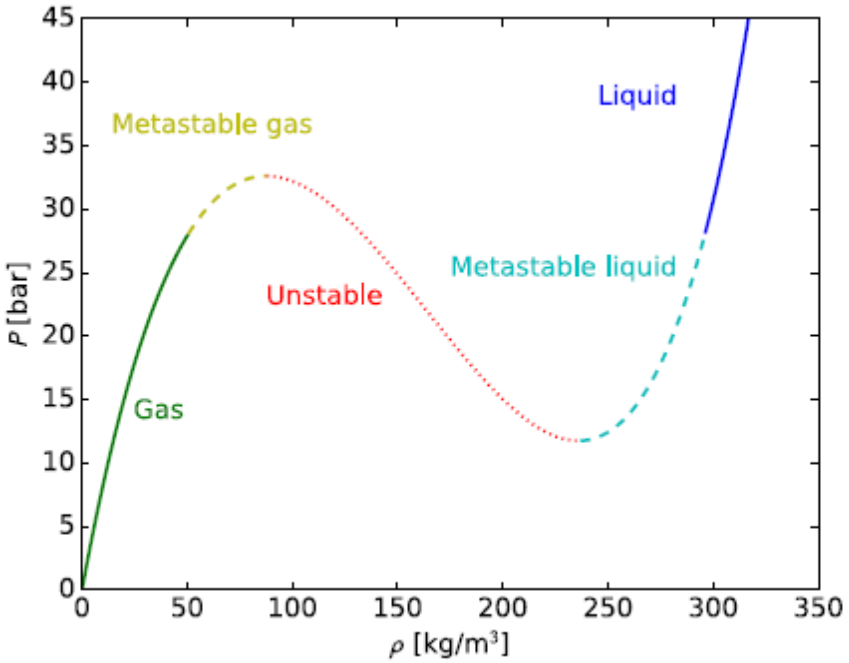

Figure 6- Illustration of stable, metastable and unstable regions in multiphase fluids using pure methane isotherms at 175K obtained using the Peng-Robinson equation of state [56].

2.3.Lattice Boltzmann Methods for Multiphase Flows

Lattice Boltzmann method (LBM) simulates ersatz or synthetic matter rather than real matter and an explicit assumption is made that links between simulation and reality can be made by setting dimensionless numbers to the same values [9]. LBM works by colliding and propagating fictitious particles on lattices which are usually square (2D) or cubic (3D), but other lattice geometries are also possible. Algorithmic calculations are carried out with distribution functions which are probabilities of finding a particle with a particular speed in an area at a particular time. In other words, the distribution function quantifies the density of mass in physical space and in velocity space.

Particle speeds must be chosen to ensure sufficient symmetry which is needed to recover the rotational invariance of the momentum flux tensor at the macroscopic level [41]. The most popular models include the D2Q9 model (9 particle velocities including a stationary particle at the centre) in two dimensions and the D3Q19 model in three dimensions. Lattices need to obey isotropy requirements dependent on the physics of the problem to be solved. For fluid dynamics problems, moments (weighted by w_i with particle speeds termed c_i) up to fifth order are usually necessary and this leads to the following requirements [12]:

$$\sum_i w_i = 1 \tag{21}$$

$$\sum_i w_i c_{i\alpha} = 0 \tag{22}$$

$$\sum_i w_i c_{i\alpha} c_{i\beta} = c_s^2 \delta_{\alpha\beta} \tag{23}$$

$$\sum_i w_i c_{i\alpha} c_{i\beta} c_{i\gamma} = 0 \tag{24}$$

$$\sum_i w_i c_{i\alpha} c_{i\beta} c_{i\gamma} c_{i\mu} = c_s^4 \left(\delta_{\alpha\beta}\delta_{\gamma\mu} + \delta_{\alpha\gamma}\delta_{\gamma\mu} + \delta_{\alpha\mu}\delta_{\beta\gamma}\right) \tag{25}$$

$$\sum_i w_i c_{i\alpha} c_{i\beta} c_{i\gamma} c_{i\mu} c_{iv} = 0 \tag{26}$$

For many practical cases the Mach number should be smaller than 0.1 [58]; hence LBM simulates nearly incompressible fluids. Since LBM is unstable at high velocities, decreasing viscosity is the main way of increasing the Reynolds number. However, decreasing viscosity comes with its own challenges.

By surveying the lattice Boltzmann equations, it is not immediately clear what are the continuum equations being simulated. Navier-Stokes equations can be obtained using the Chapman-Enskog [59] perturbative treatment of LBM models. Perturbation methods provide approximate solutions to models which are difficult to solve analytically [60]. Perturbation expansion is used because there is no convenient method of calculation of the non-equilibrium part of the distribution function. It is performed by expanding the distribution function around the equilibrium distribution using the Knudsen number as the expansion/smallness parameter in the following fashion [12]:

$$f_i = f_i^{eq} + \epsilon f_i^{(1)} \left(+ \epsilon^2 f_i^{(2)} + \cdots \right) \tag{27}$$

The terms in the brackets in the above equation are usually neglected for the purposes of finding the Navier-Stokes equations. Setting f_i to f_i^{eq} results in the Euler momentum equation; therefore irreversible losses are embedded in the non-equilibrium part of the distribution function.

2.3.1. Development - Route from Lattice Gas Cellular Automata

LBM was first proposed by McNamara and Zanetti for modelling hydrodynamics as an alternative to the lattice gas cellular automata (LGCA) [1, 9, 61]. LGCA particles are of a Boolean type, a feature which generates statistical noise. On the other hand, LBM uses real numbers which eliminates noise. The first LBM was non-linear and had the following form [9]:

$$\Delta_i f_i = C_i(f_1, \dots, f_b) \tag{28}$$

The multibody collision operator of the nonlinear LBM was too computationally intensive, but this problem was solved by the quasilinear LBM where the collision matrix in the form of a scattering matrix was calculated only once [9, 62]:

$$\Delta_i f_i = A_{ij}\left(f_j - f_j^e\right) \tag{29}$$

The nonlinearity which describes the nonlinear Navier-Stokes equation is embedded in the f_i^e term [9]. Transition to MRT [63] (multiple relaxation time) and LBGK [64] (lattice Bhatnagar-Gross-Krook) schemes is made by treating the eigenvalues as freely-tuneable parameters, i.e. relaxation times [9]. The LBGK consists of a diagonal matrix with density and momentum conservation embedded in the equilibrium distribution function [9, 65, 66]:

$$A_{ij} \to -\omega\delta_{ij} \tag{30}$$

All non-zero values in the diagonal matrix are set to the same value for the LBGK collision operator; hence, the high degree of simplification:

$$\Delta_i f_i = -\frac{1}{\tau}\left(f_j - f_j^e\right) \tag{31}$$

2.3.2. Development - Route from the Boltzmann Equation

Researchers conveniently proved that LBM can be derived from the continuous Boltzmann equation; therefore it is independent on the theoretical grounds from the LGCA [61, 67, 68]. LBM is a discretisation of the continuous Boltzmann equation [68]. The continuous Boltzmann equation has the following form [9]:

$$\left[\partial_t + \vec{v}\cdot\partial_{\vec{x}} + \vec{F}^{ext}\cdot\partial_{\vec{p}}\right]f = \int (f_1{}_{'}f_2{}_{'} - f_1 f_2)\, g\sigma\,(g,\Omega)\, d\Omega\, d\vec{p}_2 \tag{32}$$

The main source of complexity in the lattice Boltzmann equation is the collision operator. Boltzmann formulated his equation for dilute, monoatomic gases to simplify the collision

operator. Under these conditions two particles collide instantaneously, head-on in an elastic manner (rotational and vibrational energy is not taken into account, because monoatomic molecules do not rotate or vibrate).

Macroscopic variables are obtained from moments of the distribution function [12]:

$$\rho(\boldsymbol{x},t) = \int f(\boldsymbol{x},\boldsymbol{\xi},t)d^3\xi \tag{33}$$

$$\rho(\boldsymbol{x},t)\boldsymbol{u}(\boldsymbol{x},t) = \int \boldsymbol{\xi} f(\boldsymbol{x},\boldsymbol{\xi},t)d^3\xi \tag{34}$$

$$\rho(\boldsymbol{x},t)E(\boldsymbol{x},t) = \frac{1}{2}\int |\boldsymbol{\xi}|^2 f(\boldsymbol{x},\boldsymbol{\xi},t)d^3\xi \tag{35}$$

$$\rho(\boldsymbol{x},t)e(\boldsymbol{x},t) = \frac{1}{2}\int |\boldsymbol{v}|^2 f(\boldsymbol{x},\boldsymbol{\xi},t)d^3\xi \tag{36}$$

The equilibrium distribution is given by the Maxwell-Boltzmann equilibrium distribution [9, 12]:

$$f^{eq}(\boldsymbol{x},|\boldsymbol{v}|,t) = \rho\left(\frac{1}{2\pi RT}\right)^{3/2} e^{-|\boldsymbol{v}|^2/(2RT)} \tag{37}$$

The statistical nature of the above equation is clearly evident. It is derived using Lagrangian multipliers and elementary quadrature of Gaussian integrals [9]. Lagrangian multipliers are chosen to conserve density, momentum and energy and maximise the H-function which monotonically increases with time [9] (or decreases depending on the sign convention used). The important point is that collisions always move the distribution function towards equilibrium [12]. The equilibrium in question, when particle collisions are involved, is the local equilibrium rather than the global equilibrium. If the system was at global equilibrium, then there would be no dynamics present in the system which to study. The H-function takes the following form [9, 12]:

$$\mathcal{H} = \int f\,lnf\;d^3\xi \;\; or \;\; -\int f\,lnf\;d^3\xi \tag{38}$$

The collisional conservation rules can be represented by moments of the collision operator [12]:

$$\int \Omega(f)d^3\xi = 0 \tag{39}$$

$$\int \boldsymbol{\xi}\Omega(f)d^3\xi = \mathbf{0} \tag{40}$$

$$\int |\boldsymbol{\xi}|^2 \Omega(f) d^3\xi = 0 \tag{41}$$

$$\int |\boldsymbol{v}|^2 \Omega(f) d^3\xi = 0 \tag{42}$$

Lattice Boltzmann equation is obtained by discretising the continuous Boltzmann equation in velocity space, physical space and in time. The discretised lattice Boltzmann equation takes the following form [12]:

$$f_i(\boldsymbol{x} + \boldsymbol{c}_i \Delta t, t + \Delta t) = f_i(\boldsymbol{x}, t) + \Omega_i(\boldsymbol{x}, t) \tag{43}$$

The discrete equilibrium takes the following form [12]:

$$f_i^{eq}(\boldsymbol{x}, t) = w_i \rho \left(1 + \frac{\boldsymbol{u} \cdot \boldsymbol{c_i}}{c_s^2} + \frac{(\boldsymbol{u} \cdot \boldsymbol{c_i})^2}{2c_s^4} - \frac{\boldsymbol{u} \cdot \boldsymbol{u}}{2c_s^2}\right) \tag{44}$$

The equilibrium distribution has the same moments as the distribution function [12]:

$$\sum_i f_i^{eq} = \sum_i f_i = \rho \tag{45}$$

$$\sum_i \boldsymbol{c}_i f_i^{eq} = \sum_i \boldsymbol{c}_i f_i = \rho \boldsymbol{u} \tag{46}$$

The equilibrium moments are given by the following equations [12]:

$$\Pi^{eq} = \sum_i f_i^{eq} = \rho \tag{47}$$

$$\Pi_\alpha^{eq} = \sum_i f_i^{eq} c_{i\alpha} = \rho u_\alpha \tag{48}$$

$$\Pi_{\alpha\beta}^{eq} = \sum_i f_i^{eq} c_{i\alpha} c_{i\beta} = \rho c_s^2 \delta_{\alpha\beta} + \rho u_\alpha u_\beta \tag{49}$$

$$\Pi_{\alpha\beta\gamma}^{eq} = \sum_i f_i^{eq} c_{i\alpha} c_{i\beta} c_{i\gamma} = \rho c_s^2 \left(u_\alpha \delta_{\beta\gamma} + u_\beta \delta_{\alpha\gamma} + u_\gamma \delta_{\alpha\beta}\right) \tag{50}$$

The third order moment contains an error for standard lattices which leads to an error in the macroscopic momentum equation [12]. In standard lattices, it can be seen that higher-order moments depend on the lower-order moments [12]:

$$c_{i\alpha}^3 = c_{i\alpha} \left(\frac{\Delta x}{\Delta t}\right)^2 \tag{51}$$

So

$$\Pi_{xxx}^{eq} = \sum_i c_{ix}^3 f_i^{eq} = \left(\frac{\Delta x}{\Delta t}\right)^2 \sum_i c_{ix} f_i^{eq} = \left(\frac{\Delta x}{\Delta t}\right)^2 \Pi_x^{eq} \tag{52}$$

For example, the D2Q9 velocity set has only nine independent moments [12].

Discretisation in Velocity Space

Velocity space can be discretised using the Mach number expansion or the Hermite series expansion with the Hermite series being more rigorous due to its orthogonality [12].

Hermite polynomial of n-th order in d spatial dimensions takes the following form [12]:

$$\boldsymbol{H}^{(n)}(\boldsymbol{x}) = (-1)^n \frac{1}{\omega(\boldsymbol{x})} \nabla^{(n)} \omega(\boldsymbol{x}) \tag{53}$$

With the weight/generating function $\omega(\boldsymbol{x})$ [12]:

$$\omega(\boldsymbol{x}) = \frac{1}{(2\pi)^{d/2}} e^{-x^2/2} \tag{54}$$

Hermite polynomials are orthogonal with respect to $\omega(x)$ [12]:

$$\int \omega(\boldsymbol{x})\, H_{\boldsymbol{\alpha}}^{(n)}(\boldsymbol{x}) H_{\boldsymbol{\beta}}^{(m)}(\boldsymbol{x}) d^d x = \prod_{i=1}^{d} n_i!\, \delta_{nm}^{(2)}\, \delta_{\boldsymbol{\alpha\beta}}^{(n+m)} \tag{55}$$

Suitable, continuous functions can be represented as a series of Hermite polynomials [12]:

$$f(\boldsymbol{x}) = \omega(\boldsymbol{x}) \sum_{n=0}^{\infty} \frac{1}{n!} \boldsymbol{a}^{(n)} \cdot \boldsymbol{H}^{(n)}(\boldsymbol{x}), \quad \boldsymbol{a}^{(n)} = \int f(\boldsymbol{x}) \boldsymbol{H}^{(n)}(\boldsymbol{x}) d^d x \tag{56}$$

Coefficients of the Hermite series expansion are directly connected to the conserved moments which makes them highly suitable [12]. The equilibrium distribution and distribution function can be obtained up to n-th order (only terms up to the third moment are required) from the following equations [12]:

$$f^{eq}(\boldsymbol{\xi}) \approx \omega(\boldsymbol{x}) \sum_{n=0}^{N} \frac{1}{n!} \boldsymbol{a}^{(n),eq} \cdot \boldsymbol{H}^{(n)}(\boldsymbol{\xi}) \tag{57}$$

$$f(\boldsymbol{\xi}) \approx \omega(\boldsymbol{x}) \sum_{n=0}^{N} \frac{1}{n!} \boldsymbol{a}^{(n)} \cdot \boldsymbol{H}^{(n)}(\boldsymbol{\xi}) \tag{58}$$

The Gauss-Hermite quadrature rule provides the exact sums of integrals using a small number of discrete points [12]:

$$\int \omega(\boldsymbol{x}) P^{(N)}(\boldsymbol{x})\, d^d x = \sum_{i=1}^{n} w_i P^{(N)}(\boldsymbol{x_i}) \tag{59}$$

Discretisation in Space and Time

Method of characteristics is used to transform the non-dimensional discrete-velocity Boltzmann equation

$$\partial_t f_i + c_{i\alpha} \partial_\alpha f_i = \Omega_i \tag{60}$$

from a first-order hyperbolic partial differential equation into a useful ordinary differential equation form [12]:

$$\frac{df_i}{d\zeta} = \left(\frac{\partial f_i}{\partial t}\right)\frac{dt}{d\zeta} + \left(\frac{\partial f_i}{\partial x_\alpha}\right)\frac{dx_\alpha}{d\zeta} = \Omega_i\big(\boldsymbol{x}(\zeta), t(\zeta)\big) \tag{61}$$

Where "ζ" parametrises a trajectory in space and

$$\frac{dt}{d\zeta} = 1 \quad and \quad \frac{dx_\alpha}{d\zeta} = c_{i\alpha} \tag{62}$$

Integrating both sides of the ODE gives:

$$f_i(\boldsymbol{x} + \boldsymbol{c}_i \Delta t, t + \Delta t) - f_i(\boldsymbol{x}, t) = \int_0^{\Delta t} \Omega_i(\boldsymbol{x} + \boldsymbol{c}_i \zeta, t + \zeta) d\zeta \tag{63}$$

The right-hand side of the above equation needs to be discretised. It is found that the first-order discretisation leads to an equation that is second-order accurate in time [12]. The explicit forward Euler scheme is most commonly employed, leading to the familiar LBE:

$$f_i(\boldsymbol{x} + \boldsymbol{c}_i \Delta t, t + \Delta t) = f_i(\boldsymbol{x}, t) + \Delta t \Omega_i(\boldsymbol{x}, t) \tag{64}$$

Runge-Kutta methods and other implicit methods can also be employed to improve stability and accuracy, but they are memory-intensive [12].

2.3.3. Lattice Bhatnagar-Gross-Krook (Single Relaxation Time)

Lattice BGK [64] (Bhatnagar-Gross-Krook) is the simplest and most commonly used form of the collision operator. The model has only one relaxation rate, which means that physical parameters (e.g. kinetic and bulk viscosities) are set to the same value. Using this collision operator leads to boundary conditions which are dependent on viscosity.

LBGK is restricted to unity Prandtl and Schmidt numbers [17, 69, 70].

2.3.4. Multiple Relaxation Time

Multiple relaxation time (MRT) [63] collision operator is significantly better than the LBGK collision operator in terms of stability, insensitivity to spurious acoustic waves and isotropy [45, 63, 71, 72]. This makes MRT highly suitable for use in challenging cases. MRT is often employed for multiphase flows [17].

Collision is carried out in momentum space and propagation is carried out using distribution functions. Moments are relaxed using individual rates. Conversion between moments and distribution functions is linear. It is carried out using a conversion matrix and its inverse. The conversion matrix is constructed either using Gram-Schmidt orthogonalisation (more popular option due to diagonal relaxation matrix) or using Hermite polynomials [12]. Mohamad explained the practical basics of MRT codes [73]. The main equations of the MRT collision operator are as follows [12, 63, 73-75]:

$$m_k = \sum_{i=0}^{q-1} M_{ki} f_i \qquad for\ k = 0, \dots., q-1. \tag{65}$$

$$f_i = \sum_{k} M_{ik}^{-1} m_k \tag{66}$$

$$\boldsymbol{f}(\boldsymbol{x} + \boldsymbol{c}_i \Delta t, t + \Delta t) - \boldsymbol{f}(\boldsymbol{x}, t) = -\boldsymbol{M}^{-1}\boldsymbol{S}[\boldsymbol{m}(\boldsymbol{x}, t) - \boldsymbol{m}^{eq}(\boldsymbol{x}, t)]\Delta t \tag{67}$$

$$\boldsymbol{S} = diag\left(1, \omega_e, \omega_\epsilon, 1, \omega_q, 1, \omega_q, \omega_v, \omega_v\right) \tag{68}$$

Individual relaxation rates can be adjusted to increase stability. Tuning these rates is not easy and different authors suggest different values. Published work exists on tuning the MRT relaxation parameters and it can aid the task of setting the relaxation rates [75]. A convenient strategy is to initially set the MRT relaxation rates to the two relaxation time (TRT) model and then to vary them to achieve the required objective. The first, fourth and sixth relaxation rates correspond to mass and momentum conservation. Mass and momentum are conserved in collisions. Some authors advocate setting the rates corresponding to the conserved moments to an arbitrary value, e.g. zero; however to preserve the benefits of trapezoidal integration they should be set to a nonzero value [76]. ω_e is responsible for bulk viscosity relaxation, ω_ϵ corresponds to kinetic energy square, ω_q is called the energy-flux and ω_v is the kinematic viscosity mode [75]. Only the bulk viscosity and kinematic viscosity relaxation rates are hydrodynamically-relevant. The remaining modes are tuned to achieve accurate simulations.

In the relaxation matrix, $\omega_e, \omega_\epsilon$ and ω_v are symmetric modes and ω_q is an antisymmetric mode [75]. Magic parameter is a convenient tool for tuning MRT models [77]. The magic parameter used in this study was calculated in the following manner:

$$\Lambda = \left(\frac{1}{\omega_q} - \frac{1}{2}\right)\left(\frac{1}{\omega_v} - \frac{1}{2}\right) \tag{69}$$

Gram-Schmidt equilibrium moments can be calculated from known values of density and velocity [73, 74]:

$$\rho^{eq} = \rho \tag{70}$$

$$e^{eq} = -2\rho + 3\rho\left(u_x^2 + u_y^2\right) \tag{71}$$

$$\epsilon^{eq} = \rho - 3\rho\left(u_x^2 + u_y^2\right) \tag{72}$$

$$j_x^{eq} = \rho u_x \tag{73}$$

$$q_x^{eq} = -\rho u_x \tag{74}$$

$$j_y^{eq} = \rho u_y \tag{75}$$

$$q_x^{eq} = -\rho u_y \tag{76}$$

$$p_{xx}^{eq} = \rho\left(u_x^2 - u_y^2\right) \tag{77}$$

$$p_{xy}^{eq} = \rho u_x u_y \tag{78}$$

In the Gram-Schmidt approach, the conversion matrix is constructed using a set of orthogonal vectors starting with conserved moments (i.e. density and momentum) [12].

MRT is computationally more intensive than the LBGK, but it allows to recoup and even save computational resources by setting viscosity to a lower value than practicable using LBGK and by using coarser grids while maintaining the same level of accuracy [78]. This stems from the fact that lower viscosities lead to faster convergence of simulations.

MRT, when properly tuned, leads to viscosity-independent permeability [79, 80]. Therefore, using MRT is recommended for simulating multiphase systems with an appreciable viscosity ratio [78].

Adjusting the relaxation parameters to obtain high bulk viscosity (ten times greater than shear viscosity) can increase stability and reduce spurious waves [81, 82].

A cascaded LBM model, which is similar to the MRT, was reported to give improved performance at high Reynolds numbers and result in lower spurious currents [83].

2.3.5. Two Relaxation Time

The two relaxation time (TRT) method is simpler than the MRT and takes comparable computational time as the single relaxation time (SRT or BGK) collision operator whilst still producing viscosity-independent permeability for any porous medium [77]. It is much simpler to tune using the so-called "magic parameters" [77]. As previously mentioned, magic parameters are products of the relaxation rates corresponding to the symmetric and anti-symmetric collision moments [77].

2.3.6. Multiphase Models

Shan-Chen model [84, 85] proposed pseudopotential interactions with origins in the kinetic theory at the level of the Boltzmann equation [12]. The model has been extensively adopted by varied research communities which use the LBM [86, 87]. The fact that LBM and the pseudopotential model have their basis in the kinetic theory lends itself to conceptual and practical simplicity which is difficult to match. Yang and Guo found that it has connections to the second virial coefficient and the radial distribution function (RDF) in the Enskog kinetic theory bestowing it with further physical basis [88]. The free energy model [89, 90] is an example of a macroscopically-derived model in which the free energy functional is responsible for representing thermodynamics from which the chemical potential and pressure tensor can be derived [12]. Consequently, thermodynamic consistency is prescribed as a requirement a priori.

LBM models tend to employ diffuse interfaces. A characteristic of diffuse multiphase models is that an increased resolution is necessary to represent interfaces between phases. In diffuse interface models, density and pressure tensor are pivotal parameters which vary smoothly across the interface [12]. Pressure tensor is not isotropic in the presence of an interface unlike in single-phase fluids. Multiphase physics can be incorporated into governing equations in different ways, thanks to the fact that the divergence of the pressure tensor is equivalent to a body force density [12]. The pressure tensor must incorporate an appropriate equation of state and surface tension effects for valid multiphase simulations [12].

The surface tension is usually introduced in diffuse interface models using the following force expression [12]:

$$\boldsymbol{F} = \kappa\rho\nabla\Delta\rho \tag{79}$$

The pressure tensor can be shown to have the form enclosed in the square brackets [12]:

$$\partial_\alpha p_b - F_\alpha = \partial_\beta \left[\left(p_b - \frac{\kappa}{2} \left(\partial_\gamma \rho \right)^2 - \kappa \rho \partial_\gamma \partial_\gamma \rho \right) \delta_{\alpha\beta} + \kappa (\partial_\alpha \rho)(\partial_\beta \rho) \right] = \partial_\beta P_{\alpha\beta} \quad (80)$$

Multicomponent multiphase (MCMP) models are more complex and less stable than single component multiphase (SCMP) models. Nevertheless, a number of multiphase models was adapted to multicomponent cases, including the pseudopotential model [91] and the commercial PowerFLOW software [92]. Yang and Boek found that for flow in porous media applications, the multicomponent pseudopotential model is capable of simulating high density ratios but with a low viscosity ratio [93]. They also found that multicomponent free energy models and multicomponent colour gradient models can simulate high viscosity ratios with a low density ratio (roughly equal to 1) [93]. The difficulties in carrying out MCMP studies are apparent. Published work on bubble distortion uses an unrealistic density ratio of 1 and only focuses on the viscosity ratio [14]. One group published results of a rising bubble study which uses a density ratio of 1.35 and a kinematic viscosity ratio of 2.8 and a Taylor bubble study was published which uses a density ratio of 8.7 and a kinematic viscosity ratio of 1 [94]. A high density ratio study of an MPMC system focused only on reaction with no flow and used a kinematic viscosity ratio of only 1 [95]. Another MPMC study of a reactive system uses a density ratio of 25.7 and does not state the kinematic viscosity ratio used [96]. The most challenging cases involve dynamic cases with significant departure from local equilibrium and steep macroscopic gradients. Each component has its own distribution function that propagates, collides and interacts with other components. The physical velocity of a multicomponent fluid becomes the barycentric velocity [12, 97]:

$$\boldsymbol{u}_b = \frac{1}{\rho} \sum_\sigma \left(\sum_i f_i^{(\sigma)} \boldsymbol{c}_i + \frac{\boldsymbol{F}^{(\sigma)} \Delta t}{2} \right), \quad \rho = \sum_\sigma \rho^{(\sigma)} \quad (81)$$

The colour gradient model [98] was the first multiphase LBM model to be proposed in the literature. It consists of the BGK collision operator, a two-phase collision operator which generates interfacial tension and a recolouring step which generates sharp interface and prevents phases from mixing [40]. Introduction of correction terms proved necessary to rectify errors in the simulated macroscopic equations due to violation of Galilean invariance [26]. The need for inclusion of correction terms suggests that the colour gradient model is not particularly suited to the study of dynamic problems. Noteworthy research involving the colour gradient model includes simulation of miscible flows [99]

and treatment of Galilean invariance for cases dealing with multiphase flows in porous media [100]. Liu et al. classified the computational costs of the colour gradient model as average [40].

The Shan-Chen [84, 85] model is constructed by taking into account interactive forces between nearest-neighbouring particles and introducing them in the equilibrium velocity [40]. The interparticle force is computed as a simple sum [84]:

$$\boldsymbol{F}^{SC}(\boldsymbol{x}) = -\psi(\boldsymbol{x})G\sum_{i} w_i\psi(\boldsymbol{x}+\boldsymbol{c}_i\Delta t)\,\boldsymbol{c}_i\Delta t \tag{82}$$

Taylor series can be used to obtain the continuum form of the force [12, 101]:

$$\boldsymbol{F}^{SC}(\boldsymbol{x}) = -\psi(\boldsymbol{x})G\left(c_s^2\Delta t^2\nabla\psi(\boldsymbol{x}) + \frac{c_s^4\Delta t^4}{2}\nabla\Delta\psi(\boldsymbol{x})\right) \tag{83}$$

The equation of state for this model of the force is [12]:

$$p_b(\rho) = c_s^2\rho + \frac{c_s^2\Delta t^2 G}{2}\psi^2(\rho) \tag{84}$$

Incorporation of complex physicochemical processes is possible [87]. It is particularly suited to processes involving interface changes (deformation, coalescence, breakup) [87]. This model suffers from a number of shortcomings; however a number of strategies are available to alleviate them. Multirange improvements make the model suitable for studying complex fluid-wall interactions [102]. The application of the improved models to complex porous media constitutes a worthwhile research topic [40]. Shan-Chen models can be combined with the MRT [103, 104]. The pressure tensor in the pseudopotential model takes the following form (with Δt set to 1) [12, 101]:

$$P_{\alpha\beta}^{SC} = \left(c_s^2\rho + \frac{c_s^2 G}{2}\psi^2 + \frac{c_s^4 G}{4}(\nabla\psi)^2 + \frac{c_s^4 G}{2}\psi\Delta\psi\right)\delta_{\alpha\beta} - \frac{c_s^4 G}{2}(\partial_\alpha\psi)(\partial_\beta\psi) \tag{85}$$

Where, ψ is an effective density function (pseudopotential) and G plays the role of a temperature-like parameter. The model is thermodynamically consistent when $\psi(\rho) = \rho$; however, this form of pseudopotential is usually unwanted because it does not allow simulation of high density ratios [87].

Improvements which allow adjustment of surface tension independently of density are important at very small scales at which surface tension may dominate over inertial and gravitational forces [87].

Spurious velocities are one of the main shortcomings of the pseudopotential model [87]. Higher order of isotropy pseudopotential model [105] was suggested in order to lower the spurious velocities, tune surface tension and adjust thermodynamic consistency. However, higher order of isotropy models are not investigated in this work, since increasing the interfacial thickness was found to be more efficient than increasing isotropy [26, 105]. Expanding the pseudopotential interactions beyond the nearest-neighbours also requires modification of the boundary conditions making application more difficult. One of the main strengths of multirange pseudopotential models is the ability to model emulsions, sprays and other multi droplet fluid mixtures [87, 106]. This need for multirange interactions in modelling multiple small droplets or bubbles arises from the fact that pseudopotential models constructed from a single belt of interactions favour the separation of phases into a single droplet/bubble surrounded by the continuous phase.

Multipseudopotential interaction (MPI) [107, 108] is a recent model based on the pseudopotential idea which takes into account interaction forces at different ranges. The increased number of parameters gives the modeller greater control over thermodynamics and allows to reduce the thermodynamic inconsistency [107].

The free energy model [89, 90] is based on the phase-field theory [40]. This model is conceptually completely opposite to the pseudopotential model. In the free energy model, the free-energy functional is used to construct the phase interface in a thermodynamically consistent manner [40]. A non-ideal pressure tensor is introduced by modifying the equilibrium distribution function [26]. The SCMP version of this model violates Galilean invariance; however lack of Galilean invariance produces insignificant errors in the MCMP version [40]. Similarly as in the colour gradient model, the necessity to introduce correction terms does not make this model a natural candidate for dynamic cases. This model is suitable for investigating multiphase flow in porous media at low Reynolds numbers [40, 78, 109] and it can be used with the MRT [110]. It is relatively stable, but it is significantly more computationally intensive than some of the other more efficient choices available [102].

The mean-field theory model [111] is based on modelling interfacial dynamics using molecular interactions which are introduced by using a second (pressure) distribution function [40]. The interfacial dynamics are governed using the Cahn-Hilliard equation [26]. This treatment means that dynamic cases can be simulated using the model [26]. It is relatively stable, but its applications are limited to a density ratio of approximately 15

[40]. This model was used to improve the understanding of the Rayleigh-Taylor instability [112]. Significant computational overheads are a shortcoming of the mean-field theory models [40].

The stabilised diffuse-interface model is related to the mean-field theory model in the sense that two distribution functions are used [40]. It can also be seen as an LBE analogue of phase field methods [40]. It is particularly useful for solving multiphase problems involving high density ratios (up to 1000) [40]. However, this model is complex and this could have an adverse impact on its popularity and adoption [40].

The entropic model [113] is a recent addition to the list of multiphase methods for the LBM. Entropic models mainly find application in the simulation of higher Mach number single-phase flows including supersonic flow [114]. The principle of the method is based on increasing the kinematic viscosity of the unstable regions according to the H-theorem [20]. The kinematic viscosity adjustment is highly localised around the critical regions to dampen instabilities in the form of pressure waves [20]. It has been recently reported that the entropic model can be combined with the pseudopotential model for multiphase simulations [20, 115]. Combination of the pseudopotential model with the newest LBM methods highlights continued interest of the LBM community in the pseudopotential model.

2.3.7. Thermal Models

A number of groups of thermal models for the lattice Boltzmann method exists in the literature. Thermal models for the lattice Boltzmann method can be divided into the following categories [26]:

- Multispeed [116]
- Double-distribution-function (DDF) [117]
- Hybrid [118]

The DDF and Hybrid thermal models are often used with pseudopotential and phase-field multiphase LBM methods [26]. In DDF models, two distribution functions need to be solved. One set of calculations is performed to solve the hydrodynamic distribution function and another set of calculations is performed to solve the thermal distribution function. The thermal distribution functions are solved within the framework of the LBM. The DDF models can be further subdivided into internal-energy-based [119], total-energy-based [120] and temperature-based [117] models [26].

The hybrid [118, 121] models work similarly to the DDF models in the sense that the solution of the hydrodynamic equations is performed separately from the solution of the thermal equations [26]. Unlike in the case of DDF models, hybrid methods solve the temperature equations using conventional numerical methods, i.e. the finite-volume or finite-difference methods [26]. In his book, Patankar outlined numerical discretisation methods used in traditional CFD codes [47]. As an example, the fourth-order Runge-Kutta method can be used to calculate temperature evolution [122]:

$$T^{t+\delta t} = T^t + \frac{\delta_t}{6}(h_1 + 2h_2 + 2h_3 + h_4) \quad (86)$$

$$h_1 = K(T^t) \quad (87)$$

$$h_2 = K\left(T^t + \frac{\delta_t}{2}h_1\right) \quad (88)$$

$$h_3 = K\left(T^t + \frac{\delta_t}{2}h_2\right) \quad (89)$$

$$h_4 = K(T^t + \delta_t h_3) \quad (90)$$

The Runge-Kutta method is an iterative method for temporal discretisation. The form of the function *K* with temperature as the argument or independent variable depends on the temperature equation to be solved.

Li et al. [123] used the Gong-Cheng [124] model to illustrate numerical errors in thermal simulations, including failure to obey the D^2-law for droplet evaporation. The D^2-law states that the square of the droplet diameter should change linearly over time [7, 123]. It is the simplest possible description of droplet vaporisation and combustion and contains the following assumptions: spherical symmetry, no spray effects, diffusion being rate-controlling, isobaric process, flame-sheet combustion, constant gas-phase transport properties, gas-phase quasi-steadiness [7]. The other failure of the Gong-Cheng model concerned failure of nucleated bubble to break free from the nucleation source during departure [123]. Later, Li et al. [125] pointed out mistakes in Gong et al.'s [126] derivation of the temperature equation.

Recently, a number of popular thermal models for the LBM were analysed by Hu et al. [127] and ranked according to their qualities. One of the main observations was that the temperature-based models are superior to the internal-energy-based models in terms of accuracy and thermodynamic consistency [127]. The tested models were ranked from best to worst in the following order [127]:

1) Hybrid finite-difference scheme by Li et al. [122]
2) Modified internal-energy-based model by Li et al. [123]
3) Temperature-based model by Hazi and Markus [128]
4) Simplified temperature-based model by Peng et al. [129]
5) Internal-energy-based model by Zhang and Chen [130]

Hu et al. [127] also carried out simulations to investigate heat transition through a static phase interface by combining thermal models with the piecewise-linear EOS [131]. Combining piecewise-linear EOS with thermal models allowed the authors to uncouple the effect of temperature on density and prevent phase change. Simultaneously, Hu and Liu [132] developed the idea of using the piecewise-linear EOS for thermal modelling with phase change. Effects of temperature were replaced by degree of superheat, due to the assumption that the degree of superheat has little influence on the liquid properties [132]. Phase change effects were introduced into the pressure calculations [132]:

$$p_{total} = p_{EOS}(\rho) + p_v\left(\rho, T_{superheat}\right) + p_i\left(\rho, T_{superheat}\right) \tag{91}$$

$$p_v\left(\rho, T_{superheat}\right) = \frac{aT_{superheat}(\rho - \rho_l)}{(\rho_v - \rho_l)} \tag{92}$$

$$p_i\left(\rho, T_{superheat}\right) = a \cdot b|\nabla\rho|T_{superheat} \tag{93}$$

In terms of applications, Hazi and Markus [128] studied the effects of gravity, contact angle and lateral force on bubble nucleation and departure. They also showed the capability of their model to simulate nucleate pool boiling with a cavity in the heating plate [133]. Markus and Hazi extended their simulations to study the effect of heated plate configuration, surface temperature and heat flux from nucleate to film boiling [134]. Kamali et al. [135] showed the capability of their model to simulate evaporation of a flat liquid surface in contact with vapour. Zhang and Chen [130] successfully simulated boiling with the presence of bubble nucleation, bubble rising and bubble coalescence. Gong and Cheng [136] used their model to study the effect of variable surface wettability on the pool boiling process and found that spatial variability promotes the boiling process. Li et al.[122] used their hybrid pseudopotential model to construct the boiling curve and study the effects of wettability. The authors were able for the first time in the LBM community to model all the three stages of the boiling process, i.e. nucleate boiling, transition boiling and film boiling [122]. The experimentally-observed effects of surface wettability which include the promoted onset of boiling, reduction in critical heat flux and reduction in wall superheat for film boiling with increase in contact angle were also

replicated in the simulations of Li et al. [122]. Safari et al. [137] used a phase-field thermal model to study droplet evaporation and their model was successfully validated against the D^2 law [7] for a number of values of the Stefan number. Droplet shape during the evaporation process was found to be circular and surface tension was found to satisfy Laplace's law.

Thermal lattice Boltzmann models were used to study phase change materials in energy storage applications [26]. Chatterjee [138] used his model to simulate solidification of tin and melting of gallium and found that it offers significant reductions in CPU time versus a continuum model. The savings in CPU time were achieved thanks to the ability of the LBM model to use a coarser grid with the same accuracy as a continuum model with a more refined grid [138]. Interesting developments in this field also include models studying phase change in porous media [26]. Parmigiani et al. [139] demonstrated the differences in non-wetting phase distribution during melting in a 3D porous medium at different values of the Stefan number. Increasing the Stefan number resulted in the non-wetting phase moving from connected to a disconnected configuration within the porous medium [139]. Luo et al. [140] studied convection melting in the geometry of a shell and tube unit that could be used for energy storage [26]. The authors of the study found that, unsurprisingly, increasing the number of heating tubes in the shell and tube unit increases the total liquid fraction due to higher heat transfer rate as the surface area of the heating elements increases [140]. The centrosymmetric arrangement of the heating tubes was also found to be superior to the inline and staggered arrangements in terms of heat transfer performance [140].

Chapter 3 - Investigation of Pseudopotential Models

Pseudopotential models are investigated in-depth in this Chapter in order to gain as much knowledge as possible about them. This knowledge will help with more complex topics in further Chapters.

Only models for the D2Q9 velocity set are discussed in this work. Extensions of models to high velocity sets and three dimensions exist in the literature [141, 142].

3.1. Methods of Equation of State Inclusion

A number of methods is available for including non-ideal equations of state (EOS) in the pseudopotential models. Yuan and Schaefer (YS) [143] discovered that high density ratios can be simulated by replacing the original pseudopotential with a form of the pseudopotential that is obtained from rearranging the pressure equation and inserting an equation of state into the pressure term in the following manner:

$$p(\rho) = c_s^2\rho + \frac{G}{2}\psi^2(\rho) \tag{94}$$

$$\psi(\rho) = \sqrt{\frac{2(p_{EOS} - \rho c_s^2)}{G}} \tag{95}$$

In this form of the pseudopotential, the parameter *G* loses its physical meaning. It is simply set to -1, in order to keep the term inside the square root positive, and its role is taken over by the terms within the EOS. The two widely-used cubic equations of state in pseudopotential models, i.e. Carnahan-Starling [49] and Peng-Robinson [50] equations of state, take the following forms, respectively:

$$p_{CS} = \rho RT\frac{1 + \frac{b\rho}{4} + \left(\frac{b\rho}{4}\right)^2 - \left(\frac{b\rho}{4}\right)^3}{\left(1 - \frac{b\rho}{4}\right)^3} - a\rho^2 \tag{96}$$

$$p_{PR} = \frac{\rho RT}{1 - b\rho} - \frac{a\omega(T)\rho^2}{1 + 2b\rho - b^2\rho^2} \tag{97}$$

Where

$$\omega(T) = \left(1 + (0.37464 + 1.54226\alpha - 0.26992\alpha^2)\left(1 - \sqrt{T_R}\right)\right)^2 \tag{98}$$

$$T_r = \frac{T}{T_{critical}} \tag{99}$$

For example, the *a* parameter in the cubic equations of state represents attractive forces and *b* represents repulsive forces [143]. Yuan and Schaefer suggested setting *a* to 1.0, *b* to 4.0 and *R* to 1.0 in the CS EOS [49, 143]. They also suggested setting *a* to 2/49, *b* to 2/21 and *R* to 1.0 in the PR EOS [50, 143]. Yuan and Schaefer (YS) tested the Shan-Chen, Van der Waals (VdW), Redlich-Kwong, Redlich-Kwong Soave, Peng-Robinson (PR) and Carnahan-Starling (CS) equations of state and obtained the best results using the Peng-Robinson EOS [143]. In this Chapter, the Carnahan-Starling equation of state is used predominantly. Using the CS EOS has the benefit of reducing the number of parameters, since the PR EOS has an additional parameter in the form of the acentric factor. The *a* parameter in the Carnahan-Starling EOS offers control of interfacial thickness [74]. It is responsible for attractive forces in the EOS and reducing its value from the 1.0 proposed by Yuan and Schaefer expands the interface [74]. Discussion of interfacial thickness is subjective. Unless, the same cut-off percentages of bulk densities are used to calculate the interfacial thickness when comparing different methods.

An alternative method for including equations of state in the pseudopotential model is the piecewise linear EOS [131]. In a piecewise linear EOS, the following equations are used to simulate non-ideal equations of state [131]:

$$p_{EOS} = \begin{cases} \rho\theta_V & if\ \rho \leq \rho_1 \\ \rho_1\theta_V + (\rho - \rho_1)\theta_M & if\ \rho_1 < \rho \leq \rho_2 \\ \rho_1\theta_V + (\rho_2 - \rho_1)\theta_M + (\rho - \rho_2)\theta_L & if\ \rho > \rho_2 \end{cases} \quad (100)$$

The piecewise linear equations are inserted into the p_{EOS} term in the square root of the pseudopotential in the same manner as equations of state in the YS approach. From the above equation, it can be seen that the piecewise linear method offers five free, adjustable parameters, i.e. θ_V, θ_M, θ_L, ρ_1 and ρ_2 [131]. The first step is to set the pressure slopes in the vapour branch (θ_V), unstable branch (θ_M) and in the liquid branch (θ_L). Then the spinodal points (i.e. ρ_1 and ρ_2) can be obtained from two equations, one for the mechanical equilibrium and the other for the chemical equilibrium, given by the following respective equations [131]:

$$\int_{\rho_V}^{\rho_L} dp = (\rho_1 - \rho_V)\theta_V + (\rho_2 - \rho_1)\theta_M + (\rho_L - \rho_2)\theta_L = 0 \quad (101)$$

$$\int_{\rho_V}^{\rho_L} \frac{1}{\rho} dp = \log(\rho_1/\rho_V)\,\theta_V + \log(\rho_2/\rho_1)\,\theta_M + \log(\rho_L/\rho_2)\,\theta_L = 0 \quad (102)$$

Multipseudopotential interaction (MPI) [107, 108] represents another class of the pseudopotential method. Multiple thermodynamically-consistent pseudopotentials are introduced in order to allow simulation of high density ratios with the SRT collision operator. The Guo forcing scheme [144] for the BGK operator is modified to allow flexible selection of ε for each multiple pseudopotential [108]. Multiple pseudopotentials can be described by the following equations [108]:

$$\boldsymbol{F}^{MPI} = \boldsymbol{F}^{(1)} + \boldsymbol{F}^{(2)} + \cdots + \boldsymbol{F}^{(n)} \tag{103}$$

$$\boldsymbol{F}^{MPI} = \sum_{j=1}^{n} -G_j \psi_j(\boldsymbol{x}) \sum_{i=1}^{N} w_i \psi_j(\boldsymbol{x} + \boldsymbol{c}_i)\boldsymbol{c}_i \tag{104}$$

$$\psi_j(\rho) = \left(\frac{\rho}{\lambda_j \varepsilon_j + C_j \rho}\right)^{1/\varepsilon_j} \tag{105}$$

3.2.Forcing Schemes

Forcing schemes, i.e. the methods in which the forces are introduced into LBM models, have a significant impact on the simulations. The intermolecular force in the original Shan-Chen model is introduced into the streaming-collision algorithm by shifting the equilibrium velocity. This is done in the equilibrium distribution in the collision operator in the following manner [84]:

$$\boldsymbol{u}^{eq} = \boldsymbol{u} + \frac{\boldsymbol{F}^{SC}\tau}{\rho} \tag{106}$$

The original Shan-Chen model was developed for the SRT collision operator. The pseudopotential force can be introduced into LBM models using different forcing schemes. For example, it can be introduced into MRT models using forcing schemes developed specifically for the MRT collision operator. Zheng et al. [145] analysed the Ladd [146], Guo [144], Shan-Chen and the exact difference method (EDM) [147] forcing schemes for the SRT pseudopotential model and came to the conclusion that the SC and EDM forcing methods give the best stability results. Therefore, this Chapter investigates only the SC and EDM forcing methods for the SRT collision operator. The EDM takes the following form [147]:

$$f_i(\boldsymbol{x} + \boldsymbol{c}_i \Delta t, t + \Delta t) - f_i(\boldsymbol{x}, t) = \Omega_i + F_{i,EDM} \tag{107}$$

$$F_{i,EDM} = f_i^{eq}\left(\rho, \boldsymbol{u} + \frac{\boldsymbol{F}\Delta t}{\rho}\right) - f_i^{eq}(\rho, \boldsymbol{u}) \tag{108}$$

McCracken and Abraham [76] proposed a forcing scheme developed specifically for the MRT collision operator. The MRT forcing schemes discussed in this work are based on this scheme and all of them can be described by a general equation. The individual terms in the general equation are given in Table I in Appendix A and the general equation can be described as follows:

$$\boldsymbol{m}^{*} = \boldsymbol{m} - \boldsymbol{S}(\boldsymbol{m} - \boldsymbol{m}^{eq}) + \Delta t\left(\boldsymbol{I} - \frac{\boldsymbol{S}}{2}\right)\overline{\boldsymbol{S}} + \Delta t\boldsymbol{C} + \boldsymbol{S}\boldsymbol{Q}_{\boldsymbol{m}} \tag{109}$$

The forcing scheme proposed by McCracken and Abraham does not introduce unphysical viscosity-dependence [103]. This is a significant advantage and it makes carrying out simulations more predictable.

Two improvements to the MRT forcing model are analysed and discussed in the following Sections. They are referred to in this work as Li-Luo [74] and Huang-Wu [148] methods.

In the Li-Luo method, the value of ε in the mechanical stability condition is tuned using σ. The equation for setting ε takes the following form for the D2Q9 velocity set [74]:

$$\varepsilon = \frac{-2}{3}24G\sigma \tag{110}$$

Li and Luo also proposed a separate method for surface tension adjustment, which can be combined with the method for adjusting thermodynamic consistency [149]. Surface tension is adjusted according to $1 - \kappa$. Hence, setting κ to 0 results in unmodified surface tension and results of simulations with and without the $\boldsymbol{C}$ source term are the same. Increasing the value of κ reduces surface tension. Li and Luo investigated the values of κ ranging from 0 to 0.99 [149].

The Huang-Wu method, unlike the Li-Luo methods, combines thermodynamic consistency adjustment and surface tension adjustment into a single term [148]. Thermodynamic consistency is tuned using the sum of k_1 and k_2 and surface tension is tuned using k_1 only [148] in the following manner:

$$\varepsilon = -8(k_1 + k_2) \tag{111}$$

$$surface\ tension\ coefficient = 1 - 6k_1 \tag{112}$$

Huang and Wu investigated setting the surface tension coefficient ($1 - 6k_1$) from 0.1 to 2.0 [148]. The Huang-Wu method introduces modifications at the third-order in the Chapman-Enskog analysis, whereas the Li-Luo method is at the second-order. Recent

studies illustrate the importance of third-order analysis to the pseudopotential models [145, 148, 150].

In conventional pseudopotential models, ε is simply a lattice and forcing dependent numerical parameter. Its value does not have physical meaning and it needs to be adjusted on a case-by-case basis. In the MPI model, on the other hand, ε is an EOS parameter.

3.3.Thermodynamic Consistency

Thermodynamic inconsistency impedes simulation of high density ratios using pseudopotential models. The problem and improvements designed to overcome it are investigated in this Section. Numerical simulations were carried out in a 200 unit x 30 unit lattice surrounded by periodic boundaries in all four directions using flat interfaces at x = 50 and x = 150. Interface thickness was initially set to 3.5 units. Equations of state were included in the models using the square root form of the pseudopotential. Figure 7 illustrates the thermodynamic consistency test:

Figure 7- Flat interface simulation to test thermodynamic consistency (Colour illustrates density).

The problem manifests itself in gas densities deviating from the values given by the Maxwell equal-area construction [4]. The Maxwell equal-area construction can be written in the following form [25]:

$$\int_{\rho_g}^{\rho_l}(p_0 - p_{EOS})\frac{1}{\rho^2}d\rho = 0 \qquad (113)$$

Thermodynamic inconsistency stems from the fact that the mechanical stability condition has a different form than the Maxwell construction. The mechanical stability condition has the following form [151]:

$$\int_{\rho_g}^{\rho_l}\left(p_0 - \rho c_s^2 - \frac{G}{2}\psi^2\right)\frac{\psi'}{\psi^{1+\varepsilon}}d\rho = 0 \qquad (114)$$

The unmodified MRT forcing scheme deviates from the Maxwell construction to an even greater degree than the Shan-Chen and EDM forcing schemes with the SRT collision operator, as illustrated in Figure 8.

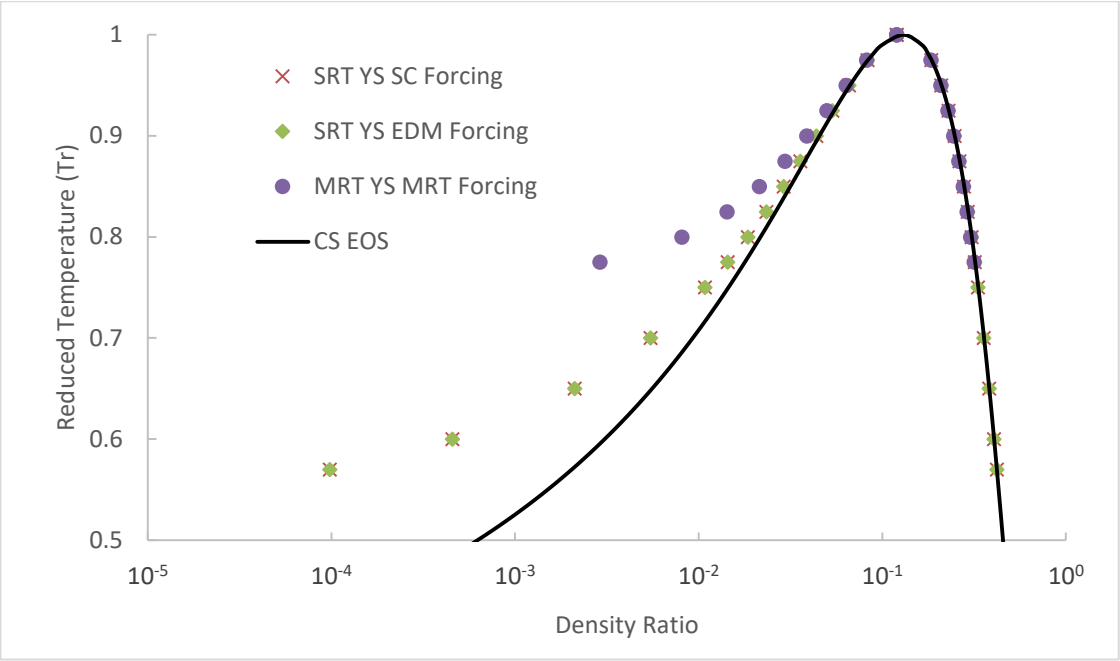

Figure 8-Thermodynamic consistency of forcing schemes without improvements ($\tau_v = 1$).

Thermodynamic consistency can be approached by modifying the value of ε using an appropriate forcing scheme improvement. Revised versions of the SRT forcing schemes were proposed, to approach thermodynamic consistency [145]. Kupershtokh also suggested a trial-and-error method to approach thermodynamic consistency by combining the local and mean-value approximations in the calculation of the interparticle force [147]. These methods are not examined in this work, instead attention is focused on improvements to the MRT models.

Figure 9 illustrates the effect of changing the value of ε using the Huang-Wu and Li-Luo forcing improvements. Both forcing improvements give results that are significantly better than the unmodified forcing scheme. For a given value of ε, both methods result in almost identical coexistence densities except for lower reduced temperatures with differences becoming noticeable around $T_r = 0.6$. The differences at lower reduced temperatures are due to terms associated with surface tension modification by the Huang-Wu scheme.

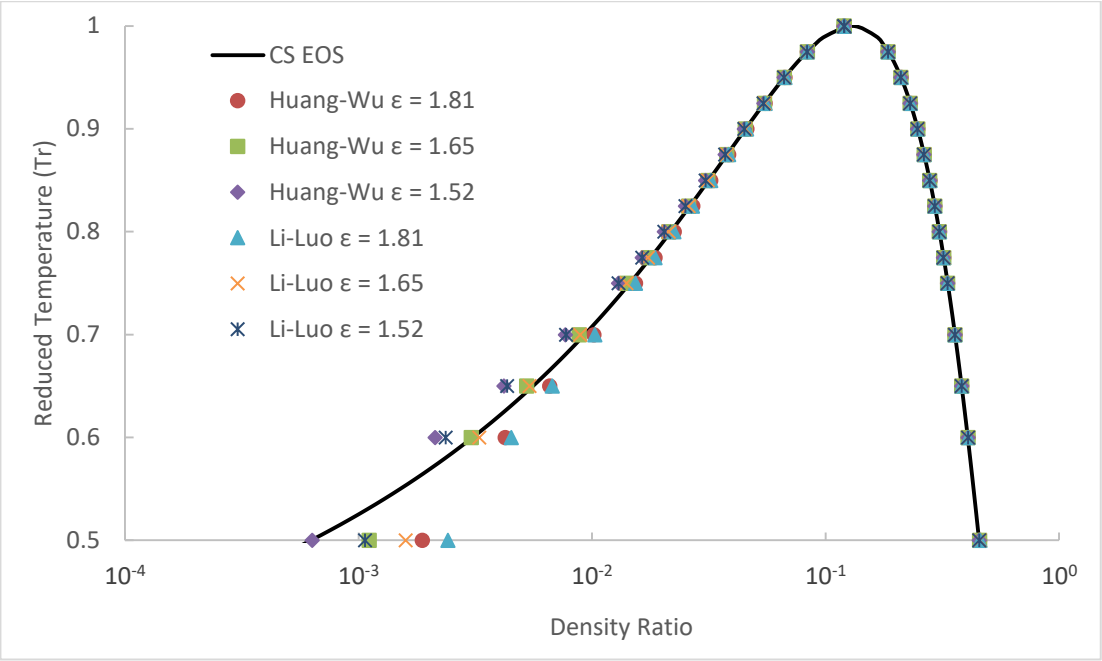

Figure 9- Thermodynamic consistency adjustment using improved forcing schemes for the MRT collision operator (k_1 = k_2 for the Huang-Wu method and $\kappa = 0$ for the Li-Luo method). Tests were carried out with $\tau_v = 1.0$ and CS EOS $a = 1.0$.

Expanding the interface alleviates thermodynamic inconsistency and reduces spurious velocities. Interface expansion becomes a useful strategy when the reduced temperature is approximately 0.6 or less.

The limits of static high density ratio simulations are explored in Figure 10. It can be seen that the Huang-Wu forcing scheme with expanded interface allows simulations of very high density ratios. It is important to realise that the whole density range may not be suitable for practicable dynamic simulations. MPI with the SRT collision operator is also capable of achieving very high density ratios in static simulations.

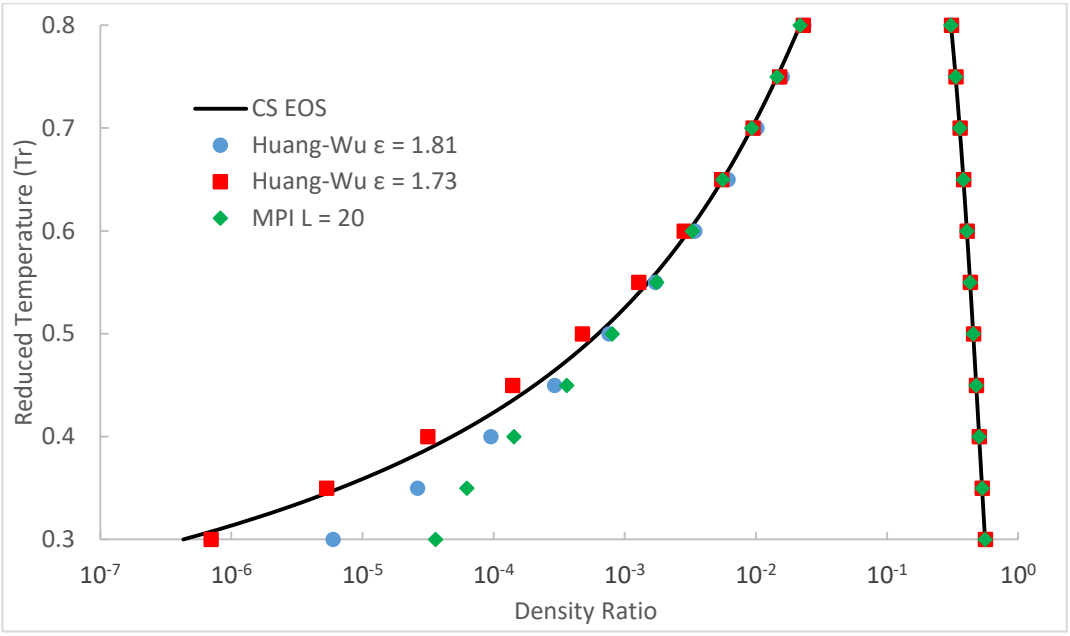

Figure 10- Thermodynamic consistency of a 50 l.u. diameter droplet simulated in a 201 x 201 lattice using the Huang-Wu forcing scheme with $k_1 = k_2$ and CS EOS a = 0.25. Tests were carried out with $\tau_v = 1.0$. The results for MPI with interface thickness equal to 20 are included for comparison.

Viscosity independence is an important asset of MRT models for multiphase simulations. It is desirable to have a model which can simulate high viscosity ratios. Besides stability at low values of kinematic viscosity, equilibrium densities of the phases should not be affected by the kinematic viscosity and, by extension, by τ_v [152]. Shear viscosity is independent of the fluid density for a given temperature and for dilute gases it is approximately equal to [153]:

$$\mu \approx \frac{\sqrt{mkT}}{a^2} \qquad (115)$$

where m is the molecular mass, k is the Boltzmann's constant, T is the temperature and a is the molecular diameter. Hence, changing the kinematic viscosity should not affect the equilibrium densities. Huang-Wu and Li-Luo forcing models give equilibrium densities practically unaffected by the value of the kinematic viscosity. Li and Luo also reported that the stability of multiphase simulations can be increased by setting the kinematic viscosities of the gas and liquid phases to different values (i.e. setting the gas kinematic viscosity to a value multiple times higher than the liquid kinematic viscosity) [74]. This can be implemented in single-component simulations by making the value of τ_v dependent on the local value of density, with critical density acting as the dividing point between the gas viscosity and the liquid viscosity. This is permissible because τ can be a function of space and time [12]. Due to the fact that it is not assumed in the Chapman-Enskog analysis that $\partial_t \tau = 0$ or $\partial_\alpha \tau = 0$ [12].

3.4.Laplace Tests of Stationary Droplets

LBM is a diffuse interface method and in order to avoid stability issues, the phases are initialized with a prescribed interface thickness using the following formula for circular shapes [154]:

$$\rho(i,j) = \frac{\rho_{liquid} + \rho_{vapour}}{2} - \frac{\rho_{liquid} - \rho_{vapour}}{2} \times \tanh\left[\frac{2\left(\sqrt{(i - i_{center})^2 + (j - j_{center})^2} - r_0\right)}{W}\right] \quad (116)$$

where, W is the interface thickness, r_0 is the spherical shape radius.

Flat, vertical interfaces can also be initialized in a diffuse manner using the following equation:

$$\rho(i,j) = \frac{\rho_{liquid} + \rho_{vapour}}{2} - \frac{\rho_{liquid} - \rho_{vapour}}{2} \times \tanh\left[\frac{2(i - interface\ location)}{W}\right] \quad (117)$$

Simulations to investigate spurious velocities were carried out by initializing a liquid droplet with a diameter of 50 lattice units surrounded by vapour in a 201 units by 201 units lattice. All four boundaries were periodic. The first set of simulations was carried out using a sharp interface, which was obtained by setting the *a* parameter in the Carnahan-Starling equation of state to 1.0. According to Li et al. [74], this choice of parameters results in interfacial thickness equal to roughly 3.5 units at a reduced temperature equal to 0.65, as illustrated in Figure 11:

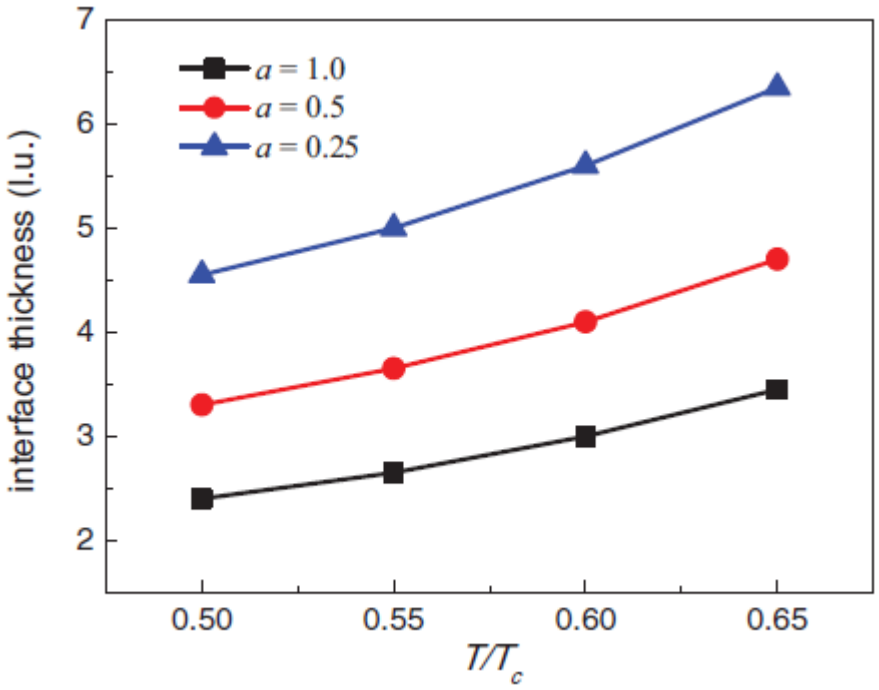

Figure 11- Effect of changing the a parameter in the Carnahan-Starling equation of state on the interfacial thickness according to Li et al. [74]

Figure 12 illustrates the simulation setup for Laplace tests.

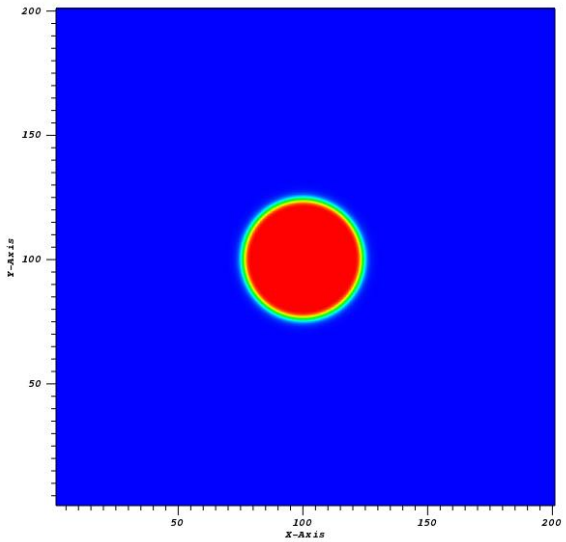

Figure 12- Droplet simulation to measure spurious velocities (Colour illustrates density).

3.4.1. Spurious Velocities

Spurious velocities were recorded as the magnitude of physical velocity at a given point:

$$Spurious\ velocity(i,j) = \sqrt{u_x(i,j)^2 + u_y(i,j)^2} \qquad (118)$$

Figure 13 illustrates spurious velocities for a wide range of density ratios obtained using different models. It should be kept in mind that the recorded density ratios were obtained,

to a lesser or greater extent, after density collapse of the vapour phase. All the three models investigated used the Yuan-Schaefer method of EOS inclusion. Carnahan-Starling EOS was used even though Peng-Robinson EOS offers higher achievable density ratio [143]. The EDM and SC forcing schemes perform the same in terms of spurious velocities when τ_v = 1.0. Upon investigation of the magnitudes of spurious velocities, it becomes clear that the SRT collision operator is unsuitable for simulations of high density ratios. Around the density ratio of 1,000, the spurious velocities are comparable to the maximum allowable lattice velocities. This magnitude of spurious velocities would render simulation results unusable. The MRT model with the Huang-Wu forcing modification gives significantly lower spurious velocities than the SRT models for a given density ratio.

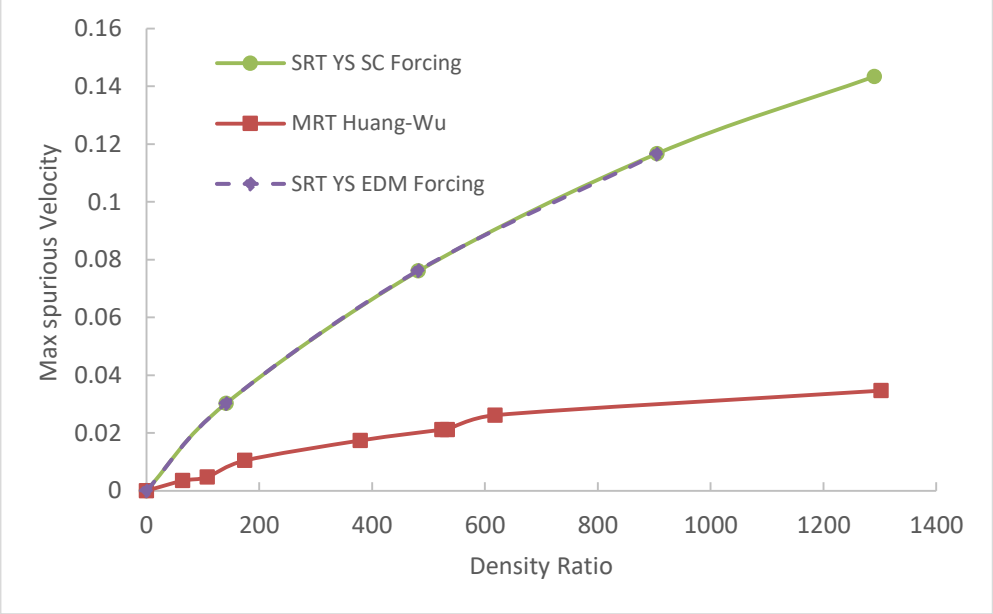

Figure 13- Spurious velocities for different models at different density ratios. The a parameter in the CS EOS was set to 1.0 for all the models in order to allow comparison.

MRT offers an improvement, but spurious velocities are still too high to simulate high density ratios. Therefore, the interface should be extended to improve thermodynamic consistency and to reduce spurious velocities. Figure 13 represents spurious velocities when τ_v = 1.0 which is ideal for stability.

Figure 14 represents the effects of changing viscosity and density ratios on spurious velocities for the Huang-Wu and Li-Luo forcing schemes. The interface was expanded by setting the value of *a* in the CS EOS to 0.25, in order to achieve stability and reduce spurious velocities. It can be seen that decreasing the kinematic viscosity has an even greater effect on spurious velocities than increasing the density ratio. Spurious velocities increase by an order of magnitude for an order of magnitude decrease in viscosity.

Viscosity varies by an order of magnitude between $\tau_v = 1.5$ ($\nu = 0.3333$) and $\tau_v = 0.6$ ($\nu = 0.0333$). It varies, again, by an order of magnitude between $\tau_v = 1.0$ ($\nu = 0.1667$) and $\tau_v = 0.55$ ($\nu = 0.0167$). In other words, halving viscosity doubles spurious velocities. Whereas, increasing density ratio by an order of magnitude from 100 to 1000 increases spurious velocities approximately 2.5 times. Both forcing modifications result in practically the same spurious velocities, for all the conditions tested, when the surface tension is unmodified by either scheme, i.e. when $k_1 = 0$ and $\kappa = 0$.

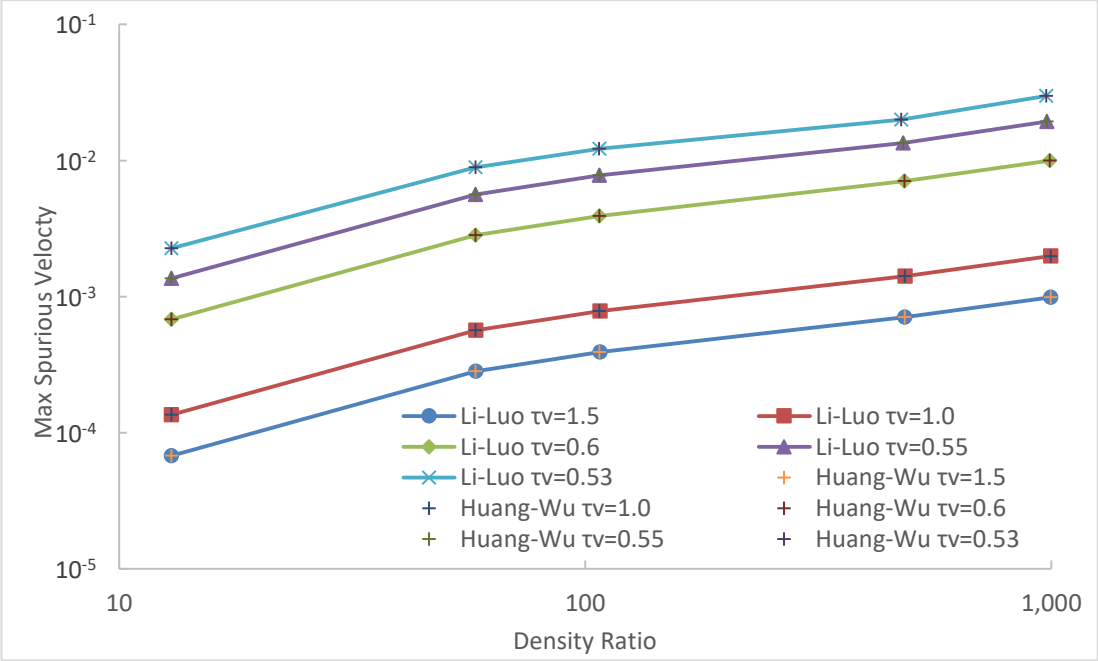

Figure 14- The effect of decreasing the kinematic viscosity on spurious velocities at different density ratios for the MRT model with the Huang-Wu and Li-Luo forcing scheme modifications (CS EOS "a" = 0.25 and ε = 1.81). Both models do not modify the surface tension when $k_1 = 0$ and $\kappa = 0$.

Figure 15 illustrates the effects of changing surface tension, by changing the k_1 coefficient, in the Huang-Wu method whilst keeping ε constant. Evidently, surface tension needs to be taken into account when investigating spurious velocities, especially when comparing different methods. Increasing surface tension to 0.0118 (by setting k_1 to -0.1163) reduces spurious velocities and reducing surface tension to 0.0043 (by setting k_1 to 0.0667) increases spurious velocities in comparison to the unmodified surface tension value of 0.007 (obtained by setting k_1 to 0).

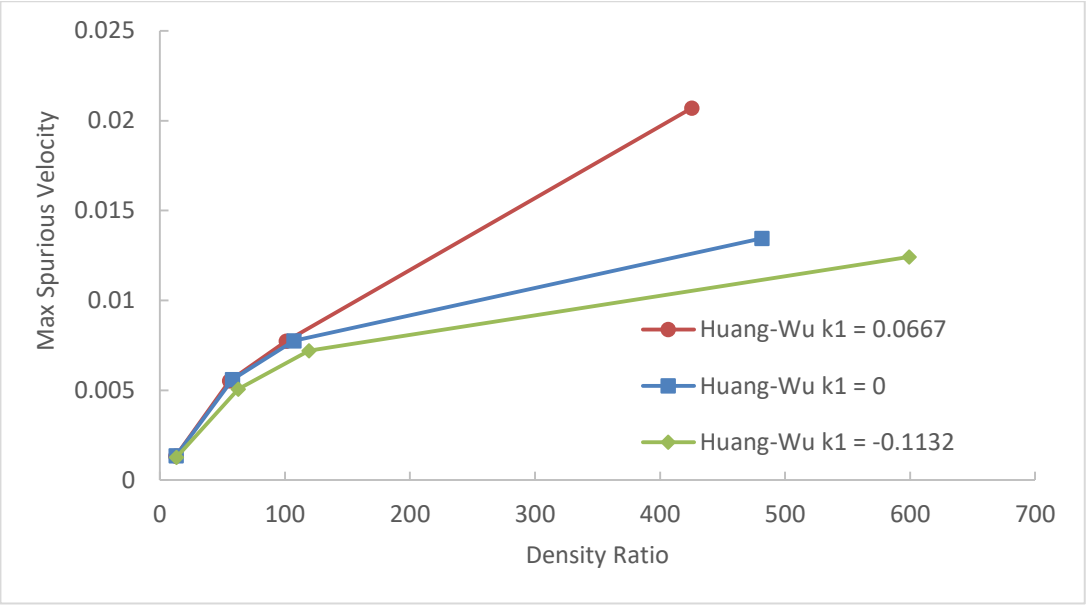

Figure 15- The effects of changing surface tension using the Huang-Wu method (T_r = 0.5, CS EOS a = 0.25, τ_v = 0.55 and ε = 1.81).

Figure 16 illustrates the effects of modifying surface tension using the Li-Luo method. The value of ε is kept constant and κ is varied to modify surface tension. Reducing surface tension by setting κ to a positive value, reduces spurious velocities. Li and Luo [149] did not mention the possibility of setting κ to a negative value to increase surface tension. Surface tension is modified by the result of $1 - \kappa$; therefore setting κ to a negative value should increase surface tension. Setting κ to -0.4 was found to increase surface tension to 0.0098, as predicted. However, increasing surface tension was found to increase spurious velocities, in contrast to the Huang-Wu method. The changing density ratios at different values of surface tension can also be observed in Figure 15 and Figure 16.

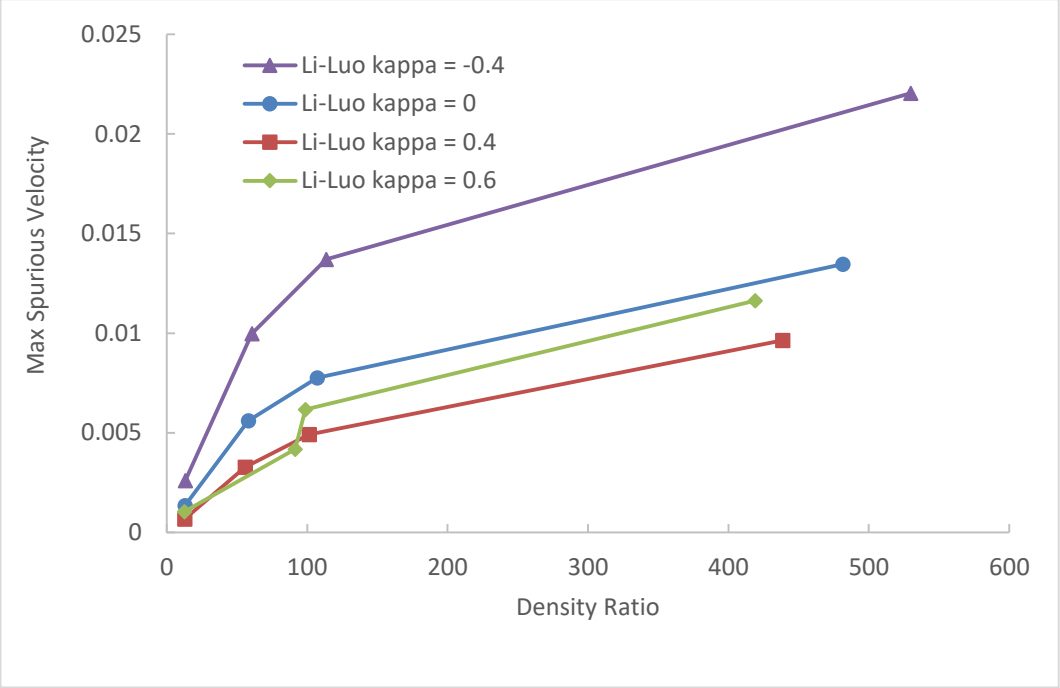

Figure 16- The effects of changing surface tension using the Li-Luo method (T_r = 0.5, CS EOS a = 0.25, τ_v = 0.55 and ε = 1.81).

Up to this point, all the results were obtained using the YS method of EOS inclusion. A piecewise linear EOS is also investigated in this paper and it is combined with the Huang-Wu forcing method to allow modification of ε and adjustment of surface tension. Li and Luo investigated the effects of changing the slopes of pressure in the vapour, unstable and liquid branches [5]. They suggested setting θ_V to $0.64c_s^2$, θ_L to c_s^2 and θ_M to $-0.04c_s^2$ [5]. Setting θ_V to a value that is similar to θ_L reduces the variation of vapour density with droplet size [5]. Interfacial thickness is expanded when the value of θ_M approaches zero [5].

ρ_L	**0.314**	**0.38**	**0.4**	**0.44**	**0.447**
ρ_V	0.0245	0.006	0.003	0.0006	0.000254
ρ_1	0.026495	0.006576	0.003362	0.000709	0.000309
ρ_2	0.31089	0.37406	0.39291	0.43154	0.43826
mechanical equilibrium	-0.00043	-0.00035	-0.00016	-2.9E-05	5.39E-06
chemical equilibrium	0.001564	-0.00093	-0.00064	-0.00029	6.69E-06

Table 1- Parameters used in the piecewise linear EOS for the purposes of carrying out simulations. For all the data points Θ_v was set to 0.21333, ϑ_L to 0.33333 and ϑ_M to -0.00667.

In order to compare the YS and the piecewise linear methods of EOS inclusion, it is necessary to set the interfacial thickness to the same value using both methods. The value of θ_M is varied to change the interfacial thickness. The slope of the interface is different

in the two methods. The YS method has a steeper interfacial slope near to the liquid phase and the piecewise linear EOS method has a steeper interface adjacent to the vapour phase. The interfacial region in the YS method has a convex shape, whereas the piecewise linear method has a concave shape. Figure 17 compares the interfacial region when 76% of equilibrium densities is used as the interface cut-off. In this work, it was decided to compare both methods by setting the value of a in the CS EOS in the YS method to 0.25 and θ_M in the piecewise linear method to $-0.02c_s^2$.

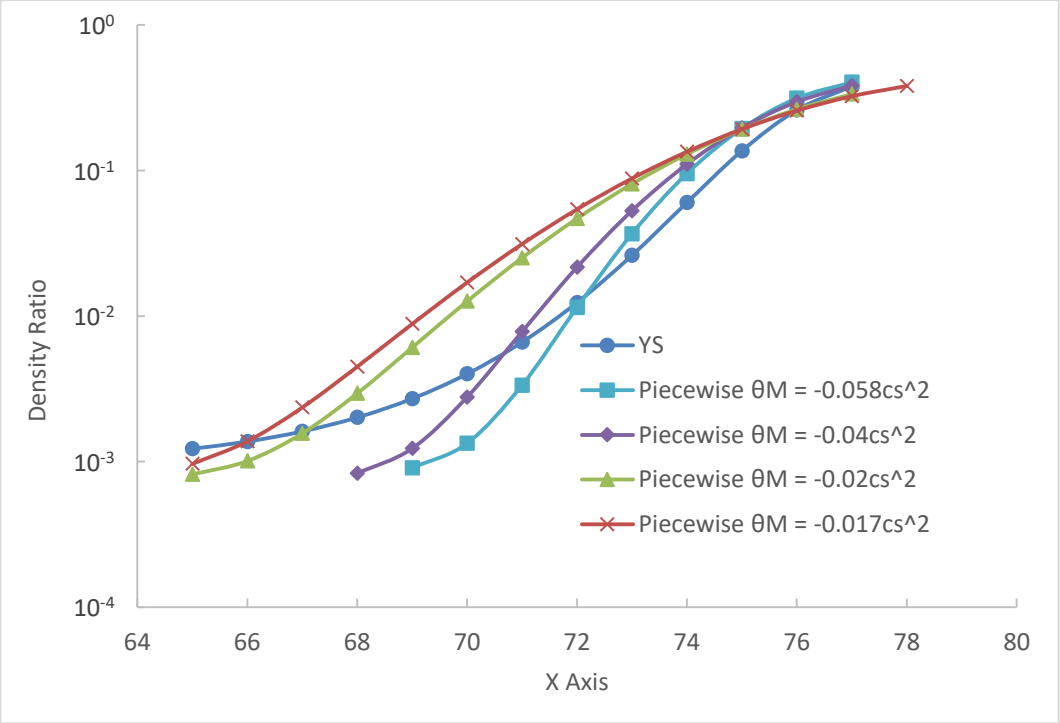

Figure 17- Interface thickness when 0.76 cut-off is applied to the equilibrium densities.

The piecewise linear EOS using the parameters listed in Table 1 has a lower surface tension than the YS method with the CS EOS. In order to reach the surface tension value of 0.007, θ_M has to be set to $-0.058c_s^2$. However, this value of θ_M results in a thinner interface which would make comparison of the two methods unfair. Therefore, the value of $1\text{-}6k_1$ was increased from 1.0 to 1.73 to obtain the same surface tension as when the YS method was used. The value of surface tension was successfully set to 0.007, as illustrated in Figure 18.

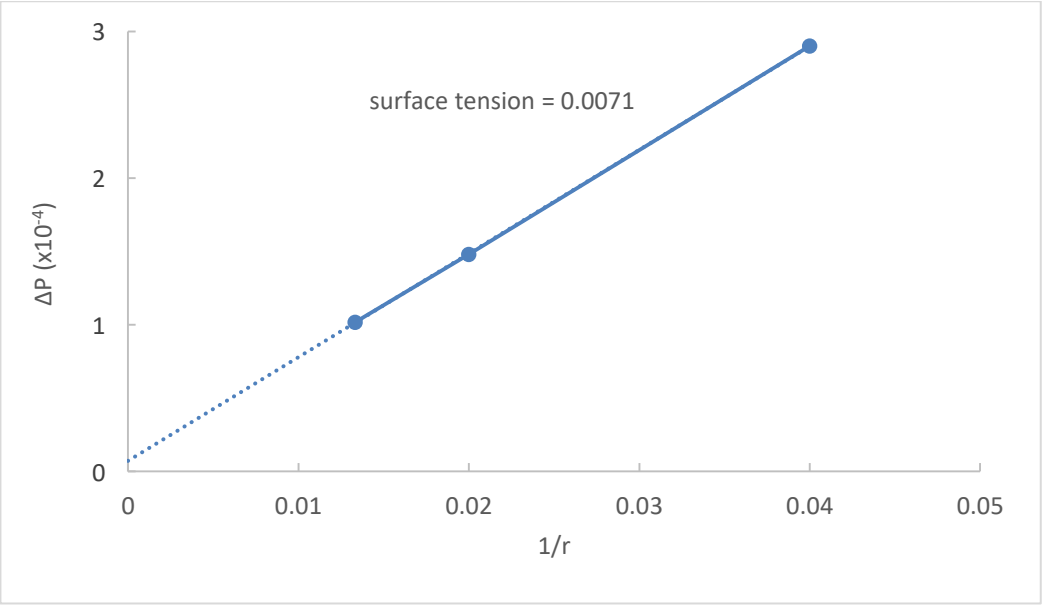

Figure 18- Laplace's law test for the piecewise linear EOS with the Huang-Wu forcing method with k_1 set to -0.1217 and ε set to 1.81. Equilibrium densities were set to the values predicted by the CS EOS at T_r = 0.5.

Figure 19 shows that spurious velocities are lower when using the piecewise linear EOS compared to when the YS method is used. However, the piecewise linear method has problems reaching equilibrium at low viscosities. Problems reaching equilibrium become apparent around $\tau_v = 0.53$. No equilibrium was reached using the piecewise linear EOS at $\tau_v = 0.53$ for $T_r = 0.5$. Also, no equilibrium was reached for a larger droplet (100 l.u. diameter) at $\tau_v = 0.55$ for $T_r = 0.5$.

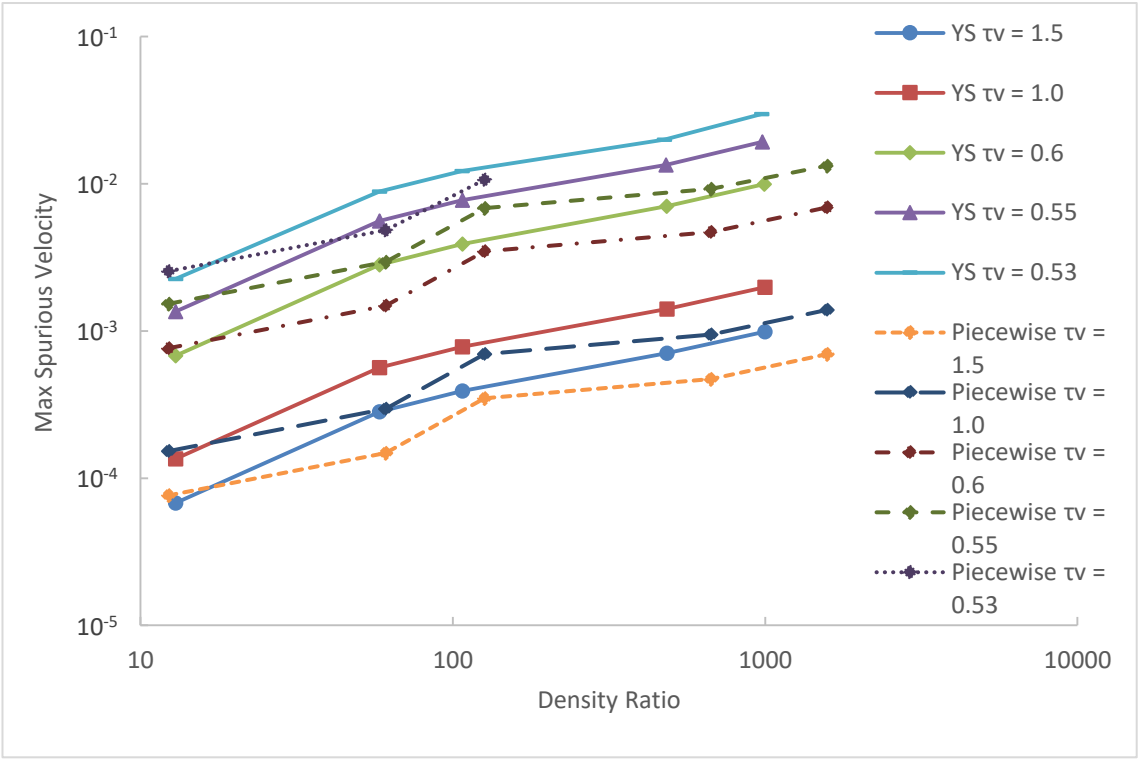

Figure 19- Comparison of spurious velocities obtained using the YS and piecewise linear EOS methods with the Huang-Wu forcing scheme. Surface tension values were the same for both models

Wu et al. [155] analysed the causes of instability of pseudopotential LBMs and proposed several strategies for extending the envelope of stable parameters. Two causes of instability are directly linked to the EOS when the YS method is used. As illustrated by Wu et al. [155], the pseudopotential becomes a complex number at high density values due to ϕ (the term inside the square root) becoming negative. A sign function is required to change the value of G from -1 to 1, in order to avoid loss of stability when high density values are encountered. Singularities of the EOS are another cause of instability that requires a limiter function restricting density to a prescribed value [155]. Figure 20 investigates the pseudopotential at different values of specific volume when the piecewise linear EOS is used. Clearly, the pseudopotential behaves differently when the EOS is introduced using the piecewise linear EOS than when it is done using the YS method. The pseudopotential is asymptotic in the vapour region, i.e. below the spinodal point ρ_1. It reaches a constant value in the liquid region above the second spinodal point, i.e. ρ_2. The pseudopotential increases monotonically in the transition region. This behaviour of the pseudopotential makes the piecewise linear EOS method more suitable for use in simulations.

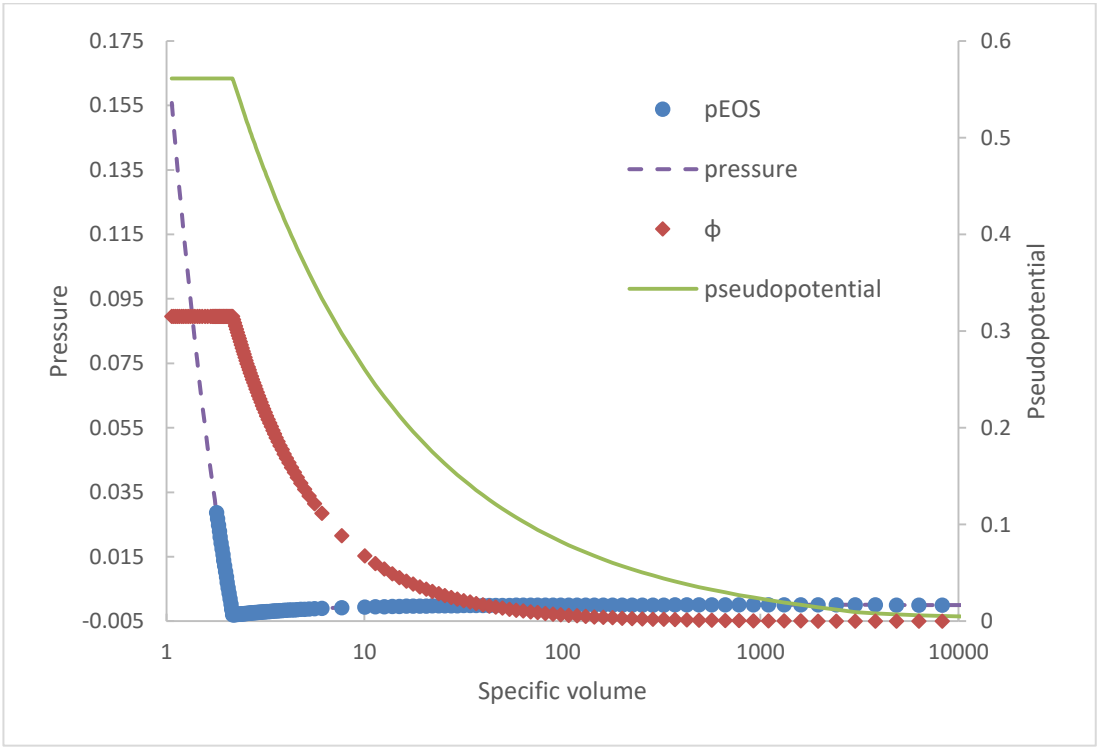

Figure 20- Behaviour of the pseudopotential when the piecewise EOS is used in response to changing specific volume.

The distribution of spurious velocity is also of interest. It is well-known that spurious velocity is the highest in the vapour phase and tends to be much lower in the liquid region. Figure 21 illustrates the distributions of spurious velocity and density and compares how they are affected for the YS and piecewise linear methods by changing the surface tension using the Huang-Wu forcing scheme. Spurious velocity is found to be the highest in the vapour region for all the cases investigated. Spurious velocities are significantly lower in the liquid region when the piecewise linear EOS is used in comparison to when the YS method is used. Density ratio generated by the piecewise linear EOS is found to be almost unaffected by changing the k_1 parameter to vary the surface tension. Whereas, density is sensitive to the k_1 parameter when the YS method is employed in the pseudopotential. This phenomenon is caused by high-order error terms introduced by the modifications to the forcing scheme. The same observation is made when the relaxation rates are varied. This strand of research is further explained in Section 3.4.3.

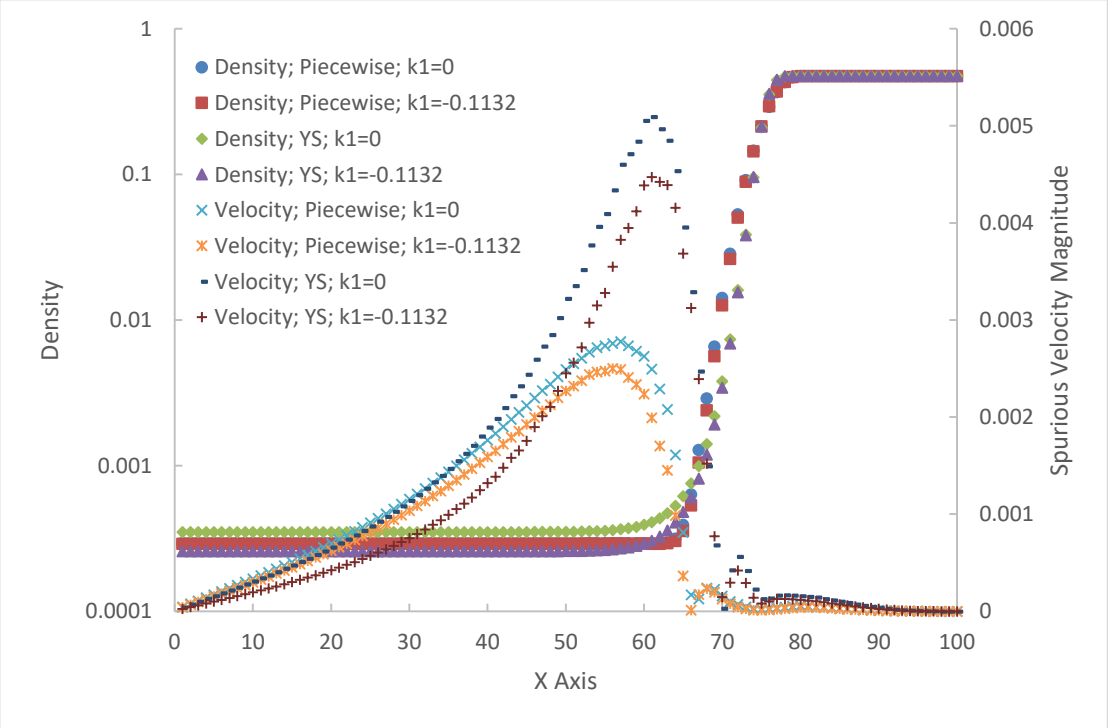

Figure 21- Density and spurious velocity distributions when surface tension is varied using the k_1 parameter in the Huang-Wu forcing scheme. ε was fixed to 1.81 and Λ was fixed to 0.0013.

3.4.2. The Effects of Viscosity Ratio on the Spurious Velocities

Li and Luo found that stability at low values of liquid kinematic viscosity can be improved by introducing a viscosity ratio between the vapour and liquid phases [74]. This strategy is further investigated in this work. It appears to resemble the strategy for improving stability in the entropic models. However, viscosity increase in the entropic models is

highly localised around the critical regions [20]. Whereas, increasing the kinematic viscosity of the vapour phase as suggested by Li and Luo affects the whole vapour region [74]. Figure 22 shows that spurious velocities are significantly reduced by increasing the kinematic viscosity ratio between the vapour and liquid phases from 1 to 20. The sensitivity of spurious velocities to density ratio increase is also almost eliminated within the examined density ratio range.

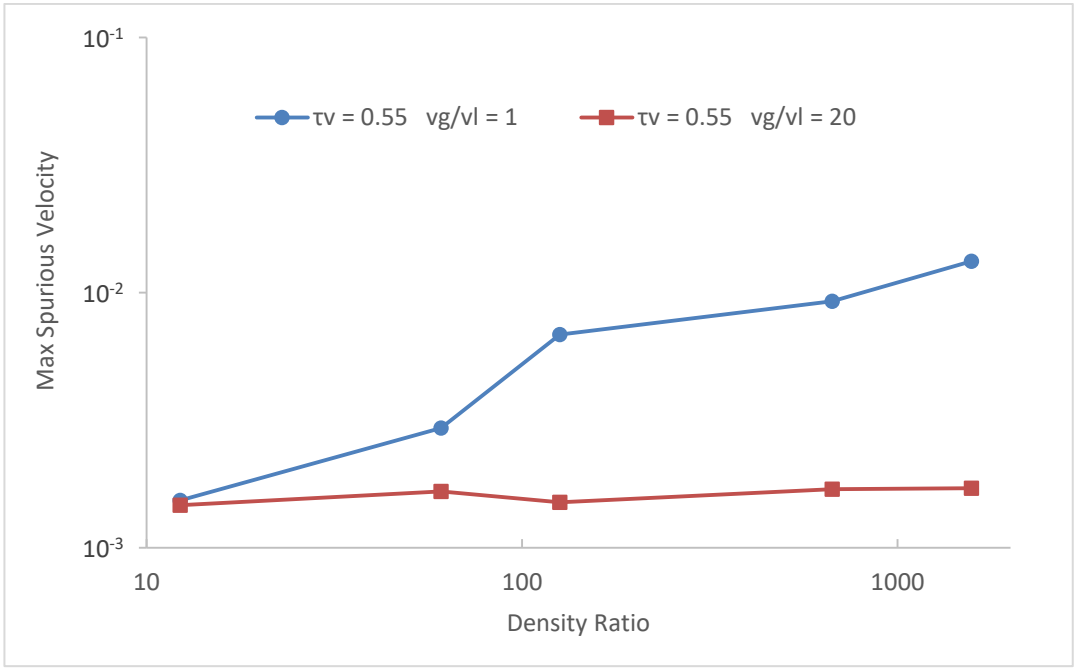

Figure 22- Reduction of spurious velocities due to an introduction of a kinematic viscosity ratio between the vapour and liquid phases. Simulations were carried out using a piecewise linear EOS and the Huang-Wu forcing scheme with ε set to 1.81.

Since a piecewise linear equation of state was found to encounter problems reaching equilibrium at low viscosities, it was decided to investigate whether introducing a kinematic viscosity ratio between the phases would alleviate the problem. As depicted in Figure 23, the lowest stable kinematic viscosity for the density ratio range can be improved ten times from 0.01667 at $\tau_v = 0.55$ to 0.00167 at $\tau_v = 0.505$ by introducing a viscosity ratio equal to 120.

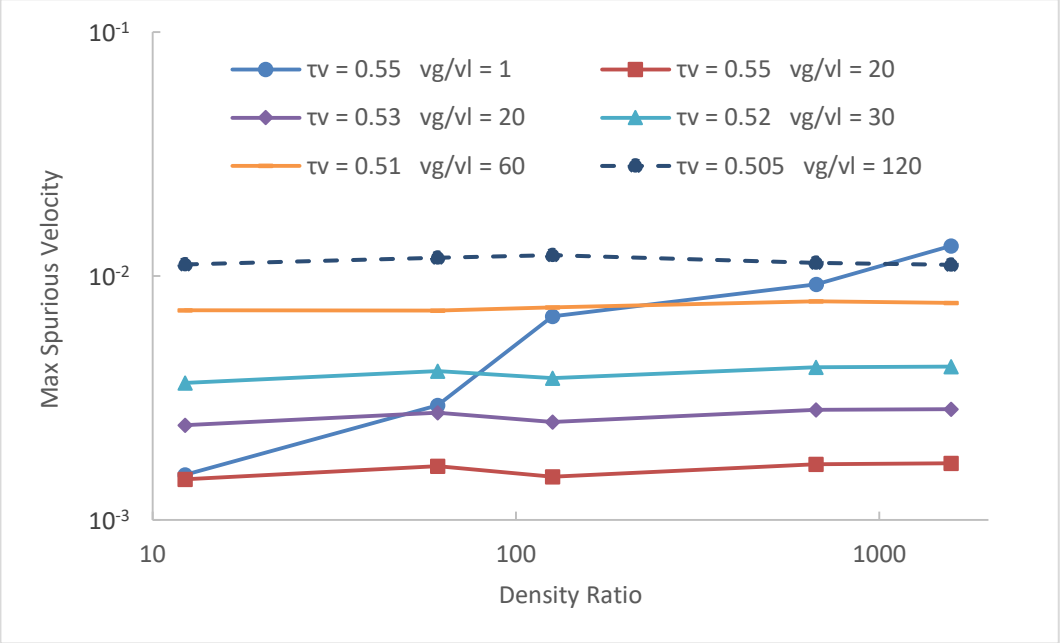

Figure 23- Simulations to explore the lowest achievable viscosities using a piecewise linear EOS combined with the Huang-Wu forcing scheme.

3.4.3. Adjustment of Multiple Relaxation Time Relaxation Rates

Simulations were carried out in order to investigate the effects of changing the relaxation rates of the MRT collision operator.

Figure 31 and Figure 32 illustrate the fact that changing the relaxation rates has a significant impact on spurious velocities (and subsequently the stability) and thermodynamic consistency. The simulations were initialized at the same reduced temperatures (T_r = 0.8, 0.65, 0.6, 0.5, 0.46), but changing the relaxation rates resulted in different density ratios. This means that the ε must be adjusted for each set of relaxation rates when the YS method is used. Wu et al. examined this and stated that it is caused by fourth-order terms [156]. Wu et al. suggested setting the anti-symmetric mode relaxation to 1.99 to reduce the effect of changing the relaxation rates on the density ratio [156]. This strategy equates to setting the magic parameter to a very low value, i.e. 0.0013 when τ_v = 1.0. Piecewise linear EOS is not significantly affected by changing the relaxation rates as illustrated in Figure 24. Density ratio obtained using the YS method diverges from that obtained using the piecewise linear EOS as the value of the magic parameter is increased. The magic parameter can be expressed as follows [77]:

$$\Lambda = \left(\frac{1}{\omega_q} - \frac{1}{2}\right)\left(\frac{1}{\omega_v} - \frac{1}{2}\right) \qquad (119)$$

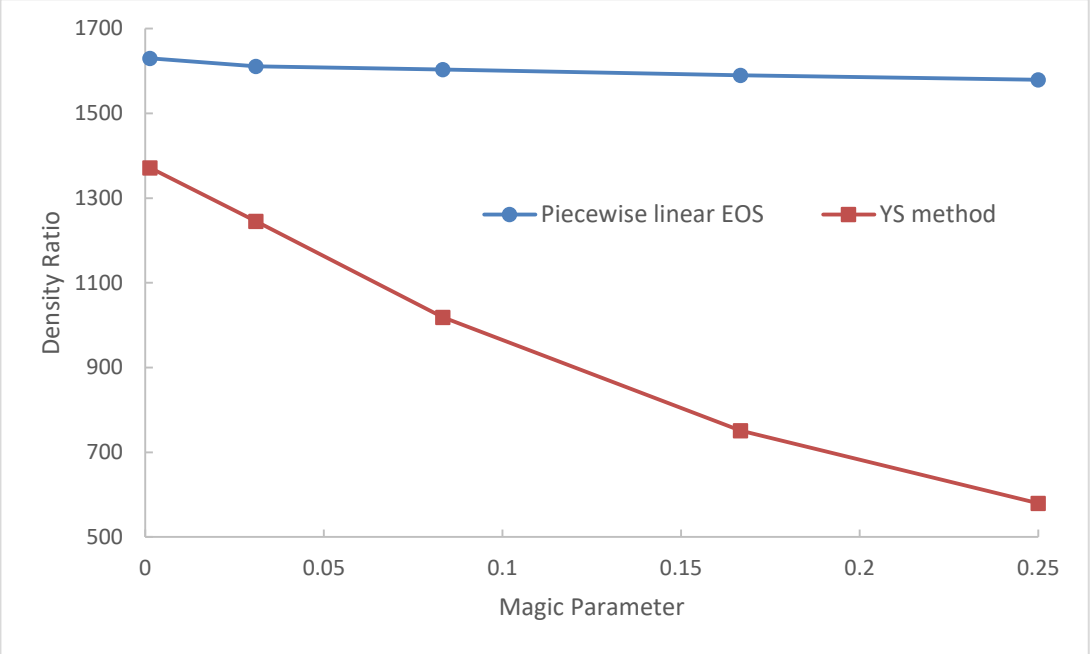

Figure 24- Comparison of the extent to which changing the magic parameter affects the density ratio for the YS method with CS EOS and for the piecewise linear EOS. Kinematic viscosity relaxation rate was fixed to 1.0, ε was fixed to 1.81 and k_1 was fixed to 0.

The parameters in the fourth-order equations responsible for the undesired effects are Q_1 and Q_8. Attention is focused on Q_1, because Q_8 is non-zero only when surface tension is modified, i.e. when $k_1 \neq 0$. Even when Q_8 is not equal to zero, its maximum value tends to be lower (between 10 and 50 times lower at the k_1 values tested) than the maximum value of Q_1 and it affects a smaller proportion of the domain than Q_1. Figure 25 shows two interesting observations. Firstly, the YS method generates significantly greater values of Q_1 than the piecewise linear EOS. In this work, it is proposed that this is the principal reason why the undesired effects are greater when the YS method is employed. Secondly, changing the magic parameter does not affect the value of Q_1 to a significant extent. Therefore, the change in the density ratio as the magic parameter is varied stems from the terms by which Q_1 is multiplied in the fourth-order equations derived by Wu et al. [156], i.e.:

$$4\left(\frac{1}{\omega_e}-\frac{1}{2}\right)\left(\frac{1}{\omega_q}-\frac{1}{2}\right)-4\left(\frac{1}{\omega_v}-\frac{1}{2}\right)\left(\frac{1}{\omega_q}-\frac{1}{2}\right), \qquad (120)$$

$$2\left(\frac{1}{\omega_e}-\frac{1}{2}\right)+6\left(\frac{1}{\omega_v}-\frac{1}{2}\right)-4\left(\frac{1}{\omega_e}-\frac{1}{2}\right)\left(\frac{1}{\omega_q}-\frac{1}{2}\right)-4\left(\frac{1}{\omega_v}-\frac{1}{2}\right)\left(\frac{1}{\omega_q}-\frac{1}{2}\right)+2. \qquad (121)$$

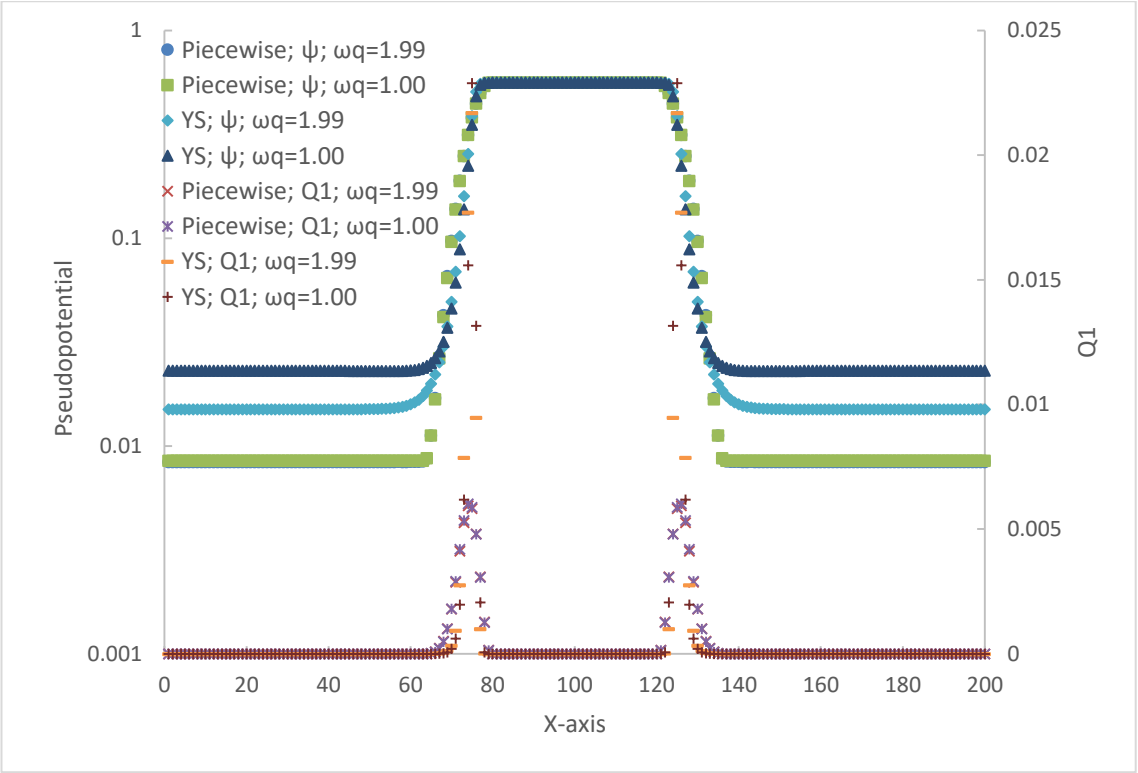

Figure 25- Comparison of the Q_1 terms generated by the Piecewise linear EOS and the YS method. The magic parameter was set to 0.0013 and 0.25 and k_1 was set to 0.

Similar observations are made regarding the magnitude of the thermodynamic consistency term in the Li-Luo method. The magnitude of the correction term generated by the YS method is significantly greater and varying the magic parameter does not have a significant influence on the magnitude of the correction term.

On the other hand, changing the surface tension by adjusting k_1 has an effect on the magnitude of Q_1 as illustrated in Figure 26 and Figure 27. Hence, the influence of surface tension on the density ratio and spurious velocities. The value of Q_1 increases as k_1 is set to greater values and this is the reason why the Huang-Wu forcing scheme has negative stability effects for low values of surface tension, i.e. when the result of $1 - 6k_1$ is lesser than 1.0.

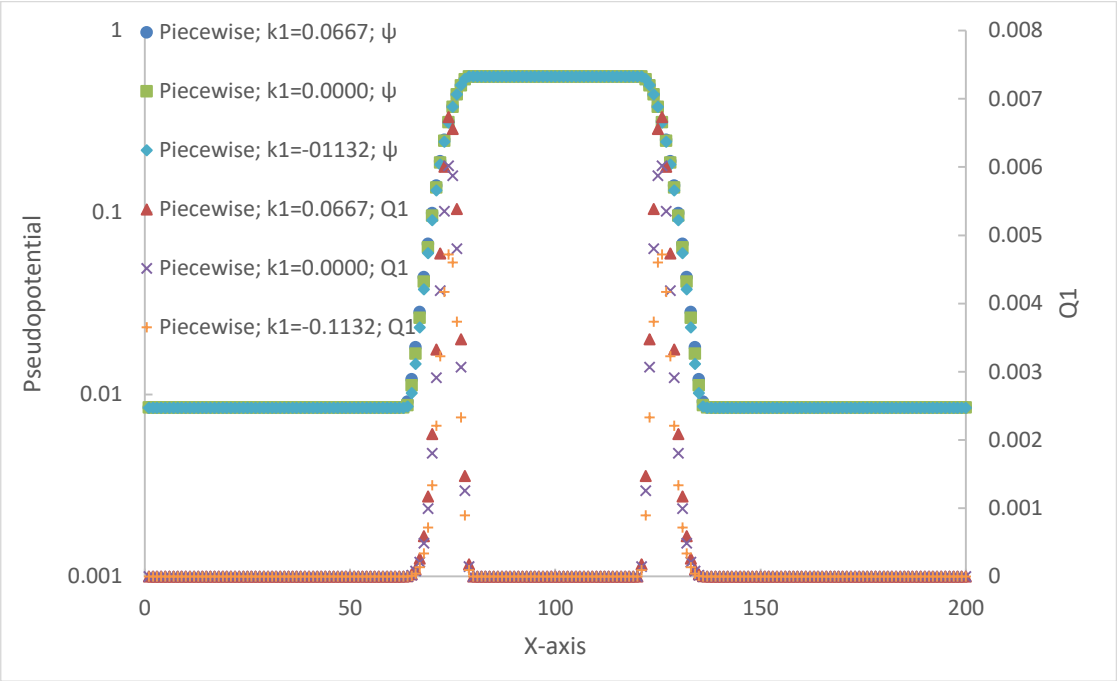

Figure 26- The effect of changing k_1 on Q_1 when the piecewise linear EOS is used. ε was fixed to 1.81 and Λ was fixed to 0.25.

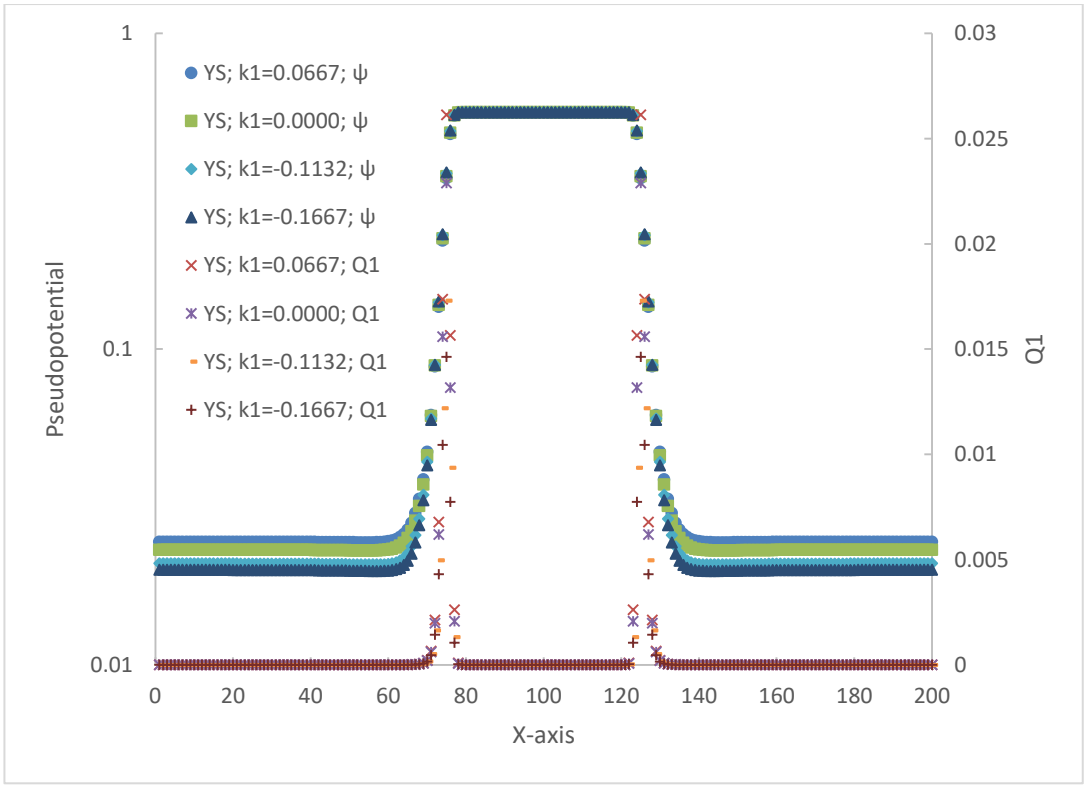

Figure 27- The effect of changing k_1 on Q_1 when the YS method is used. ε was fixed to 1.81 and Λ was fixed to 0.25.

Figure 28 illustrates the effect of the maximum value of Q_1 on the density ratio. Density ratio does not vary significantly when k_1 is adjusted and the magic parameter is changed when the piecewise linear EOS is employed due to low values of Q_1.

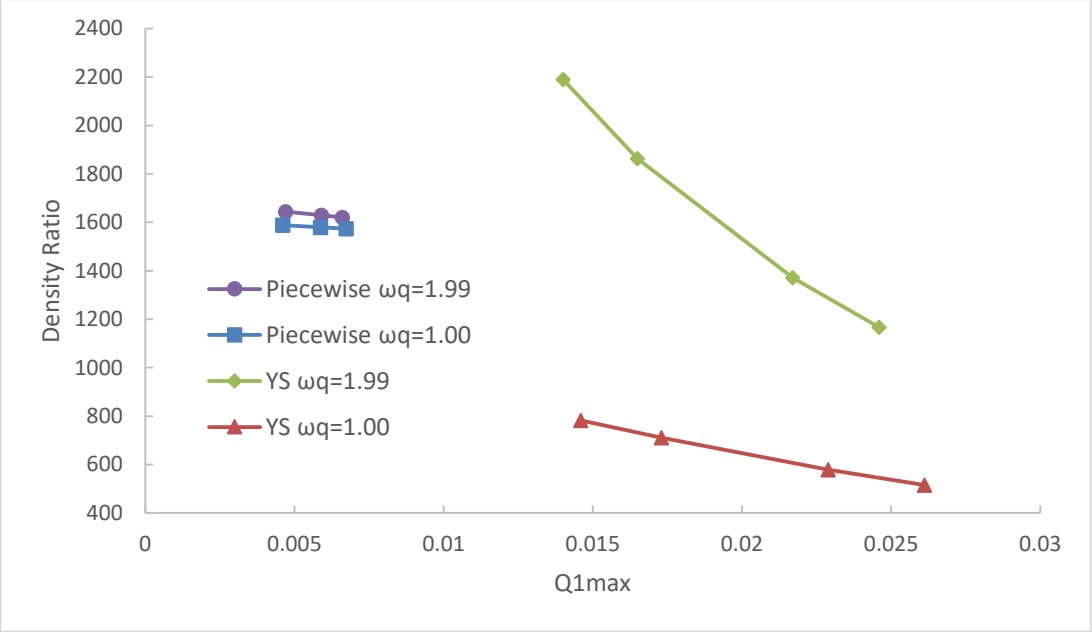

Figure 28- The effect of Q_{1max} on the density ratio at two values of the magic parameter. ε was fixed at 1.81 and k_1 was used to modify Q_1.

Both methods generate different maximum values of Q_1 due to different maximum values of the intermolecular force. The slopes of density and the pseudopotential are different in the interfacial region as illustrated in Figure 29. This means that the values of the intermolecular force (F_x and F_y in a 2D case), have different distributions with different maxima and this can be seen in Figure 30. The total value of the intermolecular force is almost identical for both methods with approximately 0.3% difference between them as shown in Table 2.

Model	**Energy Flux (ω_q)**	**$F_{x,TOTAL}$**
Piecewise Linear	1.99	0.157698
Piecewise Linear	1.00	0.157699
YS	1.99	0.158198
YS	1.00	0.158052

Table 2- Total intermolecular force for YS and Piecewise linear methods.

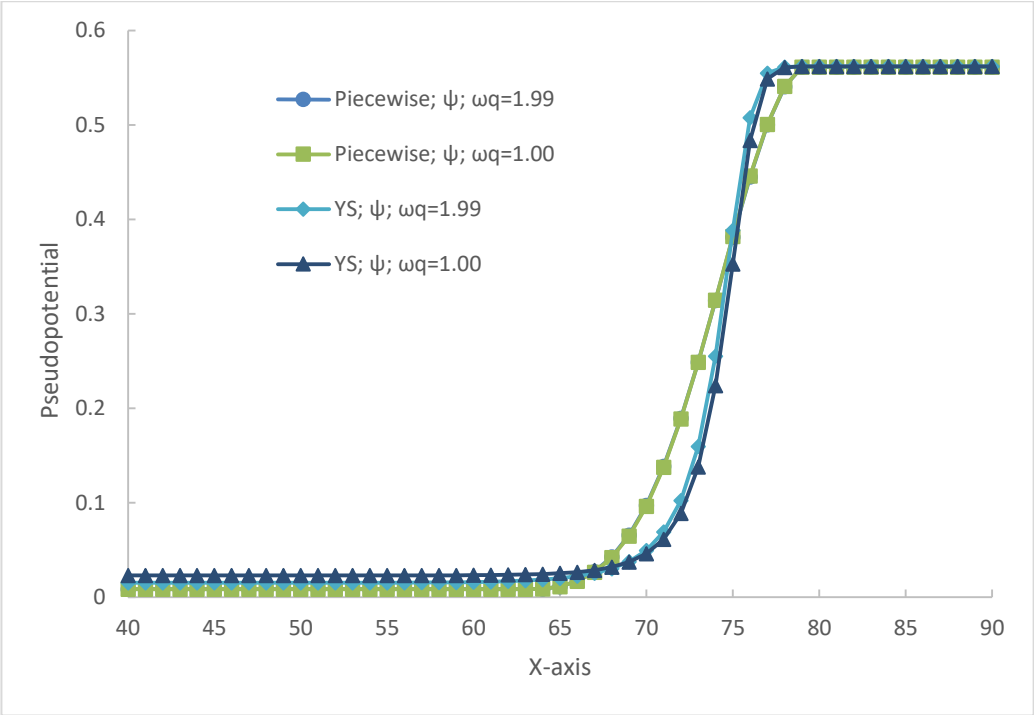

Figure 29 Pseudopotential in the interfacial region for the YS method and piecewise linear EOS.

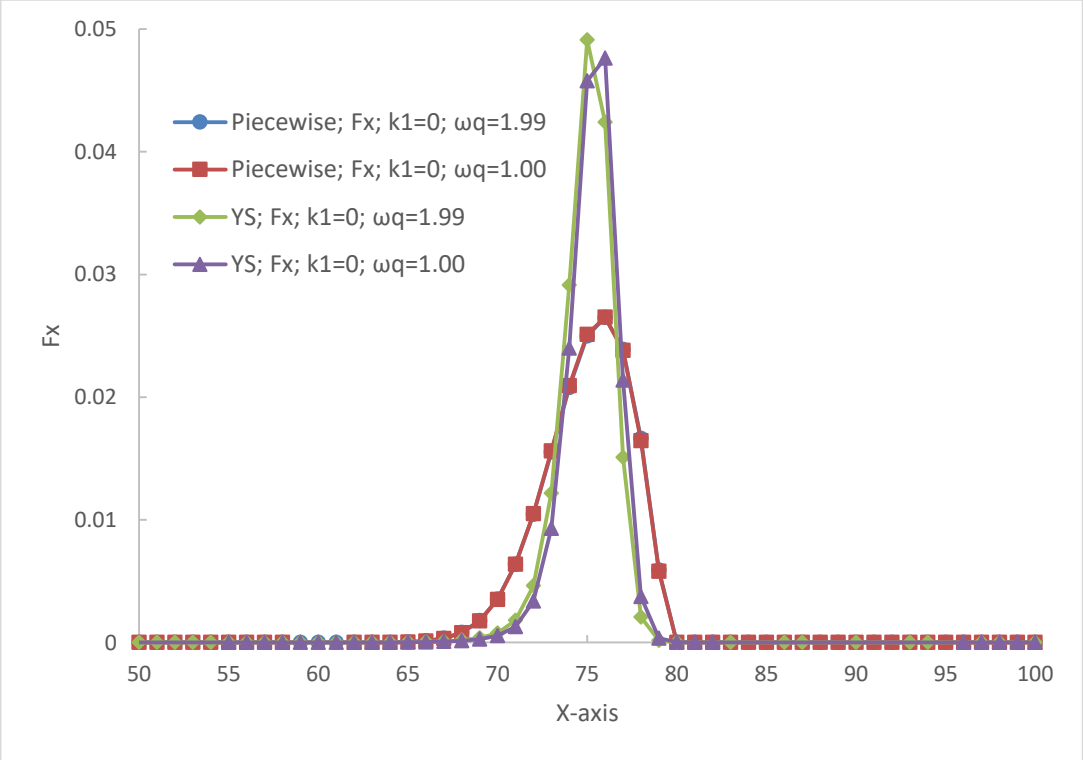

Figure 30- Distribution of the intermolecular force for the YS method and the piecewise linear EOS.

Figure 31 illustrates the fact that setting the magic parameter to 1/12 gives the best results for multiphase simulations, especially for high density ratios. Setting the magic parameter to an even lower value can result in lower spurious velocities at low density ratios. The break-even density ratio for magic parameters equal to 1/12 and 0.031 is approximately 50. Third-order spatial errors are cancelled when magic parameter is set to 1/12 [12, 148].

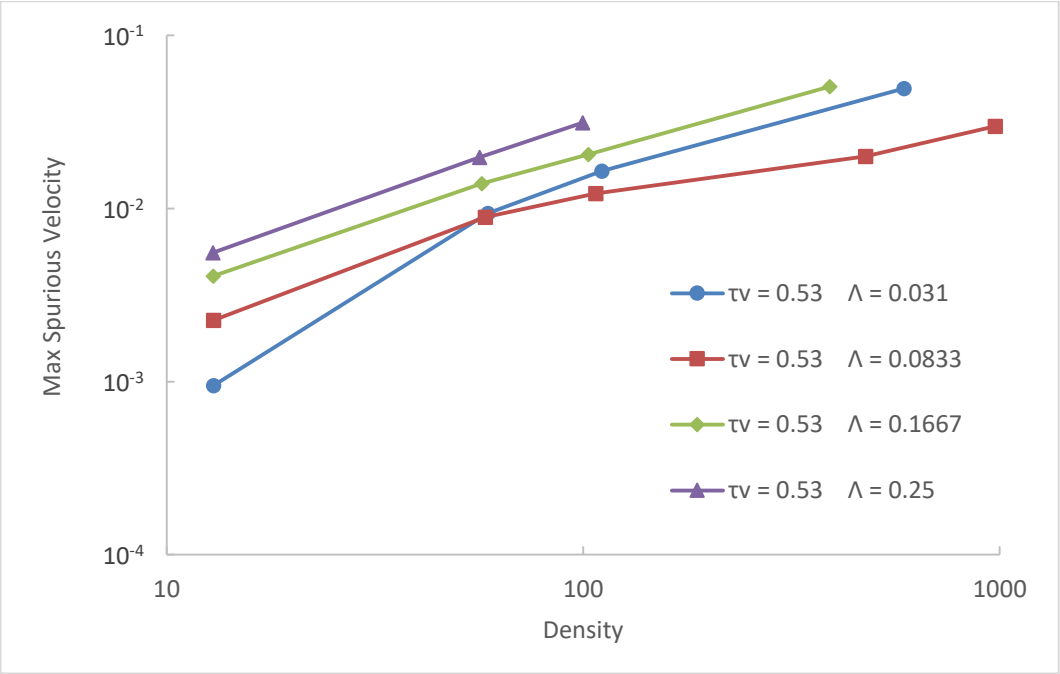

Figure 31- Tuning of the MRT relaxation times using the magic parameter. Simulations were carried out using the YS method of EOS inclusion (CS "a" = 0.25) with ε set to 1.81 using the Huang-Wu forcing method (k_1 = 0 and k_2 = -0.2264).

Figure *32* illustrates the fact that increasing the bulk viscosity to multiple times the kinematic viscosity increases the stability of simulations. Stability at the lowest reduced temperature tested, i.e. 0.46, was achieved when bulk viscosity was higher than the kinematic viscosity. Increasing bulk viscosity was found to slightly increase the maximum spurious velocities, in the case of a static droplet suspended in a gravity-free domain. However, in dynamic cases increasing the value of bulk viscosity can significantly reduce spurious waves generated in the vapour phase as illustrated in Section 3.5.

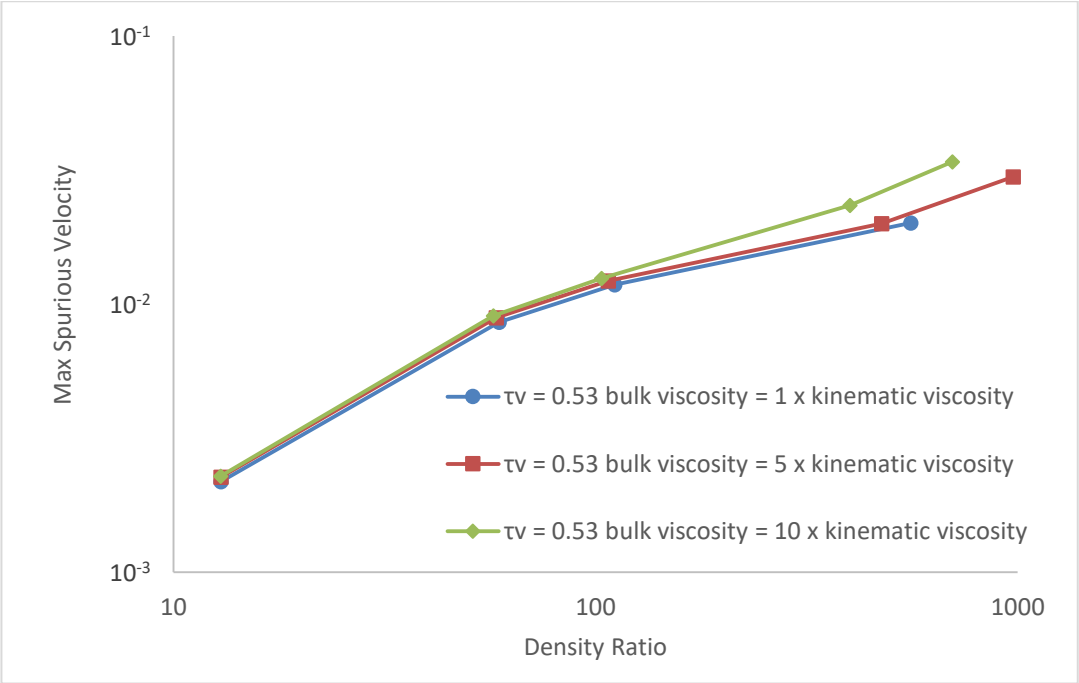

Figure 32- The effects of increasing the bulk viscosity to multiple times the value of the kinematic viscosity. Simulations were carried out using the YS method of EOS inclusion (CS "a" = 0.25) with epsilon set to 1.81 using the Huang-Wu forcing method (k_1 = 0 and k_2 = -0.2264).

3.4.4. Laplace Test with Hybrid Scheme (Piecewise Linear-YS)

A hybrid scheme proposed as a part of this doctoral project is presented in this Section. The reason for this hybrid scheme lies in the need to further understand the intermolecular force distribution and its effect on spurious velocities.

The hybrid scheme takes the following form:

$$p_{EOS} = \begin{cases} \rho RT \dfrac{1 + \frac{b\rho}{4} + \left(\frac{b\rho}{4}\right)^2 - \left(\frac{b\rho}{4}\right)^3}{\left(1 - \frac{b\rho}{4}\right)^3} - a\rho^2 & if\ \rho \leq \rho_2 \\ \rho_1\theta_V + (\rho_2 - \rho_1)\theta_M + (\rho - \rho_2)\theta_L & if\ \rho > \rho_2 \end{cases} \quad (122)$$

This form of the equation of state means that up to the liquid region the interactions are dictated by the YS method and in the liquid region they are dictated by the piecewise linear method. Figure 33 illustrates the observation that the intermolecular force distribution of the hybrid scheme is the same as that of the YS method.

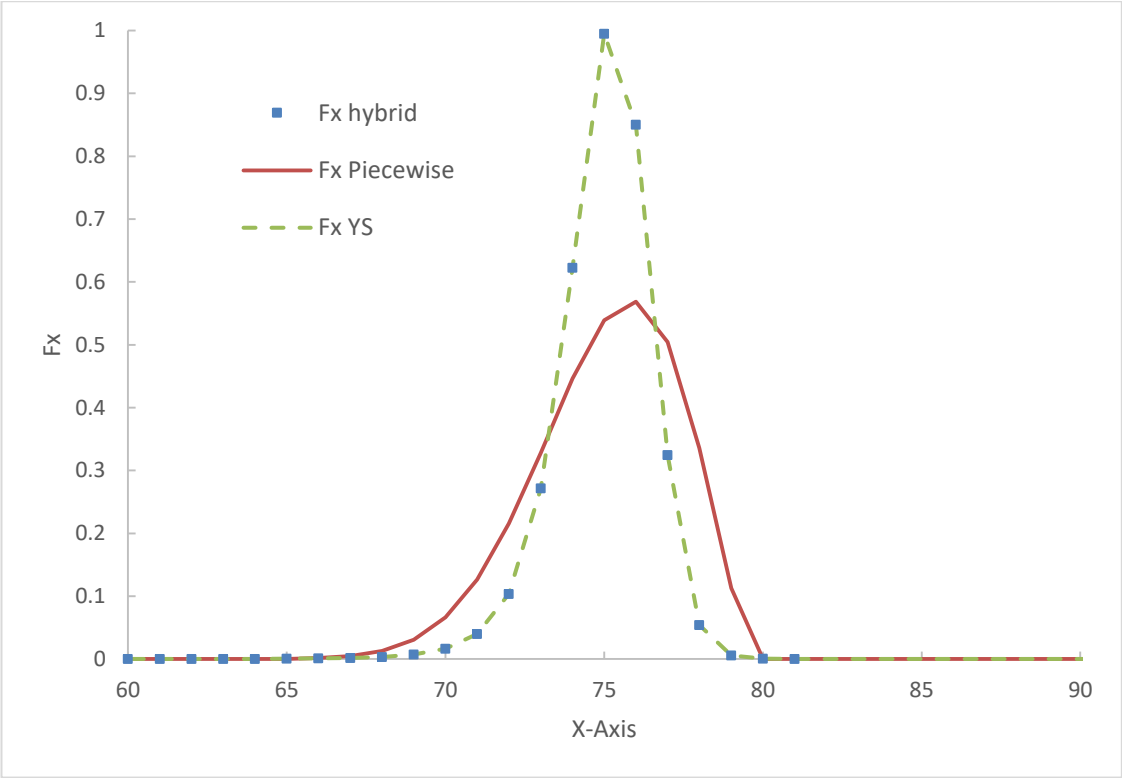

Figure 33- Intermolecular force distribution of the three schemes.

Figure 34 illustrates that the hybrid method performs the same as the YS method in terms of the density and velocity fields. This clearly indicates that spurious velocities are affected by the intermolecular force distribution. The differences between the two schemes are caused by the intermolecular force distribution rather than by the form of the pseudopotential in the liquid region.

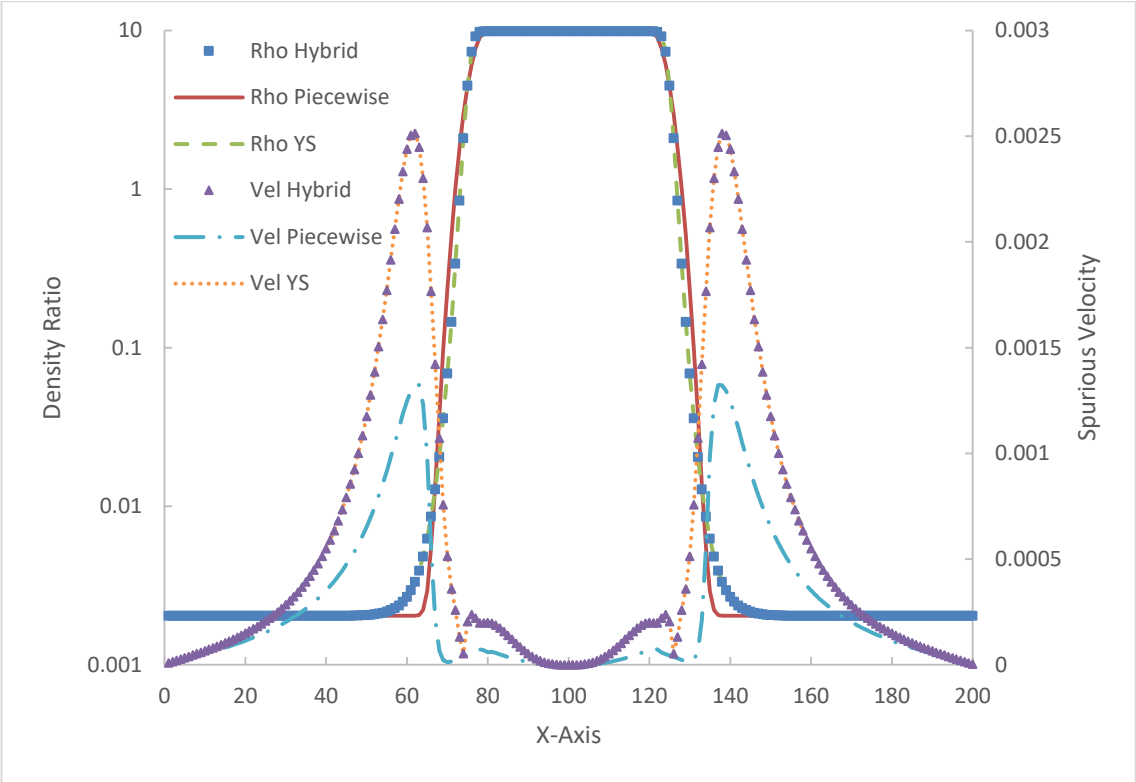

Figure 34- Velocity and density fields generated by the three schemes.

3.5.Simulations of Droplet Splashing on a Thin Liquid Film

The well-studied problem of a droplet splashing on a thin liquid film is used as an example of the dynamic capabilities of the schemes. The investigated parameters include the kinematic viscosity, bulk viscosity, reduced temperature and the viscosity ratio between the phases.

The setup consisted of a 600 units by 250 units lattice with periodic boundaries on the left and right-hand sides and a simple bounce-back boundary on the bottom wall. 25 units deep liquid film was resting on the bottom wall and a droplet with a diameter of 100 units was initialised with a prescribed impact velocity. Figure 35 illustrates formation of satellite droplets during the impact of a droplet on a thin liquid film at Reynolds number (Re) equal to 1000 and Weber number (We) equal to 110.

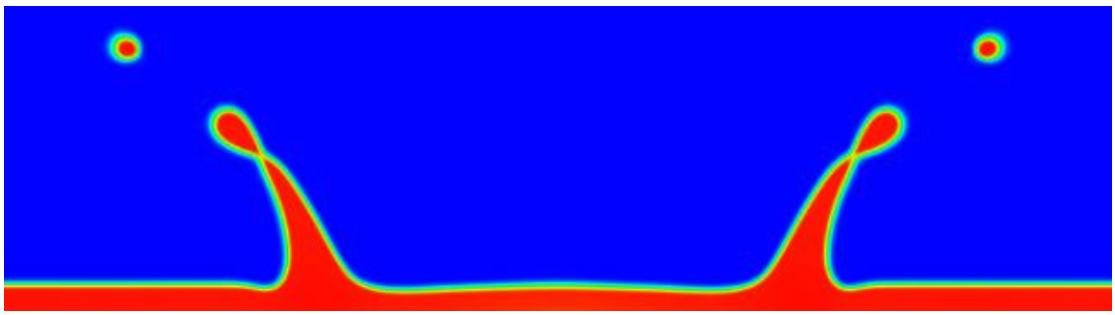

Figure 35- Formation of a liquid crown during simulation of a droplet impact on a thin liquid film (Re = 1000 and We = 110).

Figure 36 investigates the effect of the chosen schemes and parameters on the achievable Reynolds number.

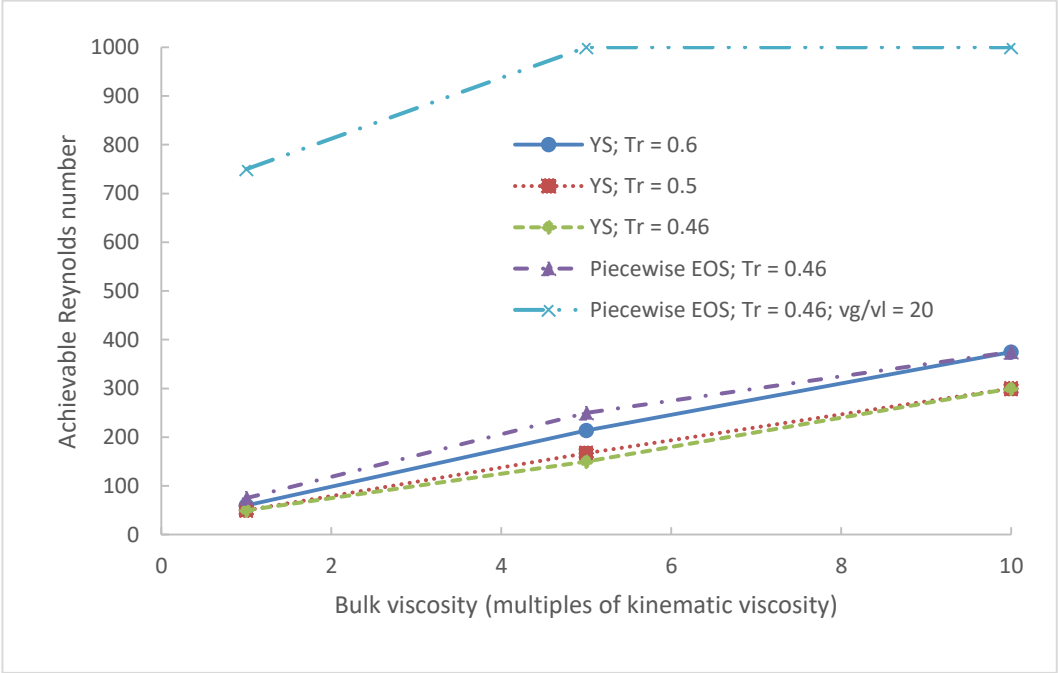

Figure 36- Stability graph showing the effects of bulk viscosity, method of EOS inclusion and reduced temperature on the achievable Reynolds number.

Clearly, increasing the value of bulk viscosity to five or ten times the value of kinematic viscosity significantly improves the stability of dynamic simulations. Bulk viscosity has a greater influence on the stability than the reduced temperature. Reynolds number of 300 was achieved even at high density ratios when bulk viscosity was ten times the value of kinematic viscosity. Instability in the problem of a splashing droplet is triggered by high velocity regions in the vapour phase as illustrated in Figure 37.

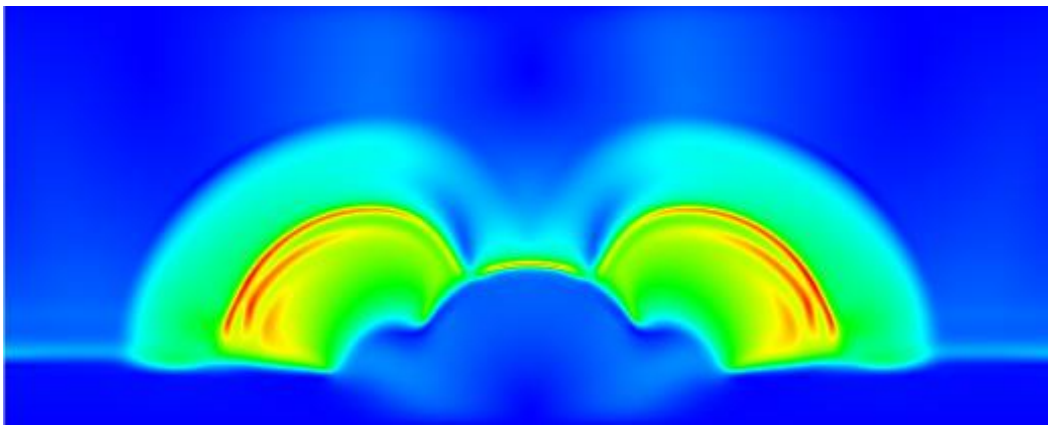

Figure 37- Formation of high velocity waves when bulk viscosity was equal to kinematic viscosity. Colour illustrates velocity magnitude.

The formation of these high velocity regions can be inhibited by increasing the value of bulk viscosity as illustrated in Figure 38. Hence, the significant improvement of stability when bulk viscosity is increased.

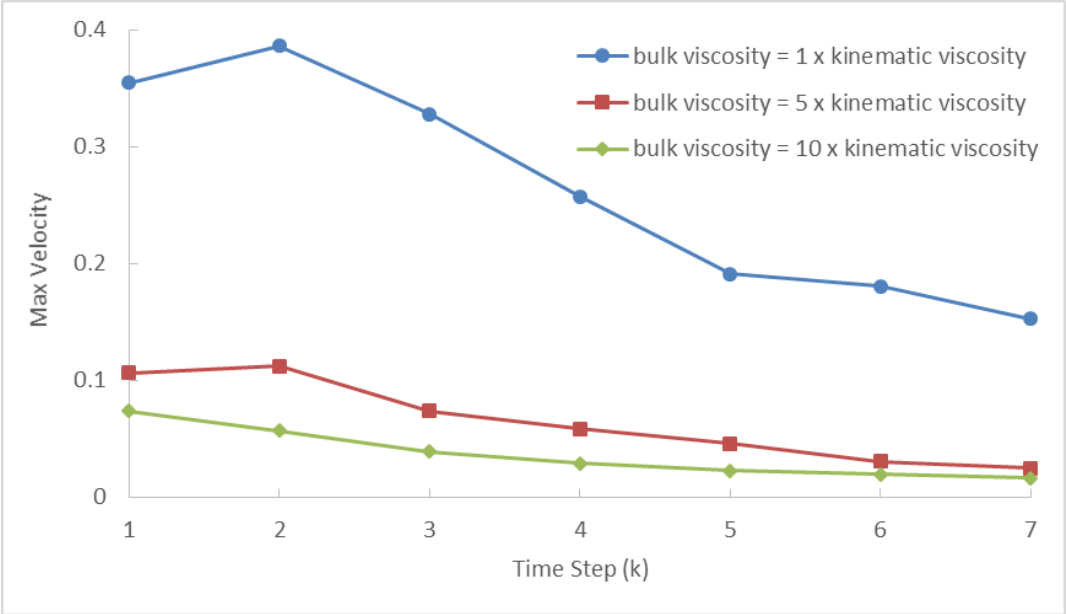

Figure 38- Velocity waves attenuation due to bulk viscosity increase.

The piecewise linear EOS offers improved performance allowing to increase the Reynolds number by approximately 50% when the bulk viscosity is the same as or five times the value of kinematic viscosity.

Introducing a viscosity ratio between the phases was found to be the most effective strategy for achieving high Reynolds numbers. Evidently, this strategy has a significant effect on the stability and allows to achieve a Reynolds number in the region of 1,000 even when the bulk viscosity is equal to kinematic viscosity.

3.6.Fluid-Solid Interactions

The ability to conveniently model fluid-solid interactions is one of the greatest strengths of LBM. The discrete particle speeds lead to a large number of possible ways of modelling fluid-solid interactions.

3.6.1. Present Models and Suggested Model for Improved Fluid-Solid Interactions

A number of ways to introduce fluid-solids interactions in pseudopotential models were proposed in the literature. Good fluid-solid interactions should allow the user to simulate a wide-range of contact angles and reduce spurious currents for fluids with high density ratios that are in contact with solids. Spurious currents are exacerbated when high density ratios are combined with low viscosities. Ideally, the interactions also should not modify the liquid and vapour densities. Li et al. [157] categorised fluid-solid interactions into density-based [158, 159] and pseudopotential-based [25, 160, 161]. Li et al. also proposed a modified pseudopotential-based interaction [157].

The density-based interactions by Martys and Chen [158] and Kang et al. [159] take the following forms, respectively:

$$\boldsymbol{F}_{ads} = -G_w \rho(\boldsymbol{x}) \sum_i \omega_i s(\boldsymbol{x} + \boldsymbol{c}_i)\, \boldsymbol{c}_i \qquad (123)$$

$$\boldsymbol{F}_{ads} = -G_w n(\boldsymbol{x}) \sum_i n_w(\boldsymbol{x} + \boldsymbol{c}_i)\, \boldsymbol{c}_i \qquad (124)$$

The pseudopotential-based interactions by Raiskinmaki et al. [160] and Sukop and Thorne [25] take the following form:

$$\boldsymbol{F}_{ads} = -G_w \psi(\boldsymbol{x}) \sum_i \omega_i s(\boldsymbol{x} + \boldsymbol{c}_i)\, \boldsymbol{c}_i \qquad (125)$$

The pseudopotential-based interaction by Benzi et al. [161] takes the following form:

$$\boldsymbol{F}_{ads} = -G\psi(\boldsymbol{x}) \sum_i \omega_i \psi(\rho_w) s(\boldsymbol{x} + \boldsymbol{c}_i)\, \boldsymbol{c}_i \qquad (126)$$

The modified pseudopotential-based interaction by Li et al. [157] takes the following form:

$$\boldsymbol{F}_{ads} = -G_w \psi(\boldsymbol{x}) \sum_i \omega_i S(\boldsymbol{x} + \boldsymbol{c}_i)\, \boldsymbol{c}_i \qquad (127)$$

$$S(\boldsymbol{x} + \boldsymbol{c}_i) = \phi(\boldsymbol{x}) s(\boldsymbol{x} + \boldsymbol{c}_i) \qquad (128)$$

Where the simplest choice of interaction contains $\phi(\boldsymbol{x}) = \psi(\boldsymbol{x})$. It appears that fluid-solid interactions should mimic the fluid-fluid interactions [157]. In this doctoral work, the modified pseudopotential-based interaction was adopted, because the pseudopotential-based interactions were not able to simulate high density ratios.

The modified pseudopotential-based interaction is explored further in this project than in the original work of Li et al. [157]. In this work, the $\phi(\boldsymbol{x})$ parameter was set to the Carnahan-Starling EOS, like the fluid-fluid pseudopotential $\psi(\boldsymbol{x})$, but the *a* parameter was modified independently from its value in the $\psi(\boldsymbol{x})$. Therefore, the $\phi(\boldsymbol{x})$ parameter assumed the independent form $\psi_{ads}(\boldsymbol{x})$:

$$\psi_{ads}(\rho) = \sqrt{\frac{2\left[\left(\rho RT\,\frac{1+\frac{b\rho}{4}+\left(\frac{b\rho}{4}\right)^2-\left(\frac{b\rho}{4}\right)^3}{\left(1-\frac{b\rho}{4}\right)^3} - a_{ads}\rho^2\right) - \rho c_s^2\right]}{G}} \tag{129}$$

Thus, the fluid-solid interactions, in this Section, were calculated using the following equation:

$$\boldsymbol{F}_{ads} = -G_w\psi_{ads}(\boldsymbol{x})\sum_i \omega_i\psi_{ads}(\boldsymbol{x})s(\boldsymbol{x}+\boldsymbol{c}_i)\,\boldsymbol{c}_i \tag{130}$$

And the results were compared to the simplest choice of the modified pseudopotential-based interaction proposed by Li et al. [157]:

$$\boldsymbol{F}_{ads} = -G_w\psi(\boldsymbol{x})\sum_i \omega_i\psi(\boldsymbol{x})s(\boldsymbol{x}+\boldsymbol{c}_i)\,\boldsymbol{c}_i \tag{131}$$

The idea behind modifying the *a* parameter in the Carnahan-Starling EOS for fluid-solid interactions independently from the *a* parameter in the Carnahan-Starling EOS for fluid-fluid interactions, is to reduce the attractive forces between the fluid and the solid without widening the fluid-fluid interface. Reducing the strength of attractive forces tends to lower spurious velocities. G_w can then be used to adjust the contact angle.

For a piecewise linear EOS, the same strategy can be attained by setting $\theta_{M,ads}$ separately from θ_M.

3.6.2. Simulations of Stationary Droplet on a Wall

Simulations were carried out in a 201 lattice units (lu) by 201 lattice units lattice. The 50 lu diameter droplet was initialised in the same state for all the tests as illustrated in Figure 39. The initial bubble position can have an effect on the spurious velocities when the final

contact angle is different than the initial contact angle. First, the Huang-Wu and Li-Luo models are compared to investigate their performance in simulating different contact angles. Secondly, the effect of adjusting the surface tension using the Huang-Wu forcing scheme is investigated. Finally, varying the a_{ads} parameter in the modified-pseudopotential interaction is investigated.

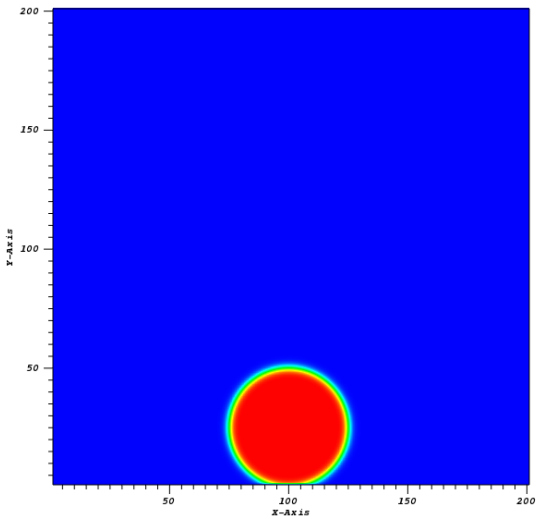

Figure 39- Initial state of a droplet in contact with a solid surface to investigate fluid-solid interactions (Colour illustrates density).

Figure 40 shows that the Huang-Wu and Li-Luo modifications perform in a similar manner when simulating fluid-solid interactions. Spurious currents increase from wetting to non-wetting contact angles using both forcing modifications.

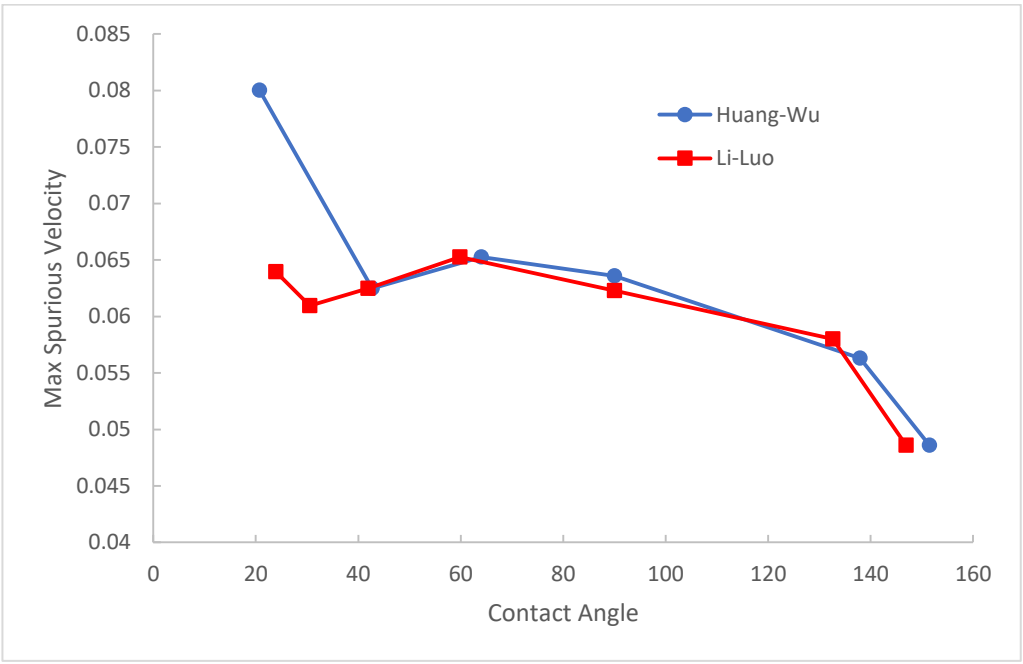

Figure 40- Spurious velocities for different contact angles using the modified-pseudopotential interaction and the Huang-Wu and Li-Luo forcing modifications. Simulations are for a high density ratio, i.e. Tr = 0.5 (density ratio approximately 730).

Both forcing schemes in Figure 40 are set to not modify the surface tension. This is an important qualification in order to ensure that the comparison is fair. Figure 41 clearly illustrates that modifying the surface tension has a significant effect on the magnitude of spurious velocities generated by fluid-solid interactions. This fact can be exploited when it is desired to optimise the fluid-solid interactions and to reduce spurious velocities in the vicinity of fluid-solid interfaces.

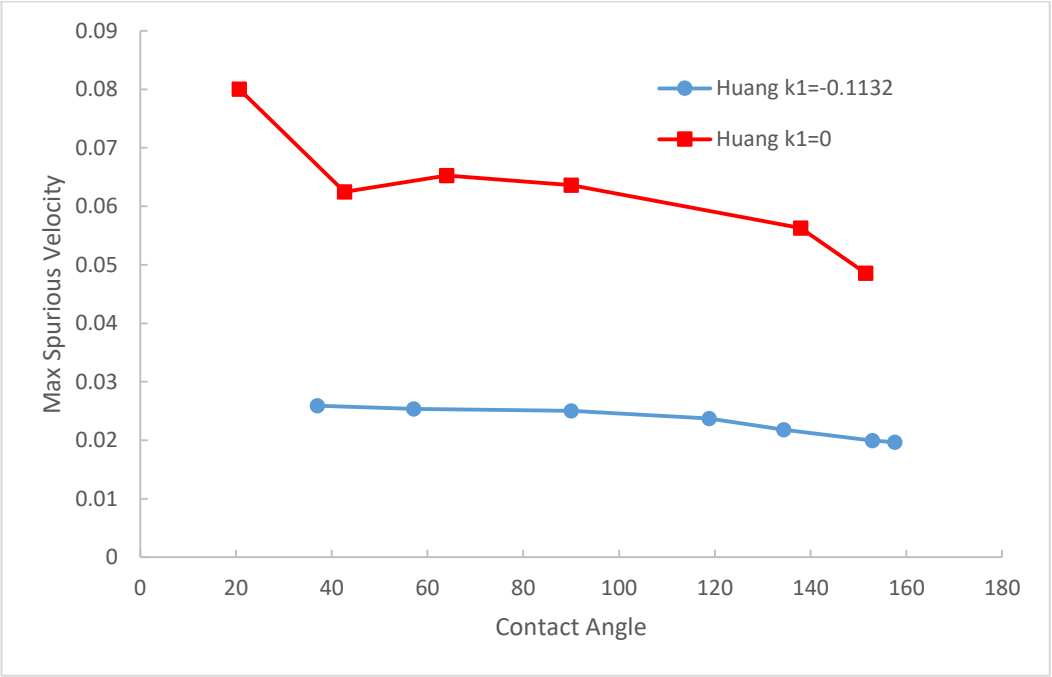

Figure 41- Effect of modifying surface tension on spurious velocities when the Huang-Wu forcing scheme is used.

The rationale for setting a_{ads} in ψ_{ads} separately from a in ψ is presented in Figure 42. It is clear that reducing the value of a_{ads} below 0.25 can reduce the spurious velocities even further. Lowering the value of a_{ads} weakens the attractive interactions which helps to reduce spurious velocities. The G_w parameter can be adjusted to achieve the desired contact angle. Figure 43 illustrates the relationship between a_{ads} and spurious velocities generated at a contact angle of approximately 155°. Another interesting aspect of the proposed method is that the influence of contact angle on spurious velocities is significantly lessened. This is a significant advantage for modelling non-wetting contact angles.

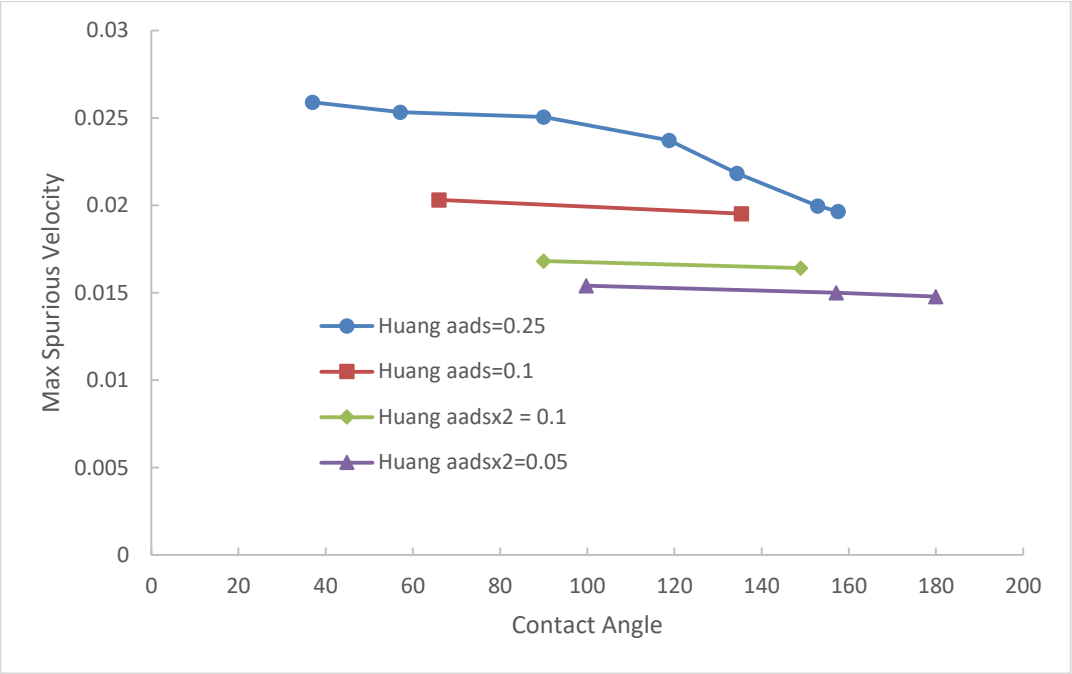

Figure 42- The effect of reducing the a_{ads} parameter in the CS EOS in the modified-pseudopotential interaction for different contact angles (τ_v = 1.0 and Tr = 0.5).

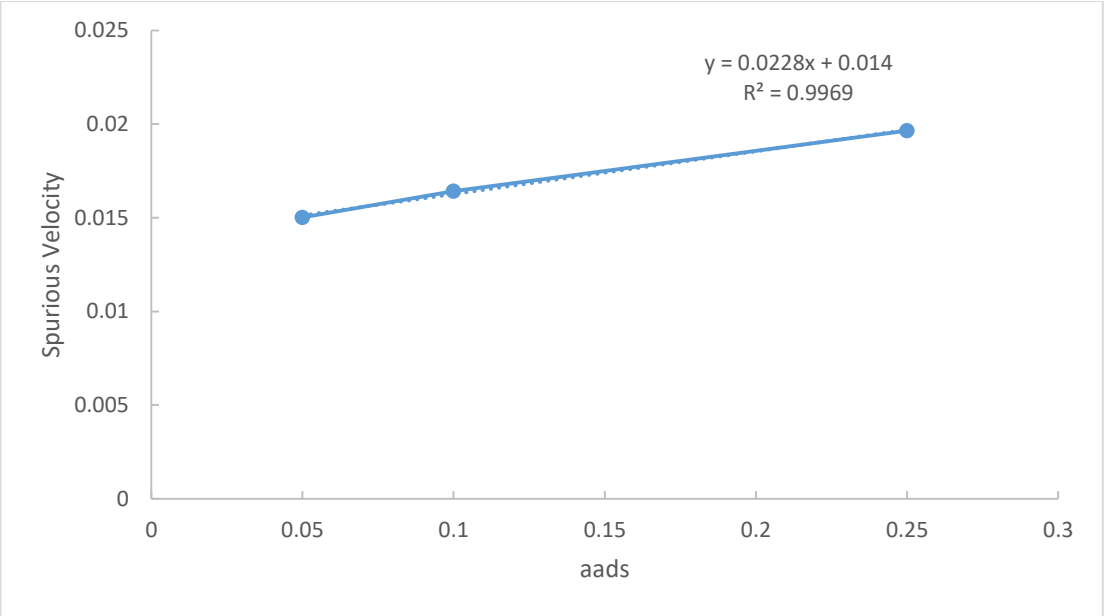

Figure 43- Relationship between a_{ads} and spurious velocities at a contact angle of approximately 155°.

Figure 44 illustrates the findings that the proposed method of modifying fluid-solid interactions is not effective for reducing spurious velocities generated when the piecewise linear EOS is used.

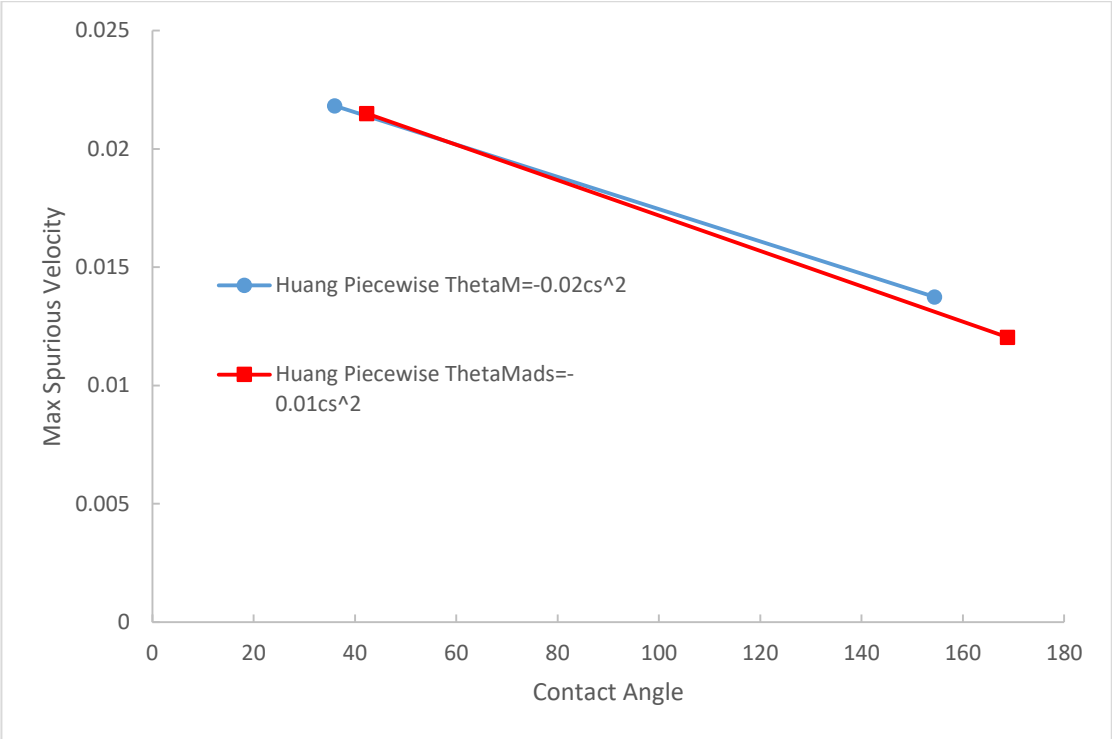

Figure 44- The effect of the proposed fluid-solid interaction modification on spurious velocities generated when the piecewise linear EOS is used.

Chapter 4 – Application of Multipseudopotential Interaction Model with Multiple Relaxation Time Collision Operator

This Chapter deals with an MPI model combined with the MRT collision operator. This coupling has been performed for the first time in this project.

4.1.Interparticle Interactions

MPI consists of multiple interactions which are additive and together make up the total interaction force. Conventional pseudopotential models have a single interparticle force. In order to compare the magnitude of the different interparticle forces, the pseudopotentials should be multiplied by their respective *G* values. The following graphs illustrate the interaction strength at the binodal curve.

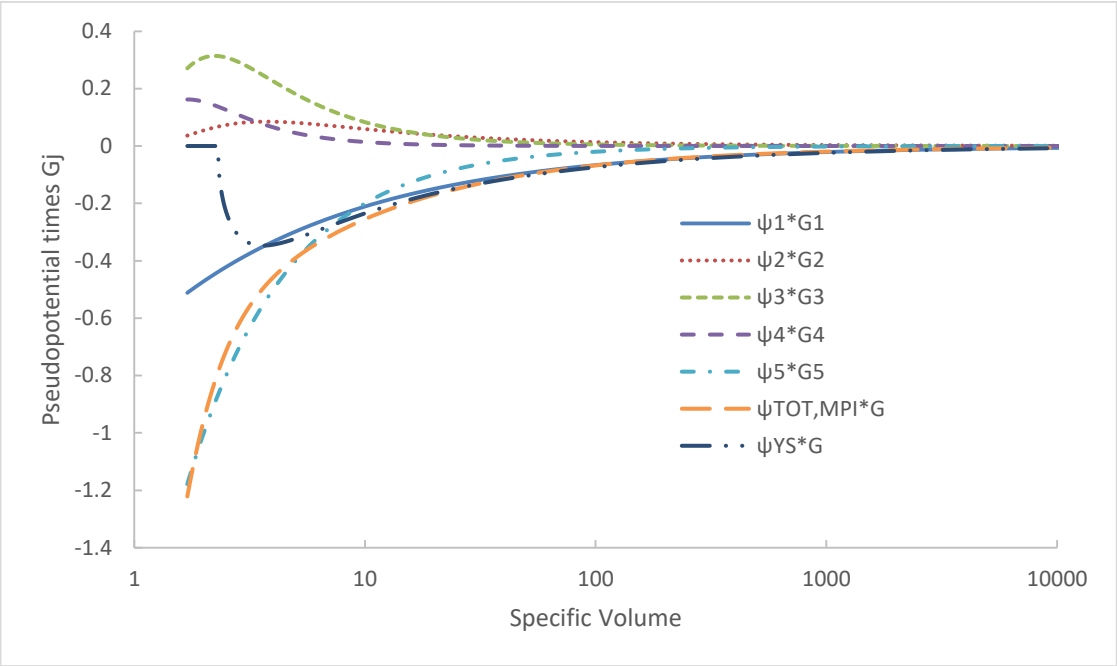

Figure 45- Breakdown of the MPI into separate multipseudopotential and comparison of the total MPI interaction force with the corresponding YS force.

The total pseudopotential forces generated by the MPI and Yuan-Schaefer models depend on the interfacial thickness. The comparative performance of the two schemes varies depending on the chosen EOS parameters. The following subsections illustrate examples of different behaviours by the schemes.

4.1.1. Sharp Interface (CS EOS a = 1, b = 4; interface thickness parameter = 4)

The Yuan-Schaefer model is unsuitable for simulation of high density ratios with a sharp interface. The pseudopotential force becomes undefined at high values of density which are required for simulation of low reduced temperatures, i.e. high density ratios. On the

other hand, MPI generates correct intermolecular forces in this case as illustrated in Figure 46.

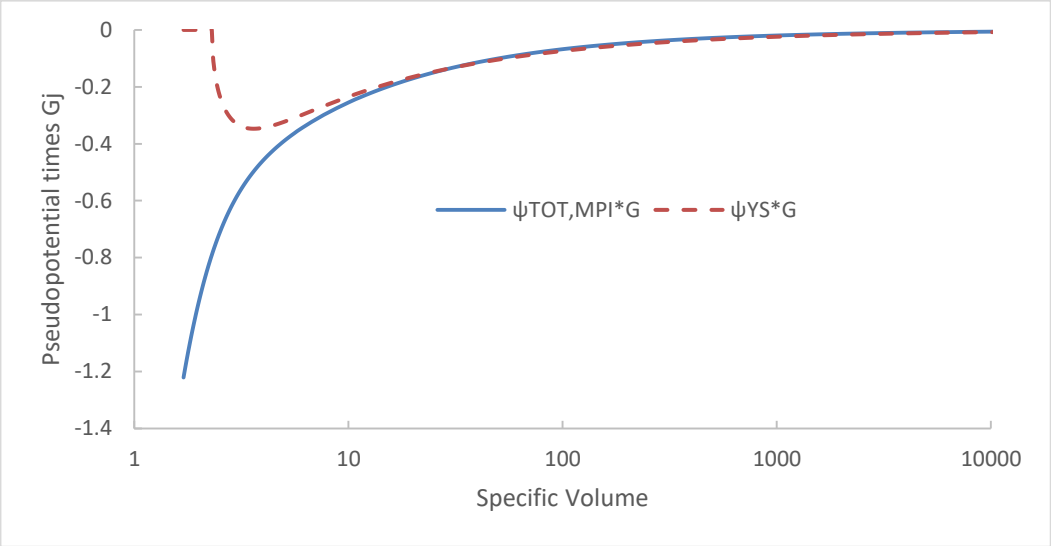

Figure 46- Pseudopotential forces generated by MPI and YS forces when the interface is sharp.

4.1.2. Practical interface thickness (CS EOS a = 0.01, b = 0.2; interface thickness parameter = 20)

In order to simulate high density ratios, the interfacial thickness should be set to approximately 20 lattice units when using both the Yuan-Schaefer and MPI models. At this thickness, the pseudopotential does not become undefined for either model. However, the YS method still exhibits undesired effects at very low values of specific volume, i.e. at very low reduced temperatures, as illustrated in Figure 47.

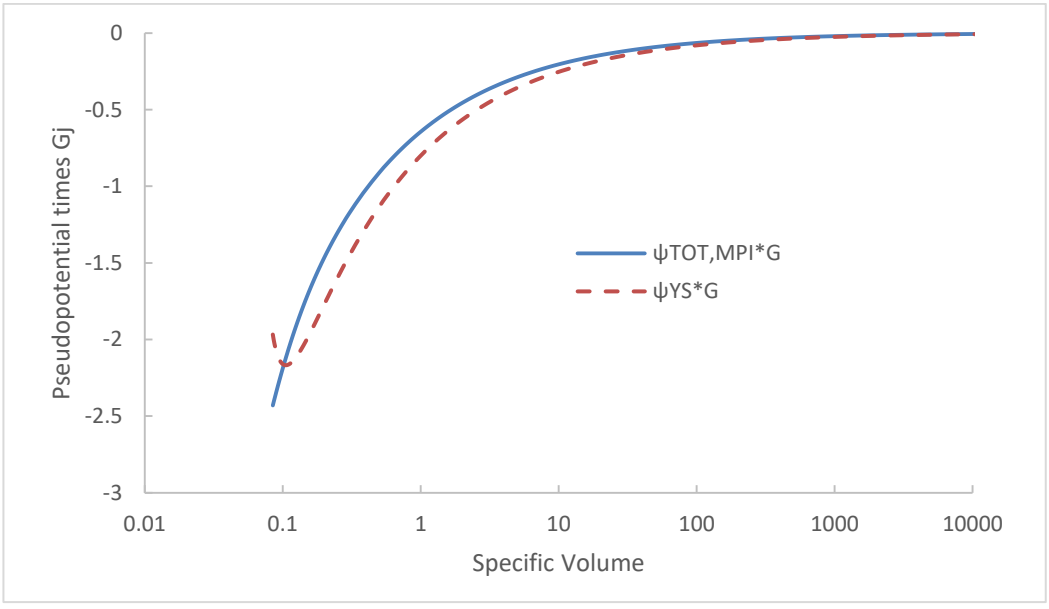

Figure 47- Pseudopotential forces generated by MPI and YS methods when the interfacial thickness is set to a practicable thickness.

4.1.3. Thick Interface

- (CS EOS a = 0.0025, b = 0.1; interface thickness parameter = 40)

When this set of EOS parameters is used, MPI crashes when density reaches 20 due to negative denominator in the fourth multipseudopotential. On the other hand, the Yuan-Schaefer model generates desired intermolecular force as illustrated in Figure 48.

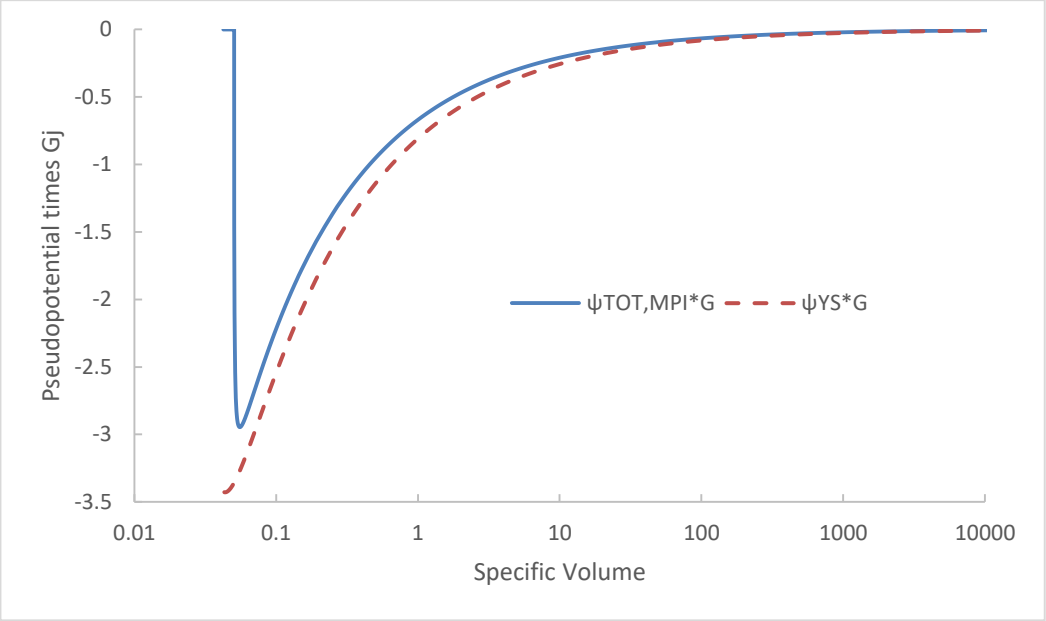

Figure 48- Pseudopotential forces generated by the two models for diffuse interfacial thickness when CS EOS a parameter is set to 0.0025.

- (CS EOS a = 0.005, b = 0.2; interface thickness parameter = 40)

MPI does not crash when the EOS parameters are changed as illustrated in Figure 49.

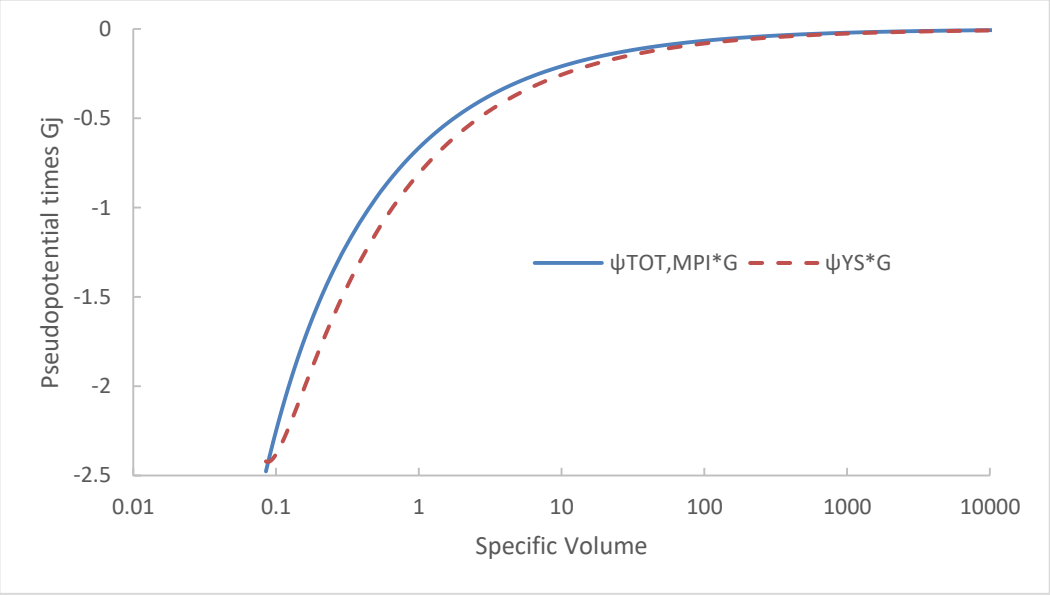

Figure 49 - Pseudopotential forces generated by the two models for diffuse interfacial thickness when CS EOS a parameter is set to 0.005.

4.1.4. Interactions at a Constant Temperature across the Phase Envelope

The purpose of this Subsection is to compare the interactions across the phase envelope at a constant temperature. In Figure 50, it can be seen that the only method to avoid generation of undefined pseudopotential forces across the phase envelope is the piecewise linear EOS. The other two methods generate undefined pseudopotential forces within the liquid region due to an inherent inability of cubic equations of state to calculate pressure within that region.

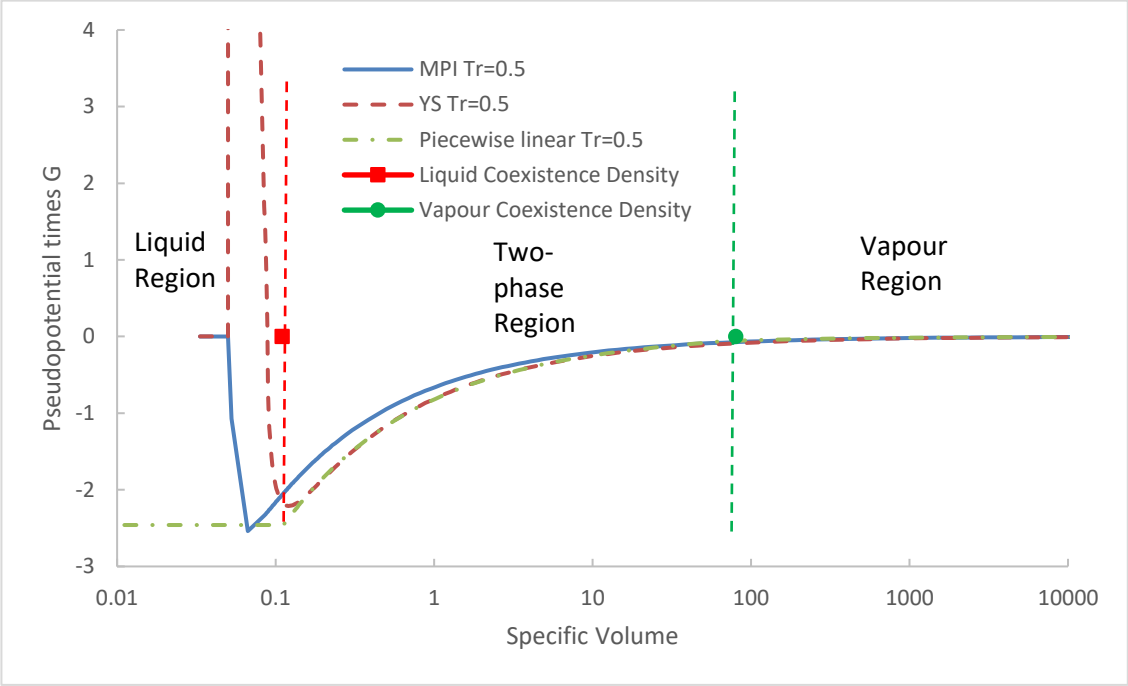

Figure 50- Pseudopotential forces generated by the YS, MPI and piecewise linear methods across the phase envelope.

4.2.Achievement of Thermodynamic Consistency

4.2.1. Modification for Achievement of Thermodynamic Consistency

The MPI obtained coexistence densities deviate from the thermodynamically consistent values for both SRT and MRT collision operators and this can be seen in Figure 51.

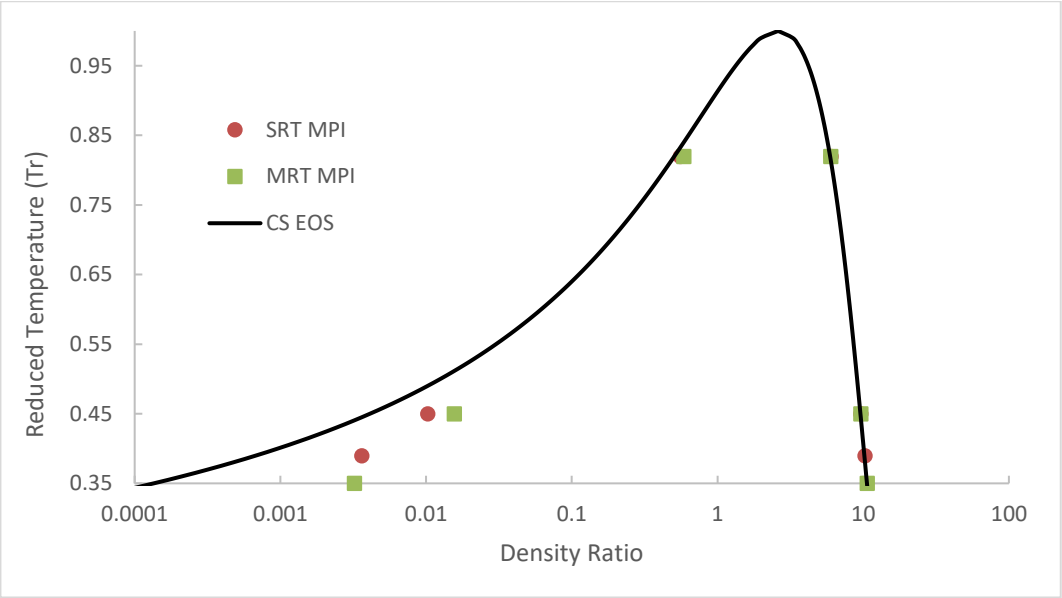

Figure 51- Deviation of MPI from the thermodynamic coexistence densities when the SRT and MRT collision operators are used.

The solution is to split epsilon into two separate values, i.e. one for use in the EOS and a second one for use in the forcing scheme:

$$\psi_j = \left(\frac{\rho}{\lambda_j \varepsilon_j + C_j \rho}\right)^{1/\varepsilon_j} \tag{132}$$

ε_j should be split into $\varepsilon_{EOS,j}$ and $\varepsilon_{Forcing,j}$:

$$\psi_j = \left(\frac{\rho}{\lambda_j \varepsilon_j + C_j \rho}\right)^{1/\varepsilon_{EOS,j}} \tag{133}$$

This modification allows the user to set the ε to a different value in the forcing scheme than in the pseudopotential calculation, in order to adjust the density ratio without affecting the equation of state recovered by the MPI model. Introduction of unnecessary modifications to the equation of state is not desired. For example, the value of $\varepsilon_{Forcing,j}$ can be set to 0.89 times the value of $\varepsilon_{EOS,j}$:

$$\varepsilon_{Forcing,j} = 0.89\varepsilon_{EOS,j} \tag{134}$$

The Li-Luo method [74] of achievement of thermodynamic consistency for the MRT collision operator can then be modified to the following:

$$6\left(u_x F_x + u_y F_y\right) + \sum_j \frac{12\frac{\varepsilon_{Forcing,j}}{-16G_j}\left|\boldsymbol{F_j}\right|^2}{{\psi_j}^2 \Delta t(\tau_e - 0.5)} \tag{135}$$

Figure 52 shows that the modification splitting ε into two separate values allows to approach thermodynamic consistency across the entire range of reduced temperature.

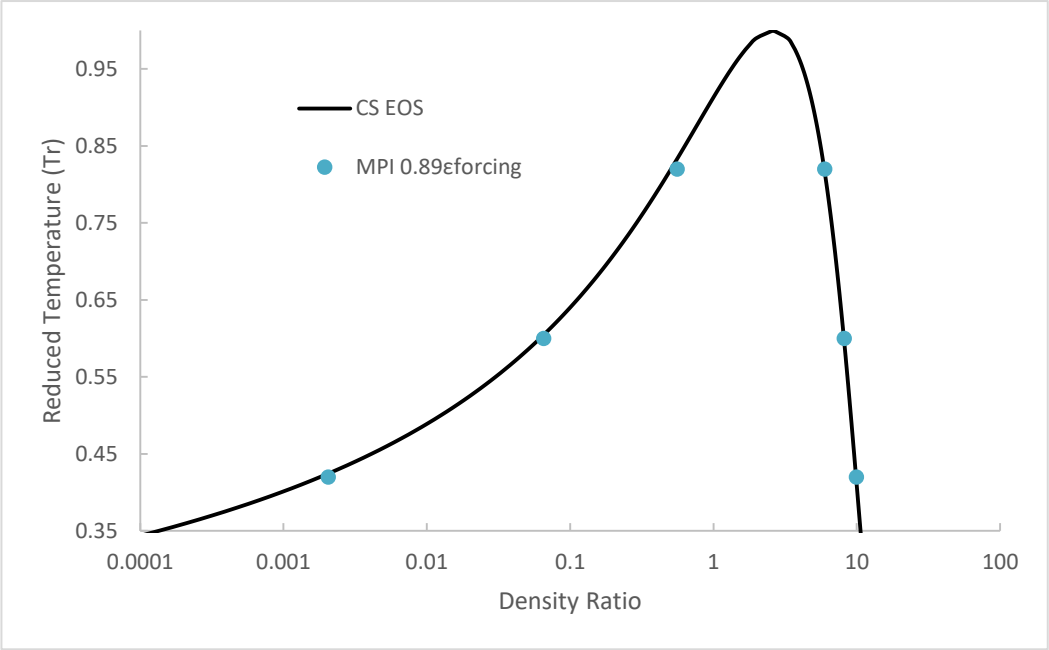

Figure 52- The modification allows to recover thermodynamically consistent densities for the entire temperature range without the need for further manipulation and fitting.

4.2.2. Factors Affecting Thermodynamic Consistency

Clearly, thermodynamic consistency is affected by changing droplet diameter for both MPI and Yuan-Schaefer models. This is evident in the density ratio values depicted in Figure 53. The behaviour of MPI and YS models is very similar.

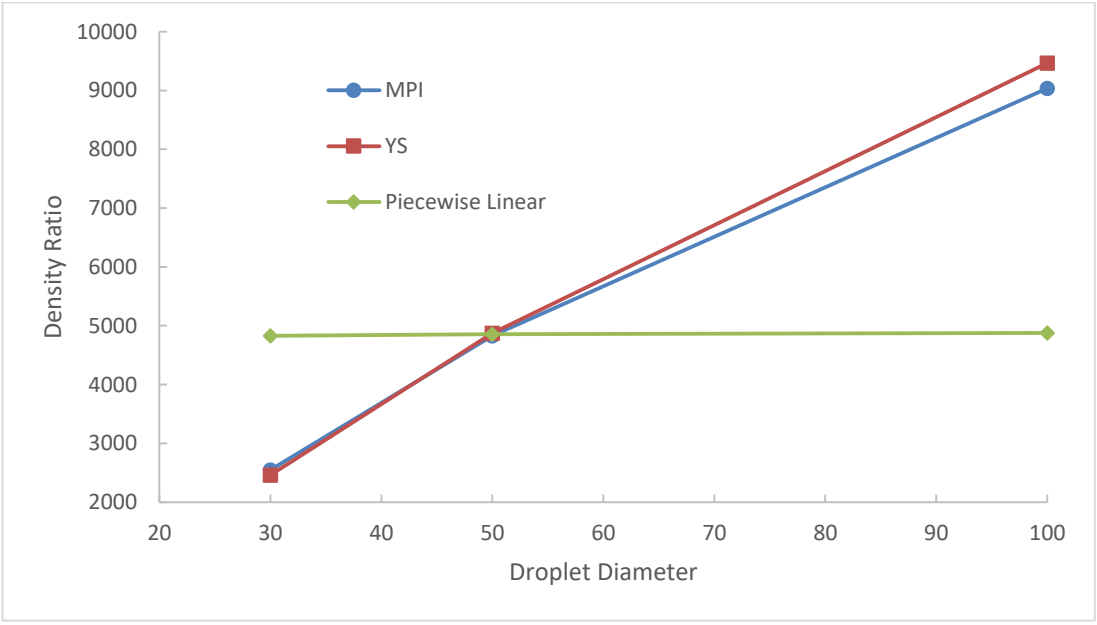

Figure 53- Effect of changing droplet diameter on the obtained density ration using the MPI, YS and piecewise linear methods of EOS inclusion.

Adjusting the relaxation parameters also affects the thermodynamic consistency of MPI and Yuan-Schaefer models as illustrated in Figure 54.

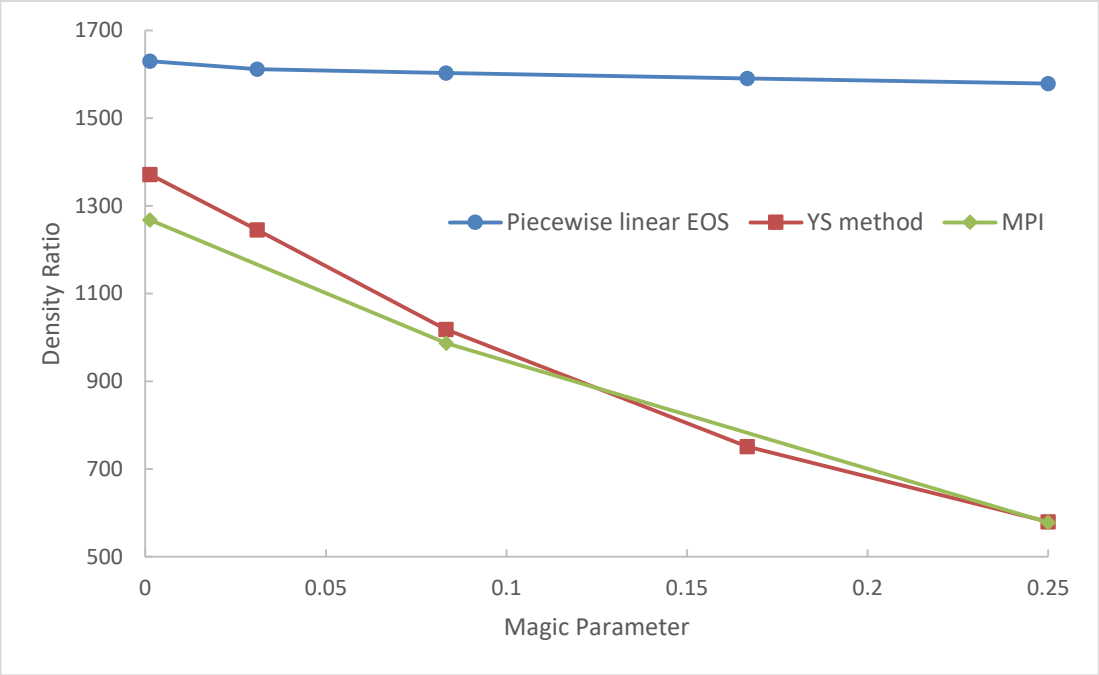

Figure 54- Effect of changing the magic parameter on the obtained density ratio in droplet simulations using the MPI, YS and piecewise linear methods.

4.3.Laplace Test of Stationary Droplets

Figure 56 shows the resultant spurious velocity magnitude for the MPI and YS simulations. The comparison of the intermolecular force generated by both methods at the same conditions is presented in Figure 55. Both Yuan-Schaefer and MPI models give practically the same spurious velocities when the same EOS parameters are used. This is caused by the fact that both models generate almost identical intermolecular interaction force.

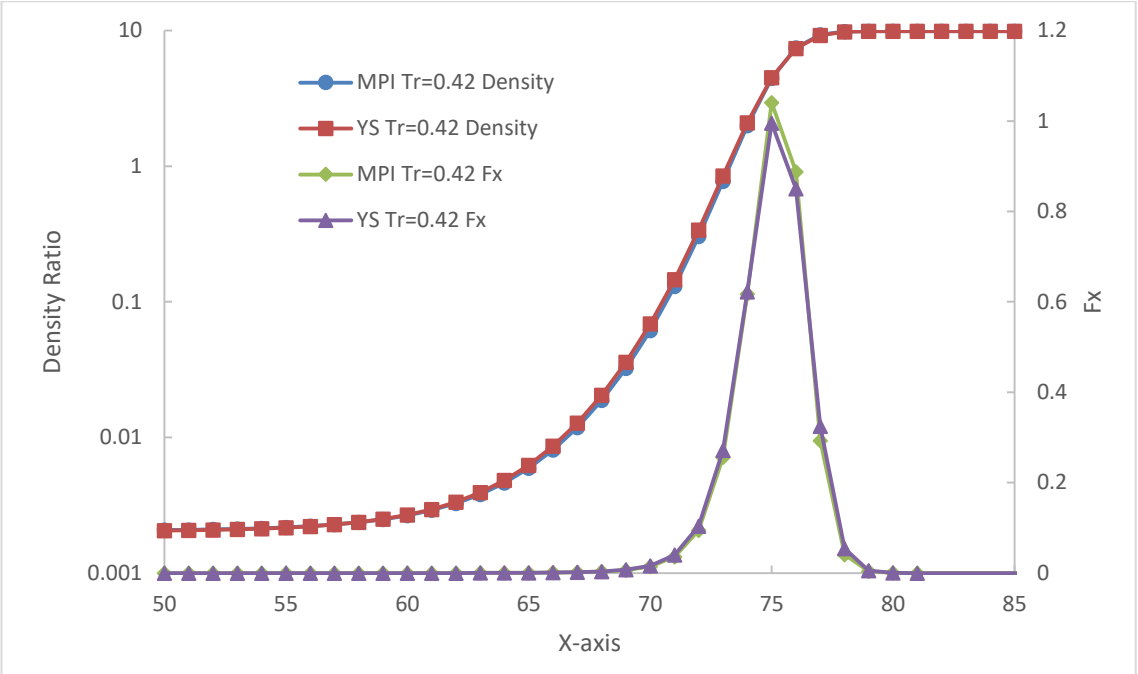

Figure 55- Interparticle force generated by MPI and YS methods at the same density ratio.

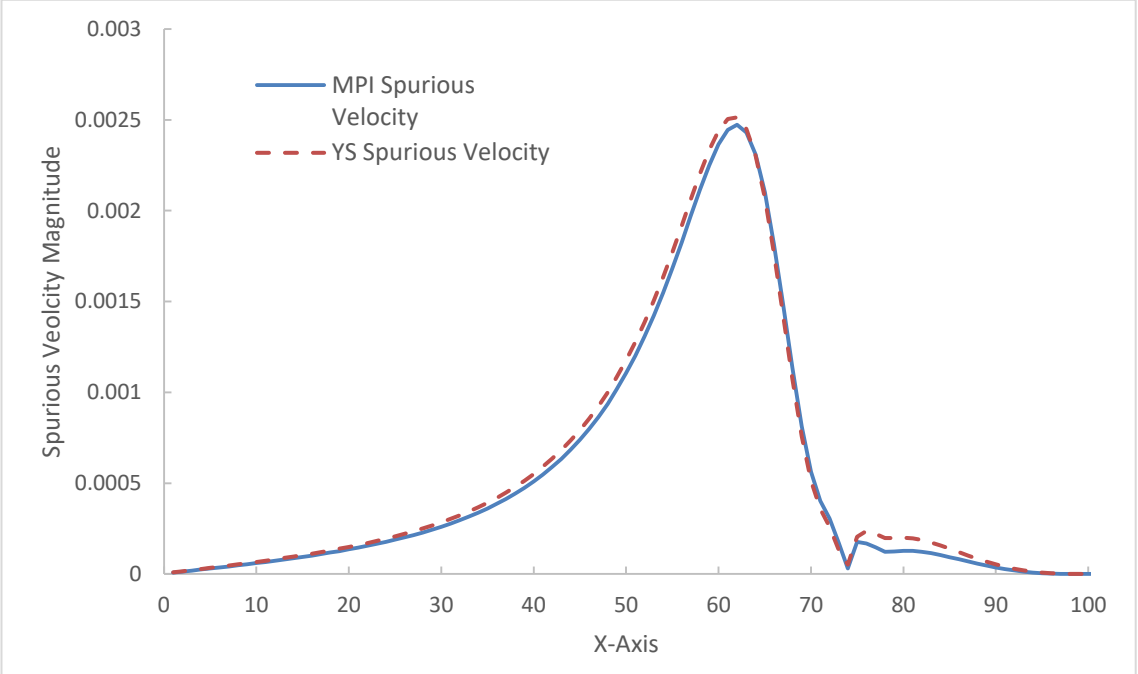

Figure 56- Spurious velocity magnitude generated by the MPI and YS methods at T_r = 0 .42 (τ_v = 1 and Λ = 1/12).

Chapter 5 - Hydrodynamic Multiple Relaxation Time Multipseudopotential Interaction Model Combined with Thermal LBM Models

5.1.Numerical Background

In this Chapter the MRT-MPI model described in Chapter 4 is combined with two thermal models in order to extend its capability to the study of thermal effects. Based on the recommendations of Hu et al. [127] and Li et al. [123], the models used in this thesis belong to the modified temperature-based DDF and hybrid thermal LBM categories. The equations that need to be solved in the 4th order Runge-Kutta scheme used in the hybrid thermal LBM model [122] are the following:

$$T^{t+\delta t} = T^t + \frac{\delta_t}{6}(h_1 + 2h_2 + 2h_3 + h_4) \tag{136}$$

$$h_1 = K(T^t) \tag{137}$$

$$h_2 = K\left(T^t + \frac{\delta_t}{2}h_1\right) \tag{138}$$

$$h_3 = K\left(T^t + \frac{\delta_t}{2}h_2\right) \tag{139}$$

$$h_4 = K(T^t + \delta_t h_3) \tag{140}$$

$$K(T^t) = -\boldsymbol{u}\cdot\nabla T + \frac{\lambda}{\rho c_V}\nabla\cdot(\lambda\nabla T) - \frac{T}{\rho c_V}\left(\frac{\partial p_{EOS}}{\partial T}\right)_\rho \nabla\cdot\boldsymbol{u} \tag{141}$$

The equations constituting the modified temperature-based DDF model by Li et al. [123] take the following forms:

$$g_\alpha(\boldsymbol{x} + \boldsymbol{e}_\alpha\delta_t, t+\delta_t) = g_\alpha^*(\boldsymbol{x}, t) \tag{142}$$

$$\boldsymbol{g}^* = \boldsymbol{M}^{-1}\boldsymbol{m}^* \tag{143}$$

$$\boldsymbol{m}^* = \boldsymbol{m} - \boldsymbol{\Lambda}(\boldsymbol{m} - \boldsymbol{m}^{eq}) + \delta_t\boldsymbol{S} \tag{144}$$

The thermal model is implemented using the MRT collision operator with [123]:

$$\boldsymbol{\Lambda} = diag(s_0, s_1, s_2, s_3, s_4, s_5, s_6, s_7, s_8) \tag{145}$$

$$\boldsymbol{m}^{eq} = T\big(1, -2, 2, u_x, -u_x, u_y, -u_y, 0, 0\big)^T \tag{146}$$

$$\boldsymbol{S} = (S_0, 0, 0, 0, 0, 0, 0, 0, 0)^T \tag{147}$$

$$S_0 = \phi + 0.5\delta_t \partial_t \phi \tag{148}$$

Where:

$$\phi = \frac{1}{\rho c_V} \nabla \cdot (\lambda \nabla T) - \nabla \cdot (k \nabla T) + T \left[1 - \frac{1}{\rho c_V} \left(\frac{\partial p_{EOS}}{\partial T} \right)_\rho \right] \nabla \cdot \boldsymbol{u} \tag{149}$$

$$k = \eta c_s^2 \delta_t \tag{150}$$

$$\eta = \left(\frac{1}{s_3} - \frac{1}{2} \right) = \left(\frac{1}{s_5} - \frac{1}{2} \right) \tag{151}$$

In addition, the third and fourth temperature distribution functions in the moment space are modified in order to remove the $\partial_{t0}(T\boldsymbol{u})$ error according to [123]:

$$m_{3,New}^* = m_3^* + \delta_t \left(1 - \frac{s_3}{2} \right) s_4 \left(m_4 - m_4^{eq} \right) \tag{152}$$

$$m_{5,New}^* = m_5^* + \delta_t \left(1 - \frac{s_5}{2} \right) s_6 \left(m_6 - m_6^{eq} \right) \tag{153}$$

The partial derivative responsible for phase-change was taken to be the following for the Peng-Robinson and Carnahan-Starling equations of state, respectively:

$$\left(\frac{\partial p_{PR}}{\partial T} \right)_\rho = \frac{\rho R}{1 - b\rho} \tag{154}$$

$$\left(\frac{\partial p_{CS}}{\partial T} \right)_\rho = \rho R \frac{1 + \frac{b\rho}{4} + \left(\frac{b\rho}{4} \right)^2 - \left(\frac{b\rho}{4} \right)^3}{\left(1 - \frac{b\rho}{4} \right)^3} \tag{155}$$

Gradient terms were calculated using the second-order isotropic difference scheme:

$$\partial_i T(\boldsymbol{x}) \approx \frac{1}{c_s^2 \delta_t} \sum_\alpha \omega_\alpha T(\boldsymbol{x} + \boldsymbol{e}_\alpha \delta_t) e_{\alpha i} \tag{156}$$

Laplacian terms can be calculated using the second-order isotropic difference scheme [26, 162] or using the isotropic discrete Laplacian operators [163]. The second-order isotropic difference scheme takes the following form [26]:

$$\nabla^2 T(x) \approx \frac{2}{c_s^2 \delta_t^2} \sum_\alpha \omega_\alpha [T(\boldsymbol{x} + \boldsymbol{e}_\alpha \delta_t) - T(\boldsymbol{x})] \tag{157}$$

The isotropic discrete Laplacian operator takes the following form [163]:

$$\mathrm{L}(\boldsymbol{x})_{D2Q9} \equiv \nabla^2 T(x) = \frac{1}{6}\left[4\sum_{i=1}^{4} T_i^{(1)} + \sum_{i=1}^{4} T_i^{(2)} - 20T^{(0)}\right] \tag{158}$$

The second-order isotropic difference scheme was used exclusively to obtain the data discussed in this thesis.

5.2.Thermal Multipseduopotential Interaction Model

The simplest way of including thermal effects in the multipseudopotential model is to combine the hydrodynamic model with one of the thermal models and to make the temperature terms in MPI location-dependent with temperature updated by the thermal model. In isothermal models, the temperature term is constant throughout the computational domain and it is prescribed for the entire simulation duration during initialisation. For the Peng-Robinson equation of state, thermal MPI becomes the following:

$$G_1(\boldsymbol{x}) = -\frac{2}{3} \tag{159}$$

$$G_2(\boldsymbol{x}) = \frac{2}{c^2} T(\boldsymbol{x}) \tag{160}$$

$$G_3(\boldsymbol{x}) = \frac{2}{c^2} \frac{\omega\big(T(\boldsymbol{x})\big)a}{2b\sqrt{2}} \tag{161}$$

$$G_4(\boldsymbol{x}) = -\frac{2}{c^2} \frac{\omega\big(T(\boldsymbol{x})\big)a}{2b\sqrt{2}} \tag{162}$$

$$\omega\big(T(\boldsymbol{x})\big) = \left(1 + (0.37464 + 1.54226\alpha - 0.26992\alpha^2)\left(1 - \sqrt{T_R(\boldsymbol{x})}\right)\right)^2 \tag{163}$$

With the intermolecular multipseudopotential force calculated according to:

$$\boldsymbol{F} = \sum_{j=1}^{n} -G_j(\boldsymbol{x})\psi_j(\boldsymbol{x}) c_s^2 \sum_{\alpha=1}^{N} w(|\boldsymbol{e}_\alpha|^2)\psi_j(\boldsymbol{x} + \boldsymbol{e}_\alpha)\boldsymbol{e}_\alpha \tag{164}$$

It is clear that the ψ_j term does not contain temperature-related parameters:

$$\psi_j = \left(\frac{\rho}{\lambda_j \varepsilon_j + C_j \rho}\right)^{1/\varepsilon_j} \tag{165}$$

Peng-Robinson ψ_j Parameters			
j-th term	$\boldsymbol{\varepsilon_j}$	$\boldsymbol{\lambda_j}$	$\boldsymbol{C_j}$
1	2	$\frac{1}{2}$	0
2	2	$\frac{1}{2}$	-b
3	2	$\frac{1}{2}$	$b\left(1+\sqrt{2}\right)$
4	2	$\frac{1}{2}$	$b\left(1-\sqrt{2}\right)$

Table 3- MPI equation of state parameters that do not contain temperature.

Hence, thermal MPI implemented in this way incorporates thermal effects only at the local site $\boldsymbol{x}$ in the calculation of the intermolecular force $\boldsymbol{F}$. This formulation of the intermolecular force is suitable for isothermal cases, where the temperature is constant throughout the computational domain. In order to visualise the fact that thermal effects are only incorporated at the local site and not in the neighbouring sites, in the following equation the only term that contains temperature is $G_j(\boldsymbol{x})$:

$$\boldsymbol{F} = \sum_{j=1}^{n} -G_j(\boldsymbol{x})\psi_j(\boldsymbol{x})c_s^2 \sum_{\alpha=1}^{N} w(|\boldsymbol{e}_\alpha|^2)\psi_j(\boldsymbol{x}+\boldsymbol{e}_\alpha)\boldsymbol{e}_\alpha \qquad (166)$$

In reality, intermolecular forces reflect the effect of temperatures of the interacting particles. This effect is naturally present in thermal models using the square root form of the pseudopotential including the thermal YS models. In these models, temperature effects are equally-weighted at $\boldsymbol{x}$ and $\boldsymbol{x}+\boldsymbol{e}_\alpha$. Temperature containing terms in pseudopotential models employing the square root form of ψ are $\psi(\boldsymbol{x})$ and $\psi(\boldsymbol{x}+\boldsymbol{e}_\alpha)$ in following equation:

$$\boldsymbol{F} = -G(\boldsymbol{x})\psi(\boldsymbol{x})c_s^2 \sum_{\alpha=1}^{N} w(|\boldsymbol{e}_\alpha|^2)\psi(\boldsymbol{x}+\boldsymbol{e}_\alpha)\boldsymbol{e}_\alpha \qquad (167)$$

Unmodified thermal MPI without temperature being included at $\boldsymbol{x}+\boldsymbol{e}_\alpha$ sites can simulate droplet evaporation, but it cannot simulate bubble nucleation during boiling. Instead of vapour being generated, a high pressure zone is created adjacent to the heating element without phase change occurring as illustrated in Figure 57, see section 5.2.2. for the flow configuration. Eventually, the accumulation of energy in the liquid without phase change leads to generation of fluctuation at the liquid-vapour interface.

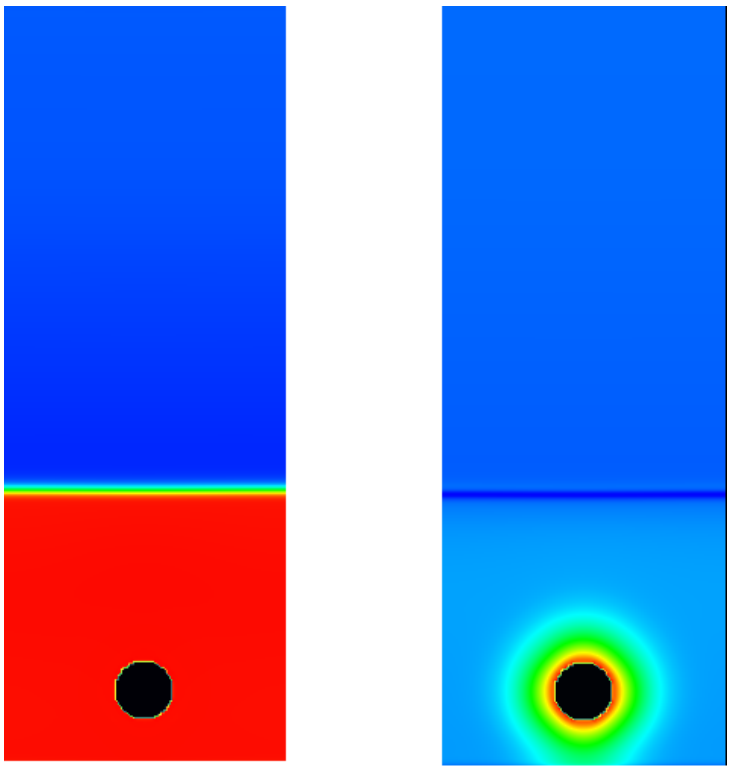

Figure 57- Density field on the left hand side and pressure field on the right hand side to illustrate the results of unmodified thermal MPI in bubble nucleation simulations. The black tube in the liquid phase is used as the heating element.

In order to accurately incorporate thermal effects, the thermal MPI model needs to be modified. The intermolecular force can be rewritten in the following manner in order to allow inclusion of thermal effects at $\boldsymbol{x}$ and $\boldsymbol{x}+\boldsymbol{e}_\alpha$:

$$\boldsymbol{F} = \sum_{j=1}^{n} -\sqrt{G_{thermal,j}(\boldsymbol{x})}G_{sign,thermal,j}\psi_j(\boldsymbol{x})c_s^2\sum_{\alpha=1}^{N} w(|\boldsymbol{e}_\alpha|^2)\sqrt{G_{thermal,j}(\boldsymbol{x}+\boldsymbol{e}_\alpha)}\psi_j(\boldsymbol{x}+\boldsymbol{e}_\alpha)\boldsymbol{e}_\alpha \quad (168)$$

A second G term is introduced to allow incorporation of thermal effects at $\boldsymbol{x}+\boldsymbol{e}_\alpha$ sites. In order to take account of the fact that a second G term has been introduced, it is necessary to take the square root of the G terms. This treatment of the G terms means that both terms are equally-weighted in the calculation of the intermolecular forces. A sign function is also necessary in order to take the negative signs outside of the square root terms to prevent generation of complex numbers. For the Peng-Robinson equation of state, the following expressions are used in the corrected thermal MPI:

$$G_{thermal,1}(\boldsymbol{x}) = \frac{2}{3} \quad (169)$$

$$G_{thermal,2}(\boldsymbol{x}) = \frac{2}{c^2} T(\boldsymbol{x}) \tag{170}$$

$$G_{thermal,3}(\boldsymbol{x}) = \frac{2}{c^2} \frac{\omega\big(T(\boldsymbol{x})\big)a}{2b\sqrt{2}} \tag{171}$$

$$G_{thermal,4}(\boldsymbol{x}) = \frac{2}{c^2} \frac{\omega\big(T(\boldsymbol{x})\big)a}{2b\sqrt{2}} \tag{172}$$

$$G_{sign,thermal,1} = -1 \tag{173}$$

$$G_{sign,thermal,2} = 1 \tag{174}$$

$$G_{sign,thermal,3} = 1 \tag{175}$$

$$G_{sign,thermal,4} = -1 \tag{176}$$

5.2.1. Simulations of Stationary Droplet Evaporation

Thermal MPI model implemented in this way can correctly simulate droplet evaporation and bubble nucleation during boiling. In order to validate conformity to the D^2 law, simulations were carried out in a 200 x 200 gravity-free domain with periodic boundary conditions at all four sides. The vapour surrounding the liquid droplet was initialised at a superheated temperature that was higher than the saturation temperature of the liquid by 0.14 times the critical temperature ($0.14T_c$). The superheat was enforced at the periodic boundaries during the simulation. Heat capacity at constant volume was equal to 5. The value of thermal conductivity (λ) was constant in the computational domain at 2/3, leading to the following simplification in the temperature equations:

$$\nabla \cdot (\lambda \nabla T) = \lambda \nabla^2 T \tag{177}$$

Bulk viscosity was set to be equal to kinematic viscosity. The magic parameter was set to 1/12 in the hydrodynamic MRT collision operator. All of the relaxation rates in the thermal diagonal matrix ($\boldsymbol{\Lambda}$) were set to 1.0. Resulting in the *k* parameter in the temperature equation being equal to 1/6. In the modified temperature double distribution function (DDF) model of Li et al., *k* is simply a constant without physical meaning [123]. The simulations were carried out at a reduced temperature of 0.86 with the acentric factor equal to 0.344 and Peng-Robinson $a = 3/49$, $b = 2/21$ and $R = 1$.

From this point onwards, the corrected MPI thermal models will be used and the term "corrected" will be dropped. Figure 58 shows the shrinking of the droplet size in time.

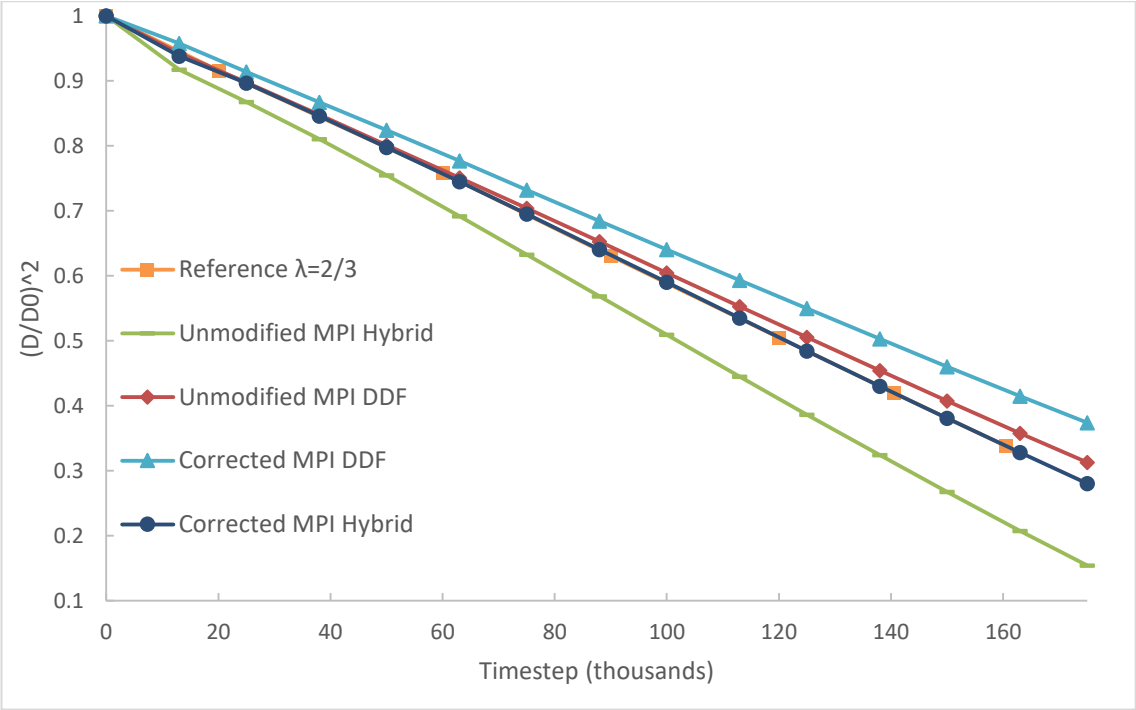

Figure 58- Verification of D^2 law during droplet evaporation for unmodified and corrected thermal MPI. Reduced temperature was set to 0.86 and the superheat with respect to the saturation temperature was set to 0.14 times the critical temperature. Thermal conductivity was set to 2/3 and heat capacity at constant volume was set to 5. Acentric factor was set to 0.344, PR a to 3/49 and PR b to 2/21. Comparison to data in Reference [8].

Figure 59 compares droplet evaporation rates obtained using the YS and MPI thermal models. The rate of evaporation obtained using the MPI hybrid model is the same as the rate of evaporation for a 4^{th} order Runge-Kutta hybrid model detailed in Reference [8]. The simulation parameters were chosen to be the same as those in the Reference [8]. MPI thermal models provide straight lines in simulations of droplet evaporation that fulfil the D^2 law. Therefore, MPI is well suited to thermal simulations. In comparison, YS thermal models provide slightly less straight lines with a steeper drop in droplet diameter in the first 13 thousand timesteps. The rates of evaporation obtained using the MPI models are lower than those obtained using the YS models.

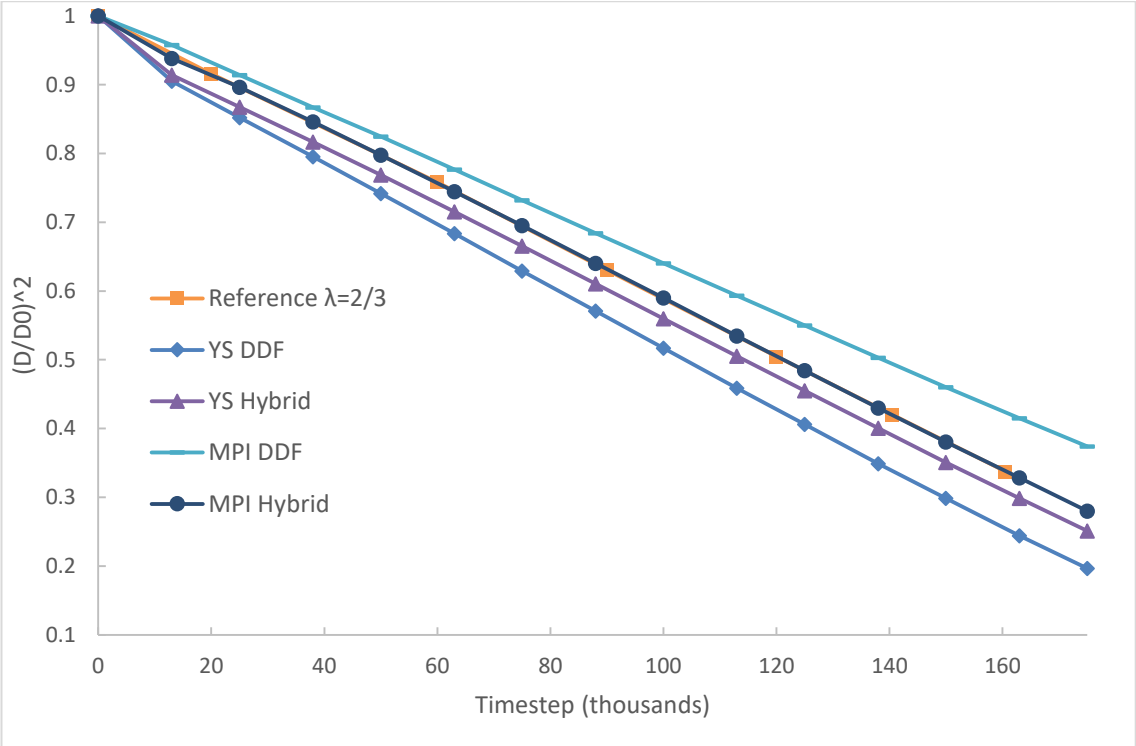

Figure 59- Comparison of droplet evaporation rates of YS and MPI thermal models. Reference [8] data plotted for validation purposes. Tr = 0.86, initial droplet diameter = 60, superheat = 0.14Tc, cv = 5, thermal conductivity = 2/3, acentric factor =0.344, PR a = 3/49 and PR b = 2/21.

5.2.2. Simulations of Bubble Nucleation

The black circle submerged in the liquid phase is meant to represent a heating element, which could be a tube in a heat exchanger supplying heat to the liquid phase. Thus, simulation of complex heat exchanger geometries is possible using the models. The domain size was 150 nodes in the x direction by 400 nodes in the y direction. Top and bottom boundaries were set to bounce-back and the left and right hand side boundaries were periodic. Liquid was located in the bottom of the computational domain up to a thickness of 150 lattice units with the space above it filled with vapour. The diameter of the heating element was set to 30 lattice units and its centre was located 40 lattice units above the bottom boundary in the middle of the x-axis. Heat was supplied to the liquid phase along the entire length of the circumference of the heating element. The temperature of the heating element was set to 1.25 times the critical temperature ($1.25T_c$). Heat capacity at constant volume (c_v) was set to 5.0 and kinematic viscosity was set to 0.1 (τ_v=0.8). The value of gravity was set to -2.5×10^{-5} in the y direction and the gravity force was implemented using the difference between the local density and the average density within the fluid domain:

$$F_{gravity,y} = -2.5 \times 10^{-5}\left(\rho - \rho_{average}\right) \qquad (178)$$

This method of introducing gravity prevents injection of net momentum into the simulation domain [87]. In the hydrodynamic relaxation matrix, the value of bulk viscosity was set to the same value as the kinematic viscosity. The hydrodynamic MRT magic parameter was set to 1/12. All of the relaxation rates in the thermal diagonal matrix ($\boldsymbol{\Lambda}$) were set to 1.0. Hence, k in the temperature equation was equal to 1/6. Thermal diffusivity (χ) was set to 0.06. This value of thermal diffusivity was used in the calculation of thermal conductivity. Thermal conductivity (λ) was set to be variable and it was obtained from the following equation:

$$\lambda = \rho c_V \chi \tag{179}$$

Opting for a location-dependent value of thermal conductivity necessitates the following treatment of $\nabla \cdot (\lambda \nabla T)$ in the temperature equation:

$$\nabla \cdot (\lambda \nabla T) = \lambda \nabla^2 T + \nabla \lambda \cdot \nabla T \tag{180}$$

A cubic equation of state was employed in the simulations. The chosen equation of state was the Peng-Robinson equation of state, because it offers good stability and is widely used in the literature allowing comparison to published results. The models are compared at a reduced temperature of 0.86 with parameters in the Peng-Robinson equation of state set to a = 3/49, b = 2/21, R = 1 and the acentric parameter equal to 0.344 (the value for water). Both models generate a bubble that departs the heating element at the 9,700 timestep. As mentioned above, MPI results in a lower rate of evaporation than the YS model. Hence, the bubble generated by the MPI model is slightly smaller than the bubble generated by the YS model. Figure 60 shows the snapshots of the bubble nucleation and departure from a heating element with YS DDF and MPI DDF models. Both models can predict bubble and departure from a heating element, but bubble sizes are different.

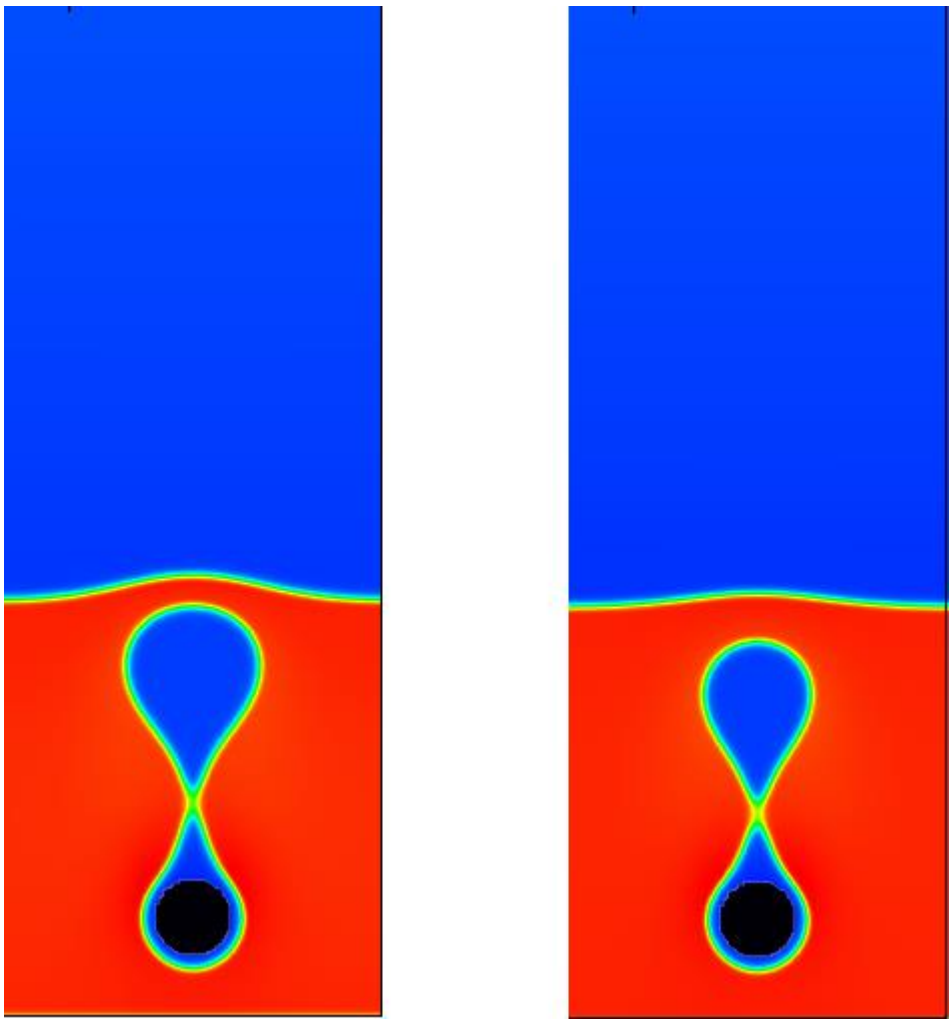

Figure 60- Comparison of bubble nucleation and departure from a heating element. The image on the left hand side was obtained using the YS DDF model and the image on the right had side was obtained using the MPI DDF model. The time step at which the bubble broke free from the heating element was 9,700 for both models.

5.3.Introduction of the G Thermal Weightings into Multipseudopotential Interaction Model

The intermolecular force expression in the thermal MPI model can be modified to allow different weightings of $G_{thermal,j}(\boldsymbol{x})$ and $G_{thermal,j}(\boldsymbol{x}+\boldsymbol{e}_\alpha)$. The weightings can be modified by setting powers of the *G* terms to the following:

$$\boldsymbol{F}=\sum_{j=1}^{n}-G_{thermal,j}(\boldsymbol{x})^{\frac{\chi}{2}}G_{sign,thermal,j}\psi_j(\boldsymbol{x})c_s^2\sum_{\alpha=1}^{N}w(|\boldsymbol{e}_\alpha|^2)G_{thermal,j}(\boldsymbol{x}+\boldsymbol{e}_\alpha)^{\frac{2-\chi}{2}}\psi_j(\boldsymbol{x}+\boldsymbol{e}_\alpha)\boldsymbol{e}_\alpha \quad (181)$$

Lower-case Greek letter Chi (χ) was introduced into the above expression to allow modification of the *G* weightings. Table 4 lists the effects of changing the *G* weightings on bubble nucleation. Based on the findings, equal weighting of the *G* terms in thermal

MPI is the appropriate choice. This weighting coincides with the treatment of thermal effects in thermal YS models.

χ	Power of $G_{thermal,j}(x)$	Power of $G_{thermal,j}(x + e_\alpha)$	Relative weighting and observations
2	1	$\frac{0}{2}$	(100% and 0%) original thermal MPI – no nucleation and generation of fluctuation at liquid-vapour interface
1.5	$\frac{3}{4}$	$\frac{1}{4}$	(75% and 25%) no nucleation – generation of two-phase mixture
1.1	$\frac{11}{20}$	$\frac{9}{20}$	(55% and 45%) bubble nucleation no departure
1	$\frac{1}{2}$	$\frac{1}{2}$	Equal weighting – correct bubble nucleation
0.9	$\frac{9}{20}$	$\frac{11}{20}$	(45% and 55%) Bubble nucleation
0.75	$\frac{3}{8}$	$\frac{5}{8}$	(37.5% and 62.5%) Unstable after 100 timesteps
0.5	$\frac{1}{4}$	$\frac{3}{4}$	(25% and 75%) unstable
0	$\frac{0}{2}$	1	(0% and 100%) Immediately unstable

Table 4- Investigation of the effects of changing the G weightings on bubble nucleation.

5.4.Surface Tension Adjustment in Thermal Multipseudopotential Interaction Model

Thermal MPI can be combined with either the Li-Luo method [149] or Huang-Wu method [148] of surface tension modification. In this Section, the effects of decreasing and increasing surface tension are examined in bubble nucleation simulations using the thermal MPI DDF model. The Li-Luo [149] method has to be adapted for use with the MPI model into the following expression:

$$\boldsymbol{Q} = \sum_{j=1}^{n} \kappa \frac{G_j}{2} \psi_j(\boldsymbol{x}) \sum_{\alpha=1}^{8} w(|\boldsymbol{e}_\alpha|^2) \left[\psi_j(\boldsymbol{x} + \boldsymbol{e}_\alpha) - \psi_j(\boldsymbol{x})\right] \boldsymbol{e}_\alpha \boldsymbol{e}_\alpha \tag{182}$$

And the Huang-Wu [148] method should take the following form in order to allow surface tension modification in MPI models:

$$\boldsymbol{Q_m} = \begin{bmatrix} 0 \\ 3\sum_{j=1}^{n}\left(k_1 + 2\left(\frac{\varepsilon_j}{-8} - k_1\right)\right)\frac{\left|\boldsymbol{F_j}\right|^2}{G_j{\psi_j}^2} \\ -3\sum_{j=1}^{n}\left(k_1 + 2\left(\frac{\varepsilon_j}{-8} - k_1\right)\right)\frac{\left|\boldsymbol{F_j}\right|^2}{G_j{\psi_j}^2} \\ 0 \\ 0 \\ 0 \\ 0 \\ k_1\sum_{j=1}^{n}\frac{F_{x,j}^2 - F_{y,j}^2}{G_j{\psi_j}^2} \\ k_1\sum_{j=1}^{n}\frac{F_{x,j}F_{y,j}}{G_j{\psi_j}^2} \end{bmatrix} \tag{183}$$

As mentioned in Section **Error! Reference source not found.**, the Li-Luo method is etter for reducing surface tension and the Huang-Wu method is more suitable for increasing surface tension. Consequently, the Li-Luo method was employed to reduce surface tension and the Huang-Wu method was used to increase surface tension. Simulations were carried out using the same parameters as those described in Subsection 5.2.2. Figure 61 illustrates bubble departure from the heating element as surface tension is reduced from the unmodified value of surface tension, i.e. from surface tension coefficient = 1.0.

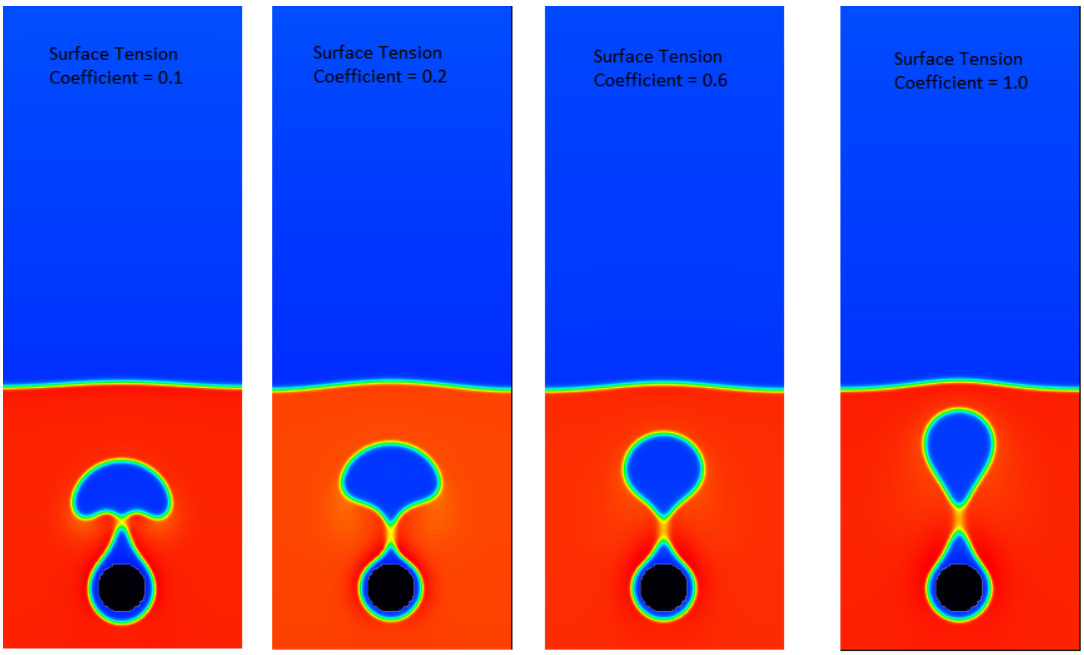

Figure 61- Effect of reducing surface tension on the departure of a nucleated bubble from the heating element.

Surface tension was reduced using the κ (kappa) parameter in the MPI-adapted Li-Luo method [149]. For example, in order to set the surface tension coefficient to 0.1, κ was set to 0.9. Surface tension coefficient equal to 0.1 results in surface tension that is 10 times lower than the unmodified surface tension. Clearly, as surface tension is reduced the shape of the bubble changes from teardrop to a dome-like shape. According to Figure 62, higher values of surface tension require generation of larger bubbles in order for departure from the heating element to take place. This is caused by the fact that in order for a bubble to depart the heating element, where the contact line is static, the buoyancy force needs to overcome the surface tension generated forces [164]. Therefore, higher values of surface tension require greater buoyancy forces for successful bubble departure. Bubbles of greater volumes are subject to greater buoyancy forces.

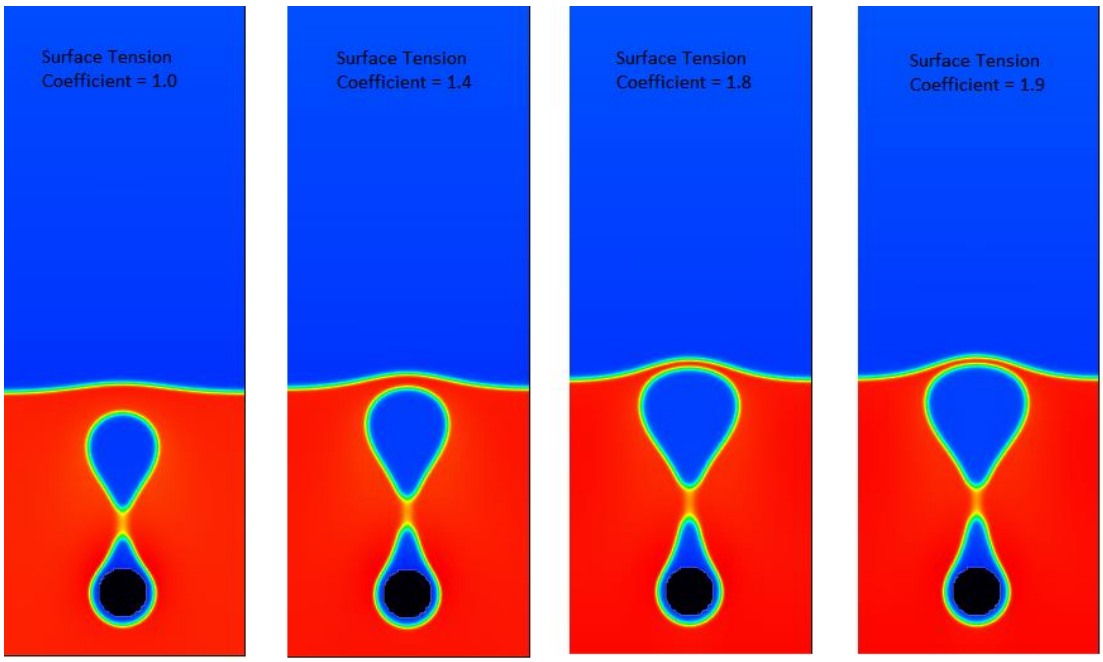

Figure 62- Effect of increasing surface tension on the departure of a nucleated bubble.

Surface tension was increased using the MPI-adapted Huang-Wu method. k_1 was adjusted to increase surface tension according to surface tension coefficient = $1 - 6k_1$, whilst ε was kept constant by adjusting k_2 as required. An observation can be made that the higher the value of surface tension, the longer it takes for the bubble to depart the heating element. The amount of timesteps taken to departure versus the surface tension coefficient is plotted in Figure 63. The trend exhibits an observable departure from linearity. Detailed parameters at bubble departure are listed in Table 5.

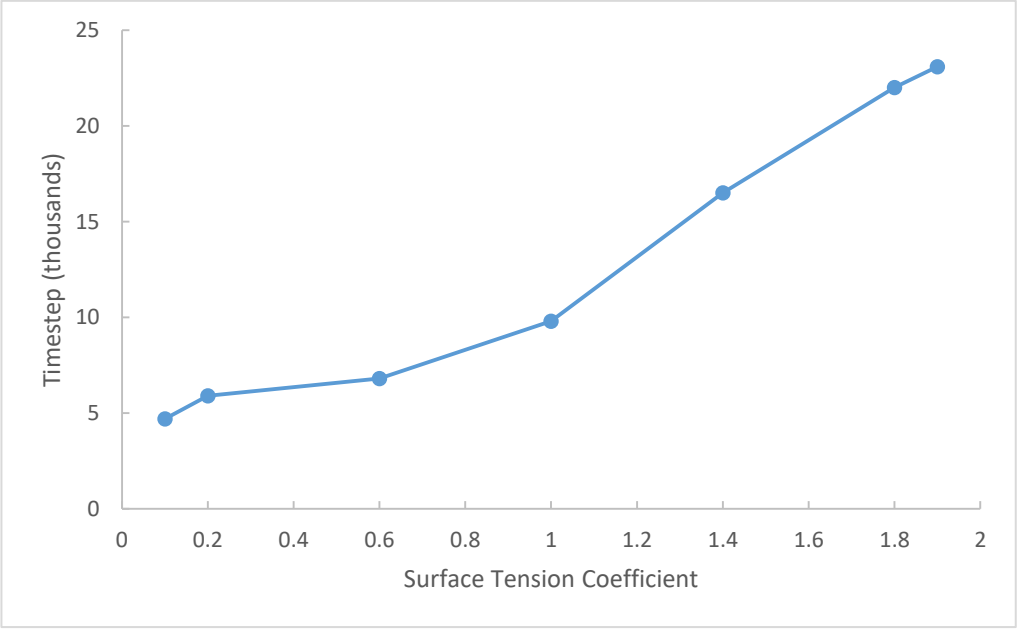

Figure 63- Amount of timesteps taken for the nucleated bubble to break free from the heating element at different values of surface tension.

Surface Tension Coefficient	Surface Tension	Departure Time	Departure Diameter	Velocity	Density	We
0.1	0.00701	4700	60.54	0.0207	0.4817	1.7833
0.2	0.01402	5900	60.93	0.0079	0.5017	0.136
0.6	0.04206	6800	48.73	0.017	0.5369	0.179
1	0.0701	9800	42.81	0.0144	0.5708	0.0724
1.4	0.09814	16500	49.61	0.0107	0.5162	0.0299
1.8	0.12618	22000	59.6	0.0089	0.5142	0.0192
1.9	0.13319	23100	61.65	0.0087	0.5135	0.0178

Table 5- Data at bubble departure used to calculate the Weber number.

The values of bubble diameter, velocity and density were calculated across the widest point of the departing bubble. They were used to calculate the Weber number (We) for the departing bubbles.

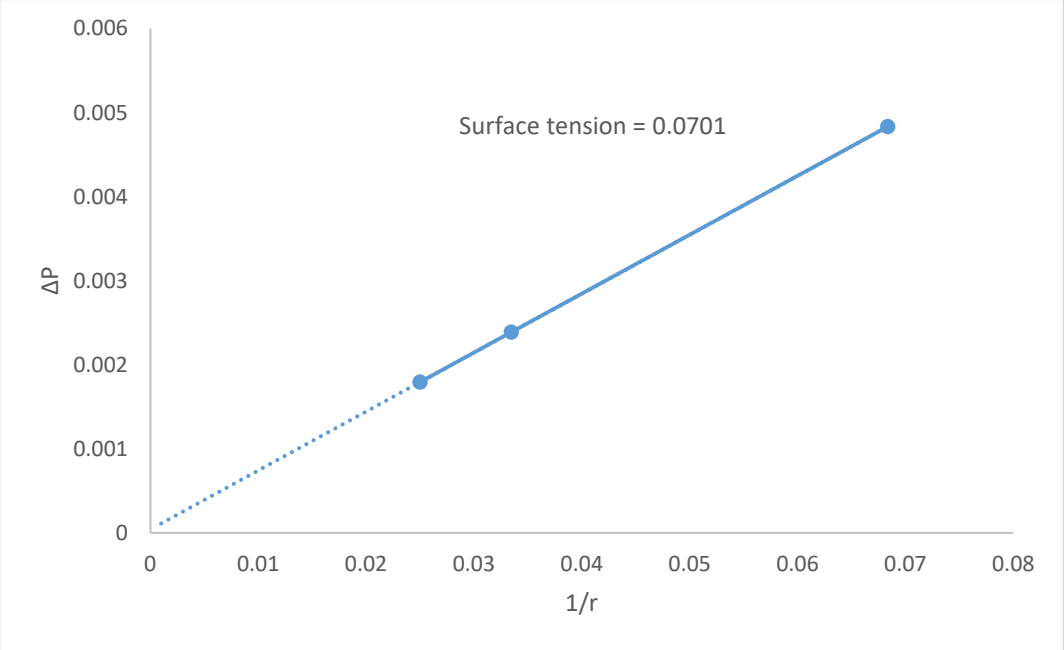

Figure 64- Surface tension tests in order to calculate Weber number.

The trend of Weber number versus the surface tension coefficient is plotted in Figure 65. Higher values of surface tension result in lower values of the Weber number of the departing bubble. Around We ≈ 2, bubble deformation from a teardrop shape is obvious and resembles a dome rather than a teardrop. At this stage, bubble shape becomes significantly more deformable during its buoyancy-driven ascent to the surface than at lower Weber numbers.

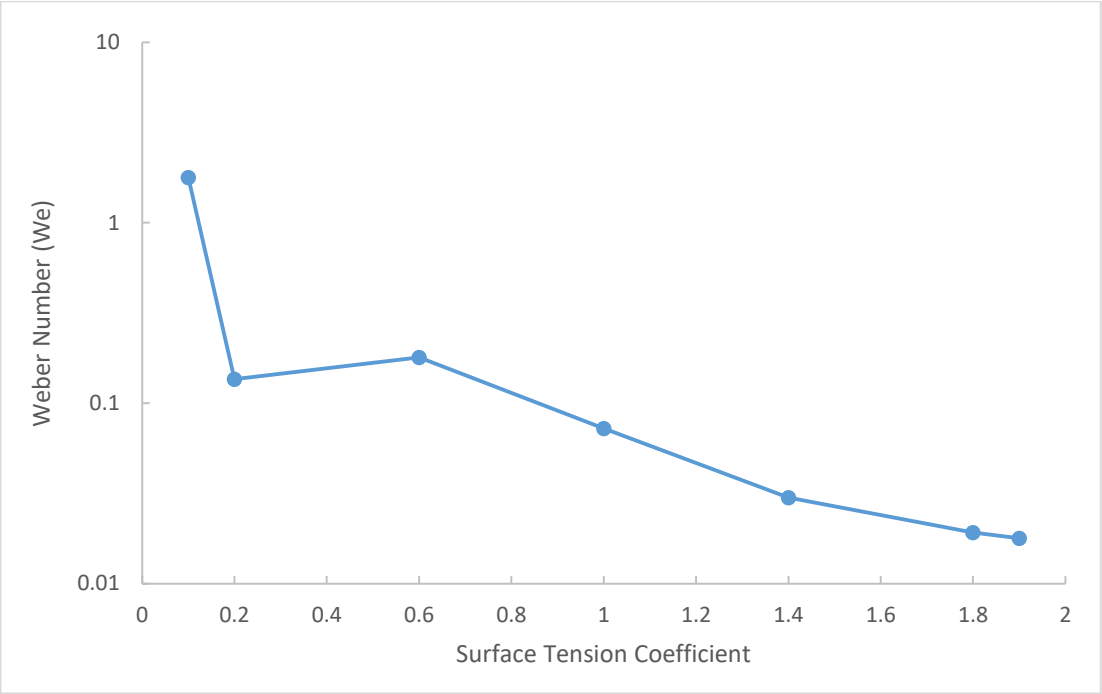

Figure 65- Semi-log Trend of the Weber number of the departing bubbles at different values of the surface tension coefficient.

Figure 66 illustrates the effect of reducing surface tension on the bubbles as they reach the liquid surface. Lower values of surface tension provide insufficient force to keep the spherical shape of bubbles resulting in their evident deformation. In addition, lower surface tension bubbles disturb the liquid surface to a lesser degree as they break through the surface. The lower surface tension bubbles are smaller as they departed the heating element sooner than their higher surface tension counterparts. Also, less energy is released as the bubbles break-up. In Figure 67 it can be observed that as surface tension is increased, larger bubbles reach the liquid surface and they cause greater disturbance of the liquid surface. At higher values of surface tension, the process of break-up of bubbles at liquid surface is sufficiently violent to generate secondary droplets. Figure 68 illustrates generation of a secondary droplet during the break-up process of a bubble with the surface tension coefficient equal to 1.9. On the other hand, the process of a bubble with the surface tension coefficient equal to 0.1 reaching the liquid surface is comparatively uneventful.

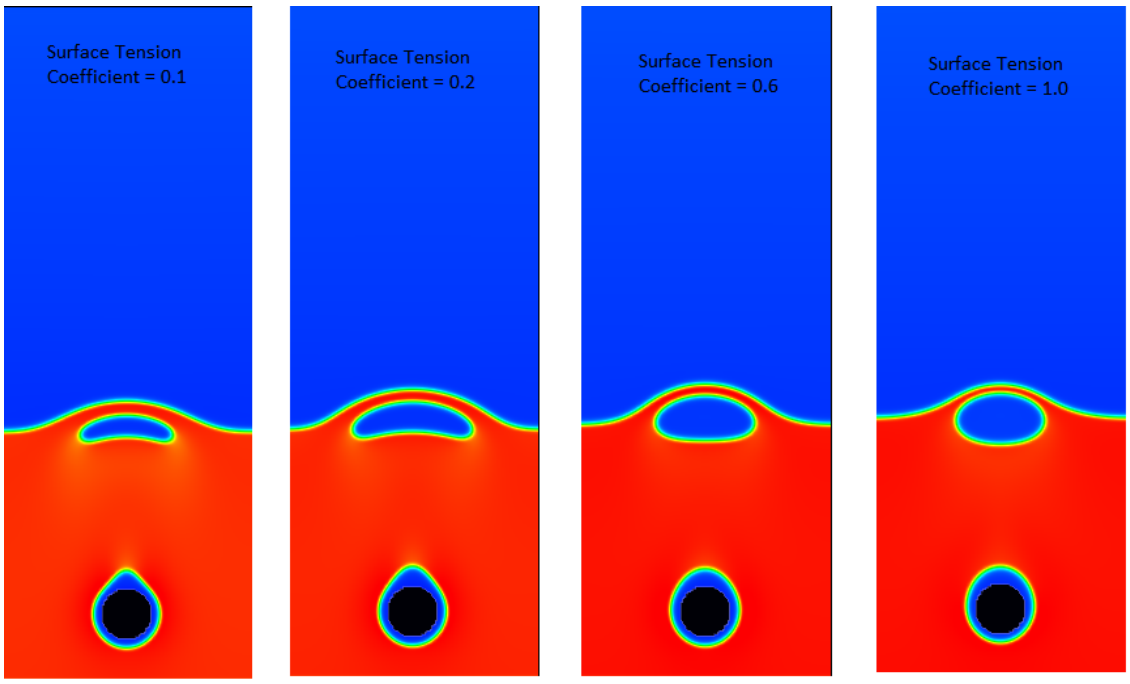

Figure 66- Effect of reducing surface tension on the bubble approach to the liquid surface.

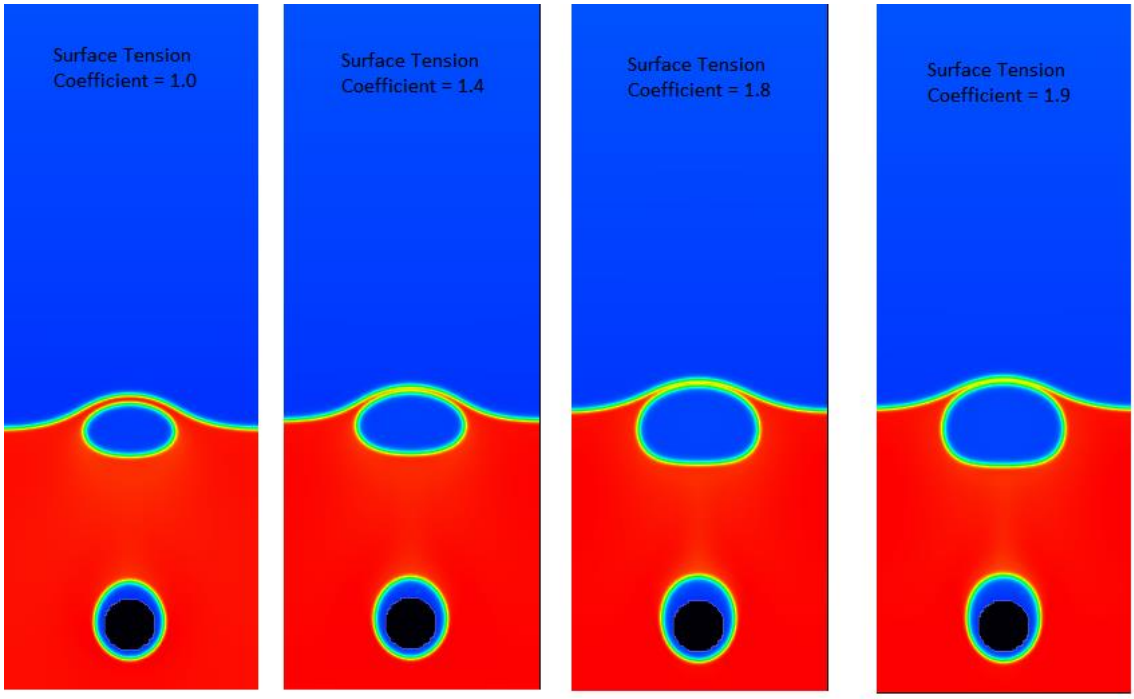

Figure 67- Bubble approach to the liquid surface at increased values of surface tension.

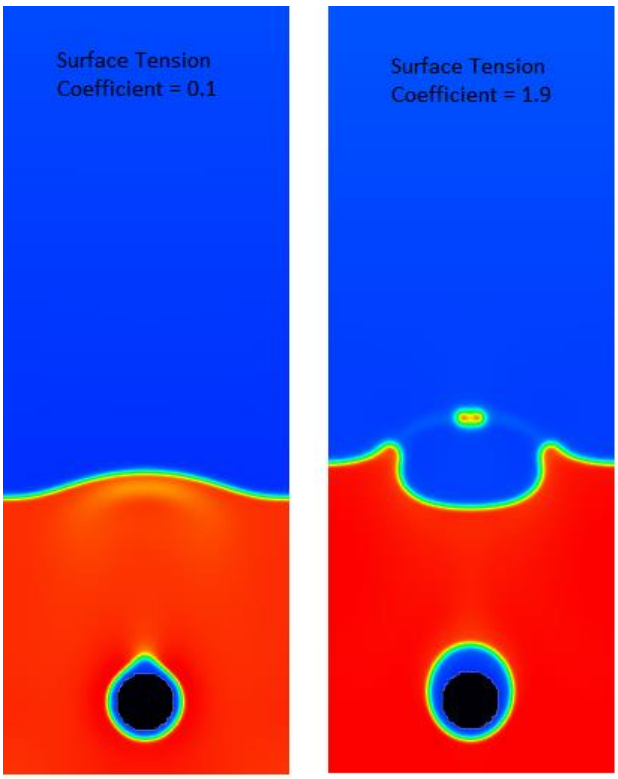

Figure 68- Generation of secondary droplets as a high surface tension bubble breaks through the liquid surface compared to relatively quiescent liquid surface during emergence of a low surface tension bubble.

5.5.Achievement of Lower Reduced Temperatures

In this Section, the methods of achieving lower reduced temperatures are investigated using the pseudopotential thermal models. First, a new method of carrying out thermal simulations using the piecewise-linear EOS is described. Secondly, the stable envelopes of reduced temperatures are presented.

5.5.1. Thermal Piecewise-Linear EOS Model

A new method of carrying out thermal simulations using the piecewise-linear EOS is presented here. It is clear that there are no temperature terms in the original piecewise-linear EOS [131]:

$$p_{EOS} = \begin{cases} \rho\theta_V & if\ \rho \leq \rho_1 \\ \rho_1\theta_V + (\rho - \rho_1)\theta_M & if\ \rho_1 < \rho \leq \rho_2 \\ \rho_1\theta_V + (\rho_2 - \rho_1)\theta_M + (\rho - \rho_2)\theta_L & if\ \rho > \rho_2 \end{cases} \quad (184)$$

Temperature was introduced into the model by making the spinodal points temperature-dependent:

$$p_{EOS} = \begin{cases} \rho\theta_V & if\ \rho \leq \rho_1(T) \\ \rho_1(T)\theta_V + \big(\rho - \rho_1(T)\big)\theta_M & if\ \rho_1(T) < \rho \leq \rho_2(T) \\ \rho_1(T)\theta_V + \big(\rho_2(T) - \rho_1(T)\big)\theta_M + \big(\rho - \rho_2(T)\big)\theta_L & if\ \rho > \rho_2(T) \end{cases} \quad (185)$$

The spinodal points were calculated at a number of reduced temperatures for the Peng-Robinson EOS with the piecewise-linear EOS prescribing pressure slopes in each phase. The parameters were chosen in order to allow comparison with the YS and MPI thermal models which use the Peng-Robinson EOS directly. The spinodal points obtained are listed in Table 6.

T_r	T	ρ_1	ρ_2
1	0.109378	2.657309	2.657309
0.95	0.103909	1.03	4.9009
0.9	0.09844	0.59	5.861942
0.85	0.092972	0.35	6.572979
0.8	0.087503	0.204	7.136564
0.75	0.082034	0.114	7.60679
0.7	0.076565	0.059	8.002541
0.65	0.071096	0.0275	8.343035
0.6	0.065627	0.0111	8.640901

Table 6- Spinodal points calculated at a number of reduced temperatures for the Peng-Robinson EOS with a = 3/49, b = 2/21, R = 1 and acentric factor equal to 0.344. In the piecewise-linear EOS Θ_v was set to 0.21333, ϑ_L to 0.33333 and ϑ_M to -0.00333.

The spinodal points were plotted and polynomial equations were used to estimate the trends in a number of sections of the reduced temperature range as illustrated in Figure 69. The polynomial equations were then used in the thermal model to calculate the spinodal points at temperatures within the temperature range under investigation:

$$\rho_1(T_r = 1.0 - 0.9) = 19849T^2 - 3935.9T + 195.7 \quad (186)$$

$$\rho_1(T_r = 0.9 - 0.8) = 1571.4T^2 - 256.91T + 10.652 \quad (187)$$

$$\rho_1(T_r = 0.8 - 0.6) = 10138T^3 - 1921.1T^2 + 123.48T - 2.6842 \quad (188)$$

$$\rho_2(T_r = 1.0 - 0.9) = -21441T^2 + 4162.8T - 196.16 \quad (189)$$

$$\rho_2(T_r = 0.9 - 0.8) = -2465T^2 + 341.82T - 3.8995 \quad (190)$$

$$\rho_2(T_r = 0.8 - 0.6) = -16225T^3 + 2771.6T^2 - 205.9T + 14.802 \quad (191)$$

Table 7 compares the values of spinodal points obtained using the polynomial equations with the values calculated using the mechanical and chemical equilibrium equations.

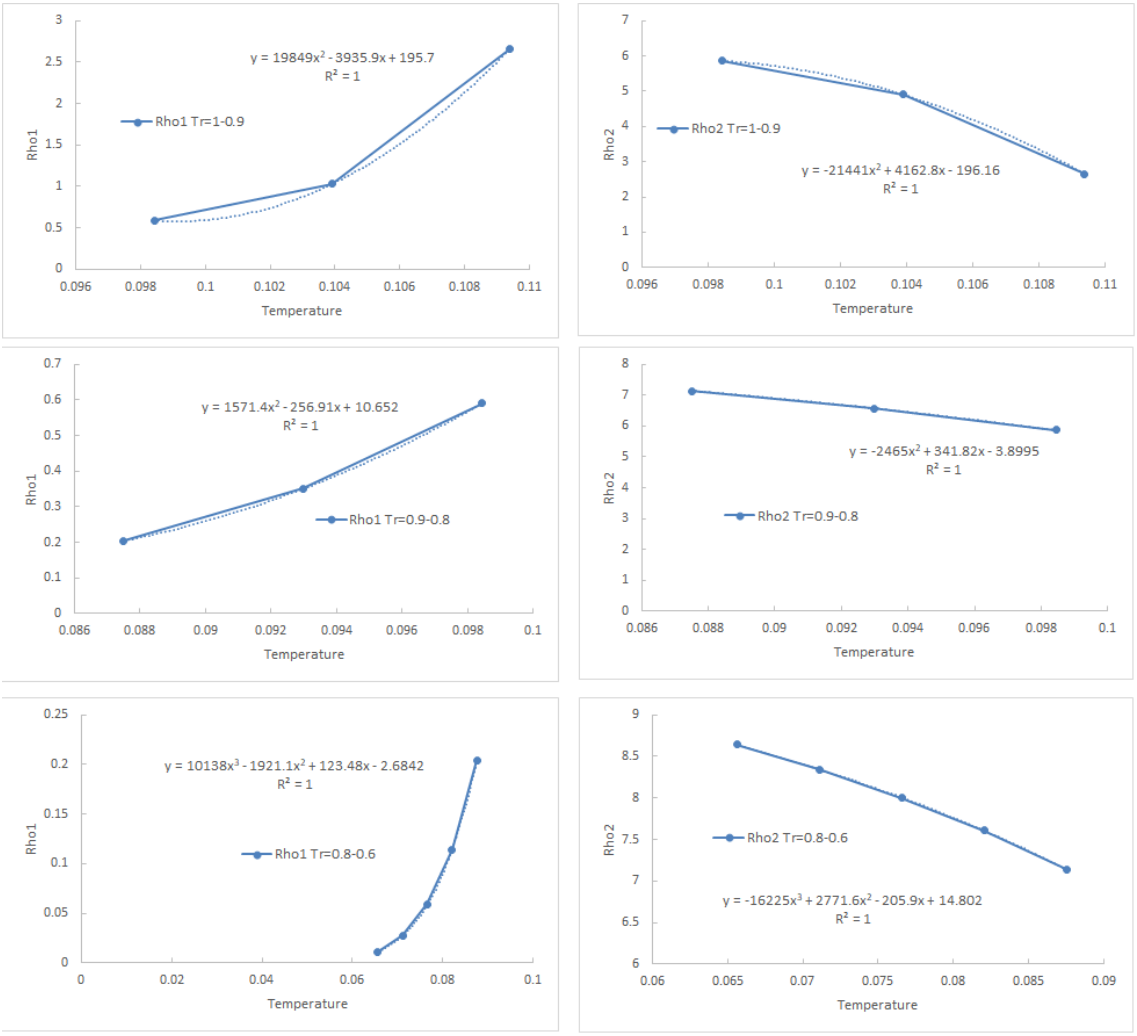

Figure 69- Spinodal fitting at different temperatures using polynomial equations.

T_r	ρ_1	ρ_2	ρ_1 polynomial	ρ_1 polynomial/ ρ_1	ρ_2 polynomial	ρ_2 polynomial/ ρ_2
1	2.6573	2.6573	2.6637	1.0024	2.6482	0.9966
0.95	1.03	4.9009	1.0359	1.0057	4.8921	0.9982
0.9	0.59	5.8619	0.5894	0.9989	5.8623	1.0001
0.85	0.35	6.573	0.3494	0.9983	6.5733	1.0000
0.8	0.204	7.1366	0.2036	0.9980	7.1369	1.0000
0.75	0.114	7.6068	0.1139	0.9990	7.6058	0.9999
0.7	0.059	8.0025	0.0585	0.9916	8.0025	1.0000
0.65	0.0275	8.343	0.0275	1.0001	8.3421	0.9999
0.6	0.0111	8.6409	0.0109	0.9844	8.6404	0.9999

Table 7- Comparison of the spinodal points obtained from the polynomial equations with the spinodal points calculated using the mechanical and chemical equilibrium equations.

Droplet evaporation simulations were carried out in order to compare the performance of the new piecewise-linear thermal model with the YS and MPI thermal models. Figure 70 shows the evaporation rates for the different hybrid models at a reduced temperature equal to 0.86 and Figure 71 illustrates the evaporation rates of the different DDF models at a reduced temperature set to 0.8. It is clear that the piecewise-linear models with temperature-dependent spinodal points produce the highest rates of evaporation. The evaporation lines obtained using the piecewise-linear models are also the least straight which is a negative factor for the model.

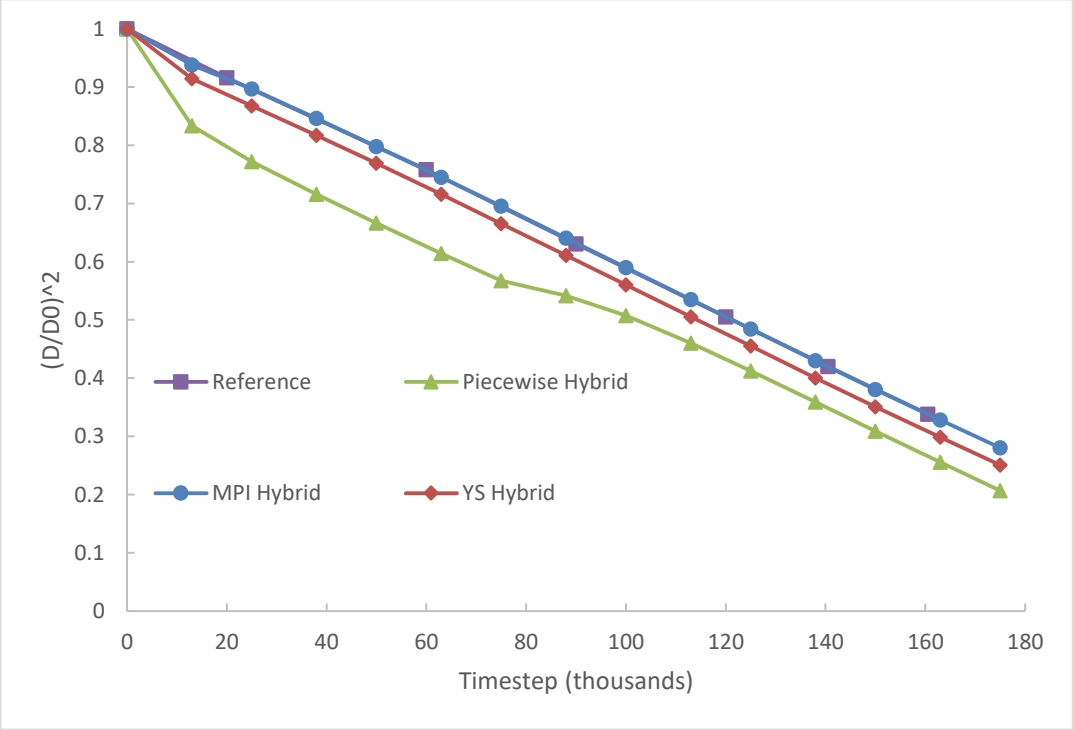

Figure 70- Comparison of the evaporation rates of different models at a reduced temperature of 0.86. Reference [8] data included for comparison.

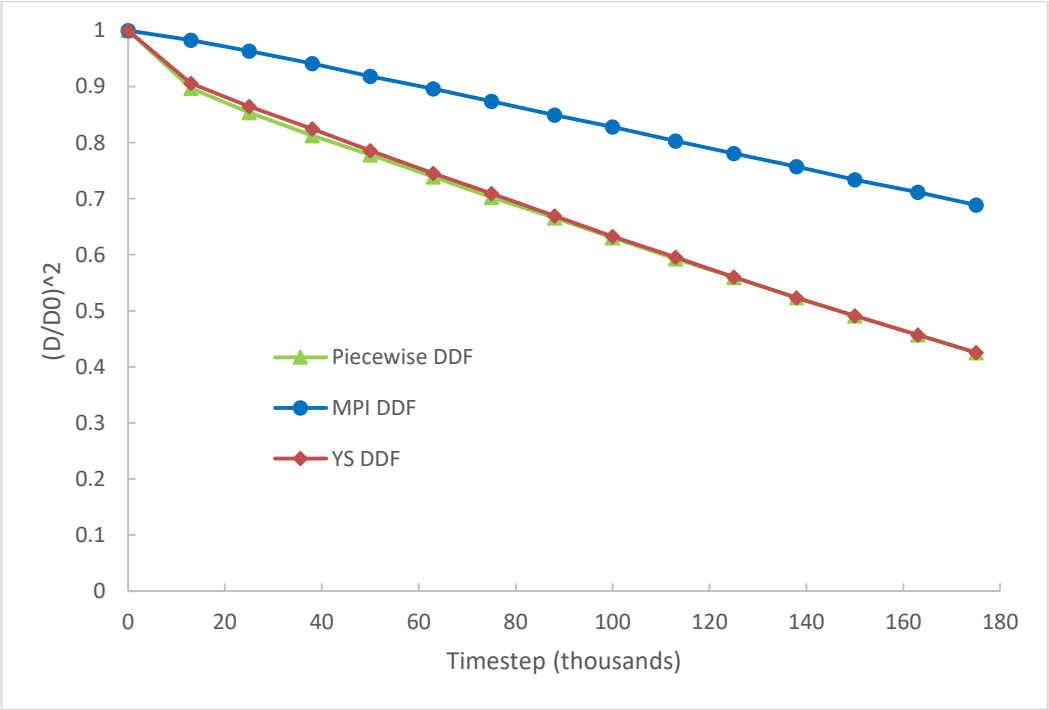

Figure 71- Comparison of the evaporation rates of different models. The reduced temperature was equal to 0.8.

5.5.2. Envelope of Stable Reduced Temperatures

Now that a novel piecewise-linear thermal model has been presented, it is possible to investigate reduced temperature simulation capabilities of the three pseudopotential-based thermal models. First of all, in order to facilitate discussion of the temperature lowering capabilities of the pseudopotential-based models, any differences between the hybrid and modified temperature DDF models should be highlighted. According to Table 8, DDF models are more stable than hybrid models. The simulations were carried out as droplet evaporation cases with the superheat applied being greater than the liquid saturation temperature by 0.14 times the critical temperature (i.e. superheat = T_{sat} + $0.14T_c$). Hence, DDF models are more suitable for the investigation of the lowest achievable reduced temperatures.

Reduced Temperature	YS Thermal DDF	YS Thermal Hybrid	MPI Thermal DDF	MPI Thermal Hybrid
0.86	Stable	Stable	Stable	Stable
0.8	Stable	Unstable	Stable	Unstable

Table 8- Temperature reduction stability results obtained using hybrid and DDF models. Simulations were carried out using the Peng-Robinson EOS with a = 3/49, b = 2/21, R = 1 and acentric factor = 0.344.

Table 9 compares the reduced temperature lowering capabilities of the YS thermal DDF model, MPI thermal DDF model and piecewise-linear thermal DDF model. Again, the simulations were carried out for droplet evaporation with the superheat greater than the saturation temperature by $0.14T_c$. YS and piecewise-linear models achieved the same reduced temperature of 0.8, whilst MPI thermal model was able to achieve a lower than the other two models reduced temperature of 0.78. This suggests that MPI thermal models are more suitable for carrying out simulations whose purpose is to investigate thermal effects at low reduced temperatures.

Reduced Temperature	**YS Thermal**	**MPI Thermal**	**Piecewise Thermal**
0.86	Stable	Stable	Stable
0.8	Stable	Stable	Stable
0.78	Unstable	Stable	Unstable
0.76	Unstable	Unstable	Unstable

Table 9- Temperature reduction stability results for the three different pseudopotential-based thermal models combined with DDF. Simulations were carried out using the Peng-Robinson EOS with a = 3/49, b = 2/21, R = 1 and acentric factor = 0.344.

Clearly, thermal models have problems in carrying out simulations at low reduced temperatures. The simulations discussed above were carried out using the Peng-Robinson equation of state with *a* set to 3/49, *b* to 2/21, *R* to 1 and the acentric factor set to the value for water (i.e. 0.344). The usual strategy for improving the stability of simulations is to increase interfacial thickness. In Figure 72, it can be observed that the simulation at a reduced temperature of 0.78 with $a = 3/49$ and $b = 2/21$ is on the verge of the stable simulation envelope. The sign that the simulation is close to instability manifests itself in the fluctuations of droplet diameter around 13 thousand and 50 thousand timesteps. Therefore, in order to improve stability and achieve lower reduced temperatures, an attempt can be made to increase the interfacial thickness. This can be achieved by lowering the value of the *a* parameter in the cubic EOS, as originally demonstrated by Li et al. [74]. However, this strategy offers only limited success in achieving lower reduced temperatures in thermal simulations. In Figure 72 it can be seen that increasing interfacial thickness allows to lower the achievable reduced temperature down to 0.76. In order to achieve even lower reduced temperatures, the *b* parameter in the cubic EOS also has to be decreased. Coexistence densities are not dependent on the *a* parameter in the Peng-

Robinson and Carnahan-Starling equations of state. However, they are dependent on the *b* parameter, which means that the coexistence densities have to be recalculated when the *b* parameter is adjusted. Adjusting the values of both parameters in the Peng-Robinson EOS allows to achieve stable droplet evaporation simulations at $T_r = 0.6$. As depicted in Figure 72, the rate of evaporation decreases at a constant superheat applied to the droplet as the reduced temperature is lowered. Even as the superheat is increased, the rate of evaporation is not a straight line at high density ratios. In the early stages of evaporation simulations at $T_r = 0.6$, the droplet diameter even exceeds the initial diameter. This indicates that it is difficult to achieve good accuracy at lower reduced temperatures, even if the simulations are stable.

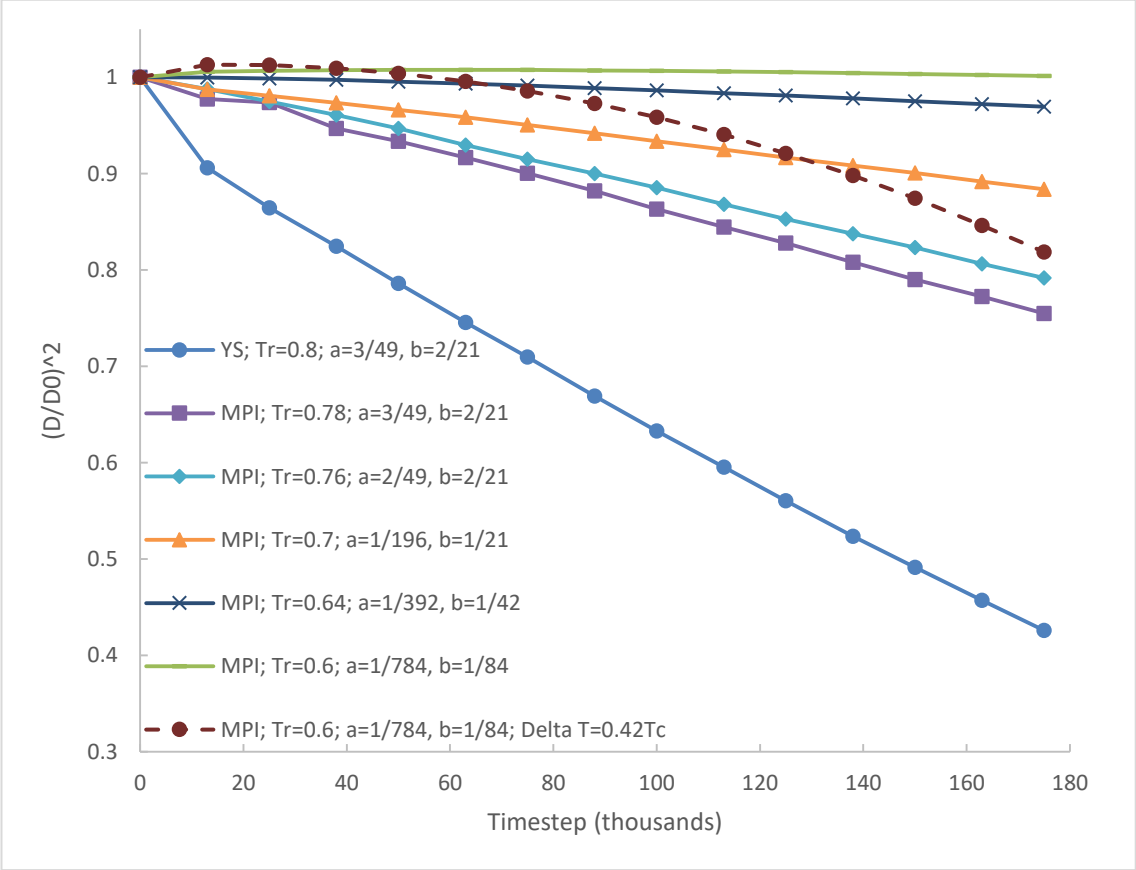

Figure 72- Results of droplet evaporation simulations at a range of reduced temperatures. Simulations at lower reduced temperatures were made possible but to lowering of the a and b parameters in the Peng-Robinson EOS.

Figure 73 examines the effect of changing the *a* and *b* parameters in the Peng-Robinson equation of state on the rate of evaporation of a droplet when the thermal MPI DDF model is applied at $T_r = 0.6$. The main problem encountered involves the rate of evaporation not conforming to the D^2 law. Increasing interfacial thickness can have beneficial effects on the rate of evaporation. For example, at a constant value of *b* equal to 1/168 the rate of evaporation improved as *a* was decreased from 1/1568 to 1/3136 and then again as it was

decreased further to 1/6272. The best results were achieved when *a* was equal to 1/6272 and *b* was equal to 1/168. Lowering the value of *b* to 1/336 whilst keeping *a* at 1/6272 did not improve the results obtained. Lowering both *a* and *b* parameters even further from those identified as optimal (i.e. from *a* = 1/6272, *b* = 1/168), again did not improve the rate of evaporation.

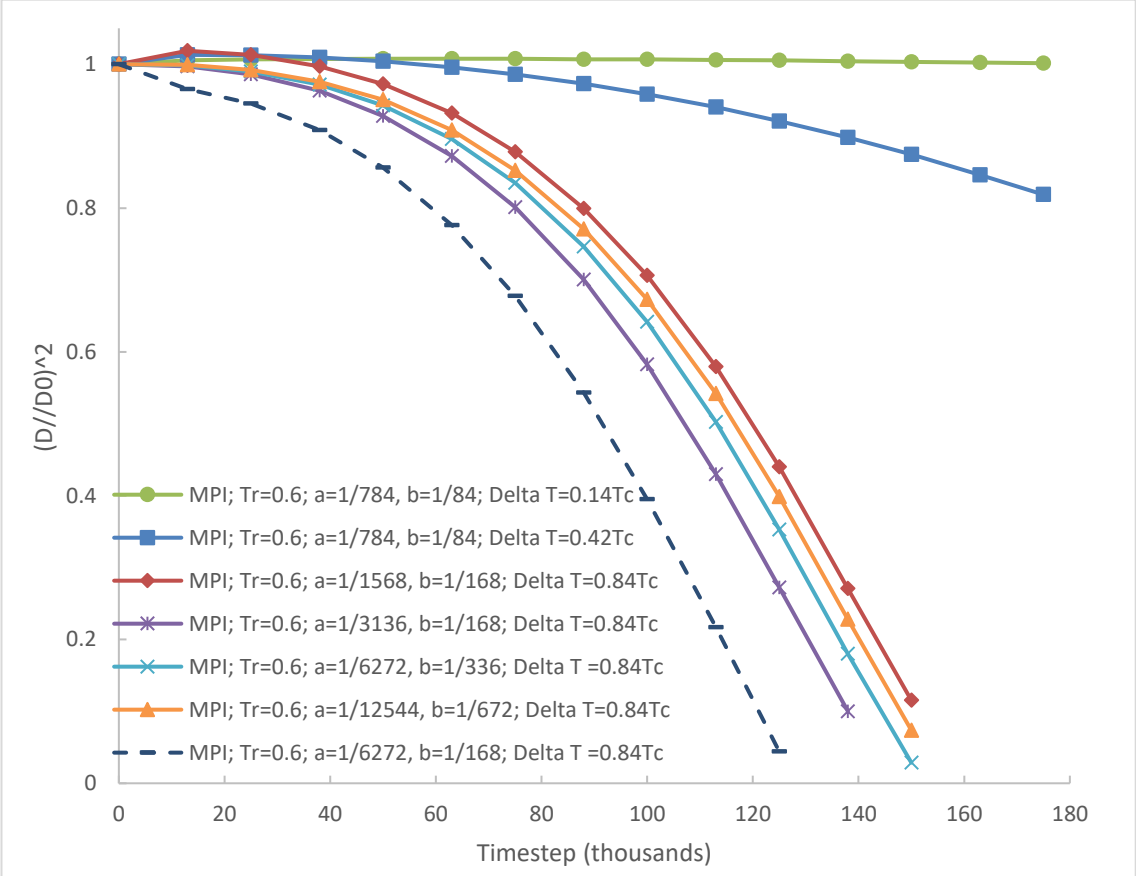

Figure 73- Details of the effect of adjusting the Peng-Robinson EOS parameters on droplet evaporation at Tr=0.6.

5.6.Effect of Multiple Relaxation Time and Forcing Scheme Parameters on Droplet Evaporation

In discussions of thermal models in the literature some material parameters are not mentioned. For example, Li et al. [123] and Li et al. [8] employed the MRT collision operator with methods of adjusting thermodynamic consistency, but did not mention the settings of the MRT relaxation rates or of the ε parameter for adjusting thermodynamic consistency in the forcing scheme. These parameters have an effect on the rate of evaporation and could affect the slope and any deviation from linearity of the D^2 plots. They are briefly explored in Figure 74 and in Figure 75. It can be seen in Figure 74 that increasing the value of bulk viscosity decreases the rate of evaporation. Decreasing ε has an effect on the coexistence densities and it slows down the reduction in the droplet's

diameter, as depicted in Figure 75. The effects of these parameters should be kept in mind when comparing different models.

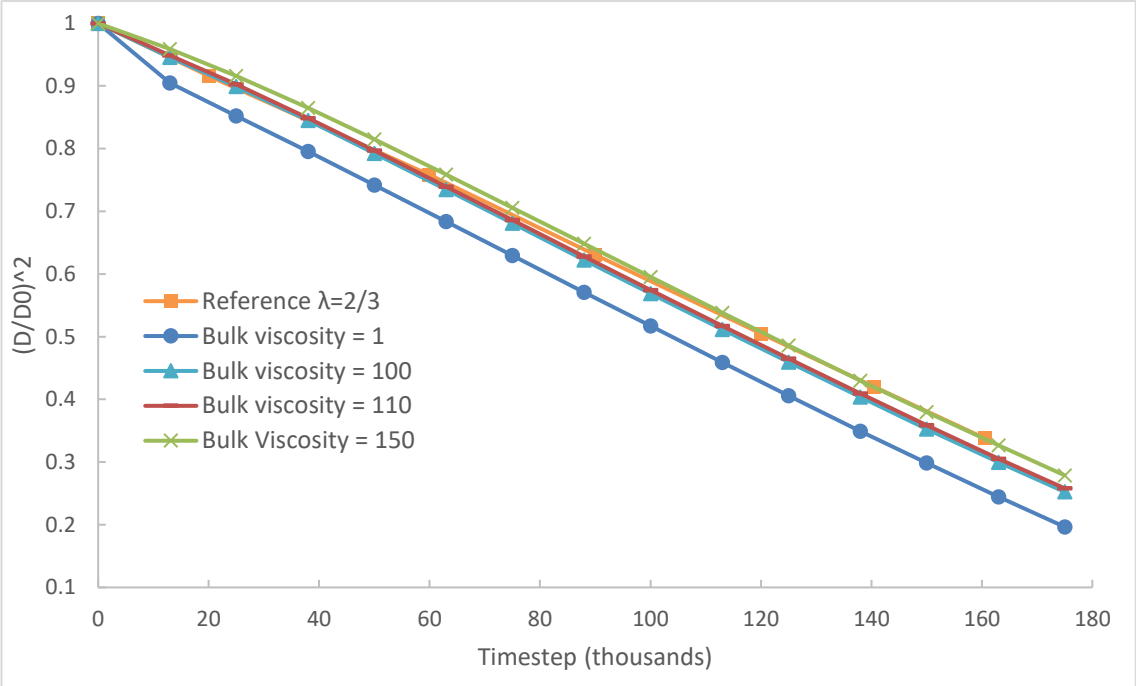

Figure 74- The effect of increasing bulk viscosity as a multiple of kinematic viscosity on the rate of droplet evaporation. Comparison to data in Reference [8].

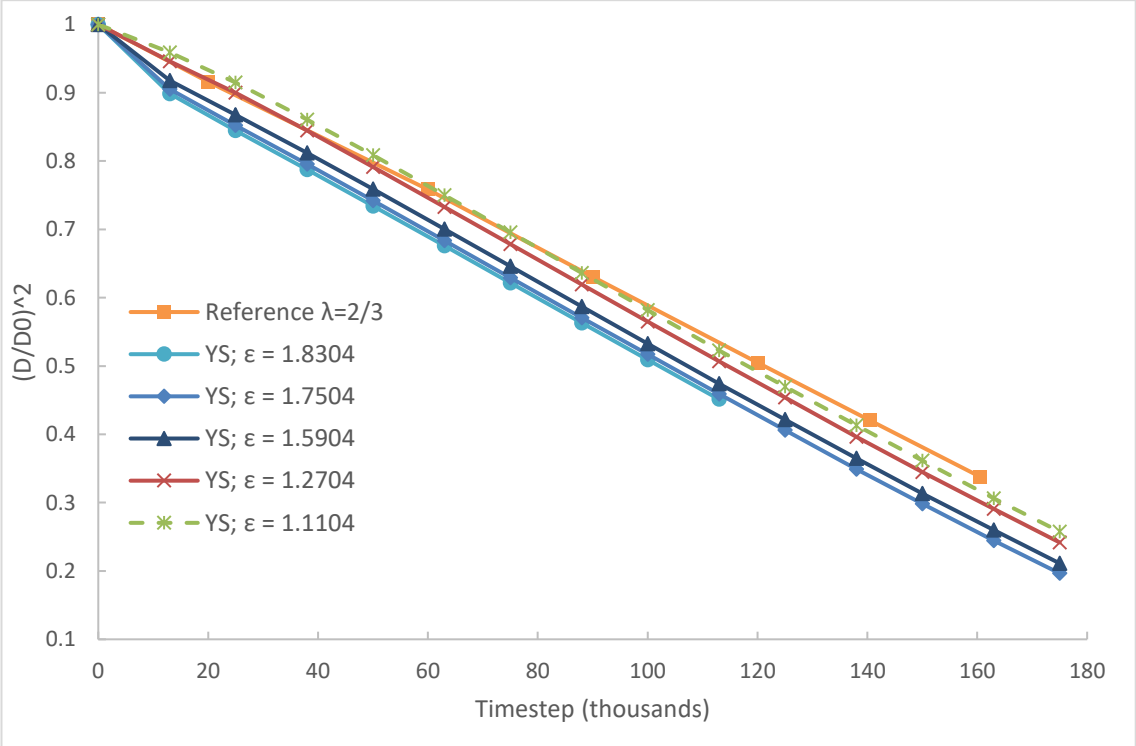

Figure 75- The influence of modifying ε in the Huang-Wu scheme [148] for the adjustment of thermodynamic consistency. k_1 was set to 0 in order to avoid modifying surface tension and k_2 was varied in order to change the value of ε. Evaporation rates are compared to data in Reference [8].

Chapter 6 - Application of the Thermal Model to Phase Change Simulations

6.1.Experimental Data

Salem's doctoral work [3] highlighted the practical interest of the effect of subatmospheric pressures on boiling. The interest is of industrial significance and there is a shortage of research published in the literature on this topic [3]. Simulation methods capable of investigation of subatmospheric pressures were also highlighted as being sought after [3]. The purpose of this Chapter is to attempt to tackle this topic and make progress towards addressing the unfulfilled needs. After discussing experimental data, LBM simulations will be carried out and simulation results will be compared to the experimental data.

Figure 76 illustrates Salem's [3] experiments of boiling at subatmospheric pressures using a brass tube submerged in water. The experiments were carried out at the following pressures from top to bottom 50 mbar, 120 mbar, 500 mbar and 850 mbar, respectively. A number of heat fluxes ranging from 15 kW/m^2 to 80 kW/m^2 were investigated by Salem [3]. The experimental images of bubble nucleation at subatmospheric pressures clearly indicate that pressure has an effect on the size of bubbles nucleated adjacent to the heating tube. The lower the pressure the larger the size of nucleated bubbles. The heat flux has an effect on the rate of bubble nucleation.

Figure 77 illustrates the results of the same experiment, but with the brass tube replaced by a stainless steel tube. The experiments with the stainless steel tube were carried out at pressures of 120 mbar, 500 mbar and 850 mbar from top to bottom, respectively. The same range of heat flux from 15 kW/m^2 to 80 kW/m^2 was employed to obtain the results by Salem [3]. The same trends can be observed with regards to the effect of pressure on the size of nucleated bubbles and the influence of heat flux on the rate of boiling.

Salem reported that pressure affected the shape of nucleated bubbles [3]. At lower pressures, bubbles leaned towards "mushroom" shapes, whereas at higher pressures their shapes were closer to being circular. Lower pressures were found to require higher heat flux to achieve boiling [3]. In practice, this translated into the need for higher wall superheat. Salem found that lowering pressure resulted in generation of bubbles with diameter in the region of centimetres [3].

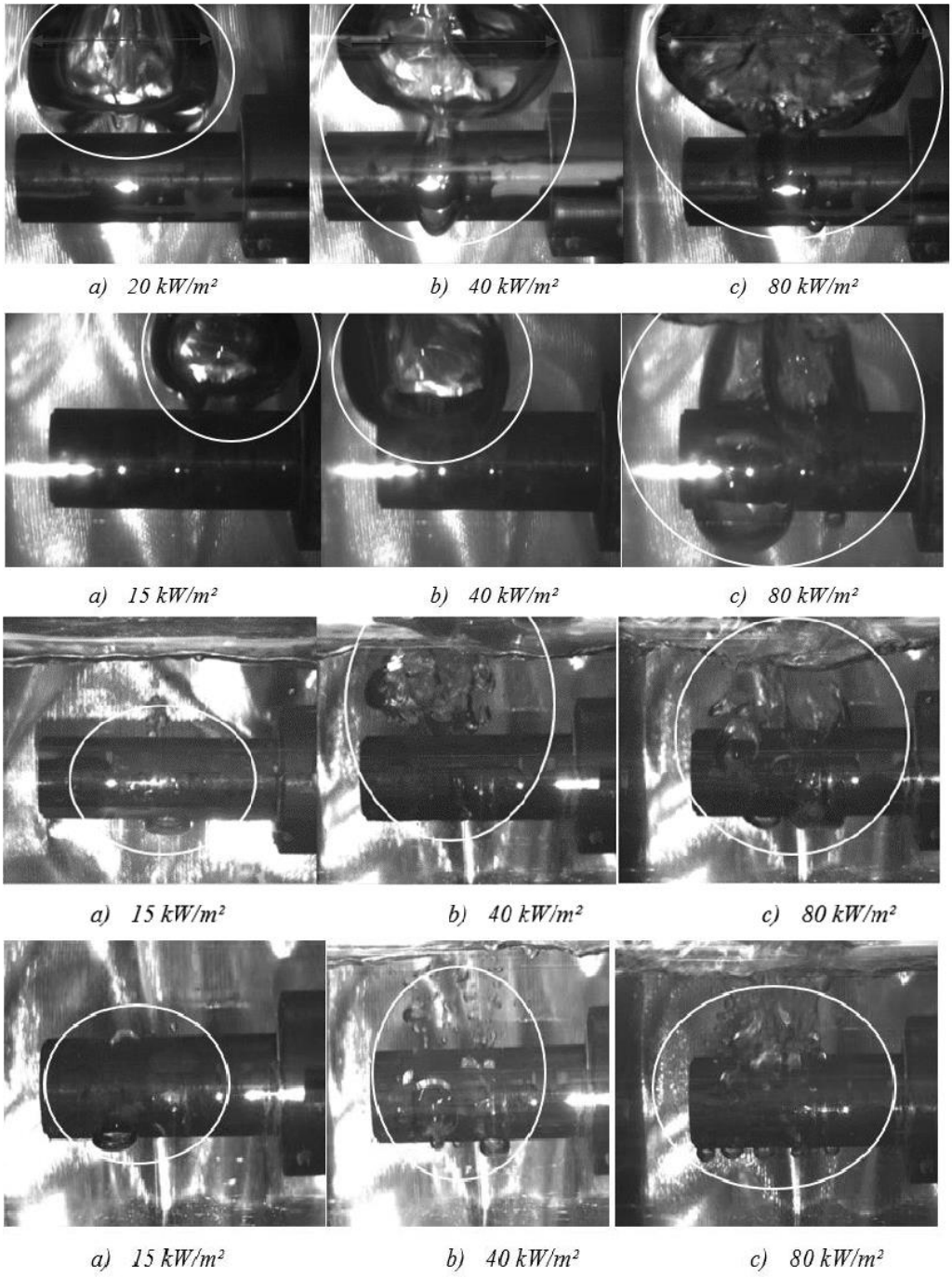

Figure 76- Boiling experiments at different pressures and heat fluxes. Heat supplied from a brass tube. The pressures for the rows are 50 mbar, 120 mbar, 500 mbar and 850 mbar from top to bottom, respectively. Experimental data from Reference [3].

Surface properties of the heating element were also found to have an influence on the boiling characteristics at subatmospheric pressures [3]. Surface properties such as surface roughness, wettability and thermal conductivity are likely to have an influence on the boiling process and generation of bubbles. Surface roughness is an example of a geometric structure that can affect the performance of heat transfer surfaces [35]. Surface roughness is not normally investigated using the lattice Boltzmann method, because it is

a parameter in the range of tens of micrometres. Simple bounce-back boundary condition commonly used to introduce solid surfaces in LBM simulations, on the other hand, results in staircase approximation of solid shapes. Commercial steel pipes have surface roughness of around 0.046 mm in absolute terms [165]. Stachowicz illustrated material defects in brass sheets with the scale used of 50 micrometres [166]. Material defects can play a role in bubble nucleation by providing nucleation sites. Siedel et al. [167] investigated pool boiling characteristics using two artificially created nucleation sites with a diameter of 200 μm and depth of 500 μm. Baltis and Geld [168] found two nucleation sites to interact with each other in flow boiling experiments when they are separated by 10 mm.

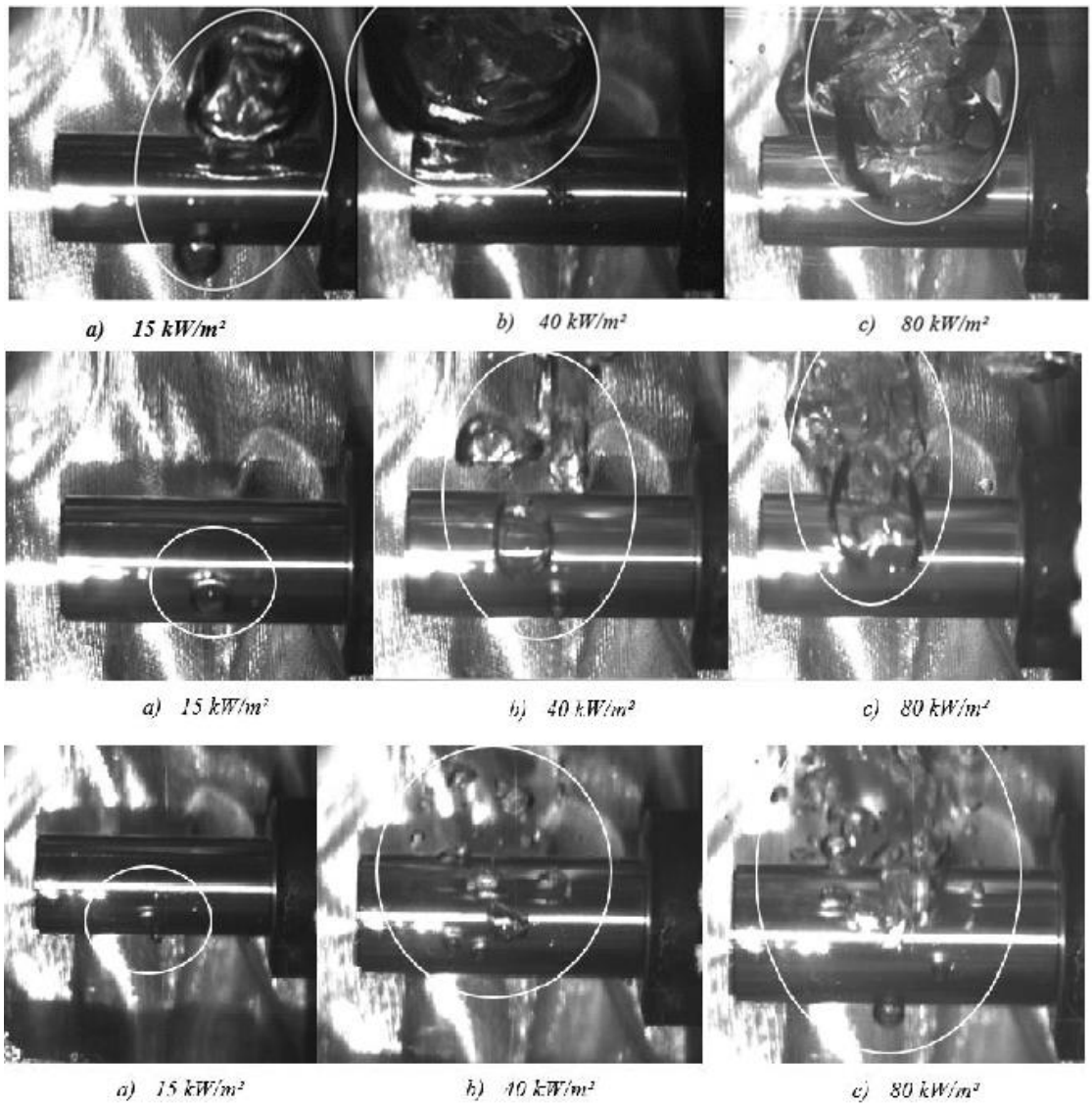

Figure 77- Boiling experiments at different heat fluxes and pressures. The tube in the photos was made of stainless steel and supplied heat to the liquid. The pressures in the experiments were 120 mbar, 500 mbar and 850 mbar from top to bottom, respectively. Experimental data from Reference [3].

The influence of subatmospheric pressure on nucleated bubble diameter is plotted in Figure 78 for Salem's [3] experiments illustrated above. The trends are plotted for the two tube materials used, i.e. brass and stainless steel, and for the separate heat flux values. It is evident that lowering the pressure has the same effect of increasing bubble diameter for all the data series. The extent of bubble diameter increase with decreasing pressure is significant.

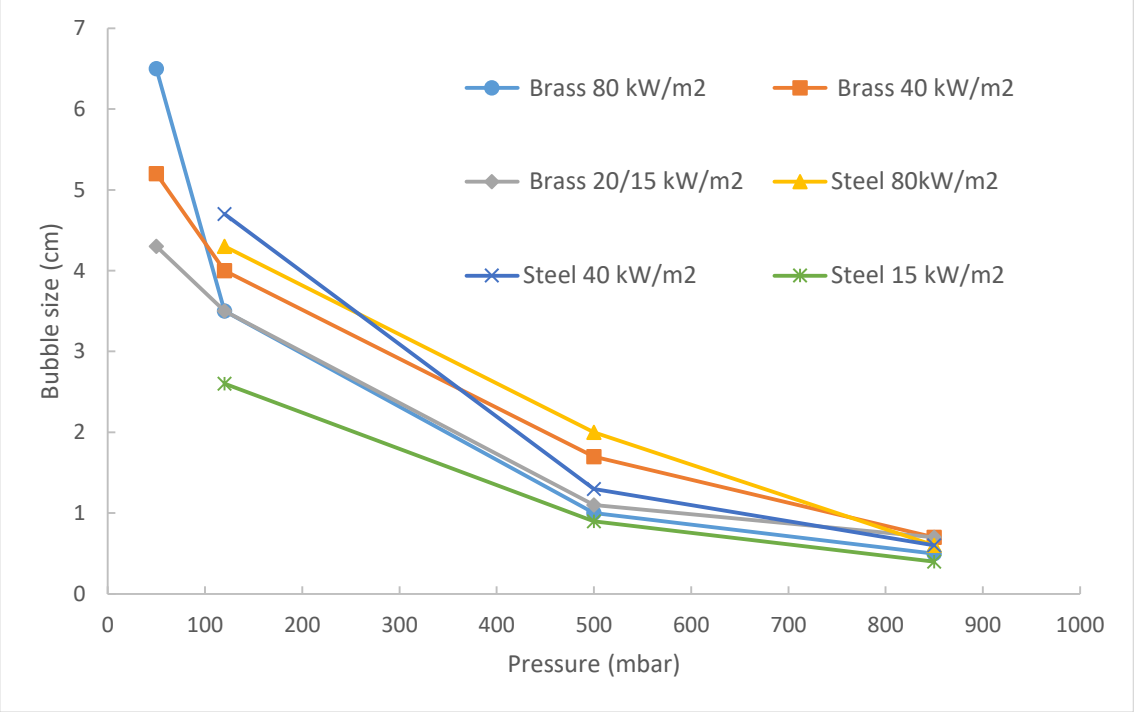

Figure 78- The effect of lowering pressure on bubble nucleation during boiling. Results for brass and stainless steel heating tubes at different values of heat flux.

6.2 Simulation Results

This Section provides data of lattice Boltzmann method simulations carried out to investigate Salem's [3] findings. The experimental set-up is illustrated in Figure 79. The simulations were carried out using the YS DDF and MPI DDF thermal models. The pressure boundary condition was located at the top of the domain. It was used to modify pressure within the simulation domain. The Zou-He pressure boundary for the north side takes the following form [25, 169]:

$$u_{y,0} = -1 + \frac{\left(f_0 + f_1 + f_3 + 2(f_2 + f_5 + f_6)\right)}{\rho_0} \qquad (192)$$

$$f_4 = f_2 - \frac{2}{3}\rho_0 u_{y,0} \qquad (193)$$

$$f_7 = f_5 - \frac{1}{6}\rho_0 u_{y,0} + \frac{1}{2}(f_1 - f_3) \quad (194)$$

$$f_8 = f_6 - \frac{1}{6}\rho_0 u_{y,0} + \frac{1}{2}(f_3 - f_1) \quad (195)$$

Where ρ_0 is adjusted to set the pressure at the boundary.

Bottom boundary was set to bounce-back and the left and right hand side boundaries were periodic. The bottom part of the computational domain was filled with liquid up to a depth of 150 lattice units. Vapour was located above the liquid with a depth of 250 lattice units. Hence, the pressure boundary condition was located at the top of the vapour band. The centre of the heating tube was set 40 lattice units above the bottom boundary in the middle of the x-axis, i.e. 125 lattice units from the left and right hand side periodic boundaries. The heating tube was a circle of 15 lattice unit radius. Energy in the form of superheat to nucleate bubbles was supplied to the liquid phase along the entire length of the circumference of the heating element. The temperature of the heating element was set to 1.25 times the critical temperature ($1.25T_c$). The temperature field of the fluid was initialised at the saturation temperature. The density field was initialised in a diffuse manner with a linear interface.

Heat capacity at constant volume (c_v) was set to 5.0 and kinematic viscosity was set to 0.1 (τ_v = 0.8). The value of gravity was set to -2.5×10^{-5} in the y direction and the gravity force was implemented using the difference between the local density and the average density within the fluid domain:

$$F_{gravity,y} = -2.5 \times 10^{-5}\left(\rho - \rho_{average}\right) \quad (196)$$

In the hydrodynamic relaxation matrix, the value of bulk viscosity was set to the same value as the kinematic viscosity. The hydrodynamic MRT magic parameter was set to 1/12. All of the relaxation rates in the thermal diagonal matrix ($\boldsymbol{\Lambda}$) were set to 1.0. Hence, k in the temperature equation was equal to 1/6. Thermal diffusivity (χ) was set to 0.06, resulting in a variable thermal conductivity (λ) obtained from the following equation:

$$\lambda = \rho c_V \chi \quad (197)$$

The parameters in the Peng-Robinson equation of state were set to a = 3/49, b = 2/21 and R = 1. The acentric parameter in the Peng-Robinson equation of state was set to the value for water, i.e. 0.344.

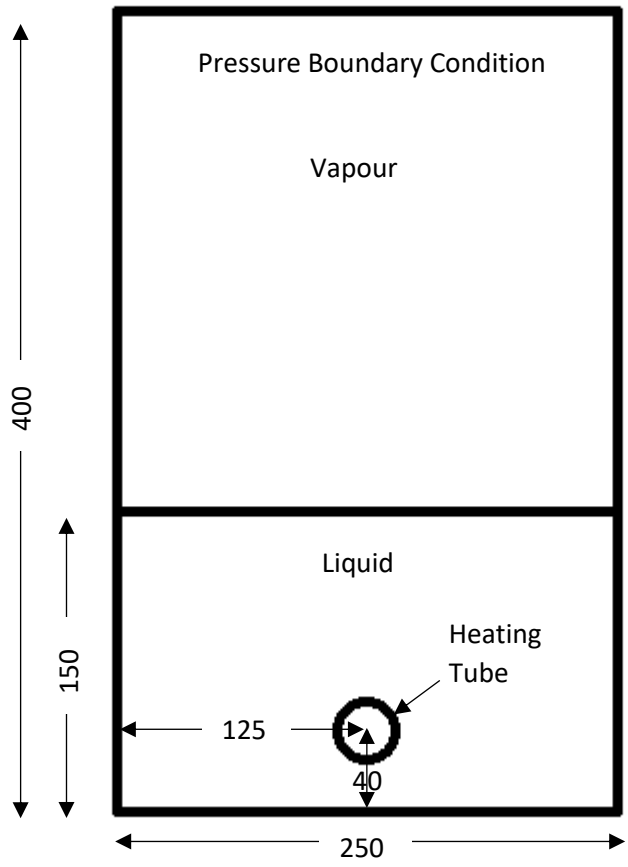

Figure 79- Simulation set-up for thermal bubble nucleation experiments at lowered pressures.

Table 10 and Table 11 list the results of bubble nucleation simulations at lowered pressures. The average pressure at departure was calculated as an average of the pressures in all of the fluid nodes within the computational domain. The bubble diameter was taken to be the greatest width of the departing bubble. The velocity and density values were obtained by averaging them across the widest point of the departing bubble.

Pressure	Departure Timestep	Bubble Diameter	Departure Average Pressure	Velocity	Density	We
Pressure 1	8100	63.89	0.041546	0.0246	0.6147	0.5186
Pressure 2	7900	94.99	0.034884	0.0181	0.5217	0.3551
Pressure 3	6700	183.32	0.024798	0.021	0.3294	0.5806

Table 10- Details of properties of departing bubbles during MPI DDF simulations at Tr = 0.9 for the three pressure simulation runs.

Pressure	Departure Timestep	Bubble Diameter	Departure Average Pressure	Velocity	Density	We
Pressure 1	9200	55.95	0.028994	0.0159	0.487	0.0983
Pressure 2	8100	132.41	0.018609	0.0257	0.3293	0.4121
Pressure 3	7500	186.04	0.013878	0.029	0.2773	0.6202

Table 11- Details of properties of departing bubbles during YS DDF simulations at Tr = 0.86 for the three pressure simulation runs.

Figure 80 illustrates bubble departure at the three pressures tested at $T_r = 0.9$ using the MPI DDF thermal model and Figure 81 depicts the equivalent at $T_r = 0.86$ using the YS DDF thermal model. The effects of decreasing the pressure on bubble nucleation observed experimentally can be clearly demonstrated in the results of the LBM simulations. The lower the pressure in the simulation domain the larger the size of bubbles nucleated during simulations of nucleate pool boiling. Salem [3] also mentioned that larger bubbles tend to be "mushroom" shaped rather than spherical. Deformation of departing bubbles into "mushroom"- or dome-shaped bubbles can be observed in Figure 80 and to a lesser degree in Figure 81.

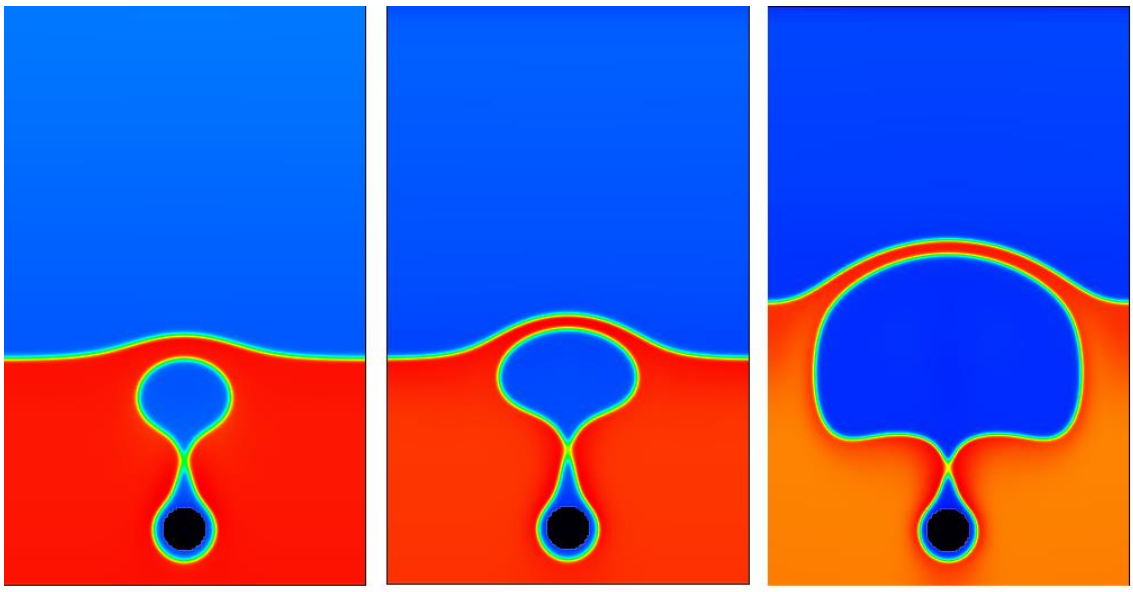

Figure 80- Bubbles at departure from the heating tube for the three pressures. The simulations were carried out with MPI DDF thermal model at a reduced temperature of 0.9. Decreasing pressure from left to right hand side.

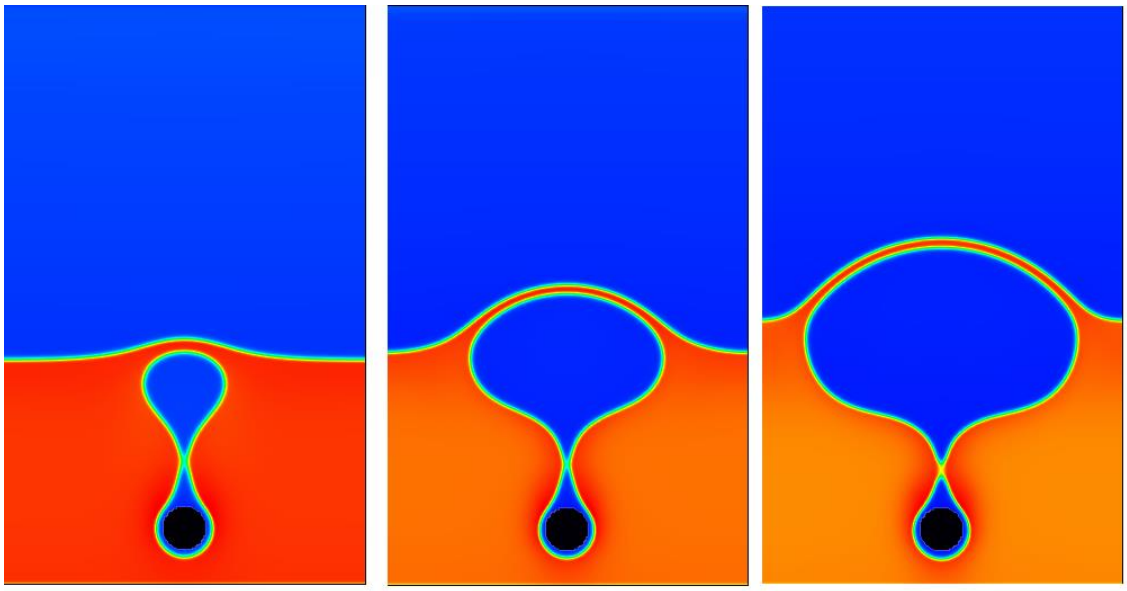

Figure 81- Illustration of bubbles breaking away from the heating tube at the three different pressures tested. The simulations were carried out using the YS DDF thermal model at Tr = 0.86. Decreasing pressure from left to right hand side.

Bubble deformation can be explained using the Weber number. If bubble deformation occurs, then lower pressures must results in an increase in the inertia force in relation to the surface tension force. At low bubble diameters the surface tension force is sufficient to keep spherical bubble shape, whereas at larger bubble diameters the inertia force is greater and the surface tension force is no longer sufficient to prevent bubble deformation. The Weber numbers calculated in Table 10 and Table 11 are plotted in Figure 82.

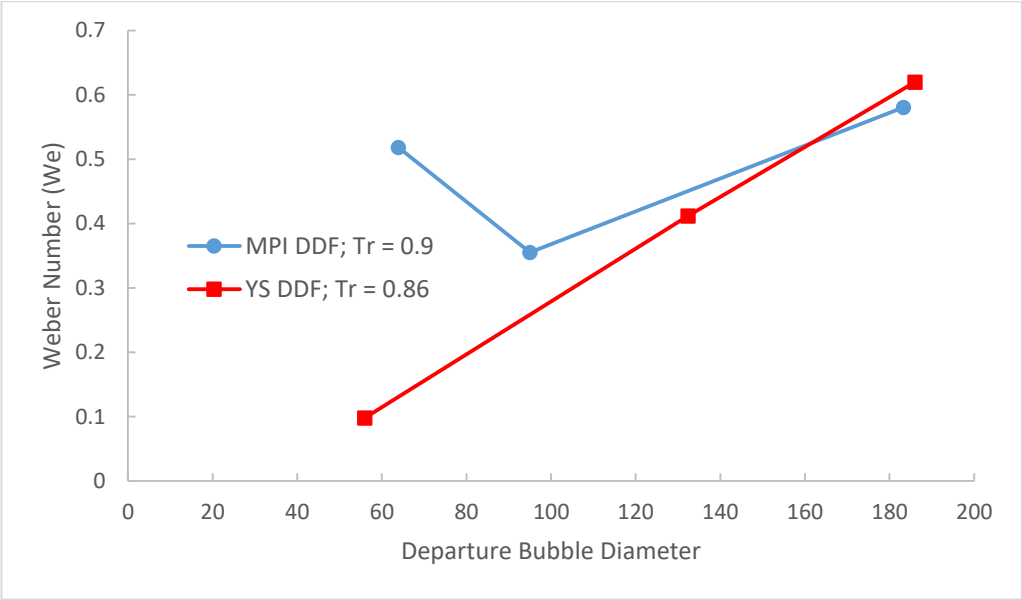

Figure 82- Weber number for the departing bubbles at different pressures for the two reduced temperatures tested.

The plot shows that the largest bubbles have the highest values of the Weber number. In the calculations it was assumed that pressure does not affect surface tension. A decrease in pressure in the LBM simulations resulted in an increase in the surface tension and this can be observed in Figure 83. At all of the pressures tested, Laplace's law was satisfactorily obeyed. In a one-component system where liquid is in equilibrium with its vapour it is not possible for the pressure to vary as stated in the Lewis-Randall equation describing the change of surface tension with pressure [170]. In two-component systems a decrease in pressure results in an increase of surface tension [170]. This was overserved for water in contact with low molecular weight gases [171].

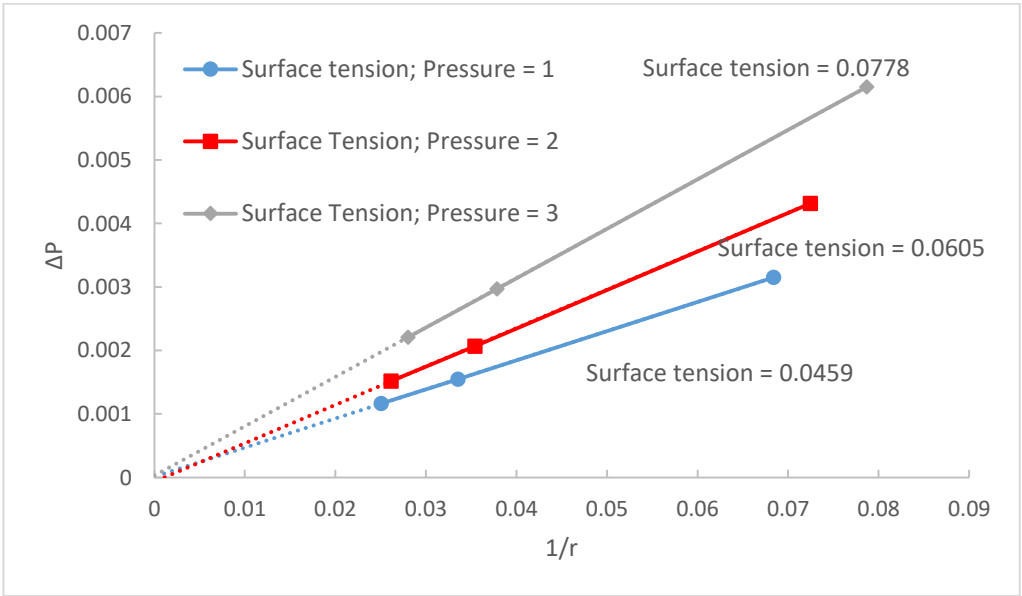

Figure 83- Effect of pressure on surface tension in LBM simulations with MPI DDF thermal model at Tr = 0.9.

The effect of pressure on the diameter of bubbles departing the heating element is illustrated in Figure 84. Lowering the pressure results in an increase in the diameter of the departing bubbles. The same trend can be observed at both reduced temperatures.

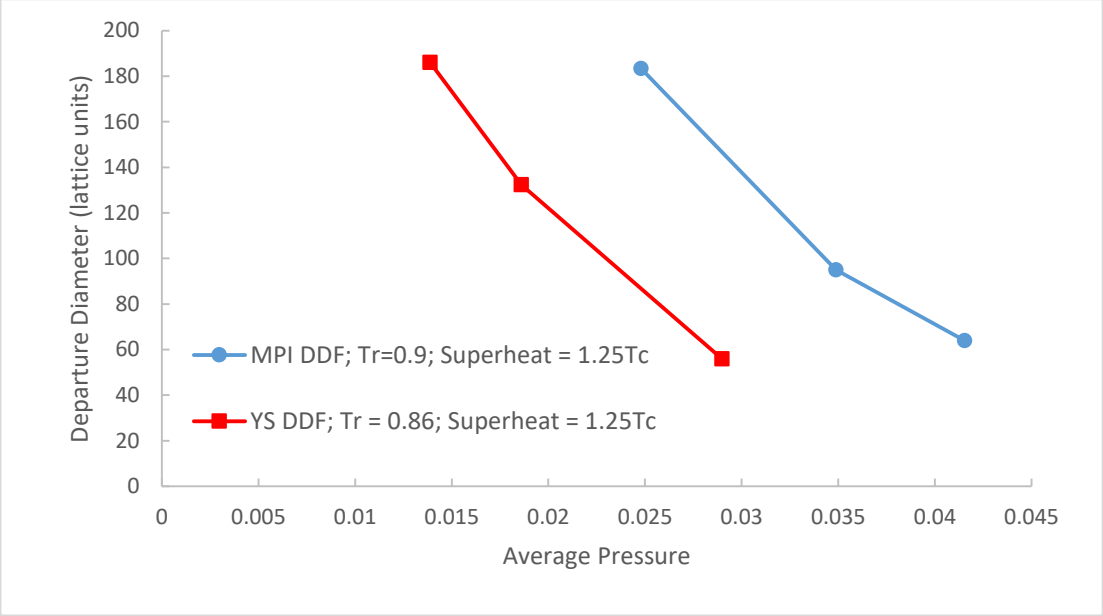

Figure 84- Effect of pressure on diameter of departing bubbles for the two reduced temperatures tested.

6.3 Normalisation of Data and Comparison

In order to investigate the data further and to compare experimental and simulation data on the same plot, the data has to be normalised. First, the simulation pressure is normalised in order to examine the effect of reduced temperature. The simulations were carried out at significantly higher reduced temperatures than the experiments. The critical temperature of water is 374 °C (647 K) [172]. Salem [3] reported fluid temperatures in the range from 30 °C to 100 °C. This means that the experiments were carried out at reduced temperatures ranging from approximately 0.47 to 0.58. Therefore, it is important to gauge the extent to which reduced temperature affects the pressure-related phenomena present in nucleate pool boiling. In Figure 85 the same trend can be observed at both reduced temperatures. Therefore, it can be assumed that reduced temperature does not affect the observed trends in bubble nucleation at pressures decreased from the saturation point.

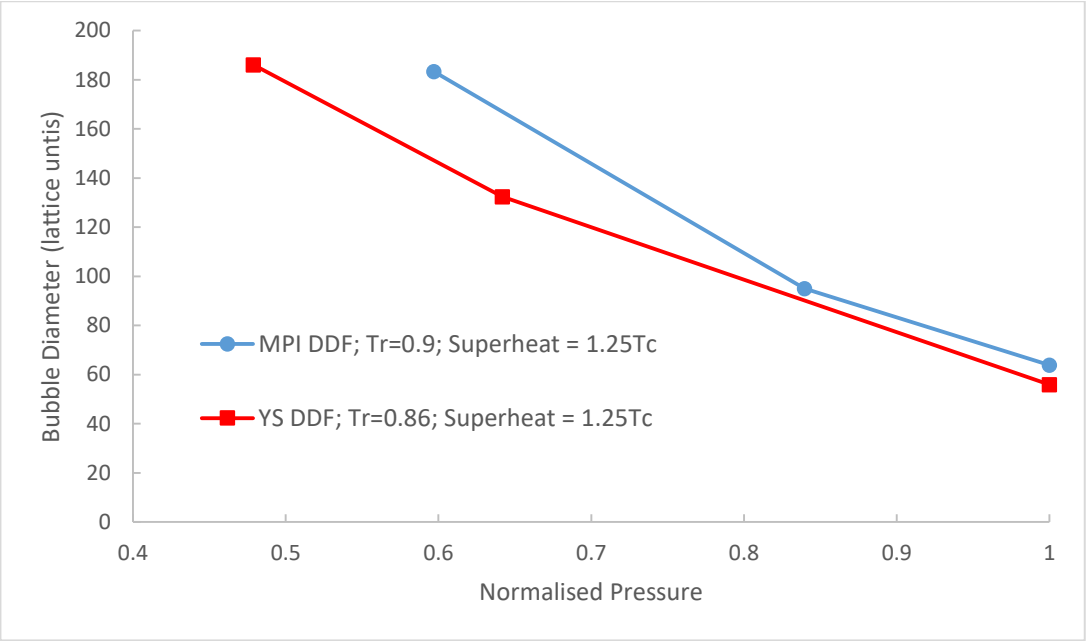

Figure 85- The effect of pressure on bubble nucleation at the two reduced temperatures for which simulations were carried out.

In order to normalise the experimental results, pressure is normalised at 1 bar and bubble size is normalised to bubble size at 1 bar. This is done to display bubble size relative to bubble size at 1 bar rather than in absolute terms, i.e. centimetres. Trends of experimental results are extrapolated to 1 bar in order to obtain the extent of bubble size at 1 bar. This process is illustrated in Figure 86 for one of the experimental data series.

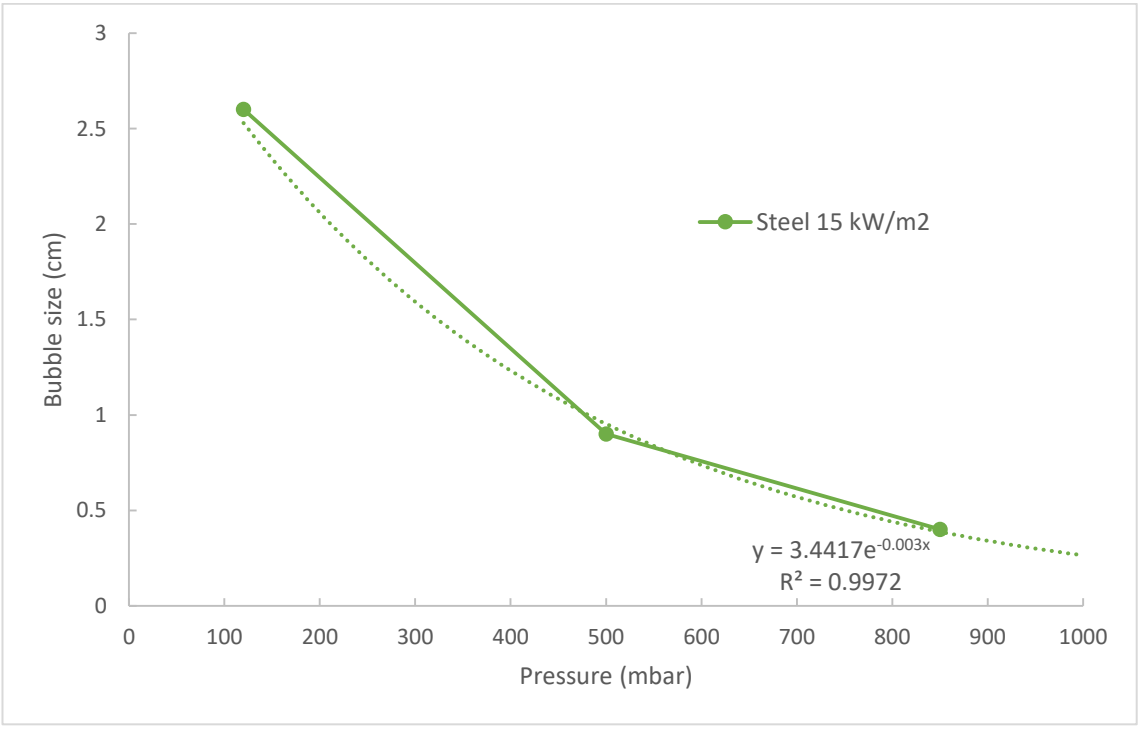

Figure 86- Extrapolating bubble size to 1 bar to obtain normalised bubble diameters.

After the normalisation process is complete, both experimental and simulation data can be plotted on the same graph for comparison. The results are illustrated in Figure 87. The agreement between simulation and experimental results is good with simulation results down to a pressure of 0.5. The simulation results are located in between experimental results for brass and stainless steel. This is despite the fact that the simulation results were carried out at significantly higher reduced temperatures. Lower reduced temperatures would require simulation of high density ratios. High density ratios tend to be accompanied by higher numerical errors which could have a significant influence on the quality of simulation results. Stable simulations were achieved at a reduced temperature of 0.6. However, there was no success in terms of achieving nucleated bubble departure from the heating tube. Nucleated bubbles did not depart the heating element because simulations with high gravity forces caused excessive velocities in the vapour phase. Very low density of the vapour phase was the cause of the high velocity. Lower gravity forces were insufficient to lift bubbles up through the liquid phase to the surface. Nevertheless, the results agree well with Salem's [3] findings. Consequently, LBM can be used to study subatmospheric pressure nucleate pool boiling.

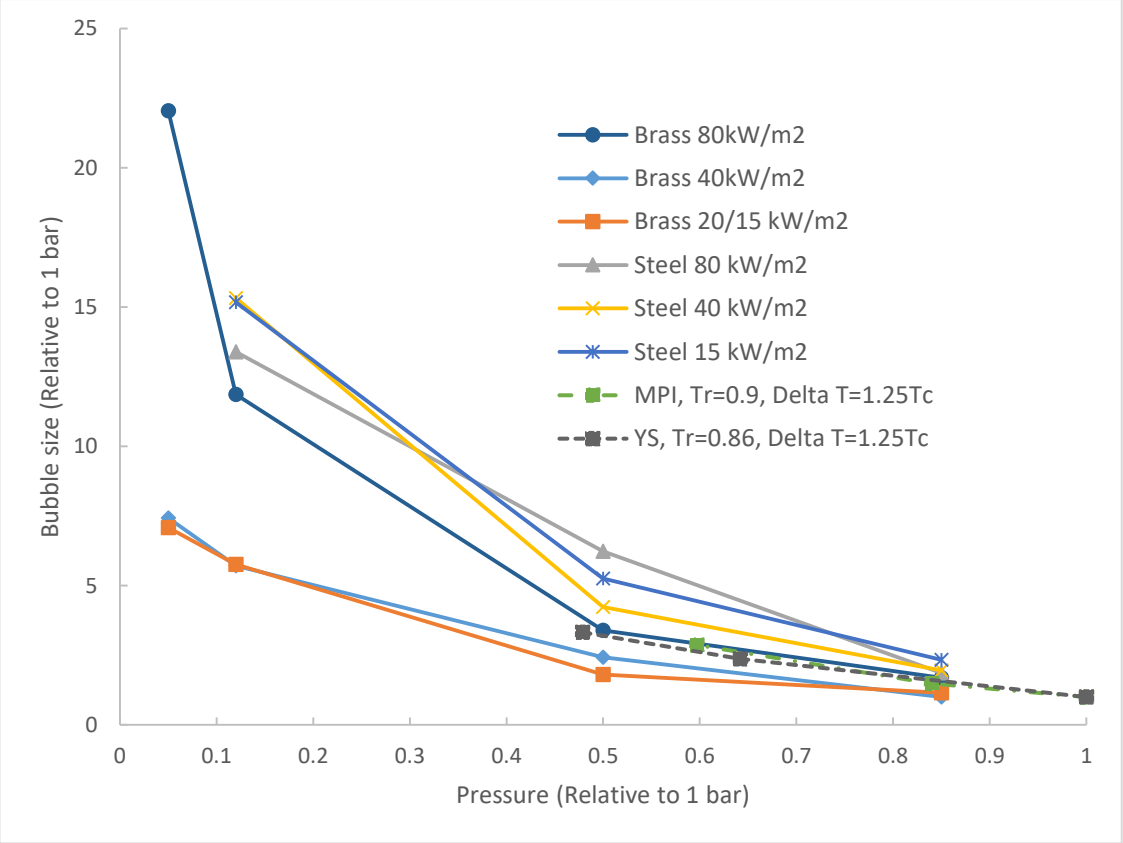

Figure 87- Effect of pressure on bubble nucleation. Experimental [3] and simulation results.

For water, bubble diameter is inversely proportional to pressure, i.e. $D_b \sim P^{-1}$ [164, 173]. This relationship has been well-captured in the LBM simulations carried out as part of this doctoral work and in Salem's [3] experimental results.

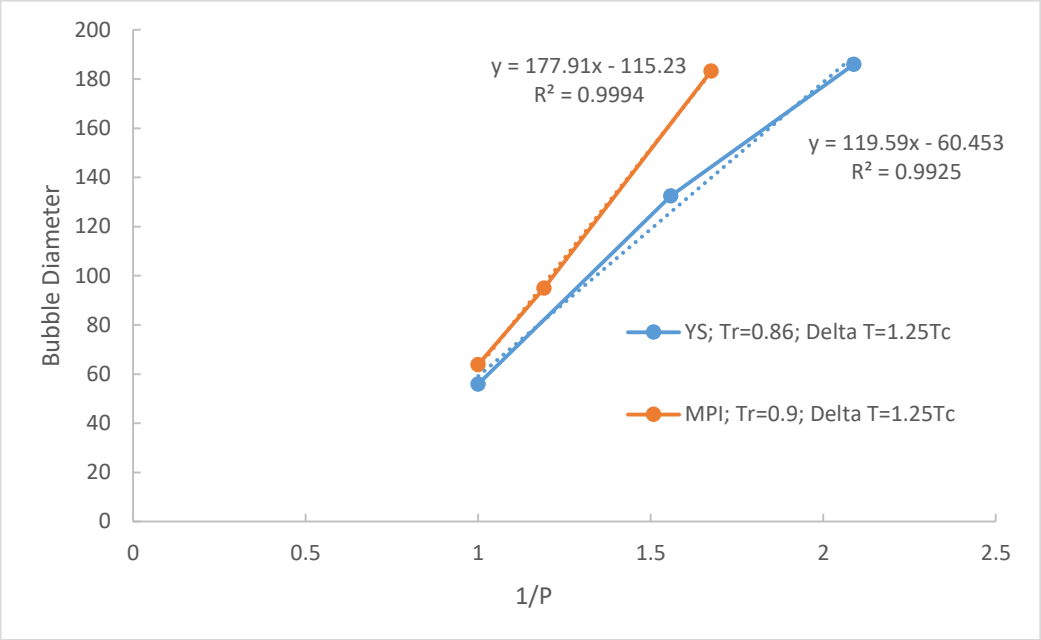

Figure 88- Examination of the inverse relationship between bubble diameter at departure from the heating element and pressure for LBM simulations.

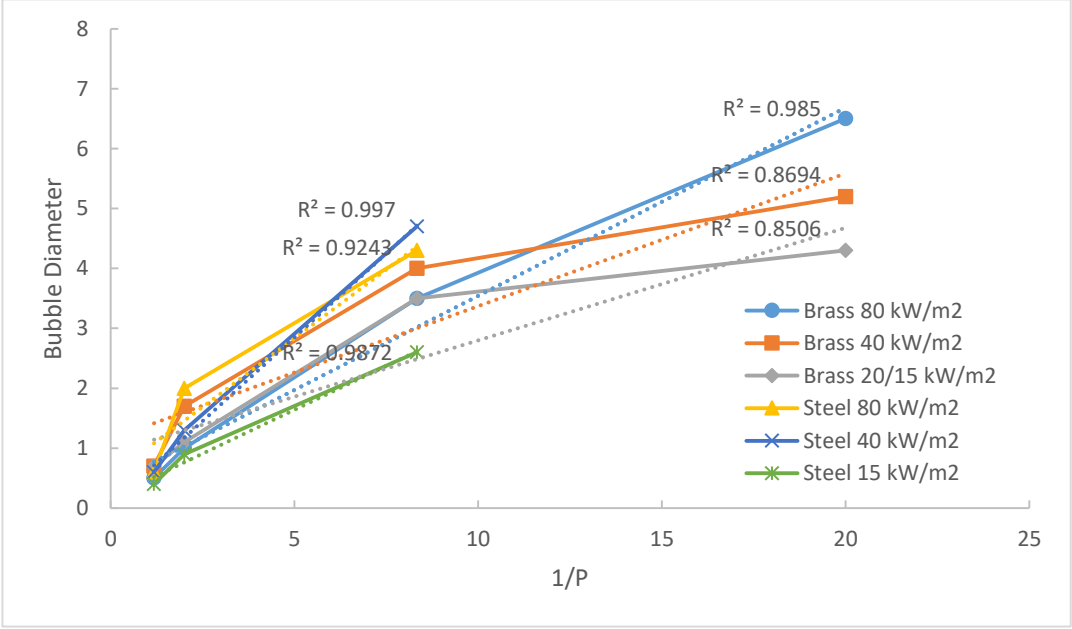

Figure 89- Examination of the inverse relationship between bubble diameter at departure from the heating element and pressure for Salem's [3] experimental data.

Bubble detachment from the heating element is a complex phenomenon and its mechanics have still not been conclusively determined, which means that no satisfactory comprehensive theory of bubble detachment mechanics is available to us [164, 174, 175].

One important consideration that needs to be taken into account when considering the physics of bubble detachment is the contact-line motion [164].

Fritz [176] constructed a semi-empirical equation for the bubble diameter at departure from the heating element [164]:

$$D_b = 0.0208\theta e \left[\frac{\sigma}{g(\rho_l - \rho_v)}\right]^{1/2} \qquad (198)$$

The most prominent shortcoming of Fritz's [176] correlation concerns the inability of the equation to reflect the strong dependence of bubble diameter at departure from the heating element on pressure [164].

In the case of a static contact line it can be assumed that there is no formation of a microlayer, leading to the buoyancy force balancing a considerable surface tension force [164]. This model is termed the pinned-contact-line (PCL) model [164]. When the contact line is mobile, the surface tension force becomes unimportant leading to the buoyancy force competing with the downward hydrodynamic (drag) force [164]. The term given to the mobile contact line model is the depinned-contact-line (DCL) model [164].

Bond numbers were calculated for the experimental and simulation data in order to investigate whether the comparison between simulation and experimental data is valid.

$$Bo = \frac{(\rho_w - \rho_g)gL^2}{\sigma} \qquad (199)$$

Where the characteristic length was taken to be droplet radius.

In order to calculate Bond number values for the experimental data, the following properties of saturated liquid and vapour were obtained from steam tables:

P (mbar)	ρ_L (kg/m^3)	ρ_G (kg/m^3)	σ (N/m)
850	961.8001776	0.507067566	0.059845898
500	970.9544371	0.308627765	0.062431124
120	988.2697349	0.080915185	0.06804125
50	994.7069626	0.035478222	0.07074036

Table 12- Properties of saturated water and steam at subatmospheric pressures according to the IAPWS IF-97 steam tables [177].

The following Bond number values were obtained for simulation results using the MPI DDF thermal model at Tr = 0.9:

Pressure	Bubble Diameter	ρ_L	ρ_G	Bond Number
Pressure 1	63.89	5.87023	0.6147	2.921121
Pressure 2	94.99	6.030266	0.5217	5.134746
Pressure 3	183.32	6.059849	0.3294	15.47066

Table 13- Bond number values for simulation results obtained using the MPI DDF thermal model with g = 2.5x10^{-5} and surface tension values from Figure 83.

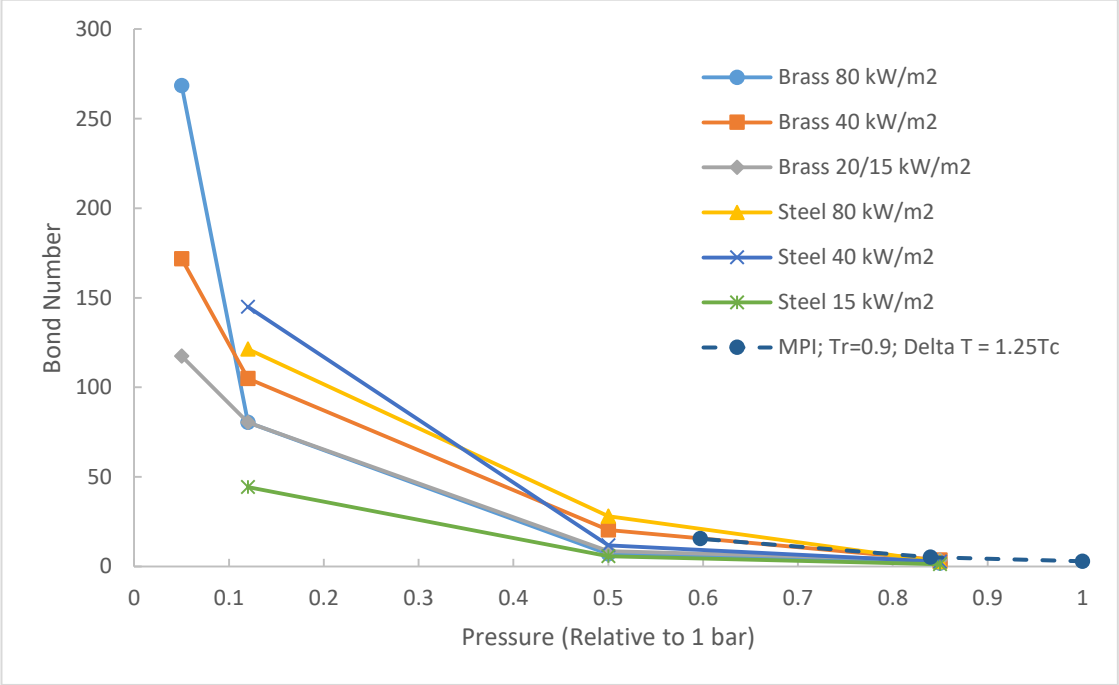

Figure 90- Comparison of Bond number values for the experimental [3] and simulation data.

The agreement between the experimental and simulation Bond number values is good confirming that the matching observations of bubble size and shape at lowered pressures in experiments and in simulations have their basis in physics.

Chapter 7 - Conclusions

The main findings of this study are listed in this Chapter and a number of recommendations is proposed for further study at the end of this Chapter.

It is well-known that using sharp interfaces in the pseudopotential models can lead to generation of undefined interaction forces which render simulations unstable. In this work it is shown that even when the interface is thick, generation of undefined pseudopotential values is still possible for certain choices of parameters. Therefore, it is suggested that it is important to have an understanding of the way in which different methods generate intermolecular forces.

A hybrid pseudopotential model was developed in order to investigate the influence of intermolecular force distribution on simulations. It was found that spurious velocities are affected by the intermolecular force distribution besides being affected by the total value of the intermolecular force.

It has been observed that the introduction of a viscosity ratio between the phases almost eliminates the influence of density ratio on the generated values of spurious velocity. In dynamic simulations of a droplet splashing on a thin liquid film, the techniques for improving stability of simulations were ranked in the following order of decreasing efficacy:

- Introduction of a kinematic viscosity ratio between the phases
- Increase in the value of bulk viscosity
- Replacing the YS [143] method of EOS inclusion with the piecewise linear [131] method
- Increasing the reduced temperature/ reducing the density ratio.

The modified pseudopotential-based model of Li et al. [157] for fluid-solid interactions was reformulated in order to allow adjustment of fluid-solid forces, which mimic fluid-fluid forces, separately from fluid-fluid interactions.

A method was developed of coupling the multipseudopotential interaction model with the MRT collision operator and of adjusting thermodynamic consistency. It was found that splitting the ε parameter into two separate values works well for adjusting the thermodynamic consistency for the entire temperature range.

A thermal MPI model was developed by reformulating the interparticle force expression to include temperature effects at local and neighbouring sites. Thermal MPI models were found to be an attractive method for simulating droplet evaporation and bubble nucleation in nucleate pool boiling. Hybrid thermal MPI model was found to obey the D^2 law [7] closely and the DDF thermal MPI model was found to be more stable than the other models tested at lower reduced temperatures. Stable thermal simulations were carried out at realistically low reduced temperatures (i.e. T_r = 0.6). Stability was achieved by simultaneously lowering the *a* and *b* parameters in the Peng-Robinson equation of state. However, main problems encountered at low reduced temperatures involved departure from the D^2 law [7] and inability of nucleated bubbles to depart the heating element due to buoyancy.

LBM was applied to study nucleate pool boiling at subatmospheric pressures. In the LBM simulations, the effect of increasing bubble diameter with decreasing pressure was captured and obeyed the $D_b \sim P^{-1}$ [164, 173] relationship. Bubble shape was found to correctly transform from spherical to mushroom shaped. Bond number comparison showed that the physics observed in the simulations can be compared to the real life experimental results. The results of LBM simulations on bubble diameter increase with decreasing pressure fall in between the experimental results for the brass and stainless steel tubes. Lower pressures appeared to promote slightly higher Weber numbers. Surface tension in LBM simulations was found to increase as the pressure within the simulation domain was decreased, a trend which can be observed in the physical world.

7.1. Future work

For further studies, the listed aspects of the proposed model should be studied:

- Carry out multiphase thermal simulations in heat exchanger geometries. Such studies would have practical interest and could investigate the efficiency of heat transfer of different arrangements. For example, tubes in shell and tube heat exchangers are usually arranged in an equilateral triangular, square, or rotated square pattern [31].
- A worthwhile research topic would consist of development of thermal models capable of accurate simulations at low reduced temperatures. Currently, this target appears to be out of reach of the presently available thermal LBM models.
- Investigate the effects variation of physical properties, e.g. viscosity, with temperature. Viscosity can be location, time and condition dependent in LBM

simulations. In this work, viscosity was made dependent on density in order to improve stability of simulations.

- The effects of bulk viscosity in LBM simulations should be further compared to its effects in real life. For example, Wu et al. briefly touched the subject [155] and mentioned Cramer's [178] measurements of bulk viscosity values of different fluids.
- Where the physics of secondary droplets is of interest, simulations should be carried out in larger domains in order to better resolve secondary droplets.

Appendix A

Term	Model				
	MRT Forcing Scheme	Li-Luo Thermodynamic Adjustment	Li-Luo Surface Tension Adjustment	Li-Luo Thermodynamic and Surface Tension Adjustments	Huang-Wu Thermodynamic and Surface Tension Adjustments
$\bar{S}$					
0	0	0	0	0	0
1	$6(u_xF_x + u_yF_y)$	$6(u_xF_x + u_yF_y) + \frac{12\sigma\lvert\boldsymbol{F}\rvert^2}{\psi^2\Delta t(\tau_e - 0.5)}$	$6(u_xF_x + u_yF_y)$	$6(u_xF_x + u_yF_y) + \frac{12\sigma\lvert\boldsymbol{F}\rvert^2}{\psi^2\Delta t(\tau_e - 0.5)}$	$6(u_xF_x + u_yF_y)$
2	$-6(u_xF_x + u_yF_y)$	$-6(u_xF_x + u_yF_y) - \frac{12\sigma\lvert\boldsymbol{F}\rvert^2}{\psi^2\Delta t(\tau_\varepsilon - 0.5)}$	$-6(u_xF_x + u_yF_y)$	$-6(u_xF_x + u_yF_y) - \frac{12\sigma\lvert\boldsymbol{F}\rvert^2}{\psi^2\Delta t(\tau_\varepsilon - 0.5)}$	$-6(u_xF_x + u_yF_y)$
3	F_x	F_x	F_x	F_x	F_x
4	$-F_x$	$-F_x$	$-F_x$	$-F_x$	$-F_x$
5	F_y	F_y	F_y	F_y	F_y
6	$-F_y$	$-F_y$	$-F_y$	$-F_y$	$-F_y$
7	$2(u_xF_x - u_yF_y)$	$2(u_xF_x - u_yF_y)$	$2(u_xF_x - u_yF_y)$	$2(u_xF_x - u_yF_y)$	$2(u_xF_x - u_yF_y)$
8	$(u_xF_y + u_yF_x)$	$(u_xF_y + u_yF_x)$	$(u_xF_y + u_yF_x)$	$(u_xF_y + u_yF_x)$	$(u_xF_y + u_yF_x)$
C					
0			0	0	
1			$1.5\omega_e(Q_{xx} + Q_{yy})$	$1.5\omega_e(Q_{xx} + Q_{yy})$	
2			$-1.5\omega_\epsilon(Q_{xx} + Q_{yy})$	$-1.5\omega_\epsilon(Q_{xx} + Q_{yy})$	
3			0	0	
4			0	0	
5			0	0	
6			0	0	
7			$-\omega_v(Q_{xx} - Q_{yy})$	$-\omega_v(Q_{xx} - Q_{yy})$	
8			$-\omega_v Q_{xy}$	$-\omega_v Q_{xy}$	
Q_m					
0					0
1					$3(k_1 + 2k_2)\frac{\lvert\boldsymbol{F}\rvert^2}{G\psi^2}$
2					$-3(k_1 + 2k_2)\frac{\lvert\boldsymbol{F}\rvert^2}{G\psi^2}$
3					0
4					0
5					0
6					0
7					$k_1\frac{F_x^2 - F_y^2}{G\psi^2}$
8					$k_1\frac{F_xF_y}{G\psi^2}$

Table I - Where F_α are the total forces which can include, depending on the case being simulated, fluid-fluid interactions, fluid-solid interactions and external forces (e.g. gravity) and $\lvert\boldsymbol{F}\rvert^2 = \left(F_x^{int\,2} + F_y^{int\,2}\right)$ (F_α^{int} stands for intermolecular, i.e. fluid-fluid interactions).

References

[1] G. R. McNamara and G. Zanetti, "Use of the Boltzmann Equation to Simulate Lattice-Gas Automata," *Physical Review Letters,* vol. 61, no. 20, pp. 2332-2335, 11/14/ 1988.

[2] H. E. Van Den Akker, "Lattice Boltzmann simulations for multi-scale chemical engineering," *Current Opinion in Chemical Engineering,* vol. 21, pp. 67-75, 2018, doi: 10.1016/j.coche.2018.03.003.

[3] S. M. M. Salem, "Experimental Studies of Sub-Atmospheric Pressure Boiling of Water on Various Tubes and Plates," PhD, Institute of Mechanical, Process and Energy Engineering, Heriot-Watt University, Edinburgh, 2019.

[4] Boltzmann, *Lectures on gas theory / by L. Boltzmann*. 1964.

[5] Q. Li and K. H. Luo, "Thermodynamic consistency of the pseudopotential lattice Boltzmann model for simulating liquid–vapor flows," *Applied Thermal Engineering,* vol. 72, no. 1, pp. 56-61, 2014/11/05/ 2014, doi: https://doi.org/10.1016/j.applthermaleng.2014.03.030.

[6] E. S. Kikkinides, A. G. Yiotis, M. E. Kainourgiakis, and A. K. Stubos, "Thermodynamic consistency of liquid-gas lattice Boltzmann methods: Interfacial property issues," *Physical Review E,* vol. 78, no. 3, p. 036702, 09/08/ 2008, doi: 10.1103/PhysRevE.78.036702.

[7] C. K. Law, "Recent advances in droplet vaporization and combustion," *Progress in Energy and Combustion Science,* vol. 8, no. 3, pp. 171-201, 1982, doi: 10.1016/0360-1285(82)90011-9.

[8] Q. Li, Q. J. Kang, M. M. Francois, and A. J. Hu, "Lattice Boltzmann modeling of self-propelled Leidenfrost droplets on ratchet surfaces," *Soft Matter,* vol. 12, no. 1, pp. 302-312, 2015, doi: 10.1039/c5sm01353d.

[9] S. Succi, *The lattice Boltzmann equation for fluid dynamics and beyond / by Sauro Succi*. Oxford: Oxford: OUP, 2013.

[10] B. E. Rapp, "Chapter 9 - Fluids," in *Microfluidics: Modelling, Mechanics and Mathematics*, B. E. Rapp Ed. Oxford: Elsevier, 2017, pp. 243-263.

[11] S. G. Kandlikar and M. R. King, "Chapter 1 - Introduction," in *Heat Transfer and Fluid Flow in Minichannels and Microchannels (Second Edition)*, S. G. Kandlikar, S. Garimella, D. Li, S. Colin, and M. R. King Eds. Oxford: Butterworth-Heinemann, 2014, pp. 1-9.

[12] T. Kruger, *The lattice Boltzmann method : principles and practice / Timm Krüger and others*. Switzerland: Switzerland : Springer, 2017.

[13] a. P M Adler and H. Brenner, "Multiphase Flow in Porous Media," *Annual Review of Fluid Mechanics,* vol. 20, no. 1, pp. 35-59, 1988, doi: doi:10.1146/annurev.fl.20.010188.000343.

[14] S. Hassine, M. Dymitrowska, V. Pot, and A. Genty, "Gas Migration in Highly Water-Saturated Opalinus Clay Microfractures Using a Two-Phase TRT LBM," *Transport in Porous Media,* vol. 116, no. 3, pp. 975-1003, 2017, doi: 10.1007/s11242-016-0809-5.

[15] a. S P Sutera and R. Skalak, "The History of Poiseuille's Law," *Annual Review of Fluid Mechanics,* vol. 25, no. 1, pp. 1-20, 1993, doi: 10.1146/annurev.fl.25.010193.000245.

[16] H. Darabi, A. Ettehad, F. Javadpour, and K. Sepehrnoori, "Gas flow in ultra-tight shale strata," *Journal of Fluid Mechanics,* vol. 710, pp. 641-658, 2012, doi: 10.1017/jfm.2012.424.

[17] M. Wörner, "Numerical modeling of multiphase flows in microfluidics and micro process engineering: a review of methods and applications," *Microfluidics and Nanofluidics,* vol. 12, no. 6, pp. 841-886, 2012, doi: 10.1007/s10404-012-0940-8.

[18] C. Pozrikidis, *Fluid Dynamics Theory, Computation, and Numerical Simulation / by Constantine Pozrikidis*, 2nd ed. ed. Boston, MA: New York, NY : Springer US : Imprint: Springer, 2009.

[19] P. K. Unnikrishnan, V. Vaikuntanathan, and D. Sivakumar, "Impact dynamics of high Weber number drops on chemically modified metallic surfaces," *Colloids and Surfaces*

A: Physicochemical and Engineering Aspects, vol. 459, pp. 109-119, 2014, doi: 10.1016/j.colsurfa.2014.06.027.

[20] A. Montessori, P. Prestininzi, M. La Rocca, and S. Succi, "Entropic lattice pseudo-potentials for multiphase flow simulations at high Weber and Reynolds numbers," *Physics of Fluids,* vol. 29, no. 9, p. <xocs:firstpage xmlns:xocs=""/>, 2017, doi: 10.1063/1.5001253.

[21] N. I. Kolev, *Multiphase flow dynamics 2 mechanical interactions / Nikolay Ivanov Kolev*, [4th ed.]. ed. Berlin, Heidelberg: Berlin : Springer, 2011.

[22] J. Campbell, "Chapter 2 - Entrainment," in *Complete Casting Handbook (Second Edition)*, J. Campbell Ed. Boston: Butterworth-Heinemann, 2015, pp. 17-90.

[23] R. Lenormand, E. Touboul, and C. Zarcone, "Numerical models and experiments on immiscible displacements in porous media," *Journal of Fluid Mechanics,* vol. 189, pp. 165-187, 2006, doi: 10.1017/S0022112088000953.

[24] B. Berkowitz and R. P. Ewing, "Percolation Theory and Network Modeling Applications in Soil Physics," *Surveys in Geophysics,* journal article vol. 19, no. 1, pp. 23-72, 1998, doi: 10.1023/a:1006590500229.

[25] M. C. Sukop and D. T. Thorne, *Lattice boltzmann modeling: An introduction for geoscientists and engineers*. 2006, pp. 1-174.

[26] Q. Li, K. H. Luo, Q. J. Kang, Y. L. He, Q. Chen, and Q. Liu, "Lattice Boltzmann methods for multiphase flow and phase-change heat transfer," *Progress in Energy and Combustion Science,* vol. 52, pp. 62-105, 2016, doi: 10.1016/j.pecs.2015.10.001.

[27] T. Sobota, "Fourier's Law of Heat Conduction," in *Encyclopedia of Thermal Stresses*, R. B. Hetnarski Ed. Dordrecht: Springer Netherlands, 2014, pp. 1769-1778.

[28] I. M. Mahbubul, "4 - Thermophysical Properties of Nanofluids," in *Preparation, Characterization, Properties and Application of Nanofluid*, I. M. Mahbubul Ed.: William Andrew Publishing, 2019, pp. 113-196.

[29] Bird, *Transport phenomena / by R. Byron Bird and others*. Wiley, 1960.

[30] H. Dong, J. He, C. Duan, and Y. Zhao, "A Self-Consistent Physical Model of the Bubbles in a Gas Solid Two-Phase Flow," (in English), *Applied Sciences,* vol. 8, no. 3, Mar 2018

2019-11-13 2018, doi: http://dx.doi.org/10.3390/app8030360.

[31] J. M. Coulson, *Coulson & Richardson's chemical engineering / J.M. Coulson and J.F. Richardson with J.R. Backhurst and J.H. Harker* (Coulson and Richardson's chemical engineering). Oxford, Boston : Butterworth-Heinemann, 1996.

[32] T. L. Bergman, *Incropera's principles of heat and mass transfer / Theodore L. Bergman, Adrienne S. Lavine*, Global [8th] ed. ed. Hoboken, N.J.: Hoboken, N.J. : Wiley, 2017.

[33] R. Chen, M.-C. Lu, V. Srinivasan, Z. Wang, H. H. Cho, and A. Majumdar, "Nanowires for Enhanced Boiling Heat Transfer," *Nano Letters,* vol. 9, no. 2, pp. 548-553, 2009/02/11 2009, doi: 10.1021/nl8026857.

[34] M. Arik, A. KoŞar, H. Bostanci, and A. Bar-Cohen, "Pool Boiling Critical Heat Flux in Dielectric Liquids and Nanofluids," in *Advances in Heat Transfer*, vol. 43, Y. I. Cho and G. A. Greene Eds.: Elsevier, 2011, pp. 1-76.

[35] Y. Koizumi, "Chapter 1 - Outline of Boiling Phenomena and Heat Transfer Characteristics," in *Boiling*, Y. Koizumi, M. Shoji, M. Monde, Y. Takata, and N. Nagai Eds. Boston: Elsevier, 2017, pp. 1-11.

[36] D. Bonn, J. Eggers, J. Indekeu, J. Meunier, and E. Rolley, "Wetting and spreading," *Reviews of Modern Physics,* vol. 81, no. 2, pp. 739-805, 05/27/ 2009, doi: 10.1103/RevModPhys.81.739.

[37] M. Worner, "Numerical modeling of multiphase flows in microfluidics and micro process engineering: A review of methods and applications," *Microfluidics and Nanofluidics,* vol. 12, no. 6, pp. 841-886, 2012, doi: 10.1007/s10404-012-0940-8.

[38] B. J. Alder and T. E. Wainwright, "Studies in Molecular Dynamics. I. General Method," *The Journal of Chemical Physics,* vol. 31, no. 2, pp. 459-466, 1959, doi: 10.1063/1.1730376.

[39] G. A. Bird, "Approach to Translational Equilibrium in a Rigid Sphere Gas," *The Physics of Fluids,* vol. 6, no. 10, pp. 1518-1519, 1963, doi: 10.1063/1.1710976.
[40] H. Liu *et al.*, "Multiphase lattice Boltzmann simulations for porous media applications," *Computational Geosciences,* vol. 20, no. 4, pp. 777-805, 2016, doi: 10.1007/s10596-015-9542-3.
[41] R. R. Nourgaliev, T. N. Dinh, T. G. Theofanous, and D. Joseph, "The lattice Boltzmann equation method: Theoretical interpretation, numerics and implications," *International Journal of Multiphase Flow,* vol. 29, no. 1, pp. 117-169, 2003, doi: 10.1016/S0301-9322(02)00108-8.
[42] O. Dardis and J. McCloskey, "Lattice Boltzmann scheme with real numbered solid density for the simulation of flow in porous media," *Physical Review E. Statistical Physics, Plasmas, Fluids, and Related Interdisciplinary Topics,* vol. 57, no. 4, pp. 4834-4834, 1998, doi: 10.1103/PhysRevE.57.4834.
[43] W. F. Noh and P. Woodward, "SLIC (Simple Line Interface Calculation)," in *Proceedings of the Fifth International Conference on Numerical Methods in Fluid Dynamics June 28 – July 2, 1976 Twente University, Enschede*, A. I. van de Vooren and P. J. Zandbergen Eds. Berlin, Heidelberg: Springer Berlin Heidelberg, 1976, pp. 330-340.
[44] S. Osher and J. A. Sethian, "Fronts propagating with curvature dependent speed: Algorithms based on Hamilton-Jacobi formulations - NASA-CR-178382," ed: Sponsoring Organization: NASA Langley Research Center, 1987.
[45] *Computational methods for multiphase flow / by Andrea Prosperetti and Gretar Tryggvason*. CUP, 2009.
[46] C. W. Hirt and B. D. Nichols, "Volume of fluid (VOF) method for the dynamics of free boundaries," *Journal of Computational Physics,* vol. 39, no. 1, pp. 201-225, 1981/01/01/ 1981, doi: https://doi.org/10.1016/0021-9991(81)90145-5.
[47] *Numerical heat transfer and fluid flow / by Suhas V. Patankar*. Hemisphere, 1980.
[48] O. Wilhelmsen *et al.*, "Thermodynamic Modeling with Equations of State: Present Challenges with Established Methods," *Industrial & Engineering Chemistry Research,* vol. 56, no. 13, pp. 3503-3515, 2017, doi: 10.1021/acs.iecr.7b00317.
[49] N. F. Carnahan and K. E. Starling, "Equation of State for Nonattracting Rigid Spheres," *The Journal of Chemical Physics,* vol. 51, no. 2, pp. 635-636, 1969, doi: 10.1063/1.1672048.
[50] D.-Y. Peng and D. B. Robinson, "A New Two-Constant Equation of State," *Industrial & Engineering Chemistry Fundamentals,* vol. 15, no. 1, pp. 59-64, 1976/02/01 1976, doi: 10.1021/i160057a011.
[51] G. Soave, "Equilibrium constants from a modified Redlich-Kwong equation of state," *Chemical Engineering Science,* vol. 27, no. 6, pp. 1197-1203, 1972/06/01/ 1972, doi: https://doi.org/10.1016/0009-2509(72)80096-4.
[52] B. I. Lee and M. G. Kesler, "A generalized thermodynamic correlation based on three-parameter corresponding states," *AIChE Journal,* vol. 21, no. 3, pp. 510-527, 1975, doi: 10.1002/aic.690210313.
[53] J. F. Ely and I. M. F. Marrucho, "8 The corresponding-states principle," in *Experimental Thermodynamics*, vol. 5, J. V. Sengers, R. F. Kayser, C. J. Peters, and H. J. White Eds.: Elsevier, 2000, pp. 289-320.
[54] W. G. Chapman, K. E. Gubbins, G. Jackson, and M. Radosz, "SAFT: Equation-of-state solution model for associating fluids," *Fluid Phase Equilibria,* vol. 52, pp. 31-38, 1989/12/01/ 1989, doi: https://doi.org/10.1016/0378-3812(89)80308-5.
[55] O. Kunz and W. Wagner, "The GERG-2008 Wide-Range Equation of State for Natural Gases and Other Mixtures: An Expansion of GERG-2004," *Journal of Chemical & Engineering Data,* vol. 57, no. 11, pp. 3032-3091, 2012/11/08 2012, doi: 10.1021/je300655b.
[56] P. Aursand, M. A. Gjennestad, E. Aursand, M. Hammer, and Ø. Wilhelmsen, "The spinodal of single- and multi-component fluids and its role in the development of

modern equations of state," *Fluid Phase Equilibria,* vol. 436, no. C, pp. 98-112, 2017, doi: 10.1016/j.fluid.2016.12.018.
[57] Y. Saito, "Pseudocritical Phenomena near the Spinodal Point," *Progress of Theoretical Physics,* vol. 59, no. 2, pp. 375-385, 1978.
[58] Y. T. Feng, K. Han, and D. R. J. Owen, "Coupled lattice Boltzmann method and discrete element modelling of particle transport in turbulent fluid flows: Computational issues," *International Journal for Numerical Methods in Engineering,* vol. 72, no. 9, pp. 1111-1134, 2007, doi: 10.1002/nme.2114.
[59] Chapman, *Mathematical theory of non-uniform gases an account of the kinetic theory of viscosity, thermal conduction and diffusion in gases / by S. Chapman and T.G. Cowling*, 2nd ed. ed. 1960.
[60] J. D. Logan, *Applied mathematics / J. David Logan*, 4th ed. ed. Hoboken, N.J.: Wiley, 2013.
[61] C. Pan, L.-S. Luo, and C. T. Miller, "An evaluation of lattice Boltzmann schemes for porous medium flow simulation," *Computers and Fluids,* vol. 35, no. 8, pp. 898-909, 2006, doi: 10.1016/j.compfluid.2005.03.008.
[62] F. J. Higuera and J. Jiménez, "Boltzmann Approach to Lattice Gas Simulations," *EPL (Europhysics Letters),* vol. 9, no. 7, p. 663, 1989.
[63] D. d'Humieres, "Generalized lattice-boltzmann equations," vol. 159, (Progress in Astronautics and Aeronautics: AIAA, 1994, pp. 450-450.
[64] P. L. Bhatnagar, E. P. Gross, and M. Krook, "A Model for Collision Processes in Gases. I. Small Amplitude Processes in Charged and Neutral One-Component Systems," *Physical Review,* vol. 94, no. 3, pp. 511-525, 05/01/ 1954.
[65] J. M. V. A. Koelman, "A Simple Lattice Boltzmann Scheme for Navier-Stokes Fluid Flow," *EPL (Europhysics Letters),* vol. 15, no. 6, p. 603, 1991.
[66] Y. H. Qian, D. D. Humières, and P. Lallemand, "Lattice BGK Models for Navier-Stokes Equation," *EPL (Europhysics Letters),* vol. 17, no. 6, p. 479, 1992.
[67] X. He and L.-S. Luo, "A priori derivation of the lattice Boltzmann equation," *Phys. Rev. E,* vol. 55, no. 6, pp. R6333-R6336, 06/01/ 1997.
[68] X. He and L.-S. Luo, "Theory of the lattice Boltzmann method: From the Boltzmann equation to the lattice Boltzmann equation," *Phys. Rev. E,* vol. 56, no. 6, pp. 6811-6817, 12/01/ 1997.
[69] L.-S. Luo and S. S. Girimaji, "Theory of the lattice Boltzmann method: Two-fluid model for binary mixtures," *Physical Review E - Statistical, Nonlinear, and Soft Matter Physics,* vol. 67, no. 3 2, pp. 036302/1-036302/11, 2003, doi: 10.1103/PhysRevE.67.036302.
[70] P. Lallemand and L.-S. Luo, "Theory of the lattice Boltzmann method: Dispersion, dissipation, isotropy, Galilean invariance, and stability," *Phys. Rev. E,* vol. 61, no. 6, pp. 6546-6562, 06/01/ 2000.
[71] D. D'Humieres, M. Bouzidi, and P. Lallemand, "Thirteen-velocity three-dimensional lattice Boltzmann model," *Physical Review E - Statistical, Nonlinear, and Soft Matter Physics,* vol. 63, no. 6 II, pp. 066702/1-066702/7, 2001, doi: 10.1103/PhysRevE.63.066702.
[72] D. D'Humières, I. Ginzburg, M. Krafczyk, P. Lallemand, and L.-S. Luo, "Multiple-Relaxation-Time Lattice Boltzmann Models in Three Dimensions," *Philosophical Transactions: Mathematical, Physical and Engineering Sciences,* vol. 360, no. 1792, pp. 437-451, 2002.
[73] A. A. Mohamad, *Lattice Boltzmann Method*. Dordrecht: Dordrecht : Springer, 2011.
[74] Q. Li, K. H. Luo, X. J. Luo, and X. J. Li, "Lattice Boltzmann modeling of multiphase flows at large density ratio with an improved pseudopotential model," *Physical Review E - Statistical, Nonlinear, and Soft Matter Physics,* vol. 87, no. 5, 2013, doi: 10.1103/PhysRevE.87.053301.

[75] S. Khirevich, I. Ginzburg, and U. Tallarek, "Coarse- and fine-grid numerical behavior of MRT/TRT lattice-Boltzmann schemes in regular and random sphere packings," *Journal of Computational Physics,* vol. 281, pp. 708-742, 2015, doi: 10.1016/j.jcp.2014.10.038.

[76] M. E. McCracken and J. Abraham, "Multiple-relaxation-time lattice-Boltzmann model for multiphase flow," *Physical Review E - Statistical, Nonlinear, and Soft Matter Physics,* vol. 71, no. 3, 2005, doi: 10.1103/PhysRevE.71.036701.

[77] D. d'Humières and I. Ginzburg, "Viscosity independent numerical errors for Lattice Boltzmann models: From recurrence equations to "magic" collision numbers," *Computers & Mathematics with Applications,* vol. 58, no. 5, pp. 823-840, 9// 2009, doi: http://dx.doi.org/10.1016/j.camwa.2009.02.008.

[78] X.-D. Niu, T. Munekata, S.-A. Hyodo, and K. Suga, "An investigation of water-gas transport processes in the gas-diffusion-layer of a PEM fuel cell by a multiphase multiple-relaxation-time lattice Boltzmann model," *Journal of Power Sources,* vol. 172, no. 2, pp. 542-552, 10/25/ 2007, doi: http://dx.doi.org/10.1016/j.jpowsour.2007.05.081.

[79] E. Fattahi, C. Waluga, B. Wohlmuth, U. Rüde, M. Manhart, and R. Helmig, "Lattice Boltzmann methods in porous media simulations: From laminar to turbulent flow," *Computers and Fluids,* vol. 140, pp. 247-259, 2016, doi: 10.1016/j.compfluid.2016.10.007.

[80] H. Li, C. Pan, and C. T. Miller, "Pore-scale investigation of viscous coupling effects for two-phase flow in porous media," *Physical Review E - Statistical, Nonlinear, and Soft Matter Physics,* vol. 72, no. 2, 2005, doi: 10.1103/PhysRevE.72.026705.

[81] D. Yu, R. Mei, L.-S. Luo, and W. Shyy, "Viscous flow computations with the method of lattice Boltzmann equation," *Progress in Aerospace Sciences,* vol. 39, no. 5, pp. 329-367, 7// 2003, doi: http://dx.doi.org/10.1016/S0376-0421(03)00003-4.

[82] P. J. Dellar, "Bulk and shear viscosities in lattice Boltzmann equations," *Physical Review E - Statistical, Nonlinear, and Soft Matter Physics,* vol. 64, no. 3 I, pp. 312031-3120311, 2001, doi: 10.1103/PhysRevE.64.031203.

[83] D. Lycett-Brown and K. H. Luo, "Multiphase cascaded lattice Boltzmann method," *Computers and Mathematics with Applications,* vol. 67, no. 2, pp. 350-362, 2014, doi: 10.1016/j.camwa.2013.08.033.

[84] X. Shan and H. Chen, "Lattice Boltzmann model for simulating flows with multiple phases and components," *Physical Review E. Statistical Physics, Plasmas, Fluids, and Related Interdisciplinary Topics,* vol. 47, no. 3, pp. 1815-1815, 1993, doi: 10.1103/PhysRevE.47.1815.

[85] X. W. Shan and H. D. Chen, "SIMULATION OF NONIDEAL GASES AND LIQUID-GAS PHASE-TRANSITIONS BY THE LATTICE BOLTZMANN-EQUATION," (in English), *Physical Review E,* Article vol. 49, no. 4, pp. 2941-2948, Apr 1994, doi: 10.1103/PhysRevE.49.2941.

[86] H. Huang, M. C. Sukop, and X.-Y. Lu, "Introduction," in *Multiphase Lattice Boltzmann Methods: Theory and Application*: John Wiley & Sons, Ltd, 2015, pp. 1-17.

[87] L. Chen, Q. Kang, Y. Mu, Y.-L. He, and W.-Q. Tao, "A critical review of the pseudopotential multiphase lattice Boltzmann model: Methods and applications," *International Journal of Heat and Mass Transfer,* vol. 76, pp. 210-236, 2014, doi: 10.1016/j.ijheatmasstransfer.2014.04.032.

[88] K. Yang and Z. Guo, "Multiple-relaxation-time lattice Boltzmann model for binary mixtures of nonideal fluids based on the Enskog kinetic theory," *Science Bulletin,* vol. 60, no. 6, pp. 634-647, 2015, doi: 10.1007/s11434-015-0752-9.

[89] Swift, Osborn, and Yeomans, "Lattice Boltzmann simulation of nonideal fluids," *Physical review letters,* vol. 75, no. 5, p. 830, 1995, doi: 10.1103/PhysRevLett.75.830.

[90] M. R. Swift, E. Orlandini, W. R. Osborn, and J. M. Yeomans, "Lattice Boltzmann simulations of liquid-gas and binary fluid systems," *Physical Review E,* vol. 54, no. 5, pp. 5041-5052, 11/01/ 1996.

[91] J. Bao and L. Schaefer, "Lattice Boltzmann equation model for multi-component multi-phase flow with high density ratios," *Applied Mathematical Modelling,* vol. 37, no. 4, pp. 1860-1871, 2013, doi: 10.1016/j.apm.2012.04.048.

[92] H. Otomo *et al.*, "Studies of accurate multi-component lattice Boltzmann models on benchmark cases required for engineering applications," *Journal of Computational Science,* vol. 17, pp. 334-339, 2016/11/01/ 2016, doi: https://doi.org/10.1016/j.jocs.2016.05.001.

[93] J. Yang and E. Boek, *Computers & Mathematics with Applications,* vol. 65, no. 6, 2013, doi: 10.1016/j.camwa.2012.11.022.

[94] M. R. Kamali and H. E. A. Van Den Akker, "Simulating gas-liquid flows by means of a pseudopotential lattice boltzmann method," *Industrial and Engineering Chemistry Research,* vol. 52, no. 33, pp. 11365-11377, 2013, doi: 10.1021/ie303356u.

[95] L. Chen, Q. Kang, Q. Tang, B. A. Robinson, Y.-L. He, and W.-Q. Tao, "Pore-scale simulation of multicomponent multiphase reactive transport with dissolution and precipitation," *International Journal of Heat and Mass Transfer,* vol. 85, pp. 935-949, 2015, doi: 10.1016/j.ijheatmasstransfer.2015.02.035.

[96] M. R. Kamali, S. Sundaresan, H. E. A. Van den Akker, and J. J. J. Gillissen, "A multi-component two-phase lattice Boltzmann method applied to a 1-D Fischer-Tropsch reactor," *Chemical Engineering Journal,* vol. 207-208, pp. 587-595, 2012, doi: 10.1016/j.cej.2012.07.019.

[97] M. Sega, M. Sbragaglia, S. S. Kantorovich, and A. O. Ivanov, "Mesoscale structures at complex fluidfluid interfaces: a novel lattice Boltzmann/molecular dynamics coupling," *Soft Matter,* vol. 9, no. 42, pp. 10092-10107, 2013, doi: 10.1039/c3sm51556g.

[98] Gunstensen, Rothman, Zaleski, and Zanetti, "Lattice Boltzmann model of immiscible fluids," *Physical review. A, Atomic, molecular, and optical physics,* vol. 43, no. 8, p. 4320, 1991, doi: 10.1103/PhysRevA.43.4320.

[99] E. G. Flekkøy and H. J. Herrmann, "Lattice Boltzmann models for complex fluids," *Physica A: Statistical Mechanics and its Applications,* vol. 199, no. 1, pp. 1-11, 1993/10/01/ 1993, doi: https://doi.org/10.1016/0378-4371(93)90091-H.

[100] S. Leclaire, A. Parmigiani, O. Malaspinas, B. Chopard, and J. Latt, "Generalized three-dimensional lattice Boltzmann color-gradient method for immiscible two-phase pore-scale imbibition and drainage in porous media," *Physical Review E,* vol. 95, no. 3, p. 033306, 03/14/ 2017, doi: 10.1103/PhysRevE.95.033306.

[101] D. Lycett-Brown and K. H. Luo, "Improved forcing scheme in pseudopotential lattice Boltzmann methods for multiphase flow at arbitrarily high density ratios," *Physical Review E - Statistical, Nonlinear, and Soft Matter Physics,* vol. 91, no. 2, p. <xocs:firstpage xmlns:xocs=""/>, 2015, doi: 10.1103/PhysRevE.91.023305.

[102] G. Falcucci, S. Ubertini, D. Chiappini, and S. Succi, "Modern lattice Boltzmann methods for multiphase microflows," *IMA Journal of Applied Mathematics,* vol. 76, no. 5, pp. 712-725, 2011, doi: 10.1093/imamat/hxr014.

[103] Z. Yu and L.-S. Fan, "Multirelaxation-time interaction-potential-based lattice Boltzmann model for two-phase flow," *Physical Review E - Statistical, Nonlinear, and Soft Matter Physics,* vol. 82, no. 4, 2010, doi: 10.1103/PhysRevE.82.046708.

[104] A. Kuzmin and A. A. Mohamad, "Multirange multi-relaxation time Shan–Chen model with extended equilibrium," *Computers and Mathematics with Applications,* vol. 59, no. 7, pp. 2260-2270, 2010, doi: 10.1016/j.camwa.2009.08.042.

[105] M. Sbragaglia, R. Benzi, L. Biferale, S. Succi, K. Sugiyama, and F. Toschi, "Generalized lattice Boltzmann method with multirange pseudopotential," *Physical Review E - Statistical, Nonlinear, and Soft Matter Physics,* vol. 75, no. 2, 2007, doi: 10.1103/PhysRevE.75.026702.

[106] S. Chibbaro, G. Falcucci, G. Chiatti, H. Chen, X. Shan, and S. Succi, "Lattice Boltzmann models for nonideal fluids with arrested phase-separation," *Physical Review E,* vol. 77, no. 3, p. 036705, 03/20/ 2008.

[107] S. Khajepor, J. Wen, and B. Chen, "Multipseudopotential interaction: A solution for thermodynamic inconsistency in pseudopotential lattice Boltzmann models," *Physical Review E - Statistical, Nonlinear, and Soft Matter Physics,* vol. 91, no. 2, 2015, doi: 10.1103/PhysRevE.91.023301.

[108] S. Khajepor and B. Chen, "Multipseudopotential interaction:A consistent study of cubic equations of state in lattice Boltzmann models," 2016.

[109] L. Hao and P. Cheng, "Pore-scale simulations on relative permeabilities of porous media by lattice Boltzmann method," *International Journal of Heat and Mass Transfer,* vol. 53, no. 9–10, pp. 1908-1913, 4// 2010, doi: http://dx.doi.org/10.1016/j.ijheatmasstransfer.2009.12.066.

[110] C. M. Pooley, H. Kusumaatmaja, and J. M. Yeomans, "Contact line dynamics in binary lattice Boltzmann simulations," *Physical Review E - Statistical, Nonlinear, and Soft Matter Physics,* vol. 78, no. 5, 2008, doi: 10.1103/PhysRevE.78.056709.

[111] X. He, S. Chen, and R. Zhang, "A Lattice Boltzmann Scheme for Incompressible Multiphase Flow and Its Application in Simulation of Rayleigh–Taylor Instability," *Journal of Computational Physics,* vol. 152, no. 2, pp. 642-663, 1999/07/01/ 1999, doi: https://doi.org/10.1006/jcph.1999.6257.

[112] X. He, S. Chen, and R. Zhang, "A lattice Boltzmann scheme for incompressible multiphase flow and its application in simulation of Rayleigh-Taylor instability," *Journal of Computational Physics,* vol. 152, no. 2, 1999, doi: 10.1006/jcph.1999.6257.

[113] A. Mazloomi M, S. S. Chikatamarla, and I. V. Karlin, "Entropic Lattice Boltzmann Method for Multiphase Flows," *Physical Review Letters,* vol. 114, no. 17, p. 174502, 05/01/ 2015.

[114] N. Frapolli, S. S. Chikatamarla, and I. V. Karlin, "Entropic lattice Boltzmann model for gas dynamics: Theory, boundary conditions, and implementation," *Physical Review E,* vol. 93, no. 6, p. 063302, 06/07/ 2016, doi: 10.1103/PhysRevE.93.063302.

[115] F. Qin, A. M. Moqaddam, Q. Kang, D. Derome, and J. Carmeliet, "Entropic multiple-relaxation-time multirange pseudopotential lattice Boltzmann model for two-phase flow," *Physics of Fluids,* vol. 30, no. 3, p. 032104, 2018, doi: 10.1063/1.5016965.

[116] F. Chen, A. Xu, G. Zhang, Y. Li, and S. Succi, "Multiple-relaxation-time lattice Boltzmann approach to compressible flows with flexible specific-heat ratio and Prandtl number," *EPL (Europhysics Letters),* vol. 90, no. 5, p. 54003, 2010/06/01 2010, doi: 10.1209/0295-5075/90/54003.

[117] X. Shan, "Simulation of Rayleigh-B\'enard convection using a lattice Boltzmann method," *Physical Review E,* vol. 55, no. 3, pp. 2780-2788, 03/01/ 1997, doi: 10.1103/PhysRevE.55.2780.

[118] P. LALLEMAND and L.-S. LUO, "HYBRID FINITE-DIFFERENCE THERMAL LATTICE BOLTZMANN EQUATION," *International Journal of Modern Physics B,* vol. 17, no. 01n02, pp. 41-47, 2003, doi: 10.1142/s0217979203017060.

[119] X. He, S. Chen, and G. D. Doolen, "A Novel Thermal Model for the Lattice Boltzmann Method in Incompressible Limit," *Journal of Computational Physics,* vol. 146, no. 1, pp. 282-300, 1998, doi: 10.1006/jcph.1998.6057.

[120] Z. Guo, C. Zheng, B. Shi, and T. S. Zhao, "Thermal lattice Boltzmann equation for low Mach number flows: Decoupling model," *Physical Review E,* vol. 75, no. 3, p. 036704, 03/14/ 2007, doi: 10.1103/PhysRevE.75.036704.

[121] O. Filippova and D. Hänel, "A Novel Lattice BGK Approach for Low Mach Number Combustion," *Journal of Computational Physics,* vol. 158, no. 2, pp. 139-160, 2000/03/01/ 2000, doi: https://doi.org/10.1006/jcph.1999.6405.

[122] Q. Li, Q. J. Kang, M. M. Francois, Y. L. He, and K. H. Luo, "Lattice Boltzmann modeling of boiling heat transfer: The boiling curve and the effects of wettability," *International Journal of Heat and Mass Transfer,* vol. 85, pp. 787-796, 2015/06/01/ 2015, doi: https://doi.org/10.1016/j.ijheatmasstransfer.2015.01.136.

[123] Q. Li, P. Zhou, and H. J. Yan, "Improved thermal lattice Boltzmann model for simulation of liquid-vapor phase change," *Physical Review E,* vol. 96, no. 6, p. 063303, 12/04/ 2017, doi: 10.1103/PhysRevE.96.063303.
[124] S. Gong and P. Cheng, "A lattice Boltzmann method for simulation of liquid–vapor phase-change heat transfer," *International Journal of Heat and Mass Transfer,* vol. 55, no. 17-18, pp. 4923-4927, 2012, doi: 10.1016/j.ijheatmasstransfer.2012.04.037.
[125] Q. Li, J. Y. Huang, and Q. J. Kang, "On the temperature equation in a phase change pseudopotential lattice Boltzmann model," *International Journal of Heat and Mass Transfer,* vol. 127, no. Part B, pp. 1112-1113, 2018, doi: 10.1016/j.ijheatmasstransfer.2018.07.139.
[126] W. Gong, Y. Y. Yan, S. Chen, and E. Wright, "A modified phase change pseudopotential lattice Boltzmann model," *International Journal of Heat and Mass Transfer,* vol. 125, pp. 323-329, 2018, doi: 10.1016/j.ijheatmasstransfer.2018.04.090.
[127] A. Hu, R. Uddin, and D. Liu, "Discrete methods of the energy equations in the pseudo-potential lattice Boltzmann model based simulations," *Computers & Fluids,* vol. 179, pp. 645-654, 2019/01/30/ 2019, doi: https://doi.org/10.1016/j.compfluid.2018.12.005.
[128] G. Hazi and A. Markus, "On the bubble departure diameter and release frequency based on numerical simulation results," *International Journal of Heat and Mass Transfer,* vol. 52, no. 5, pp. 1472-1480, 2009/02/01/ 2009, doi: https://doi.org/10.1016/j.ijheatmasstransfer.2008.09.003.
[129] Y. Peng, C. Shu, and Y. Chew, "Simplified thermal lattice Boltzmann model for incompressible thermal flows," *Physical Review E,* vol. 68, no. 2, 2003, doi: 10.1103/PhysRevE.68.026701.
[130] R. Zhang and H. Chen, "Lattice Boltzmann method for simulations of liquid-vapor thermal flows," *Physical Review E,* vol. 67, no. 6, p. 066711, 06/27/ 2003, doi: 10.1103/PhysRevE.67.066711.
[131] C. E. Colosqui, G. Falcucci, S. Ubertini, and S. Succi, "Mesoscopic simulation of non-ideal fluids with self-tuning of the equation of state," *Soft Matter,* 10.1039/C2SM06353K vol. 8, no. 14, pp. 3798-3809, 2012, doi: 10.1039/C2SM06353K.
[132] A. Hu and D. Liu, "A superheat degree driven liquid-vapor phase-change lattice Boltzmann model," *International Journal of Heat and Mass Transfer,* vol. 136, pp. 674-680, 2019/06/01/ 2019, doi: https://doi.org/10.1016/j.ijheatmasstransfer.2019.03.050.
[133] A. Márkus and G. Házi, "Simulation of evaporation by an extension of the pseudopotential lattice Boltzmann method: A quantitative analysis," *Physical Review E,* vol. 83, no. 4, p. 046705, 04/07/ 2011, doi: 10.1103/PhysRevE.83.046705.
[134] A. Márkus and G. Házi, "On pool boiling at microscale level: The effect of a cavity and heat conduction in the heated wall," *Nuclear Engineering and Design,* vol. 248, pp. 238-247, 2012/07/01/ 2012, doi: https://doi.org/10.1016/j.nucengdes.2012.03.027.
[135] M. R. Kamali, J. J. J. Gillissen, H. E. A. van den Akker, and S. Sundaresan, "Lattice-Boltzmann-based two-phase thermal model for simulating phase change," *Physical Review E,* vol. 88, no. 3, p. 033302, 09/13/ 2013, doi: 10.1103/PhysRevE.88.033302.
[136] S. Gong and P. Cheng, "Numerical simulation of pool boiling heat transfer on smooth surfaces with mixed wettability by lattice Boltzmann method," *International Journal of Heat and Mass Transfer,* vol. 80, pp. 206-216, 2015/01/01/ 2015, doi: https://doi.org/10.1016/j.ijheatmasstransfer.2014.08.092.
[137] H. Safari, M. H. Rahimian, and M. Krafczyk, "Extended lattice Boltzmann method for numerical simulation of thermal phase change in two-phase fluid flow," *Physical Review E,* vol. 88, no. 1, p. 013304, 07/08/ 2013, doi: 10.1103/PhysRevE.88.013304.
[138] D. Chatterjee, "An enthalpy-based thermal lattice Boltzmann model for non-isothermal systems," *EPL (Europhysics Letters),* vol. 86, no. 1, p. 14004, 2009/04 2009, doi: 10.1209/0295-5075/86/14004.

[139] A. Parmigiani, C. Huber, O. Bachmann, and B. Chopard, "Pore-scale mass and reactant transport in multiphase porous media flows," *Journal of Fluid Mechanics,* vol. 686, pp. 40-76, 2011, doi: 10.1017/jfm.2011.268.

[140] K. Luo, F.-J. Yao, H.-L. Yi, and H.-P. Tan, "Lattice Boltzmann simulation of convection melting in complex heat storage systems filled with phase change materials," *Applied Thermal Engineering,* vol. 86, pp. 238-250, 2015/07/05/ 2015, doi: https://doi.org/10.1016/j.applthermaleng.2015.04.059.

[141] A. Montessori, G. Falcucci, M. La Rocca, S. Ansumali, and S. Succi, "Three-Dimensional Lattice Pseudo-Potentials for Multiphase Flow Simulations at High Density Ratios," *Journal of Statistical Physics,* journal article vol. 161, no. 6, pp. 1404-1419, December 01 2015, doi: 10.1007/s10955-015-1318-6.

[142] S. Ammar, G. Pernaudat, and J.-Y. Trépanier, "A multiphase three-dimensional multi-relaxation time (MRT) lattice Boltzmann model with surface tension adjustment," *Journal of Computational Physics,* vol. 343, pp. 73-91, 2017/08/15/ 2017, doi: https://doi.org/10.1016/j.jcp.2017.04.045.

[143] P. Yuan and L. Schaefer, "Equations of state in a lattice Boltzmann model," *Physics of Fluids,* vol. 18, no. 4, 2006, doi: 10.1063/1.2187070.

[144] Z. Guo, C. Zheng, and B. Shi, "Discrete lattice effects on the forcing term in the lattice Boltzmann method," *Physical Review E,* vol. 65, no. 4, p. 046308, 04/10/ 2002.

[145] L. Zheng, Q. Zhai, and S. Zheng, "Analysis of force treatment in the pseudopotential lattice Boltzmann equation method," *Physical Review E,* vol. 95, no. 4, 2017, doi: 10.1103/PhysRevE.95.043301.

[146] A. J. C. Ladd and R. Verberg, "Lattice-Boltzmann Simulations of Particle-Fluid Suspensions," *Journal of Statistical Physics,* journal article vol. 104, no. 5, pp. 1191-1251, September 01 2001, doi: 10.1023/a:1010414013942.

[147] A. L. Kupershtokh, D. A. Medvedev, and D. I. Karpov, "On equations of state in a lattice Boltzmann method," *Computers & Mathematics with Applications,* vol. 58, no. 5, pp. 965-974, 9// 2009, doi: https://doi.org/10.1016/j.camwa.2009.02.024.

[148] R. Huang and H. Wu, "Third-order analysis of pseudopotential lattice Boltzmann model for multiphase flow," *Journal of Computational Physics,* vol. 327, pp. 121-139, 2016, doi: 10.1016/j.jcp.2016.09.030.

[149] Q. Li and Q. Luo, "Achieving tunable surface tension in the pseudopotential lattice Boltzmann modeling of multiphase flows," *Physical Review E - Statistical, Nonlinear, and Soft Matter Physics,* vol. 88, no. 5, 2013, doi: 10.1103/PhysRevE.88.053307.

[150] R. Huang, H. Wu, and N. A. Adams, "Eliminating cubic terms in the pseudopotential lattice Boltzmann model for multiphase flow," *Physical Review E,* vol. 97, no. 5, p. 053308, 05/22/ 2018, doi: 10.1103/PhysRevE.97.053308.

[151] X. Shan, "Pressure tensor calculation in a class of nonideal gas lattice Boltzmann models," *Physical review. E, Statistical, nonlinear, and soft matter physics,* vol. 77, no. 6 Pt 2, p. 066702, 2008, doi: 10.1103/PhysRevE.77.066702.

[152] M. L. Porter, E. T. Coon, Q. Kang, J. D. Moulton, and J. W. Carey, "Multicomponent interparticle-potential lattice Boltzmann model for fluids with large viscosity ratios," *Physical Review E,* vol. 86, no. 3, Sep 2012, Art no. 036701, doi: 10.1103/PhysRevE.86.036701.

[153] *Statistical mechanics / by K. Huang*, 2nd ed. ed. Wiley, 1987.

[154] H. Huang, M. Krafczyk, and X. Lu, "Forcing term in single-phase and Shan-Chen-type multiphase lattice Boltzmann models," *Physical Review E,* vol. 84, no. 4, p. 046710, 10/25/ 2011.

[155] Y. Wu, N. Gui, X. Yang, J. Tu, and S. Jiang, "Improved stability strategies for pseudo-potential models of lattice Boltzmann simulation of multiphase flow," *International Journal of Heat and Mass Transfer,* vol. 125, pp. 66-81, 2018, doi: 10.1016/j.ijheatmasstransfer.2018.04.021.

[156] Y. Wu, N. Gui, X. Yang, J. Tu, and S. Jiang, "Fourth-order analysis of force terms in multiphase pseudopotential lattice Boltzmann model," *Computers and Mathematics with Applications,* 2018, doi: 10.1016/j.camwa.2018.07.022.
[157] Q. Li, K. H. Luo, Q. J. Kang, and Q. Chen, "Contact angles in the pseudopotential lattice Boltzmann modeling of wetting," *Physical Review E - Statistical, Nonlinear, and Soft Matter Physics,* vol. 90, no. 5, p. <xocs:firstpage xmlns:xocs=""/>, 2014, doi: 10.1103/PhysRevE.90.053301.
[158] N. S. Martys and H. D. Chen, "Simulation of multicomponent fluids in complex three-dimensional geometries by the lattice Boltzmann method," (in English), *Physical Review E,* Article vol. 53, no. 1, pp. 743-750, Jan 1996, doi: 10.1103/PhysRevE.53.743.
[159] Q. Kang, D. Zhang, and S. Chen, "Displacement of a two-dimensional immiscible droplet in a channel," *Physics of Fluids,* vol. 14, no. 9, pp. 3203-3214, 2002, doi: 10.1063/1.1499125.
[160] P. RaiskinmГ¤ki, A. Koponen, J. Merikoski, and J. Timonen, "Spreading dynamics of three-dimensional droplets by the lattice-Boltzmann method," *Computational Materials Science,* vol. 18, no. 1, pp. 7-12, 2000, doi: 10.1016/S0927-0256(99)00095-6.
[161] R. Benzi, L. L. Biferale, M. Sbragaglia, S. Succi, and F. F. Toschi, "Mesoscopic modeling of a two-phase flow in the presence of boundaries: the contact angle," *Physical Review E Physical Review E - Statistical, Nonlinear, and Soft Matter Physics,* vol. 74, no. 2, pp. 021509-3755, 2006, doi: 10.1103/PhysRevE.74.021509.
[162] T. Lee and C.-L. Lin, "A stable discretization of the lattice Boltzmann equation for simulation of incompressible two-phase flows at high density ratio," *Journal of Computational Physics,* vol. 206, no. 1, pp. 16-47, 2005, doi: 10.1016/j.jcp.2004.12.001.
[163] S. P. Thampi, S. Ansumali, R. Adhikari, and S. Succi, "Isotropic discrete Laplacian operators from lattice hydrodynamics," *Journal of Computational Physics,* vol. 234, no. C, pp. 1-7, 2013, doi: 10.1016/j.jcp.2012.07.037.
[164] B. Shen *et al.*, "Depinning of bubble contact line on a biphilic surface in subatmospheric boiling: Revisiting the theories of bubble departure," *International Journal of Heat and Mass Transfer,* vol. 126, no. PB, pp. 715-720, 2018, doi: 10.1016/j.ijheatmasstransfer.2018.06.030.
[165] R. K. Sinnott, *Chemical engineering design / Ray Sinnott, Gavin Towler*, 5th ed. ed. Oxford: Oxford : Butterworth-Heinemann, 2009.
[166] F. Stachowicz, "On the connection between microstructure and surface roughness of brass sheets and their formability," *Acta Mechanica,* vol. 227, no. 1, pp. 253-262, 2016, doi: 10.1007/s00707-015-1416-1.
[167] S. Siedel, S. Cioulachtjian, and J. Bonjour, "Experimental analysis of bubble growth, departure and interactions during pool boiling on artificial nucleation sites," *Experimental Thermal and Fluid Science,* vol. 32, no. 8, pp. 1504-1511, 2008, doi: 10.1016/j.expthermflusci.2008.04.004.
[168] C. Baltis and C. van Der Geld, "Experimental investigation of the thermal interactions of nucleation sites in flow boiling," *International Journal of Heat and Mass Transfer,* vol. 78, no. C, pp. 1208-1218, 2014, doi: 10.1016/j.ijheatmasstransfer.2014.07.076.
[169] Q. Zou, "On pressure and velocity boundary conditions for the lattice Boltzmann BGK model," *Physics of Fluids,* vol. 9, no. 6, pp. 1591-1598, 1997, doi: 10.1063/1.869307.
[170] O. K. Rice, "The Effect of Pressure on Surface Tension," *The Journal of Chemical Physics,* vol. 15, no. 5, pp. 333-335, 1947, doi: 10.1063/1.1746507.
[171] R. Massoudi and A. D. King, "Effect of pressure on the surface tension of water. Adsorption of low molecular weight gases on water at 25.deg," *The Journal of Physical Chemistry,* vol. 78, no. 22, pp. 2262-2266, 1974/10/01 1974, doi: 10.1021/j100615a017.
[172] A. Hofmann, *Physical chemistry essentials*. 2018, pp. 1-499.

[173] N. Zuber, "Recent trends in boiling heat transfer research Part 1: nucleate pool boiling," *Applied Mechanics Reviews,* vol. 17, no. 9, pp. 663-672, 1964.

[174] S. Raj, M. Pathak, and M. K. Khan, "An analytical model for predicting growth rate and departure diameter of a bubble in subcooled flow boiling," *International Journal of Heat and Mass Transfer,* vol. 109, pp. 470-481, 2017/06/01/ 2017, doi: https://doi.org/10.1016/j.ijheatmasstransfer.2017.02.026.

[175] T. Mazzocco, W. Ambrosini, R. Kommajosyula, and E. Baglietto, "A reassessed model for mechanistic prediction of bubble departure and lift off diameters," *International Journal of Heat and Mass Transfer,* vol. 117, pp. 119-124, 2018/02/01/ 2018, doi: https://doi.org/10.1016/j.ijheatmasstransfer.2017.09.105.

[176] W. Fritz, "Maximum volume of vapor bubbles," *Physikalische Zeitschrift,* vol. 36, pp. 379-384, 1935.

[177] M. P. E. Institute. "Revised Release on the IAPWS Industrial Formulation 1997 for the Thermodynamic Properties of Water and Steam." http://www.iapws.org/relguide/IF97-Rev.html (accessed 29.04.2020.

[178] M. S. Cramer, "Numerical estimates for the bulk viscosity of ideal gases," *Physics of Fluids,* vol. 24, no. 6, 2012, doi: 10.1063/1.4729611.